Membrane Curvature During Cell Migration

by

Song Chen

A dissertation submitted in partial fulfillment
of the requirements for the degree of
Doctor of Philosophy
(Pharmacology)
in the University of Michigan
2021

Doctoral Committee:

Professor Carole Parent, Chair
Associate Professor Melanie Ohi
Associate Professor Manojkumar Puthenveedu
Professor Emily Scott

Song Chen

songche@umich.edu

ORCID iD: 0000-0003-0813-2545

Acknowledgements

First of all, I want to especially thank my mentor, Dr. Carole Parent, for her tremendous support and guidance throughout my PhD time. Although her lab was at the National Cancer Institute (NCI), she greatly welcomed me to do a rotation and helped me prepare all the required documents. After a fun and rewarding rotation, I was extremely lucky to join her lab. Dr. Parent is not only a passionate scientist for her work but also a great mentor, showed by her unconditional support for any idea that we have. Her mentorship greatly inspired my passion for science. Outside the lab, she is also a kind, caring, and generous friend. In 2017, I decided to accept her invitation and move to the University of Michigan (UM) with her. I am extremely grateful for my experience in the Pharmacology Department at UM. The training at Pharmacology not only prepared me as a young scientist but also fostered my interest in my further studies. Then, I want to thank the members of my thesis committee: Drs. Melanie Ohi, Manojkumar Puthenveedu, and Emily Scott. They have provided valuable suggestions and support for my thesis.

Second, I wish to thank all current and past members in the Parent laboratory at UM, including Peilin Shen, Dr. Shuvasree SenGupta, Dr. Cosmo Saunders, Dr. Subhash Arya, Fatima Javed, Lauren Bailey, Kristen Loesel, Yang Xu, Rachael Baliira, Jingyi Li, Shehroz Malik, Gaurie Gunasekaran, Emma Theisen, Jason Zhang, Dr. Ritankar Majumdar, and Yating Zheng. I also would like to thank all the members in the Parent lab at NCI, including Drs. Christina Stuelten, Paul Kriebel, Weiye Wang, and Bhagawat Subramanian. They not only provided me numerous helpful suggestions on my research but also made the Parent lab a fun and stimulating environment.

Next, I want to express my special appreciation to all the colleagues and collaborators for their great contributions to this thesis. I thank Dr. Wolfgang Losert, Dr. John Fourkas, Dr. Leonard Campanello, and Matt Hourwitz from the University of Maryland (UMD) for their significant contributions to studies in Chapter 2 and Chapter 3. They not only supplied us with the nanotopograhies, but also tremendously helped us with experiment design, data analysis, and manuscript preparation. I am very grateful that I had the opportunity to learn their expertise in physics and chemistry. In addition, Drs. Rachel Lee and Chenlu Wang from the Losert lab and Dr. Xiaoyu Sun from the Fourkas lab also provided valuable input on studies in Chapter 2. From the UM, I would like to thank Dr. Melanie Ohi and her lab members, Dr. Kelly Manthei, Dr. Louise Change, Dr. Clarissa Durie, Jessica Hanks, as well as Yating Zheng from the Parent lab for their tremendous help on studies in Chapter 4.

I also appreciate all the funding sources that supported my graduate studies, including the NCI-UMD Partnership for Integrative Cancer Research (NCI and UMD), the Lucchesi Predoctoral Fellowship (UM), the LSI Cubed Funding (UM), and Funds from the University of Michigan School of Medicine.

In the Pharmacology Department, I want to thank Drs. Lori Isom and Margaret Gnegy for their great leadership in the department and education. I thank Drs. Steve Fisher, Yoichi Osawa, and Ronald Holz for practicing my student seminars and helping me become a good presenter. I also want to thank my prelim committee members, including Drs. Alan Smrcka, Manojkumar Puthenveedu, and Leslie Satin for their tremendous support on my prelim. I would like to thank the administration staff in the Pharmacology Department for their help on everything outside of the science, including Elizabeth Oxford, Josh Daniels, Ingrid Shriner-Ward, Dar-Weia Liao,

Chereen Mroz, Denise Gakle, Nancy Katon, Dennis Ondreyka, Eileen Ferguson, Audrey Morton-Dziekan, and Lisa Garber.

Finally, I want to thank all my family members, especially my parents, Cuiping and Minwei, for their constant support throughout my graduate studies. Although my father had been paralyzed after cerebral bleeding for many years before he passed away, he always unconditionally supported me to study abroad and go after my dreams. My mother took all of the responsibilities to take care of my father and only asked me to focus on my study. Their love has been extremely important to me and I would not have achieved what I have now without them.

Table of Contents

List of Figures

List of Tables

List of Movies

Abstract

Biological membranes serve as a physical barrier of cell and organelles. In addition, as biological membranes house numerous proteins, they also act as signaling hubs involved in the regulation of a wide array of cellular functions, including proliferation, differentiation, communication, and migration. Migrating cells can deform their plasma membrane to adapt to structural features in their environment, and reorganize their behaviors accordingly. In addition, when responding to extracellular chemical stimuli, cells are undergoing extensive endocytosis and exocytosis thereby continuously generating intracellular membrane curvatures. However, the mechanisms by which cells sense and transmit outside structural features to generate specific responses remain mostly unknown.

The work described in this thesis aims to assess the role of extracellular and intracellular membrane curvatures during two processes that have key relevance to human health: breast cancer invasion and neutrophil-mediated inflammation. Numerous studies suggest that structural features within the cancer cell microenvironment are key regulators of cancer invasion and metastasis. Using aligned nanoscale ridges and asymmetric sawtooth structures, I explored the effects of surface topography on the migration phenotype of multiple breast cancer cell lines. I discovered that asymmetric sawtooth structures unidirectionally bias the movement of breast cancer cells in a cell-type dependent manner. I went on to show that the biased migration is driven by unidirectional actin polymerization, and regulated by distinct cortical plasticity and focal adhesion patterns. Together, this work highlights the significance of extracellular matrix (ECM) topographies in

cancer invasion and suggests that cell-ECM interactions are potential target to prevent cancer dissemination.

In the context of tissue injury or inflammation, nearby neutrophils migrate directionally to inflamed/injured sites and trigger a dramatic swarm-like recruitment of distant neutrophils by secreting the secondary chemoattractant leukotriene B_4 (LTB_4) - a process referred to as signal relay. In this context, I studied how extracellular topographies regulate neutrophil recruitment. I found that neutrophils plated on nanoridges spread and exhibit rapid calcium flashes in the absence of chemical stimuli and adhesion ligands. Remarkably, I further showed that these responses are regulated by cell membrane curvatures, as I found that neutrophil activation is mediated by β_2 integrins, and that active β_2 integrins cluster on the side walls of the nanoridges. In a parallel project, I studied how neutrophils package and release LTB_4. LTB_4 is synthesized from arachidonic acid (AA) through the sequential action of the 5-lipoxygenase (5-LO) and its associated activating protein (FLAP). LTB_4 and its synthesizing enzymes are packaged and released in extracellular vesicles called exosomes. The biogenesis of these vesicles is initiated at the nuclear envelope through the hydrolysis of nuclear AA, and the genesis of ceramide microdomains via the activation of the neutral sphingomyelinase. I aimed to visualize the structural organization of FLAP in defined lipid environments and assess if they form membrane curvatures similar to what is observed at the nuclear envelope of activated neutrophils. By reconstituting FLAP into lipids and visualizing the membrane organization of the protein:lipid assemblies using negative staining electron microscopy (EM) and cryogenic EM, I found that FLAP is assembled into specific “wagon-wheel” structures with potentially two membrane layers and multiple protrusions between the two layers. Collectively, the findings presented in my thesis reveal a novel

role for membrane curvatures in regulating various physiological and pathological processes, and provide guidance for future research.

Chapter 1

General Introduction

1.1 The overview of membrane curvature in cellular processes

Biological membranes, composed of amphiphilic phospholipids and various membrane-associated proteins, separate the cell interior from the outside environment as well as compartmentalize diverse organelles. While housing numerous receptors and channels and serving as a signaling hub, membranes are highly dynamic and can readily change shape to facilitate different cellular functions (McMahon and Boucrot, 2015). Migrating cells curve their plasma membranes to accommodate the topographic features of the extracellular matrix (ECM) (Fig. 1.1). More than passively adapting to the environment, cells are capable to bend plasma membrane outward or inward for different functions, such as actin-driven filopodium formation or clathrin-mediated endocytosis (McMahon and Gallop, 2005) (Fig. 1.1). Also, membranes of many intracellular organelles and compartments display highly complex shapes (Voeltz and Prinz, 2007) (Fig. 1.1). For example, the endoplasmic reticulum (ER) consists of nanoscale tubules and stacked micron-wide sheets that are interconnected into a perinuclear three-dimensional network (Terasaki et al., 2013; Voeltz et al., 2002). The inner membrane of mitochondria invaginate inward and forms lamellar cristae with 10-40 nM thickness, a shape that is also observed in the Golgi apparatus (Ladinsky et al., 1999; Palade, 1953). Furthermore, the membrane of endosomes is able to bud into the lumen, leading to the formation of multivesicular bodies (MVBs) (Hanson and Cashikar, 2012). In this chapter, we first describe how cells sense and respond to the extracellular curvatures

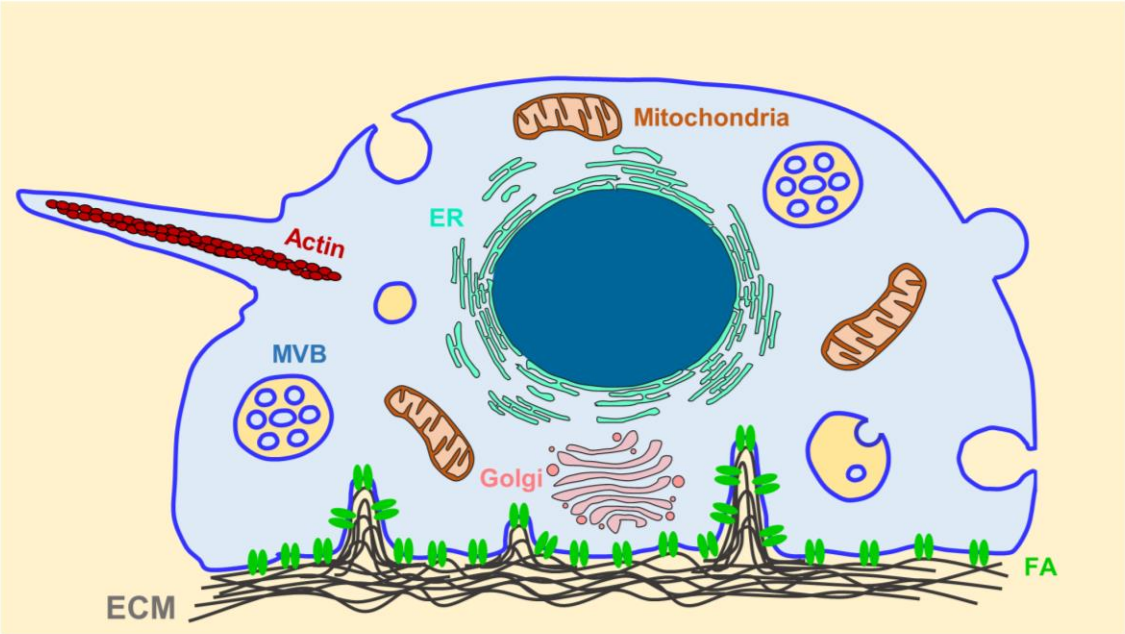

Figure 1.1: Schematic illustration of membrane curvature across different cellular compartments. First, cells can bend their plasma membrane (PM) to adapt the shape of extracellular structures. Second, actin fibers induce negative membrane curvature at cell PM for protrusion formation, such as filapodia or lamellipodia. In addition, endocytosis results in positive curvature at cell PM and endocytosed vesicles can further bud inwards to form MVBs. Finally, many intracellular organelles exhibit complex morphologies with high curvatures, like ER, Golgi apparatus, and mitochondria.

in the environment. In the second part, we will showcase typical examples of membrane curvature generated inside cells and discuss the molecular mechanisms involved.

1.2 Outside-in: sensing the extracellular curvatures

Cells in living tissues are embedded in a complex, well-defined ECM with tissue specificities. The ECM in tissues shows distinct chemical compositions and topographic features ranging from nanometers to micrometers (Frantz et al., 2010). Cells interact with ECM biochemically through signaling events and physically by changing morphology, a process termed as contact guidance. It is well accepted that the cell-ECM interaction plays a critical role in regulating cell behaviors and is involved in many pathological processes (Frantz et al., 2010). Meanwhile, tissue ECM is a highly dynamic entity that can be remolded and reconstituted throughout the whole lifetime (Robins, 2007). In this part, we first describe the structural characteristics of the ECM in several typical tissues and how scientists engineer nanotopographies to mimic the ECM *in vivo*. Then, we focus on how cell-ECM interaction regulates different cell functions. Lastly, we discuss the current understanding of the mechanisms by which cells sense and respond to the topographic features of the ECM.

1.2.1 The ECM in living tissues

The ECM in living tissue is a non-cellular three-dimensional (3D) scaffold that physically supports various embedded cell populations and biochemically interacts with these cells to maintain proper tissue morphogenesis and homeostasis. The ECM is not only heterogeneous and tissue-specific but also highly dynamic. That is, the ECM can be modified and reconstituted

throughout our lifetime. Here, we will showcase the ECM in representative tissues, including the heart, bone, and mammary gland.

1.2.1.1 Heart

The heart is a typical tissue example with complex and multiscale structures in its ECM. A variety of cells are embedded in heart ECM in a well-organized manner (Lockhart et al., 2011). The ECM architecture in the heart is composed of nano- and microscale aligned collagen and elastin bundles and interconnected basement membrane with adhesive molecules (*e.g.* laminin, fibronectin) as well as proteoglycans (Lockhart et al., 2011; Parker and Ingber, 2007). The fibers in the heart ECM also display different topographic signatures, such as cables, weaves, and coils (Ott et al., 2008) (Fig. 1.2A). The most striking feature of heart ECM is that both nanometer-sized fibrils and microscale cross-linked fiber struts that support the cardiomyocytes are well oriented in an anisotropic way (Kim et al., 2010) (Fig. 1.2B). In this defined ECM network, cardiomyocytes are forced to stretch along with the fiber orientation and mechanically coupled end-to-end in the longitude direction as well as side-to-side in the transverse direction (Parker and Ingber, 2007). This cell-ECM intertwined organization assures the cell contractility and intercellular electric connectivity that are essential for blood pumping and other heart functions (Parker and Ingber, 2007). A disruption of the fibrillary ECM network attenuates the heart systolic response without affecting the cell contractile ability (Badylak et al., 2003). Moreover, dysregulation of the ECM homeostasis and cell-ECM interaction can initiate many heart diseases, such as fibrosis, arrhythmia, and hypertension (Berk et al., 2007; Bing et al., 1997).

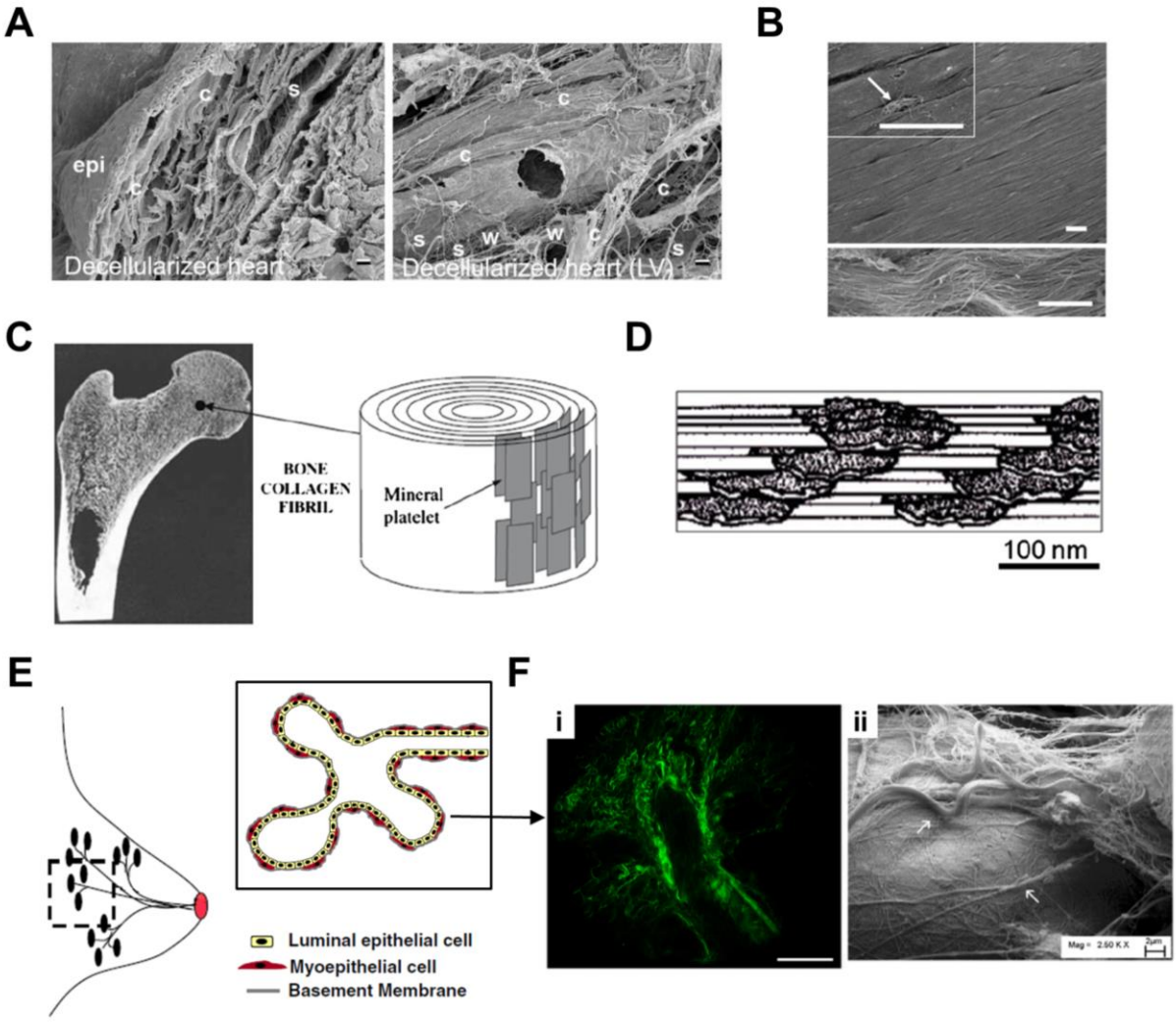

Figure 1.2: The ECM in heart, bone, and mammary gland. (A) Representative scanning electron microscopy (SEM) images of decellularized rat left ventricular (LV) and right ventricular (RV) myocardium. Weaves (w), coil (c), struts (s), and dense epicardial fibers (epi) in the ECM are labeled in images. Scale bars: 50 um. Reproduced with permission from (Ott et al., 2008). (B) SEM images of ex vivo myocardium of adult rat heart. The insert and bottom image highlight the anisotropically aligned collagen fibrils. Scale bars: 10 um. Reproduced with permission from (Kim et al., 2010). (C) The nanoscale structures of cortical bone are composed of plate-like mineral crystals with a width of 2-4 nm and a length of 100 nm. (D) Cross-sectional view of bone structures, demonstrating that the crystals are embedded in the collagen matrix. C is reproduced with permission from (Gao, 2006). D is reproduced with permission from (Gao et al., 2003), Copyright (2003) National Academy of Sciences, U.S.A. (E) A cartoon illustration of the tree-like structure of the human mammary gland. The lumen is separated from the stroma by a bilayered epithelium and a basement membrane. Reproduced with permission from (Ghajar and Bissell, 2008). (F) Multiphoton microscopy image (i) and SEM image (ii) of mouse mammary gland ducts, which illustrate the collagen matrix wrapped around the duct as well as the characteristics of collagen fibrils interacting with epithelium cells. Reproduced with permission from (Provenzano et al., 2006).

1.2.1.2 Bone

Another tissue of which the ECM has been extensively investigated is bone. As one of the most important organs, bone provides a supportive framework for the human body, produces red and white blood cells, and stores essential minerals, such as calcium, phosphate, and magnesium. The ECM of bone is a unique nanocomposite material made of a collagen-based organic component and inorganic minerals (Gentili and Cancedda, 2009) (Fig. 1.2C). In bone, nearly 90% of the organic matrix, also termed as osteoid, is collagen, and type 1 collagen is the dominant isoform (Gentili and Cancedda, 2009). The collagen network supports cell adhesion and proliferation and determines the bone tensile strength (Alford et al., 2015). The inorganic carbonate-substituted hydroxyapatite (HA) is deposited as nanometer-scale crystallites in the grooves formed by 3D collagen fibrils (Fraser et al., 1983; Weiner and Traub, 1986) (Fig. 1.2C & D). These HA crystallites, about 50 nm long, 25 nm wide, and 2-5 nm thick (Fig. 1.2C & D) control the bone compressive strength and act as chelating agents for bone mineralization by osteoblasts (Johansen and Parks, 1960; Robinson, 1952). Although considered as the strongest tissue in the human body, bone is often subjected to defects and damages, leading to a medical need for artificial bone grafts (Chan et al., 2006). Combining a collagen scaffold and HA, previous studies have shown that the biomimetic bone scaffolds decorated with HA particles enhance osteoblast growth and stimulate mineralization compared to the ones without HA decoration (Chan et al., 2006; Sachlos et al., 2006). Furthermore, deficiencies or mutations in collagen, imbalanced mineralization, and disrupted cell-ECM interaction can increase bone brittleness, stiffen bones for fracture and damage, or result in other pathological conditions (Alford et al., 2015).

1.2.1.3 Mammary gland

The ECM is also believed to play a critical role in the development and morphogenesis of the mammary gland. The most remarkable feature of the mammary gland, known as the organ that produces milk for nursing offspring, is its tree-like structures composed of many-branched tubes (Ghajar and Bissell, 2008) (Fig. 1.2E). Compared to other glandular organs, such as lung and kidney, the mammary gland is unique because the majority of its branching and remodeling is postembryonic, a process that takes place during puberty and pregnancy in females (Fata et al., 2004). Mammary ducts consist of a bilayered epithelium, in which a layer of luminal epithelial cells line the duct with associated myoepithelial cells lining the basal surface (Ghajar and Bissell, 2008) (Fig. 1.2E). A mesh-like basal membrane (BM), majorly rich in laminins and type IV collagen, separates the epithelial cells from the less structured surrounding stroma (Fata et al., 2004; Keely et al., 1995). Using both multiphoton microscopy and electron microscopy imaging, previous studies have demonstrated that a highly organized network of fibrillary collagen wraps around the epithelial cells in different directions (Provenzano et al., 2006) (Fig. 1.2F). This fiber mesh not only provides a physical constraint for the cells but also has small gaps allowing cells to interact with the stromal collagen fibers (Provenzano et al., 2006) (Fig. 1.2F). Close imaging of the interstitial ECM near the mammary ducts reveals that both straight and wavy collagen fibers are present in the stroma (Provenzano et al., 2006) (Fig. 1.2F). These collagen fibers, composed of type I collagen, are bundles of nanoscale collagen filaments (Fata et al., 2004; Provenzano et al., 2006). Interestingly, the curvature of the wavy collagen fibers is at a scale of several microns that is smaller than the size of an individual cell (Provenzano et al., 2006) (Fig. 1.2Fii). The ECM composition and structure are distinct when different locations along the ducts are compared, which is believed to be critical for proper branching morphogenesis (Fata et al., 2004; Wicha et

al., 1980). Moreover, the growth and remodeling of the ECM in the mammary gland is also of great interest in breast cancer research (Schedin and Keely, 2011).

1.2.2 The advance of nanofabrication techniques

As illustrated previously, the ECM in living tissues exhibits sophisticated 3D topographic features at different length scales and regulates cell functions through its direct or indirect interaction with cells. Although a myriad of works has studied the cell-ECM interaction *in vivo* (Alexander et al., 2008; Provenzano et al., 2006; Wolf et al., 2013), the biophysical and molecular mechanisms governing and regulating this interaction are still obscure. The challenges that prevent researchers from dissecting the mechanisms *in vivo* include uncontrolled influence from other environmental factors, complexity and diversity of ECM composition and topographic structures, and limited imaging and manipulating resolution at the singe-cell and/or subcellular level. However, using standard 2D culture, most *in vitro* studies failed to recapitulate the cell behaviors *in vivo* because of the difficulty to mimic the *in vivo* microenvironment (Cukierman et al., 2001; Grinnell, 2003). Recent advance in nanofabrication techniques has offered scientists great tools to engineer bio-inspired materials that resemble the ECM *in vivo* and to investigate the influence of ECM topographies on cell functions. In this section, we review current nanofabrication techniques for patterning surfaces in fundamental biological studies.

1.2.2.1 Electron-beam lithography

First developed by the semiconductor industry, electron-beam lithography (EBL) uses a magnetically focused beam of electrons to scan a surface that is pre-coated with an electron-sensitive resist, which changes the solubility of the exposed area in specific solvents (C. Vieu,

2000). After metal deposition, the substrate is exposed to a proper solvent to etch the beam-scanned or non-scanned area, leading to the formation of the desired metal pattern that is complementary to the pattern of coated resist (Betancourt and Brannon-Peppas, 2006; C. Vieu, 2000). With a careful development of the coating resist and a tightly focused beam, an approximate 10 nm resolution can be achieved (C. Vieu, 2000). When comprised of chemically manipulated materials, patterned substrates generated by EBL can selectively absorb specific proteins or adhesive molecules (J. W. Lussi 2005). In contrast to the protein absorption method, ECM-coated substrates can be scanned with high-energy electron beams to locally denature the ECM proteins and achieve desired ECM patterning (Rundqvist et al., 2007). However, high cost in instrumentation and maintenance, tedious operations, and limited material options confine the use of this technique in biological studies.

1.2.2.2 Electrospinning

Fibrous structures, a common ECM architecture in most tissues, can be fabricated by electrospinning micro- or nanoscale polymer fibers on the substrates. Under an external electric field, the body of a polymer solution becomes charged and the droplet extruding from the spinning tip is stretched to a cone-shape, a result of the antithetical effect of surface tension and electrostatic repulsion (Xue et al., 2019). Above a threshold voltage, a stream of the polymer solution jets out of the droplet surface towards the substrates (Xue et al., 2019). As the solvent evaporates in flight, the jets become solidified and elongated due to the electrostatic repulsion, then are deposited on the substrate as long and thin polymer fibers in a random fashion (Xue et al., 2019). To partially align the fibers, a rotating collector can be used and the alignment degree is defined by its rotating speed (Baker and Mauck, 2007). Using this technique, non-woven fiber mats can be collected with

fiber diameters on the scale of several hundred nanometers (Baker and Mauck, 2007). Moreover, fiber density, fiber diameter, and mechanical strength of the fibers are tailorable by changing operation parameters and by manipulating the composition of materials (Deitzel JM, 2001; Reneker DH, 1996). Because the resulted fibrous structure shares numerous similar features with native ECM, electrospinning is one of the most widely used and most promising techniques for biological applications. However, electrospun fiber meshes are usually considered as 2D surfaces because the gaps between fibers are not large enough for cells to migrate into the meshes. In addition, it is challenging to fabricate the electrospun fibers with subtle geometries or topographies to meet the complexity of *in vivo* ECM.

1.2.2.3 Multiphoton absorption polymerization

Another well-developed method for fabricating nanoscale topographies is multiphoton absorption polymerization (MAP), two-photon absorption in most cases. In contrast to single-photon excitation, a process in which the absorption rate remains approximately constant along a laser beam, two-photon excitation requires two photons with a doubled wavelength to reach the same region for effective absorption, resulting in the highest absorption rate at the focused point of the laser beam (Alexander K. Nguyen, 2017; LaFratta et al., 2007). When the laser beam is applied to a prepolymer resin containing photoinitiators, polymerization at the exposed area is triggered but not at the unexposed area (Alexander K. Nguyen, 2017; LaFratta et al., 2007). Acrylic resins are usually used as the prepolymer material in MAP due to their commercial availability, high cross-linking rate, and resistance to harsh solvents or high temperatures (LaFratta et al., 2007). In a vicious form, the nonpolymerized acrylic resin can be removed by washing the sample with a solvent, such as ethanol (LaFratta et al., 2007). The resolution of the MAP is determined by the

size and shape of voxels, the width of which is around 300 nm (Alexander K. Nguyen, 2017; LaFratta et al., 2007). However, a voxel that has a size under the diffraction limit can be achieved by combining with other optical and chemical techniques (K. Takada, 2005). A variety of nanoscale topographies with tunable parameters in every dimension have been created by MAP, including aligned nanoridges, asymmetric sawteeth, nanoposts, curved ridges, and kinked ridges (Sun et al., 2018). As an appealing feature for biological applications, these topographies fabricated with acrylic resins are ready to be coated by ECM proteins, such as collagen and fibronectin (Sun et al., 2018). Moreover, the patterned substrates can serve as master molds to produce a large number of replicas with identical topographies (Sun et al., 2018). Considering its numerous advantages, MAP is used as the fabrication technique to generate topographies for the work in following chapters.

1.2.3 The bio-inspired topographies mimic native ECM and regulate cell functions

As mentioned in the previous section, current nanofabrication techniques have inspired a rapid growth of materials that recapitulate native *in vivo* environment, which enables scientists to further understand the cell-ECM interaction. Growing studies have shown that engineered nanotopographies not only have the capability of regenerating cell behaviors *in vivo*, but can also influence numerous cell functions, such as cell polarity and migration, cell differentiation, and cell-cell communication.

1.2.3.1 Cell polarity and migration

A wide variety of cell types are able to sense the topographies on the surface, alter their morphologies, and ultimately exhibit different migration phenotypes. The stretched shape and

anisotropic alignment of cells can be essential for many organs and their physiological functions, such as the heart and muscle. Previous analysis of *ex vivo* rat myocardium revealed that the matrix fibers underneath the myocardial layer are well uni-directionally aligned and have a diameter approximate to 100 nm (Kim et al., 2010). The myocyte orientation strongly correlates with the alignment of ECM fibers, emphasizing the importance of topographic cues for heart organization and contraction. In early studies, arrays of anisotropic micron-size ridges or grooves are extensively used to restore the aligned myocardial organization in the heart (Deutsch et al., 2000; Motlagh et al., 2003). Although cardiomyocytes cultured on these micro-patterned surfaces exhibit a number of *in vivo*-like behaviors, such as elongated morphology and synchronized contraction (Deutsch et al., 2000; Motlagh et al., 2003), the cell-topography interaction is somewhat restricted because myocytes often became isolated on top of a single ridge or within a single groove. Recent advance in fabrication techniques has realized the generation of well-defined nanotopographies that better mimic the heart ECM fibers (Carson et al., 2016; Kim et al., 2010). Using substrates with 800 nm wide, 500 nm tall, and 800 nm separated grooves, Kim *et al.* demonstrated great myocyte alignment in monolayer, anisotropic action potential propagation as well as elevated connexin43 expression (Kim et al., 2010) (Fig. 1.3A). Surprisingly, these cell behaviors are sensitive to the dimensions of nanotopographies (Carson et al., 2016; Kim et al., 2010) and can be dynamically reorganized by modifying the physical environment in real-time (Mengsteab et al., 2016). Electrospun fibers (Badrossamay et al., 2010; Orlova et al., 2011; Zong et al., 2005) and other topographies (Luna et al., 2011) have also been employed to control cardiomyocyte morphology and functions.

During wound healing, fibroblasts rapidly migrate into the wounded site, synthesize fresh ECM, and remodel the overall tissue structure, a process that involves substantial fibroblast-ECM

interaction and directed migration. Fabricated topographies, particularly ridges or grooves, have been applied to model the dermal ECM and study the fibroblast-ECM interaction during wound healing (Anastasios Marmaras, 2012; Kim et al., 2009b; Kim et al., 2017b; Lee et al., 2018). Firstly, fibroblasts can strongly polarize and align their bodies along with the orientation of ridges or grooves with variable sizes, and exhibit directed migration (Kim et al., 2009b; Kim et al., 2017b; Lee et al., 2018) (Fig. 1.3B). In scenarios mimicking a wound healing process, either culturing fibroblasts on patterned surfaces or mounting patterned patches on the top of cells accelerates the wound closure by guiding cell migration (Anastasios Marmaras, 2012; Lee et al., 2018). Interestingly, Kim *et al.* designed a substrate with a continuous gradient of microscale ridges and observed the fastest speed for both individual and collective cell migration at an intermediate ridge density, which may provide a mechanism for efficient wound healing (Kim et al., 2009b) (Fig. 1.3B).

Directed cell migration guided by anisotropic topographies is also reported for T cells (Kwon et al., 2013; Kwon et al., 2012), neutrophils (Tan and Saltzman, 2002), endothelial cells (Potthoff et al., 2014), neural progenitors (Arocena et al., 2017), cancer cells (Tzvetkova-Chevolleau et al., 2008), as well as non-mammalian cells (Driscoll et al., 2014). Although T cells stretch their cell bodies to a much lesser extent as fibroblasts do on nanoridges, they can form polarized lamellipodia along the direction of nanoridges (Kwon et al., 2013; Kwon et al., 2012). Strikingly, adhesions are dispensable for topography-guided migration of T cells under confinement (Kwon et al., 2012). Moreover, microscale gratings with a depth of 1000 nm have been shown to enhance the counterflow migration of endothelial cells and modulate cell signaling activity to a higher level than that of cells on shallower gratings (Potthoff et al., 2014). In addition

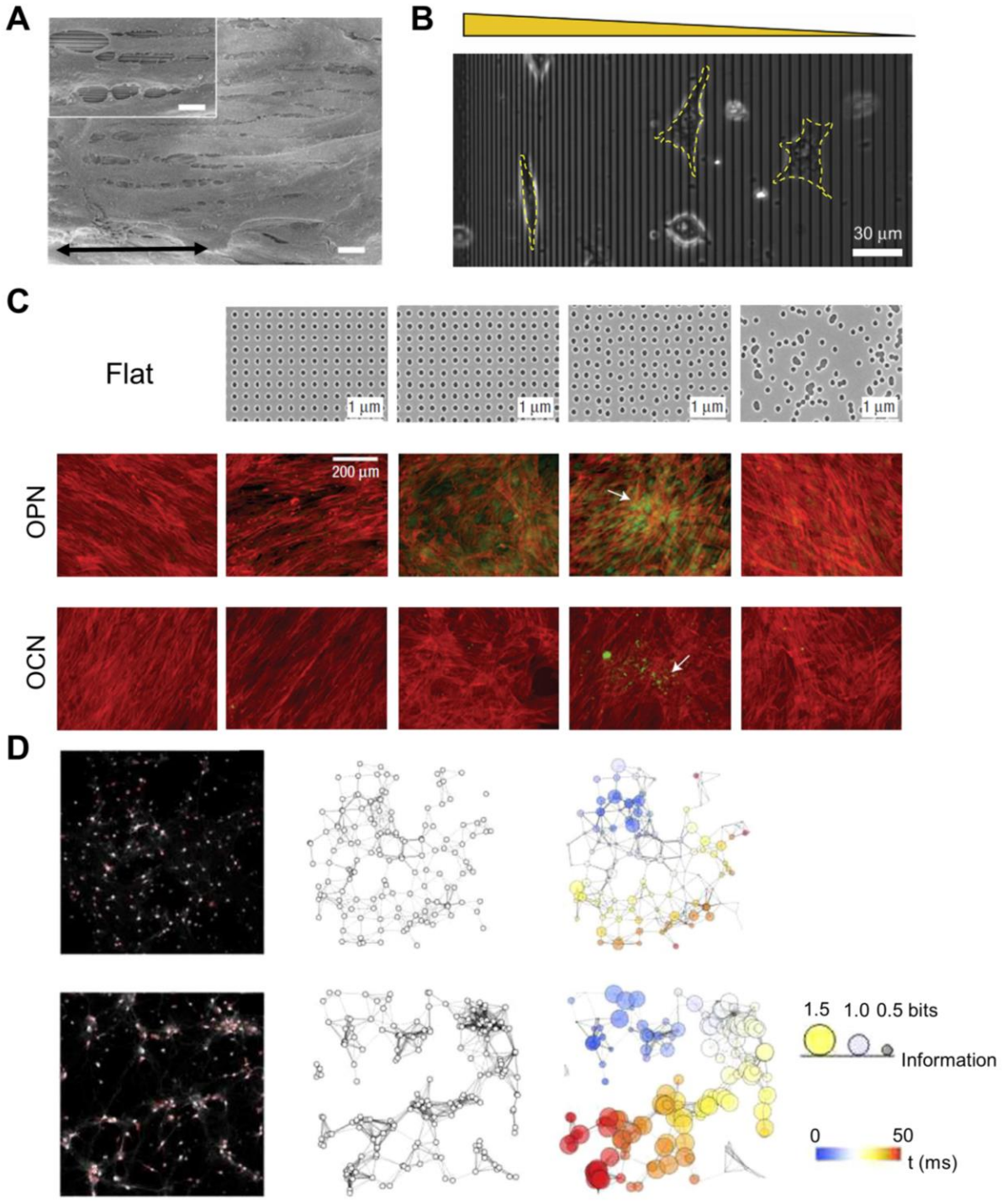
A
B
30 μm
C
Flat
1 μm
1 μm
1 μm
1 μm
OPN
200 μm
OCN
D
1.5 1.0 0.5 bits
Information
0
50
t (ms)

Figure 1.3: Surface topography regulates various cellular functions. (A) SEM image of rat ventricular myocytes on nanoscale grooves showing the anisotropic alignment of cardiomyocytes. The insert highlights the intercellular junctions between myocytes in the monolayer. Reproduced with permission from (Kim et al., 2010). (B) Phase-contrast image of NIH 3T3 fibroblast on nanoscale ridges with graded spacing shows the cell morphology difference associated with density change of the underlying topography. Reproduced with permission from (Kim et al., 2009b). (C) Osteopontin (OPN) and osteocalcin (OCN) staining of hMSCs cultured on nanofabricated substrates for 21 days. Top row are images of fabricated arrays of nanopits with different randomness. The pits all have dimensions of 120 nm in diameter, 100 nm in depth, 300 nm pitch between centers with arrangement of hexagonal, square, displaced square (50 nm from the original center) and totally random. Enhanced OPN and OCN levels were observed in cells on nanopits with a displaced square arrangement. Reproduced with permission from (Dalby et al., 2007). (D) Surface topography and roughness influence neuron intercommunication. Left column: confocal images of neural cells on flat (top) and rough silicon substrate (bottom); Middle column: artificial neural networks reproduced from the confocal images; right column: computer simulation results suggesting the increased information transport efficiency in small neural networks, circle diameter correlates with the information transmitted between over the cell networks during the indicated time frame. Reproduced with permission from (Onesto et al., 2017).

to normal cells, metastatic cancer cells also polarize and migrate bi-directionally in response to nanoridges (Chen et al., 2019; Ray et al., 2017a; Tzvetkova-Chevolleau et al., 2008).

Artificial topographies other than anisotropic ridges or grooves can also regulate cell polarity and migration. Isotropic nanopillar arrays with a changeable spacing can induce a different degree of mouse stem cell polarization, yet the cell orientation is random (Bucaro et al., 2012). Moreover, Kim *et al.* demonstrated that the angle of slanted nanocilia dictates the polarized orientation of fibroblasts and that cells transit from a bi-directional polarization pattern on vertical nanocilia arrays to a uni-directional polarization pattern on nanocilia arrays with a slanted angle of 30° (Kim et al., 2017a). Thus, manipulating the surface topographic features appears to be a robust and inexpensive method to regulate cell polarity and migration for desired cell functions.

1.2.3.2 Cell differentiation

During tissue development and morphogenesis, multipotent stem cells strongly rely on numerous chemical and physical cues in the microenvironment to determine their cell fate. Taking the mammalian brain as an example, neural stem cells first give rise to neural progenitor cells that can further differentiate into distinct cell lineages, such as neurons, oligodendrocytes, and astrocytes (Obernier and Alvarez-Buylla, 2019). The differentiation of progenitors into these cell populations as well as different neuron subtypes must be tightly controlled for brain homeostasis and injury repair (Tang et al., 2017; Vieira et al., 2018). In addition to soluble factors and ECM components, growing evidence suggests a critical role of topographic cues in neuronal differentiation (Marcus et al., 2017; Moore and Sheetz, 2011). Biocompatible nanofibrous scaffolds can promote neural stem cells or progenitors favorably differentiate into neurons (Silva et al., 2004; Xu et al., 2010). When cultured on microscale parallel gratings with a 4 μm depth,

murine neural progenitor cells preferentially differentiate into neurons over astrocytes even in the astrocyte induction media, highlighting the independent effect of surface topographies on cell differentiation (Chua et al., 2014). Considering the fact that neurons are electronically active, Yang *el al.* combined anisotropic nanoridges with electrical stimuli and found that these two stimulation cues act synergistically to bias the differentiation of human neural stem cells towards the neuronal lineage (Yang et al., 2017). Interestingly, further analyses demonstrated that among the differentiated cells GABAergic and dopaminergic neurons are favored rather than glutamatergic neurons (Yang et al., 2017). Furthermore, the neuronal differentiation can be enhanced under co-culture conditions with astrocytes on patterned substrates, probably resulted from an effect of secreted factors from the astrocytes (Delgado-Rivera et al., 2009; Recknor et al., 2006). The preferential differentiation into neurons has also been reported for human mesenchymal stem cells (hMSCs). Cells cultured on surfaces patterned with nanogratings upregulate the expression of numerous neuronal markers, such as microtubule-associated protein 2 and β-Tubullin III (Teo et al., 2013; Yim et al., 2007).

The differentiation of osteoblasts, a highly specialized cell type that synthesizes and mineralizes the ECM in bone, is a key factor for bone development, remodeling, and repair (Rutkovskiy et al., 2016). The significance of physical cues in osteoblast formation has been recognized by previous studies (Kilian et al., 2010; Kim et al., 2015; McBeath et al., 2004). For example, You *et al.* showed that differentiation toward the osteoblast lineage can be synergistically enhanced by culturing hMSCs on periodic nanodots or parallel nanoridges in induction media (You et al., 2010), a phenomenon validated by Lauria *et al.* using surfaces with micropillar patterns (Lauria et al., 2016). Interestingly, arrays of slightly disordered nanopits have a superior osteogenesis potential than that of either totally ordered or random patterns (Dalby et al., 2007)

(Fig. 1.3C), highlighting the importance of the overall layout of topographies on cell behaviors. Moreover, a minor modification of the dimensions of nanotopographies is sufficient to dramatically increase their ability to guide the differentiation of hMSCs toward osteoblasts (Oh et al., 2009), which underlines the need to precisely design topographies for biomedical applications.

The role of topographies in the differentiation of hMSCs toward other cell lineages, such as adipocytes and myoblasts (da Silva Meirelles et al., 2006), has also been explored (Ahn et al., 2014; Dang and Leong, 2007; Li et al., 2012; Yu et al., 2013). Dang and Leong reported that in the absence of inductive agents aligned electrospun nanofibers induce the myogenic differentiation of hMSCs as a result of cell polarization and nuclear elongation (Dang and Leong, 2007). Strikingly, E.H. Ahn *et al.* unearthed that the cell fate of hMSCs can be biased toward either adipocytes or osteoblasts solely by changing the density of nanoposts on the substrates (Ahn et al., 2014). These studies hence prove that nanotopographic surfaces can be considered as excellent tools to direct stem cell differentiation for tissue regeneration and medical purposes.

1.2.3.3 Cell-cell communications

Cells in living tissues are not isolated but rather in continuous conversation. The control of cell-cell communication in a precise spatiotemporal manner is required for the establishment and maintenance of many organs, such as the brain (Sheikh et al., 2019), muscle (Demonbreun and McNally, 2017), and vascular system (Darland and D'Amore, 2001), and its disruption can cause developmental disorders (Mattes and Scholpp, 2018). The pivotal role of intercellular communication is especially evident for the mammalian brain, where diverse cell types transmit chemical and electrical signals. Topographic cues, in combination with other extracellular cues, are integrated by neural progenitors to support their neuronal differentiation (Silva et al., 2004),

neurite outgrowth (Klymov et al., 2015), as well as cell-cell communication (Simitzi et al., 2017). As a fundamental process for axon and dendrites formation and an effective connection, neuronal growth can be mediated by nanotopographic stimulus (Mi-Hee Kim, 2014; Staii et al., 2011). The optimal effect of topographies on neurite outgrowth has been reported by Li *et al.* using substrates decorated with an intermediate density of microparticles (Li et al., 2010) as well as by Dowell-Mesfin *et al.* in which rat hippocampal neurons are cultured on arrays of pillars with a width of 2 μm and a pitch of 1.5 μm (Dowell-Mesfin et al., 2004). Furthermore, Jang and co-workers fabricated topographic patterns composed of nanoridges with different ridge-to-groove ratios (ridge width: 350 nm, groove width: 1, 2, 3, 5 times 350 nm) and found that mouse neuroblasts extend the longest neurites along with the orientation of ridges on surfaces with a 1:5 ridge-to-groove ratio (Jang et al., 2010). These findings demonstrate the ability of neurons to sense topographic layout and dimensions.

Since neurons cluster into small networks and communicate through electrical and chemical signals, the effect of topographies on these behaviors has also been investigated. Self-assembled nanofibers (Ashleigh Cooper, 2012), islands of high-density carbon nanotubes (Tamir Gabaya, 2005), and silicon chips with nanoscale pores (Marinaro et al., 2015) have been used to improve neuron viability and promote the formation of neuron networks. In addition, lattices of cylindrical pillars at a micron-scale drive neurons to project between pillars and organize into an interconnected 3D network (Limongi et al., 2013). It is hypothesized that nerve cells in these networks are linked by a limited number of steps, probably resulting in more efficient signal transmission. Indeed, Onesto *et al.* discovered that when plated on silicon substrates with a defined nano-level topography and roughness mouse primary neurons within the small networks are more electrically active and frequently fire spontaneous calcium spikes, underlining the enhanced local

intercellular connectivity (Onesto et al., 2017) (Fig. 1.3D). Similarly, increased synaptic contact and hyperexcitability of neural cells can be achieved by the use of graphene surfaces with microscale ripples and wrinkles (Tang et al., 2013). Besides the inter-neuron communication, topography-mediated regulation of cell-cell communication between astrocytes or heterocellularly between neurons and astrocytes is also explored by other studies (Blumenthal et al., 2014; Lee et al., 2014).

Heart and skeletal muscle are two other electro-active organs, where cell-cell communication is crucial. The elongated morphology and connexin43-based cell-cell contact of cardiomyocytes empower them for coupled anisotropic contraction and action potential propagation (Laflamme and Murry, 2011). To mimic the anisotropic behaviors of cardiomyocytes, micro- and nanoscale grooves/ridges, uniaxially stretched electrospun fibers, and parallel multiscale wrinkles have been used to align the cells, upregulate connexin43 level at cell-cell connections as well as increase the longitudinal action conduction (Bursac et al., 2002; Kim et al., 2010; Luna et al., 2011; Zong et al., 2005). Fabricated topographies are also excellent templates to engineer skeletal muscle *in vitro* and recapitulate its physiological functions. Substrates with anisotropic patterns can induce the alignment of myoblasts and their differentiation into myotubes (Dugan et al., 2010; Huang et al., 2006; Wang et al., 2010), and the maturity and orientation of myotubes sequentially strengthen the reciprocal activity at the neuron-myotube interface (Ko et al., 2019). These exciting findings collectively bring insights into the mechanism by which topographic cues in the ECM influence intercellular communications.

1.2.4 Mechanisms by which cells sense and respond to topographic cues

Studies that categorize the responses and behaviors of different cell types to topographic cues have been rapidly growing over the last two decades. However, the mechanisms behind these observed phenomena remain largely unknown. The unanswered fundamental questions include how cells sense the topographies in the microenvironment (contact guidance), what the first element is in the sensing cascade, and what determines the responses of cells. Aiming to solve these questions, recent work has begun to correlate the overall cell responses with relevant intracellular signaling pathways and cytoskeletal architectures. Although the proposed answers are inconclusive and vary between cases, the initial evidence points to several interesting directions that should be further explored.

1.2.4.1 Preferential actin polymerization and protrusive activity

During cell polarization and migration, each cell dynamically reorganizes its cytoskeleton to maneuver and to adapt to the complex and changing environment. Cell protrusions, such as filopodia or lamellipodia, are actin-rich structures that act as sensors used by cells to detect their microenvironment (Bettinger et al., 2006; Ramirez-San Juan et al., 2017; Song et al., 2014). The establishment and stabilization of cellular protrusive activity are thought to determine cell polarization and initiate directed cell motion. Indeed, using the microcontact printing method, Caballero *et al.* fabricated asymmetric ratchet-like fibronectin patches on substrates and found that the long-term motion of fibroblasts is biased towards a defined positive direction as a result of the asymmetric formation of efficient protrusions, regardless of the initial cell polarity (Caballero et al., 2014; Caballero et al., 2015b). It has also been shown that cells extend protrusions to probe the physical topographies in the environment (Bettinger et al., 2006; Ramirez-San Juan et al., 2017;

Teixeira et al., 2003). A detailed study supporting this concept is done by Teixeira *et al*. In this study, the authors fabricated a collection of grooved surfaces with groove width ranging from 70 nm to 1900 nm as well as different depth and examined the cell alignment, protrusive activity, actin cytoskeleton, and focal adhesions of human corneal epithelial cells on these surfaces (Teixeira et al., 2003) (Fig. 1.4A & B). The results demonstrated that the ridges and grooves often guide the filopodia and lamellipodia formation at the leading and trailing edges of cells but severely inhibit the protrusions perpendicular to them, based on which the authors proposed that cell alignment is originated from anisotropic cell spreading and force generation (Teixeira et al., 2003) (Fig. 1.4A & B). However, the protrusive dynamics during cell spreading and subsequent migration were not well characterized, as did the relevant intracellular signaling. Combining live-cell imaging, pharmacological and genetic interventions, and quantitative analysis of protrusion dynamics, a recent study by Ramirez-San Juan *et al.* further showed that the effective guidance of ECM geometry on fibroblast migration depends on both the orientation and size of cell protrusions that are regulated by Rac activity, myosin II-mediated contractility as well as the feedback between adhesion formation and protrusive activity (Ramirez-San Juan et al., 2017). Interestingly, neurons exhibit similar protrusive behaviors that during the initial sensing process topography-aligned filopodia become stabilized by actin cytoskeleton while the non-aligned ones present continuous extension/retraction, leading to directional neurite outgrowth (Jang et al., 2010). The cell protrusion dynamics is not only modulated by the structures and dimensions of topographies (Teixeira et al., 2003) but also varies between different cell lines even on the same topography (Chen et al., 2019).

The active formation of cell protrusions requires extensive rearrangement of the actin cytoskeleton at a subcellular level, making the actin cytoskeleton a key regulator of cell-ECM

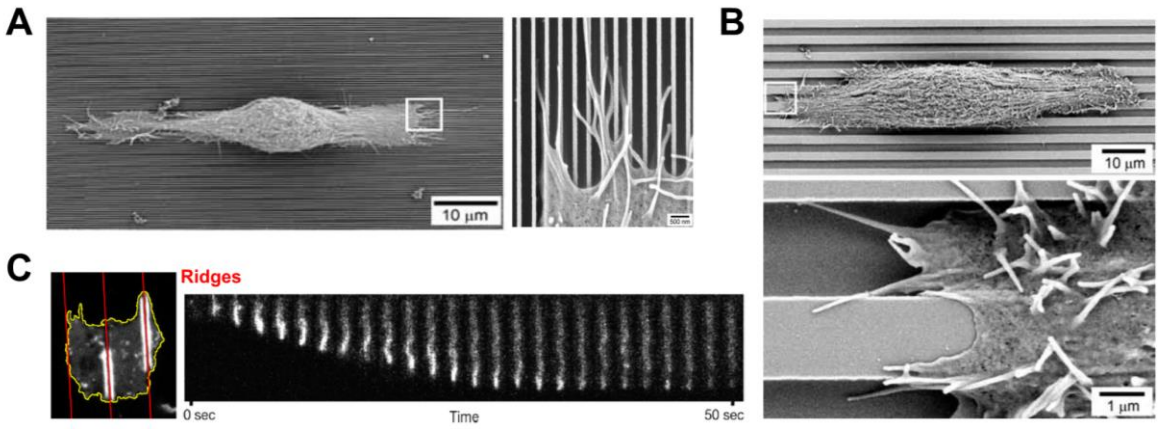

Figure 1.4: Cells exhibit guided protrusion formation and actin polymerization on topographies. (A) SEM image of a human corneal epithelial cell cultured on arrays of 70 nm wide, 600 nm tall ridges with a pitch of 400 nm. The zoom-in image of the highlighted area shows formation and guidance of cell filopodia by ridges. (B) SEM image of a human human corneal epithelial cell on ridges with a width of 1900 nm and a pitch of 4000 nm. The zoom-in image of the cell lamellipodia demonstrates the attachment of cell lamellipodia to the floor of the grooves. A and B are reproduced with permission from (Teixeira et al., 2003). (C) Left panel shows the migration of a *D. discoideum* cell expressing Lifeact-RFP protein on 5 μm spaced nanoridges with a width of 250 nm and a height of 1 μm. Right panel is a kymograph of an actin wave traveling between two adjacent 1.5 um spaced nanoridges. These images highlight that the actin waves are nucleated near ridges and travel along ridges with time. Reproduced with permission from (Driscoll et al., 2014). Article link: https://pubs.acs.org/doi/10.1021/nn406637c; Permission to reuse this material should be directed to the American Chemistry Society.

interaction and contact guidance. Although remaining controversial (Oakley and Brunette, 1993), actin condensation along ridges/grooves have been shown to start 5 minutes after cell attachment, which is the first cell response to the topography (Wojciak-Stothard et al., 1995). In addition, previous studies have shown that numerous cell types align their stress fibers along with the micro- or nanoscale ridges/grooves (Kim et al., 2009b; Kim et al., 2017b; Ventre et al., 2014). Thus, it is hypothesized that F-actin bundles aligned by the topographic features mechanically restrict the cell expansion in other directions and give rise to cell alignment. However, since actin filaments undergo constant polymerization and depolymerization, how cells actively maintain this restriction is not clear. Our recent findings on *Dictyostelium discoideum* (*D. discoideum*), a non-mammalian model system for amoeboid migration, fulfilled this gap by showing that actin polymerization in cells migrating on nanoridges is nucleated near the nanoridges and travels along the ridges in a wave-like manner (Driscoll et al., 2014) (Fig. 1.4C). We termed this phenomenon as esotaxis. The ability to exhibit esotactic behaviors is conserved in mammalian cells (Chen et al., 2019; Sun et al., 2015). Using a design of sawtooth-shaped asymmetric nanotopography, we further demonstrated that actin polymerization in *D. discoideum* can be unidirectionally biased towards the same direction as cell motion (a process called microthigotaxis) (Sun et al., 2015). In addition to *D. discoideum*, the correlation between preferential actin polymerization and biased cell migration was also observed for differentiated neutrophil-like cells as well as human breast cancer cells (Chen et al., 2019; Sun et al., 2015). Strikingly, the direction of actin polymerization and cell motility of human breast cancer cells on the asymmetric sawtooth surface is strongly dependent on cell type, suggesting a contribution of intrinsic characteristics of different cancer cells on their contact guidance behaviors (Chen et al., 2019).

Indeed, actin polymerization waves are known to be critical for cell motility and membrane dynamics. Vicker *et al.* first characterized self-organized reaction-diffusion waves of F-actin polymerization in fibroblasts, *D. discoideum*, and melanoma cells (Vicker, 2002). The spontaneous actin waves can be formed in the absence of external signals and recruit associated proteins to the membrane-anchored network (Vicker, 2002). As a result, waves of F-actin and its associated proteins propagate in a defined spatial manner and push the cell border forward (Vicker, 2002). Weiner *et al.* showed that Hem-1, a component of the leukocyte WAVE2 complex that is required for actin polymerization, exhibits propagating waves near the leading edge of polarized cells (Weiner et al., 2007). The Hem-1 waves are formed as a result of the dynamic recruitment of Hem-1 protein from its cytosolic pool and subsequent removal from the plasma membrane by actin polymerization that is triggered by Hem-1 complexes (Weiner et al., 2007). This autoinhibitory mechanism drives the wave-like propagation of both actin and Hem-1 (Weiner et al., 2007). Inspired by Weiner *et al.*, several computational studies further suggested that spontaneous waves can generate boundary deformation and directional motion of cells (Doubrovinski and Kruse, 2011; Kruse, 2016b). In terms of contact guidance response, it is possible that preferential nucleation and propagation of actin waves along the topographies is driven by, and ultimately regulate the recruitment of actin nucleators to cell membrane whose pattern is determined by the topographies. Future studies should focus on systematically imaging the waves of actin polymerization and associated proteins on topographies to examine this possibility. However, the majority of the results supporting the actin-based sensing mechanism are from amoeboid cells, such as *D. discoideum* and neutrophils, for whom adhesions are not needed to generate force and migrate.

1.2.4.2 Confined focal adhesion formation

The majority of mammalian cells use integrin-based focal adhesions (FAs) to apply force on the substrate and move. The formation of a FA starts from the engagement of integrins with their ligands on the substrate, followed by the recruitment of a variety of associated proteins, including focal adhesion kinase (FAK), paxillin, and vinculin (Mitra et al., 2005). The FA complexes not only link the ECM with the cell actin cytoskeleton (Kanchanawong et al., 2010), but also induce a wide range of biochemical signals through Rho GTPase that go on to regulate cell motility (Devreotes and Horwitz, 2015). In the context of contact guidance, it is first proposed by Ohara and Buck that cell polarization and alignment on microscale ridges are a result of the necessity to maximize the area of focal contacts (Ohara and Buck, 1979). Also, FAs are the second aligned element in fibroblasts spreading on grooved substrates (Oakley and Brunette, 1993). Moreover, previous studies have demonstrated the importance of cell adhesions in the differentiation of hMSCs sensing surface stiffness or topographic cues (Ahn et al., 2014; Kilian et al., 2010; Lauria et al., 2016; Teo et al., 2013; Yu et al., 2013). Specifically, using nanogratings with a width of 250 nm, Teo *et al.* reported that the upregulation of neuronal gene expression in hMSCs cultured on the patterned surfaces directly results from the FAK-dependent signaling, a phenomenon which can be diminished by FAK inhibition or augmented by constitutive FAK activation (Teo et al., 2013). Similarly, E.H. Ahn *et al.* found that hMSCs cultured on microposts with a variable post-to-post distance exhibit different expression levels of β_1 integrin and biased differentiation towards osteogenic or adipogenic lineages (Ahn et al., 2014). These findings collectively suggest that FA can be a key regulator of cell contact guidance and functions.

Recent studies on the texture sensing mechanism in cancer cells further support an important regulatory role of cell adhesions. Ray *et al.* fabricated submicron scale ridges and found

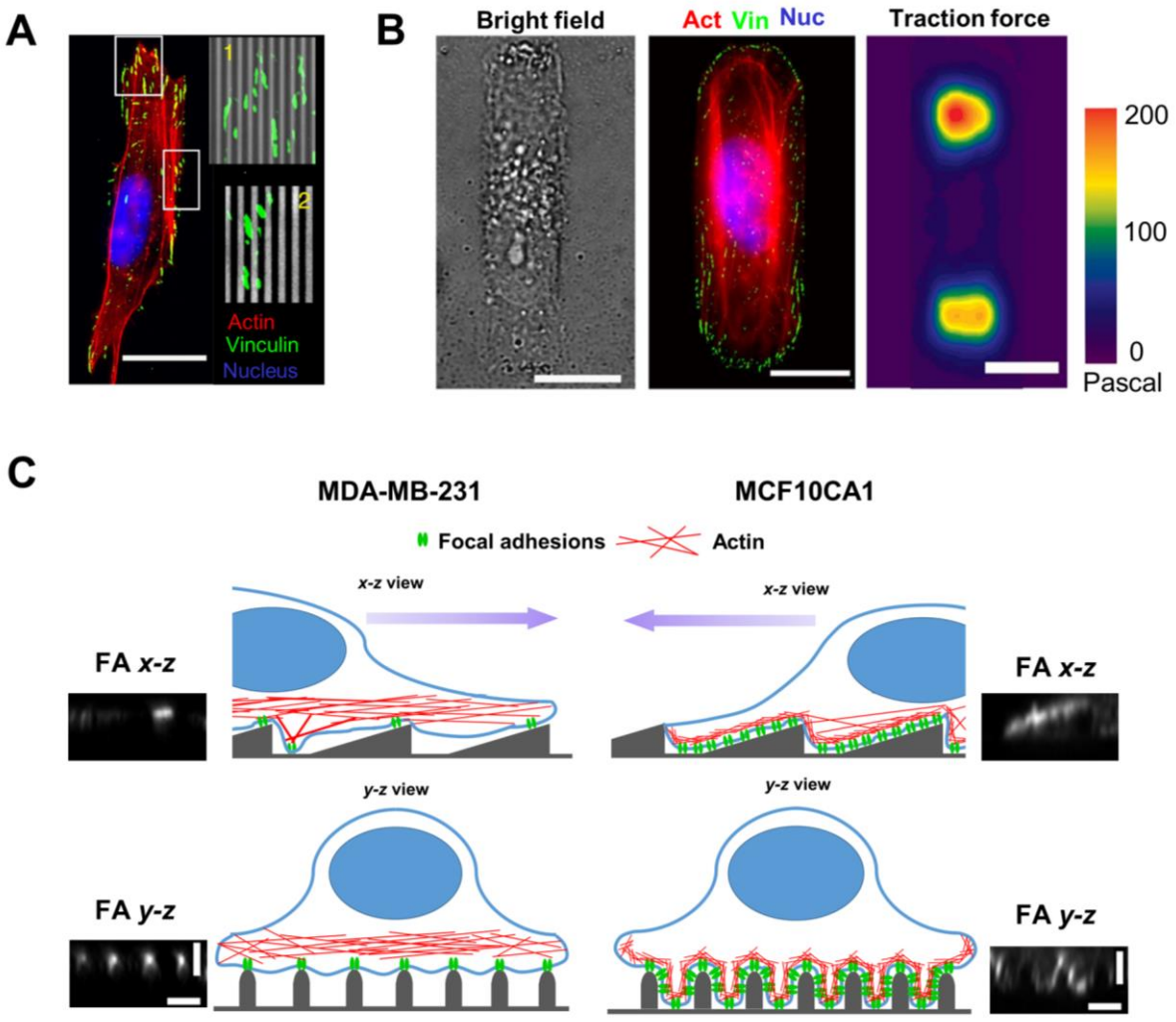

Figure 1.5: The role of FA formation in cell response to topographies. (A) Representative fluorescence images of actin (red), vinculin (green), and nucleus (blue) for a MDA-MB-231 cells on nanoscale ridges. The top insert demonstrates the high FA alignment along the ridges and the bottom insert shows non-aligned FAs overlaid on ridges and grooves from bright-field channel. (B) Bright field, fluorescence images and traction force map of a MDA-MB-231 cells cultured on ECM-coated islands with an aspect ratio of 5, showing the anisotropic distribution of FAs and traction forces. A and B are reproduced with permission from (Ray et al., 2017a). (C) Schematic illustration of the biased contact guidance and different FA pattern for MDA-MB-231 and MCF10CA1 cells. The red fibers represent actin cytoskeleton and green structures are FA complexes. The purple arrow represents the direction of cell motion. The inserts are fluorescence images of paxillin in *x-z* or *y-z* view for each cell type on nanosawteeth, showing the different FA distribution and cortical plasticity between these cell types. Reproduced with permission from (Chen et al., 2019).

that the physical constraints that are exerted on FAs by ridges lead to their directional maturation and orientation in cancer cells (Ray et al., 2017a) (Fig. 1.5A). Subsequently, actin fibers associated with the confined FAs are also aligned along the ridges, generating anisotropic forces that bias the overall cell motion (Ray et al., 2017a) (Fig. 1.5B). Relaxing the geometric constraint on FAs by increasing the groove width or by pharmacologically reducing the FA size is sufficient to disrupt the contact guidance response of cancer cells (Ray et al., 2017a). In topotaxis, cells sense a topographic gradient and undergo unidirectional migration (Park et al., 2018). Park *et al.* used arrays of nanoscale posts with a graded post density and demonstrated a biased motion of melanoma cells (Park et al., 2016). Interestingly, the biased migration direction of melanoma cells is dependent on their invasiveness as well as the density of ECM ligand (Park et al., 2016). Further analysis revealed that melanoma cells exhibit differential membrane deformability and FA penetration depth into the inter-post spaces, providing inputs for multiple signaling pathways that go on to regulate cell motility (Park et al., 2016). This mechanochemical feedback between FA-based cell-ECM contact and intracellular signaling has been validated by a computational model and experimental observations (Holmes et al., 2017; Park et al., 2017). By using a collection of human breast cancer cell lines and a surface design of asymmetric nanosawteeth, our recent work demonstrated that the migration of cancer cells can be unidirectionally guided towards a specific direction of the sawtooth in a cell-type dependent manner (Chen et al., 2019). The key differences between the cancer cell types that move towards opposite directions are distinct cortical plasticity and FA patterns (Fig. 1.5C). Particularly, we discovered that the membrane of MDA-MB-231 cells that migrate towards a defined positive direction on the sawtooth surface "floats" on top of sawtooth structures and the cells form ordered FA complexes only on the tips of nanosawteeth (Chen et al., 2019) (Fig. 1.5C). However, the MCF10CA1 cells, a metastatic mutant cell line

derived from the MCF10A cells, can curve their membranes to wrap around individual sawteeth and assemble FAs surrounding the whole sawtooth structures (Chen et al., 2019) (Fig. 1.5C). Our findings lead us to hypothesize that the distinct FA patterns between cancer cell lines regulate the bias in cell actin polymerization and migration. All these studies strongly suggest a dependence between the FA formation and contact guidance responses.

The extraordinary complexity and variability of the intrinsic components and regulatory molecules in FA complexes indeed empower them to influence many cellular processes such as cell growth, differentiation, and migration. The adhesion architectures consist of hundreds of distinct proteins in three major compartments: signaling compartment, force transduction compartment, and actin polymerizing compartment (Geiger et al., 2009; Kanchanawong et al., 2010). The recruitment of these composed proteins occurs in a well-defined spatiotemporal manner and is related to the size and maturity of the FAs (Gallant et al., 2005; Goffin et al., 2006; Pasapera et al., 2010). In addition to kinases and phosphatases, small Rho family GTPases, particularly Rho and Rac, are key modulators in FA-dependent signaling (Geiger et al., 2009; Moissoglu and Schwartz, 2006). The activation/inactivation of Rho GTPases can be controlled by FA-interacting guanine-nucleotide-exchange factors (GEFs) or GTPase-activating proteins (GAPs) (Guilluy et al., 2011). Although previous studies have attempted to examine the Rho GTPase activity in cells migrating on topographies (Rapier et al., 2010; Xia et al., 2008), the exact relation between FA formation and Rho GTPase activation is still not clear. Future works should focus on monitoring the FA formation as well as the Rho GTPase activity by using developed fluorescence resonance energy transfer (FRET) biosensors in live cells on topographies (Fritz et al., 2015; Pertz et al., 2006). Considering the important role of Rho GTPases in actin polymerization, it is also interesting to study the actin nucleation dynamic in response to FA formation and Rho GTPase signaling.

Lastly, the mechanical tension force applied by the actin fibers to FAs is required for FA growth and maturation (Balaban et al., 2001; Galbraith et al., 2002). How the tension force is distributed across the topographic structures and how the force is correlated with the FA formation would be interesting questions to be explored.

1.2.4.3 Local curvature induced protein recruitment

When migrating on topographic surfaces, cells are able to curve their plasma membrane to accommodate the geometry of topographies. Growing evidence has suggested that the curved membrane itself can act as an intermediary to participate in actin remolding and intracellular signaling through the recruitment of curvature-sensitive proteins (Gov, 2018; Lou et al., 2018). The largest group of curvature-sensitive proteins might be the family of Bin/amphiphysin/Rvs (BAR) domain proteins (Simunovic et al., 2019). In addition to their intrinsic property to deform membranes, BAR domain proteins have been shown to sense the local membrane curvature and be recruited to the curved cortex (Wu et al., 2013; Wu et al., 2018). The recruited BAR domain proteins not only can reciprocally deform the membrane but also bind to the activators of actin polymerization, which leads to the stiffening of the cortex and antagonizes the further recruitment of BAR proteins (Wu et al., 2018; Yang and Wu, 2018). As a consequence, both positive and negative feedbacks generate propagating waves of actin polymerization and local membrane deformation (Wu et al., 2018; Yang and Wu, 2018). However, the spontaneous membrane curvature sensed or generated by BAR proteins is probably much shallower than the one induced by surface topographies (Wu et al., 2018).

A recent study by Lou *et al.* provided more direct evidence to support the critical role of membrane curvature in the cell topography-sensing process. Using a design of nanobars with a

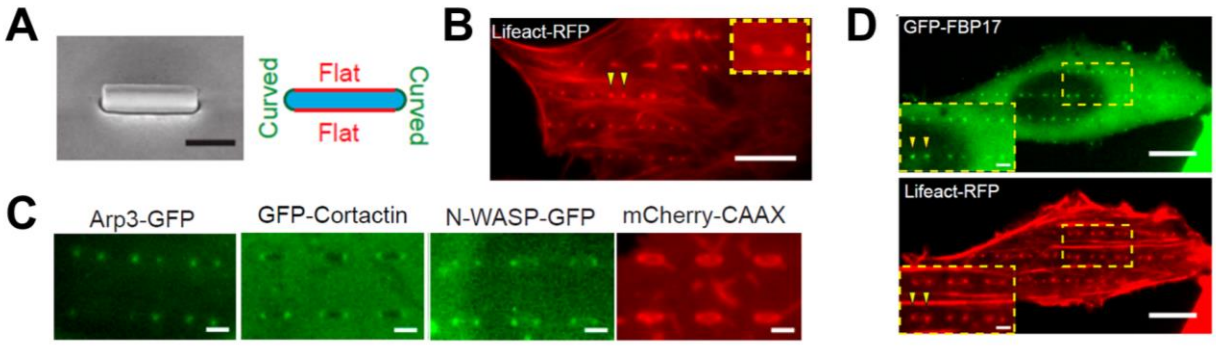

Figure 1.6: Nanostructure-induced membrane curvature recruits F-BAR protein and actin nucleators, leading to F-actin accumulation. (A) An SEM image of a nanobar with 200 nm width, 2 μm length, and 1 μm height and a schematic illustration of different vertical curvatures around a nanobar. (B) A static image of a U2OS cell expressing Liftact-RFP protein on nanobar arrays demonstrates the accumulation of Liftact-RFP signal at the nanobar ends. (C) Amplified fluorescence images of Arp3-GFP, GFP-Cortactin, N-WASP-GFP, and mCherry-CAAX indicate the accumulation of actin nucleator Arp3 and its promoting factors, N-WASP and Cortactin, at the ends of nanobars. (D) Fluorescence images of a U2OS cell expressing GFP-FBP17 and Lifeact-RFP show that both FBP17 and F-actin accumulate to the ends of nanobars. All images are reproduced with permission from (Lou et al., 2019).

high curvature at two ends but a low curvature along the sidewalls, the authors showed preferential actin polymerization at the high-curvature ends of the nanobars (Lou et al., 2019) (Fig. 1.6A & B). The curvature-induced F-actin assembly is strongly correlated with the accumulation of actin nucleating factors, including Arp2/3, N-WASP, and Cortactin, as well as curvature-sensitive F-BAR proteins (Lou et al., 2019) (Fig. 1.6C & D). Further experiments with a truncated F-BAR mutant confirmed that the ability of F-BAR proteins interacting with the actin nucleators is required for F-actin accumulation at the high curvature regions (Lou et al., 2019). In their previous studies, it has also been shown that high vertical membrane curvature induced by nanotopographies enhances clathrin-mediated endocytosis (Zhao et al., 2017). Although the authors in Lou *et al.* did not find an accumulation of FA proteins at the high-curvature regions, it is still inadequate to exclude the role of FAs in the process, especially considering that adhesive coating was used in the study. Furthermore, since cells are relatively static in the study, how cell motility influences protein accumulation and F-actin polymerization needs to be explored. Interestingly, Lou *et al.* found that the recruitment of F-BAR proteins to the curved membrane is dependent on the curvature value and only occurs when the width of nanobars is smaller than 400 nm (Lou et al., 2019). It is possible that F-BAR-mediated curvature-sensing mechanism is dominant when the induced curvature is sharp and on a small scale but other mechanisms become dominant in scenarios with shallow but big-scale curvatures. More research endeavors should be put to further tease apart the effect of curvature-based mechanism from that of other mechanisms by using adhesive inert coating or blocking integrin activation.

1.2.5 Summary and perspectives

Cells sense numerous chemical, physical, and electrical stimuli in the environment and respond to them by changing cell behaviors. The studies discussed herein and elsewhere provide solid evidence that topographic features of the ECM play a pivotal role in controlling cell functions. The effect of physical topographies in the ECM has been neglected in previous large-scale experiments due to the nano- or micron length scale of topographies. However, recent advancements in nanofabrication techniques have enabled scientists to engineer sophisticated topographies in different scales to gain insights into the mechanism of contact guidance. In this review, we showcased the popular fabrication techniques used to create *in vivo*-mimic topographies, described some but not all interesting findings on the regulation of topographies on various cell functions, and discussed several potential mechanisms by which cells sense and respond to topographic cues. This review may serve as a useful resource for researchers that are interested in and may intend to study cell-topography interactions.

All findings by far are exciting and start bringing insights into the fundamental mechanism behind cell-topography interaction, but the whole picture is still far from clear and many issues remain. Most of the topographies discussed here are fabricated on 2D surfaces. Although the 2D topographies hold reduced complexity and some relevance to *in vivo* environment, they fail to fully recapitulate the characteristics of *in vivo* ECM. On the other hand, current techniques to engineer 3D networks are insufficient to control the fine nanoscale features of a 3D matrix. For example, aligned 3D collagen matrices can be fabricated by mechanical stretching (Riching et al., 2014), magnetic alignment (Guo and Kaufman, 2007), shear flow in a microfluidic channel (Lanfer et al., 2008; Lee et al., 2006), or constrained cellular compaction (Ray et al., 2017b). However, detailed parameters and topographic features of the collagen fibers cannot be manipulated. Thus, a more

advanced fabrication method is required to generate a 3D environment with tunable topography and ECM composition. Another issue is the challenge to fabricate nanoscale topographies over a large area with high reproducibility and accuracy, which prevents scientists from performing biochemistry assays. Kim *et al.* was able to fabricate arrays of anisotropic nanoridges to cover the entire glass coverslip (~3.5 cm^2) by starting from a silicon master and by using a UV-assisted capillary nanomolding method (Kim et al., 2010). However, creating a master mold with more sophisticated topographies than lines or dots can be difficult and time-consuming, such as the sawtooth-shape topography used in Chen *et al.* (Chen et al., 2019). In addition, the majority of current results are usually dependent on specific cell types. That is, observed responses of a cell line to a topography may not hold for another cell line. Thus, more systematic approaches and studies are needed to provide a general mechanism by which cells sense the topographies and change their behaviors.

1.3 Inside-out: generating and maintaining intracellular membrane curvatures

Besides separating the cell interior from outside, biological membranes also serve as envelopes around different organelles and intracellular vesicles and hence are crucial for eukaryotic life. Membranes often exhibit complex tubular or vesicular shapes and undergo constant remolding, including invagination, scission, and fusion. Generating and maintaining the membrane curvature has central importance for these processes and numerous cellular functions. In this part, we will first describe the role of membrane curvature in intracellular trafficking and organelle shaping then discuss the mechanisms for curvature generation.

1.3.1 Membrane curvature in intracellular trafficking

Membranes are constantly turned over by trafficking intermediates between the plasma membrane and organelles. During intracellular trafficking, membrane invagination is firstly formed at one cellular compartment, then buds outwards as vesicles or tubules and eventually breaks free into the cytosol (Jarsch et al., 2016). The free vesicles are attached to microtubules or microfilaments by motor proteins and transported to another cell compartment, where membrane fusion occurs (Terasaki et al., 1986; Waterman-Storer and Salmon, 1998). The generation of membrane curvature is expected to be essential for these processes. Endocytosis at the plasma membrane and the secretory pathway between ER and Golgi apparatus are classic examples of intracellular trafficking and mediate multiple key cell functions, including nutrient uptake, receptor internalization, and protein secretion.

Endocytosis is a process used by cells to engulf extracellular materials and to deliver cargos, such as ligand-bound receptors, ion channels, or other types of molecules into the cell interior. Clathrin-mediated endocytosis (CME) is a major endocytic mechanism that is by far the most thoroughly studied. A classic CME process begins with the assembly of a clathrin coat at the plasma membrane and this clathrin-coated structure bends into the cytosol to form a shallow pit that undergoes progressive budding into a clathrin-coated vesicle with a dome-like shape (Haucke and Kozlov, 2018). However, the temporal order of these processes is still under debate. About 50 proteins have been shown to be involved in CME (Kaksonen et al., 2005; McMahon and Boucrot, 2011; Merrifield and Kaksonen, 2014), but clathrin, AP-2, and dynamin are the most central ones (Schmid and McMahon, 2007). However, these three proteins are not sufficient to initiate endocytic progress, and it is likely that other proteins are responsible to generate and maintain the membrane curvature. Epsins are found to be present in the early stage of a budding event (Schmid

and McMahon, 2007). Epsins contain a PI(4,5)P_2-binding ENTH domain that targets the protein towards cell membranes in association with clathrin and AP-2 (Chen et al., 1998; Ford et al., 2002). Upon binding to PI(4,5)P_2, the ENTH domain forms an additional amphipathic α-helix that can insert into the membrane and generate local curvature (Ford et al., 2002). AP180 or related protein CALM, which contains a homologous ANTH domain, has been shown to bend the membrane both *in vivo* and *in vitro* (Koo et al., 2015; Miller et al., 2015; Zhang et al., 1998). Similar to epsins, insertion of the N-terminal amphipathic helix within the ANTH domain of AP180/CALM is essential for curvature generation (Miller et al., 2015). On the other hand, F-BAR proteins, such as F-BAR domain only protein 1 or 2 (FCHo1 or FCHo2) and FBP17, use a scaffolding mechanism to shape the membrane (Henne et al., 2010; Henne et al., 2007). F-BAR domain can dimerize through lateral and tip-to-tip interactions and the dimeric F-BAR exhibits a shallow arc shape that resembles a crescent (Frost et al., 2008). Binding of a dimeric F-BAR to the membrane through electric attractive interactions can impose its concave shape on the membrane and generate curvature (Henne et al., 2007). It is suggested that FCHo1/2 may play a role in the initial steps of a CME pit formation (Henne et al., 2010) but FBP17 is more likely to maintain the vesicle sphere (Shimada et al., 2007; Tsujita et al., 2006). Different from F-BAR proteins, N-BAR proteins, such as amphiphysin and endophilin, not only have N-terminal amphipathic helices but also exhibit an arc-like shape upon dimerization (Gallop et al., 2006; Peter et al., 2004). The dual features of N-BAR proteins empower them to curve membrane by both hydrophobic insertion and scaffolding mechanisms and theoretically to be involved in shaping the sphere as well as the narrow neck of a CME vesicle. Finally, as a CME bud progressing, the neck gets narrower, which favors the binding of highly curved PX-BAR and N-BAR proteins SNX9/18 (Lundmark and Carlsson, 2009). The SNX9/18 further recruit dynamin to the budding neck (Lundmark and Carlsson, 2004), and the

membrane scission would be driven by the GTP hydrolysis of dynamin (Antonny, 2011). Although recent studies using correlative super-resolution light and transmission electron microscopy have provided valuable insights on the CME process (Sochacki et al., 2017), many questions, such as the recruitment sequence of endocytic proteins, and the role of clathrin in curvature generation, still need to be further explored.

The secretory pathway in eukaryotic cells is a highly evolved process to target proteins for secretion. Vesicles constantly bud from ER and traffic to the Golgi apparatus to transport properly folded proteins. The mechanism by which membrane curvature is generated is similar to the ER and Golgi. The small GTPases Arf1 and Sar1 together with their effector proteins orchestrate the structure and membrane organization of the ER and Golgi apparatus (Nie et al., 2003). Within all effector proteins of Arf1 and Sar1, coatomer protein complex I and II (COPI and COPII) can polymerize to coat the membrane (Lee et al., 2005; Manneville et al., 2008), similar to a clathrin lattice. Both Arf1 and Sar1 possess N-terminal sequences that can fold into amphipathic helices upon GTP binding (Beck et al., 2008; Krauss et al., 2008; Lee et al., 2005). Insertion of the amphipathic helices of Arf1 and Sar1 into membranes has been shown to tubulate liposomes *in vitro*, confirming their ability to deform membranes (Krauss et al., 2008; Lee et al., 2005). The turnover rate between the GTP- and GDP-bound forms of Arf1 and Sar1 is determined by their GEF and GAP proteins. Interestingly, Golgi-localized Arf1-GAP1 also has an amphipathic helix and favorably binds to the curved membrane (Antonny et al., 1997; Cukierman et al., 1995). Thus, membrane curvature might serve as a regulator of Arf1-GTP hydrolysis activity. Based on previous results, it is hypothesized that Arf1, Arf1-GAP1, and COPI can form a protein complex, and the Arf1-GTP coordinates with COPI to bend the membrane, which activates Arf1-GAP for Arf1-GTP hydrolysis (Bigay et al., 2003). The subsequent release of Arf1-GDP somewhat curves

the membrane to a further extend (Bigay et al., 2003). The Sar1 GTPase activity also positively correlates with high membrane curvature, and the binding of Sar1 to the membrane is implicated in the scission of vesicles from the membrane (Hanna et al., 2016). Some of N-BAR proteins, such as amphiphysin IIb and endophilin B, may also play a role in deforming membrane at the Golgi complex (Farsad et al., 2001; Sarret et al., 2004).

1.3.2 Membrane curvature in organelle shaping

Unlike the spherical liposomes that can spontaneously be formed by phospholipid in solution, many organelles maintain complex and dynamic morphologies, such as sheets, tubules, and cristae. For example, ER and Golgi apparatus both contain interconnected micron-size sheets and tubules, while mitochondria have complex inner membrane network. Interestingly, the shape of these organelles is highly conserved throughout phylogeny. Specialized proteins and an interplay between multiple mechanisms are required to generate and maintain the stable membrane curvatures of these organelles.

As one of the largest organelle in eukaryotic cells, ER is critical for protein synthesis, protein secretion, and regulation of intracellular Ca^{2+} level (Baumann and Walz, 2001). The sheet-like rough ER and tubular smooth ER interconnect and form a 3D contiguous membrane network in the cell cytoplasm. One mechanism to maintain the complicated morphologies of different ER domains is scaffolding by integral membrane proteins (McMahon and Boucrot, 2015). CLIMP63, a type II integral membrane protein, localizes to perinuclear ER cisternae and plays a key role in maintaining the shape and inter-membrane distance (Klopfenstein et al., 2001; Schweizer et al., 1993; Schweizer et al., 1995). Overexpression of CLIMP63 increases the ratio of ER sheets to tubules, while its depletion decreases the luminal spacing between two membrane layers of ER

sheets (Shibata et al., 2010). On the other hand, retuculon (RTN) and defective in polyposis (DP1) family members are conserved integrin membrane proteins that preferentially localize at ER tubules and promote tubule formation (Di Sano et al., 2012; Oertle et al., 2003; Voeltz et al., 2006). All RTN proteins have two closely spaced hairpin transmembrane domains that in principle can form a wedge-like structure in the outer leaflet of the ER membrane, deforming the membrane for high curvature generation (Shibata et al., 2010; Voeltz et al., 2006). Interestingly, DP1 shares a similar structural topology of RTN proteins (Voeltz et al., 2006). Both RTNs and DP1 are able to form immobile homo-oligomers, which is predicted to determine the diameter of ER tubules (Hu et al., 2008; Shibata et al., 2008). The overexpression of RTN or DP1 in cells enhances the formation of ER tubules but impedes sheet formation (Shibata et al., 2008). These studies suggest that RTN proteins and DP1 are essential and sufficient to generate ER tubules. The same mechanism is also implicated in shaping the tubular cristae of inner mitochondrial membrane. The dimerization of F_1F_0-ATP-synthease, a conserved integral membrane protein complex found in the inner membrane of mitochondria, is suggested to bend the membrane and cause tabulation (Dudkina et al., 2006; Everard-Gigot et al., 2005). The F_1F_0-ATP-synthease can potentially form oligomers and function as a scaffold for membrane curvature (Allen et al., 1989; Dudkina et al., 2006). In addition to the scaffolding mechanism used by integral membrane proteins, other mechanisms, such as association with the cytoskeleton and membrane fission and fusion, also contribute to maintaining shapes and curvatures of ER and mitochondria (Voeltz and Prinz, 2007; Westrate et al., 2015).

The nucleus is another organelle that requires a highly curved membrane for its proper function, especially for the nuclear pores. The nuclear pore complexes (NPCs) control the transport of molecules across the nuclear envelope (NE) and also are domains where the inner and outer NE

membranes are tightly curved in apposition (Hoelz et al., 2011). The NPCs are composed of a strikingly small number of proteins called nucleoporins (Nups) that can be classified into several sub-groups, including membrane-anchored Nups, scaffold Nups, and barrier Nups (Cautain et al., 2015). The membrane-anchored Nups contain amphipathic helices, allowing them to bind the membrane and orchestrate membrane curvature during NPC assembly (Doucet and Hetzer, 2010; Vollmer et al., 2012). Several scaffold Nups are COPI- and COPII-like proteins and can form a lattice that shares similarities with COPI and COPII coats, while barrier Nups are gatekeepers for cargo transportation (Beck et al., 2018; Cautain et al., 2015). Recent studies from our lab identified a novel membrane budding process at the neutrophil NE. As an essential step of secreting leukotriene B_4 (LTB_4), a secondary chemoattractant, during neutrophil chemotaxis, LTB_4 and its synthesizing enzymes are packaged and released in extracellular vesicles called exosomes (Majumdar et al., 2016). Surprisingly, the biosynthesis of these vesicles is initiated at the neutrophil NE through nuclear membrane outwards budding. Furthermore, we found that 5-lipoxygenase activating protein (FLAP), an integral transmembrane protein at the NE, is enriched at the budding regions. Since the functional form of FLAP is homotrimer that has a wedge-like shape, it is possible that the clustering of homometrimeric FLAP causes membrane curvature.

1.3.3 Mechanisms of membrane curvature generation and maintenance

As discussed in previous sections, generating and stabilizing membrane curvature is not only crucial for intracellular vesicle trafficking but also for shaping various cellular compartments. However, bending the membrane is not an easy task for cells and cannot be completed by using nonspecific mechanisms. Instead, it has become clear that the cooperation of diverse molecular

mechanisms is needed to achieve well-organized membrane architectures. Here we will further discuss several common molecular mechanisms used by cells to deform membranes.

1.3.3.1 Lipid composition and asymmetry

Lipids have intrinsic shapes that are determined by the ratio between the cross-sectional area of their polar headgroups and that of their acyl tails (Fig. 1.7A). Lipids like phosphatidylcholine and phosphatidylserine whose headgroups have a similar size as their tails do exhibit a cylindrical shape and do not induce membrane curvature (Di Paolo and De Camilli, 2006). Phosphatidylethanolamine, phosphatidic acid, and diacylglycerol, which are consisted of relatively smaller headgroups, would induce a negative curvature when enriched at one leaflet of the bilayer (Di Paolo and De Camilli, 2006; Farsad and De Camilli, 2003) (Fig. 1.7A). In the contrast, when the lipid headgroups are bigger and cluster asymmetrically at one leaflet, this will cause a positive membrane curvature (Di Paolo and De Camilli, 2006; Farsad and De Camilli, 2003) (Fig. 1.7A). Examples of such lipids include lysophosphatidylcholine or phosphatidylinositol phosphates. The transient changes in the lipid composition of one leaflet can be achieved by lipid-modifying enzymes or by lipid flippases (Farsad and De Camilli, 2003; McMahon and Boucrot, 2015). Indeed, for example, it has been shown that the conversion from sphingomyelin to ceramide by sphingomyelinases leads to inward membrane budding and the formation of intraluminal vesicles within the giant unilamellar vesicles (GUVs), a mechanism used for multivesicular body biogenesis (Trajkovic et al., 2008). However, since the asymmetry in lipid composition between two monolayers is mostly transient, it is unlikely that this mechanism significantly contributes to maintaining the complex shapes of organelles.

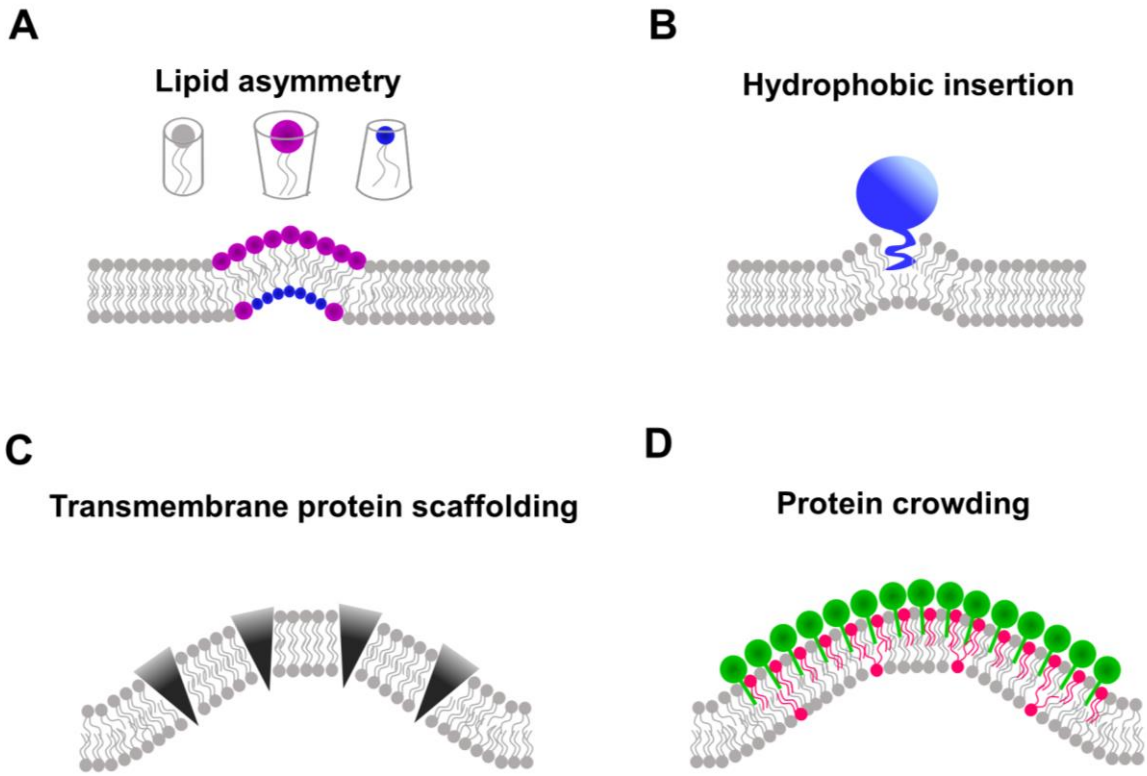

Figure 1.7: Mechanisms of membrane curvature generation. (A) The intrinsic shape and asymmetric distribution of certain lipids give rise to spontaneous membrane curvature. (B) Many proteins have amphipathic helices and the insertion of the "wedge-like" hydrophobic side of the helix induces membrane curvature. (C) Transmembrane proteins with a wedge shape can induce curvature in the lipid bilayer. (D) The recruitment of proteins to membrane through interactions with certain lipids results in protein crowding and increases lateral tension, which bends the membrane.

1.3.3.2 Insertion of protein hydrophobic domains

As mentioned above, many cytosolic proteins are targeted to the membranes through the insertion of their hydrophobic domains that can penetrate one leaflet of the membrane, which induces local membrane curvature (Voeltz and Prinz, 2007). A typical example is amphipathic helices that are present in many membrane-modeling proteins (Fig. 1.7B). When interacting with the cell membrane, these proteins change their conformations and fold a specific part of their sequences into an α-helix called amphipathic helix (Fig. 1.7B). Most of the curvature-inducing proteins involved in the endocytic or secretory pathways utilize this mechanism, including epsins, AP180, CALM, endophilin, amphiphysin, Arf family, Sar1, ArfGAP1, and ArfGEF GBF1 (Chen et al., 1998; Ford et al., 2002; Koo et al., 2015; Krauss et al., 2008; Lee et al., 2005; Miller et al., 2015; Schmid and McMahon, 2007). The translocation of cytosolic proteins to the cell membranes can also be mediated by protein C2 or C2-like domains. Previous studies have demonstrated that the insertion of the hydrophobic loops on the tip of the C2 domains is able to generate a high degree of membrane curvature (Groffen et al., 2010; Martens et al., 2007).

1.3.3.3 Scaffolding by integral membrane proteins

A conical or inverted conical shape of integral membrane proteins or protein oligomers can induce membrane curvature (McMahon and Boucrot, 2015) (Fig. 1.7C). This scaffolding effect by integral membrane proteins is suggested to maintain the membrane curvature in a more permanent manner (Fig. 1.7C). Typical examples of such mechanisms are RTN proteins and DP1 that are key in generating ER tubules (Di Sano et al., 2012; Oertle et al., 2003; Voeltz et al., 2006), as described previously. The oligomerization of RTNs or DP1 can also determine the diameter of the ER tubules (Shibata et al., 2010). The proposed mechanistic features are also shared by caveolin and F_1F_0-

ATP-synthase to induce membrane curvature for caveolae formation and shaping mitochondria respectively (Bauer and Pelkmans, 2006; Dudkina et al., 2006). Interestingly, the crosstalk between the clustering of integral membrane proteins and associated membrane deformation is not unidirectional. That is, membrane curvature may also regulate the distribution of transmembrane proteins, such as dopamine transporters and ion channels (Aimon et al., 2014; Caltagarone et al., 2015).

1.3.3.4 Protein-protein crowding

A recent study by Stachowiak *et al.* questioned the efficiency of the insertion of protein amphipathic helices on bending membranes and proposed another mechanism termed protein-protein crowding (Stachowiak et al., 2012). In this mechanism, membrane curvature is driven by increased lateral pressure that is due to the collision of membrane-bound proteins (Stachowiak et al., 2012) (Fig. 1.7D). The questioning was first raised by computational studies, which lead to the prediction that proteins with amphipathic helices need to cover nearly 100% of membrane surface to generate observed high curvature (Blood et al., 2008; Campelo et al., 2008). However, this seems unlikely under physiological conditions. By replacing the amphipathic helix in epsin ENTH domain with a hexa-his tag and by using GUVs containing DOGS-NTA-Ni, Stachowiak *et al.* found that increasing protein coverage on GUVs is able to drive tubule formation in the absence of helix insertion (Stachowiak et al., 2012). Strikingly, the tabulation phenomenon can also be observed when a non-membrane-modifying protein, such as green fluorescence protein, is used, indicating that the protein crowding mechanism might be general for any membrane-bound proteins (Stachowiak et al., 2012).

1.3.4 Conclusions and perspectives

Membrane remodeling and curvature generation play a significant role in organelle shaping and intracellular trafficking, which go on to regulate numerous cellular functions. The majority of studies discussed here and elsewhere are based on mammalian cells or yeasts. Many gaps still remain unfilled in other less-studied systems, such as fungi, plants, and parasites, in which membrane curvature could be determinant for their functions. The mechanisms by which membrane curvature is generated and maintained are diverse. In addition to the mechanisms mentioned here, several distinct mechanisms are also critical, such as scaffolding by cytoskeleton and motor proteins. It is very unlikely that the curvature generation only depends on a single mechanism. Instead, it is a result of multiple intertwined mechanisms. For example, sphingolipids and cholesterol are able to cluster into ordered microdomains, termed lipid rafts. The integral membrane proteins in the lipid bilayer can either cluster into or are excluded from the lipid rafts based on their physical properties. The change of lipid composition and clustering of transmembrane proteins make the lipid rafts “hot spots” for membrane bending. Future studies should aim to identify the involved mechanisms and compare the result between different processes in order to unravel a general principle. It is also highly possible that novel mechanisms underlying the membrane remodeling will be uncovered in the future.

1.4 Hypothesis and aims

The overall goal of the research described in this thesis is to understand how cells generate membrane curvatures, either passively or actively, during migration and how these membrane curvatures play a role in cell migration. The specific goals are to investigate the mechanisms by which cells sense and respond to the extracellular curvatures and topographies, determine the

effect of the topographic features in the ECM on cell activation and migration phenotypes, and to provide insights on how chemotaxing cells generate intracellular membrane curvatures for the release of a secondary chemoattractant. Considering the significance of directed cell migration in many physiological and pathological processes, this work will provide valuable insights on how a change in membrane curvature at different cellular compartments influences cell migration and related processes.

Chapter 2: Investigate the role of extracellular topographies in breast cancer cell metastasis

Physical guidance from the topographies in the ECM is a key regulator of cancer invasion and metastasis. However, the biophysical and molecular mechanisms by which cancer cells sense the topographic features are not well understood. The study in chapter 2 explores the effects of surface topography on the migration phenotype of multiple breast cancer cell lines using aligned nanoscale ridges and asymmetric sawtooth structures. We first use long-term live-term live cell imaging and cell tracking to perform an extensive analysis of cell migration on the nanotopographies. Further, engineered cell lines, immunofluorescence, super-resolution confocal imaging, and scanning electron microscopy (SEM) were used to examine the actin polymerization dynamics and FA distributions in the cancer cells on topographies. Finally, we used pharmacological interventions to examine the effect of regulating Rho GTPase signaling on cancer cell migration behaviors and cytoskeletal dynamics.

Chapter 3: Investigate the effect of topography-induced membrane curvature on integrin activation and signaling in human primary neutrophils

Neutrophil recruitment to inflamed or injured tissues is a key step in immune responses. Although it is well established that directed migration and signal replay play important roles in neutrophil recruitment, the effects of physical changes and stimulus of the underlay ECM are poorly understood. In chapter 3, we hypothesize that physical stimulation activates neutrophils through integrin signaling in a chemoattractant-independent manner and primes neutrophils for migration and recruitment. To test this, the study in this chapter utilizes nanoscale ridges to provide physical stimuli and performs live-cell calcium imaging on human neutrophils. In addition, the inhibitory and conformation-specific integrin antibodies are applied to determine the responsive integrins and their conformational condition in this process.

Chapter 4: Assess the structural role of multimeric FLAP in curvature generation at neutrophil nuclei upon stimulation

In response to tissue injury or inflammation, nearby neutrophils migrate directionally to the inflamed/injured site and trigger dramatic swarm-like recruitment of distal neutrophils by secreting the secondary chemoattractant LTB_4 - a process referred to as signal relay. Although the biosynthesis process of LTB_4 is well understood, how LTB_4 is packaged and released out of the cells is not clear. Based on our previous findings, we hypothesize that the clustering of trimeric FLAP in ceramide-rich microdomains triggers membrane curvature at the neutrophil nuclei for vesicle formation and LTB_4 release. To directly test this *in vitro*, human FLAP is purified from *E.coli* and reconstituted into liposomes with a defined lipid composition. Further, negative staining

and cryogenic electron microscopy (EM) are used to visualize the membrane organization of the FLAP: lipid assemblies.

Chapter 5: Summary and significance

Chapter 2

Actin Cytoskeleton and Focal Adhesions Regulate the Biased Migration of Breast Cancer Cells on Nanoscale Asymmetric Sawteeth[1]

2.1 Summary

Physical guidance from the underlying matrix is a key regulator of cancer invasion and metastasis. We explore the effects of surface topography on the migration phenotype of multiple breast cancer cell lines using aligned nanoscale ridges and asymmetric sawtooth structures. Both benign and metastatic breast cancer cells preferentially move parallel to nanoridges, with enhanced speeds compared to flat surfaces. In contrast, asymmetric sawtooth structures unidirectionally bias the movement of breast cancer cells in a cell-type dependent manner. Quantitative analysis shows that the level of bias in cell migration increases when cells move with higher speeds or with higher directional persistence. Live-cell imaging studies further reveal that actin polymerization waves are unidirectionally guided by the sawteeth in the same direction as the cell motion. High-resolution fluorescence imaging and scanning electron microscopy studies reveal that two breast cancer cell lines with opposite migrational profiles exhibit profoundly different cell cortical plasticity and focal adhesion patterns. These results suggest that the overall migration response of cancer cells to surface topography is directly related to the underlying cytoskeletal architectures and dynamics, which are regulated by both intrinsic and extrinsic factors.

[1] This study was published in ACS Nano. Song Chen, Matt J. Hourwitz, Leonard Campanello, John T. Fourkas, Wolfgang Losert, and Carole A. Parent, Actin cytoskeleton and focal adhesions regulate the biased migration of breast cancer cells on nanoscale sawteeth, *ACS Nano* 2019 **13** (2), 1454-1468, DOI: 10.1021/acsnano.8b07140

2.2 Introduction

The ability to migrate is conserved in a wide variety of cell types throughout the phylogeny and plays a pivotal role in many cellular processes (Amini-Nik et al., 2014; Friedl and Alexander, 2011; Lammermann et al., 2013; Scarpa and Mayor, 2016). Cells typically undergo directional migration with a relatively high persistence (Petrie et al., 2009), rather than moving randomly (Chen et al., 2014). However, the biological and physical mechanisms governing directed cell migration in many physiological and pathological processes are still poorly understood. In addition to the intrinsic characteristics of cells, the extracellular environment plays an important role in the guidance of cell movement. Cells can be guided by single or multiple extracellular cues, including chemoattractant gradients (chemotaxis) (Bagorda and Parent, 2008; Parent, 2004), stiffness gradients of the underlying substrate (durotaxis) (Sunyer et al., 2016), electric fields (electrotaxis) (Shanley et al., 2006), and topographic structures on the surfaces (contact guidance)(Kim et al., 2012; Nguyen et al., 2016).

Cancer invasion and metastasis, processes in which active primary tumor cells migrate to adjacent tissues and eventually colonize distant organs, are major life-threatening events in cancer patients. Contact guidance is known to regulate cell adhesion, intracellular signaling, and directed migration (Doyle et al., 2015; Provenzano et al., 2006; Provenzano et al., 2008), and as such is a key component of cancer invasion. The role of the extracellular matrix (ECM) in guiding the 3-dimensional (3D) migration of cancer cells *in vivo* has been studied extensively (Alexander et al., 2008; Provenzano et al., 2006; Provenzano et al., 2008; Ray et al., 2017b; Wolf et al., 2013). For example, the directional migration of carcinoma cells can be enhanced by aligned collagen fibers, especially for breast cancer stem cell populations (Ray et al., 2017b). Furthermore, Alexander *et al.* suggested that cancer cell dissemination patterns, including individual cell invasion, diffusively

collective invasion, and strand-like invasion, are governed by the ECM structures that the tumor cells encounter (Alexander et al., 2008). However, the topographic features dictating the invasion pattern remain unknown, as do the mechanisms by which tumor cells sense topographic features on a sub-cellular level. Nanofabrication techniques have inspired the rapid growth of materials that mimic natural *in vivo* topographies or 3D environments (Dvir et al., 2011). Recent studies have shown that engineered nanotopographies can not only cause cells to recapitulate *in vivo* migrational behaviors (Potthoff et al., 2014; Ramirez-San Juan et al., 2017; Ray et al., 2017a), but can also influence various cell functions (Onesto et al., 2017; Teo et al., 2013; Yang et al., 2017). Thus, nanopatterned substrates have the potential to provide insight into the physical and molecular mechanisms that regulate contact guidance during cancer progression.

The ability of patterned topographies to induce directional cell migration is a complex process that requires coordination between distinct cellular machineries, such as the assembly and disassembly of focal adhesions (FAs), the polymerization and depolymerization of actin filaments, and even the reorganization of organelles (Vicente-Manzanares et al., 2005). The formation of a FA is initiated by the engagement of integrins with their corresponding ligands on the substrate, followed with the recruitment of focal adhesion kinase (FAK), paxillin, vinculin, and other associated proteins (Mitra et al., 2005). The FA-associated proteins not only link the integrin receptors with the actin cytoskeleton (Kanchanawong et al., 2010), but also regulate actin polymerization and contractility through Rho GTPase signaling (Devreotes and Horwitz, 2015). Furthermore, the actin cytoskeleton controls the protrusive activity of migrating cells, which in turn mediates the formation of adhesions. Recent studies from our group on *Dictyostelium discoideum (D. discoideum)* cells and neutrophils have shown that actin polymerization occurs preferentially near nanoridges, leading to guided traveling waves that can bias cellular movement

bidirectionally (Driscoll et al., 2014). In the case of asymmetric nanotopographies this motion can be biased unidirectionally (Sun et al., 2015). It is also well established that various cell types elongate and exhibit aligned stress fibers when placed on ridges or grooves with widths and repeat distances on a subcellular scale (Kim et al., 2009b; Park et al., 2012; Ventre et al., 2014). Ray *et al*. reported that the anisotropic force originating from local FAs and the concomitant alignment of actin fibers induces the polarization and migration of carcinoma cells along ridges, and that the guidance response varies considerably among different types of carcinoma cells (Ray et al., 2017a). However, the link between the intrinsic heterogeneity of cancer cell lines and its influence on FA and actin dynamics during contact guidance is poorly understood.

Here, we study the migrational phenotypes of multiple breast cancer cell lines plated on aligned ridges and asymmetric sawtooth architectures. Data from long-term live-cell imaging enable us to perform extensive analysis of cell migration, actin polymerization dynamics, and FA distributions. Our findings elucidate the connection between the overall cell motility phenotype of breast cancer cells and their intracellular scaffolding architectures, adhesion complexes and actin cytoskeleton, and also provide insights into the biophysical mechanisms underlying contact guidance during cancer metastasis.

2.3 Results and discussion

2.3.1 Nanoridges provide bidirectional guidance for both benign and metastatic breast cancer cells

We compare the migration phenotypes of two cell lines belonging to the MCF10A cell series, a breast cancer progression model (Kadota et al., 2010; Marella et al., 2009; Tang et al., 2003), to explore contact guidance in cell lines sharing a similar genetic background but with distinct metastatic abilities. MCF10A (also referred as M1), a benign epithelial human cell line,

and its metastatic mutant cell line counterpart MCF10CA1 (also referred as M4), were studied on flat surfaces and on nanoridges composed of the same material. The M1 and M4 cells are negative for receptors for estrogen, progesterone, and HER2 (*i.e.*, triple negative) (Foulkes et al., 2010). Compared to immortalized epithelial M1 cells, the invasive M4 cells form tumors in the lungs of immunocompromised mice after tail vein injection (Santner et al., 2001; Tang et al., 2003).

Arrays of parallel nanoridges or nanogrooves (where nano- implies that their widths are on the nanoscale) have been used in previous contact guidance studies (Potthoff et al., 2014; Song et al., 2014; Tan and Saltzman, 2002). Here we use nanotopographies composed of an acrylic resin (Sun et al., 2018). Each nanoridge has a width of ~250 nm and a height of ~1 μm, and the spacing between the centers of adjacent nanoridges is 1.5 μm (Fig. 2.1A). By tracing cell boundaries over time and generating spider plots of the cell tracks, we found that both M1 and M4 cells move in a random manner on a flat acrylic surface (Fig. 2.2Ai, Aii, Ci &Cii). Polar histograms of the directions of both M1 and M4 cells demonstrate that there is no preferred direction of motion, as expected for a microenvironment in which no chemoattractant gradient nor other guidance cue is present (Fig. 2.2Aiii & Ciii). However, M1 and M4 cells migrating on nanoridges move preferentially parallel to the nanoridges (Fig. 2.2Bi, Bii, Di & Dii), as is also seen in polar histograms (Fig. 2.2Biii & Diii). This finding is consistent with previous results showing that parallel micro- or nanoscale grooves and ridges induce bidirectional guidance in a variety of cell types (Arocena et al., 2017; Driscoll et al., 2014; Song et al., 2014; Tan and Saltzman, 2002; Tzvetkova-Chevolleau et al., 2008). M1 cells exhibit a notably stronger guidance response to the nanoridges than do M4 cells (Fig. 2.2Biii & Diii), suggesting that the ability of cells to follow guidance cues is cell-type dependent. We also found that although the nanoridges provide guidance for cell migration, they do not increase the mean cell speed compared to the flat resin surface and,

in the case of M4 cells, actually decrease the mean speed (Fig. 2.2E). To explore this behavior in more detail, we measured the mean value of all velocities within a given angle range relative to the orientation of the nanoridges. We define the angle of motion as ranging from -180° to 180°, with the ridge direction along the *x* axis. Because the ridges are aligned horizontally in our images of ridges, on flat surfaces the horizontal direction in images was also defined as the *x* axis. We found that on flat surfaces, the mean velocity value is independent of angle for both cell types, within our experimental uncertainty (Fig. 2.2F). However, on nanoridges, both M1 and M4 cells exhibit a higher mean velocity when migrating along the ridge orientation than when migrating perpendicular to it (Fig. 2.2F). To confirm the significance of this increasing trend, we fitted the experimental results with a horizontal line model and a one phase decay model and compared the robustness of two models for each curve. We found that for M1 and M4 cells on flat surfaces, the fit of the horizontal line model is preferred, however the fit of the one phase decay model is preferred for the two cell lines on nanoridges ($P < 0.0001$ and $P = 0.001$ for M1 and M4 cells respectively). Together, these findings show that cells not only migrate preferentially along nanoridges, but also migrate faster along them than perpendicular to them.

Scanning electron microscopy (SEM) provides further insights into how cells interact with the nanoridges. On nanoridges, the lamellipodia of M1 cells form along nanoridges on both sides of the cell and are anchored on top of the nanoridges, without much penetration into the regions between nanoridges (Fig. 2.2G). One possible explanation for this phenomenon is that the nanoridges guide M1 cells bidirectionally because lamellipodium formation is promoted along the ridge direction and/or is suppressed perpendicular to the ridge direction. In contrast, M4 cells form lamellipodia that curve over nanoridges and into the bottom of the regions between nanoridges, and typically span several nanoridges (Fig. 2.2G, white arrows). Because contact guidance relies

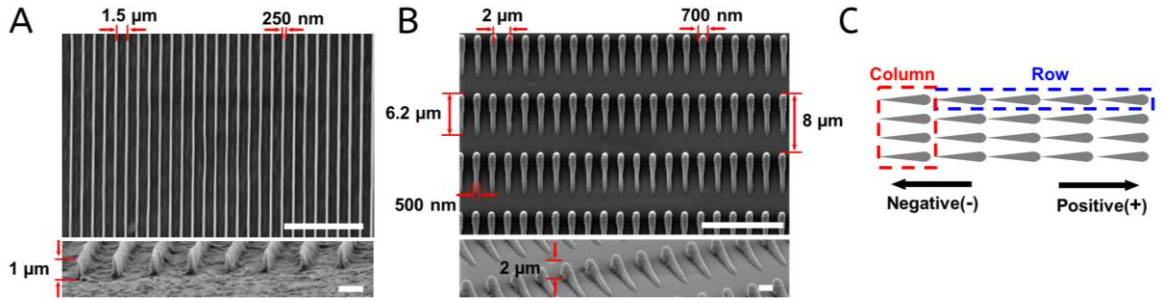

Figure 2.1: The nanotopographies used in this study. Top-view and side-view SEM images of (A) the nanoridges and (B) the asymmetric sawteeth used in this study. The scale bars in the top- and side-view images are 10 µm and 1 µm, respectively. (C) Schematic depicting a sawtooth row (blue box) and a sawtooth column (red box), as well as the direction defined as positive.

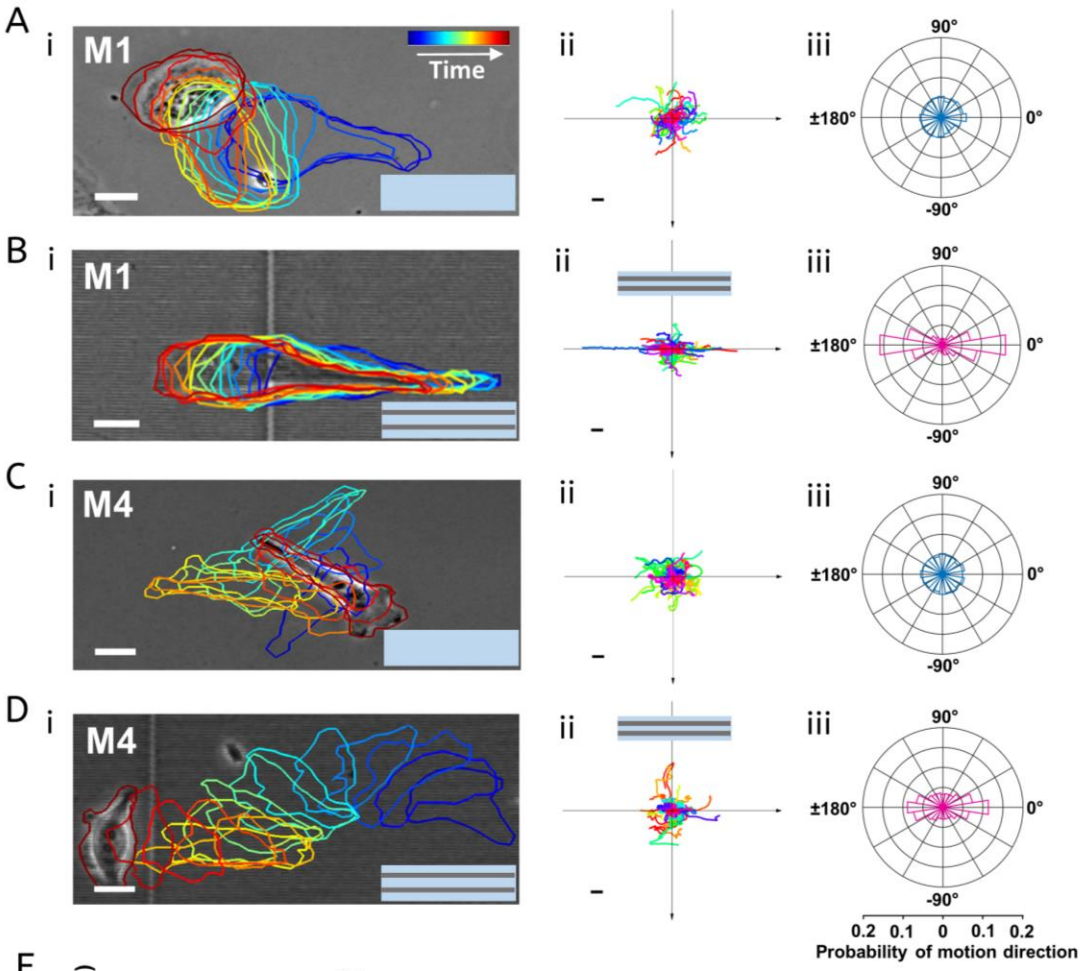
A
i
M1
Time
ii
iii
90°
±180°
0°
-90°
B
i
M1
ii
iii
90°
±180°
0°
-90°
C
i
M4
ii
iii
90°
±180°
0°
-90°
D
i
M4
ii
iii
90°
±180°
0°
-90°
0.2 0.1 0 0.1 0.2
Probability of motion direction

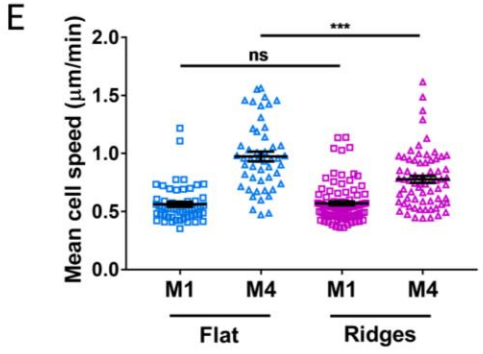
E
Mean cell speed (μm/min)
2.0
1.5
1.0
0.5
0.0
ns
***
M1
M4
M1
M4
Flat
Ridges

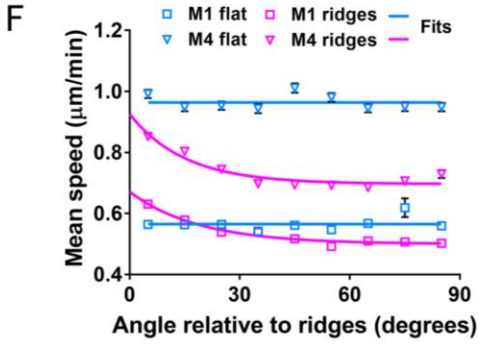
F
M1 flat
M1 ridges
Fits
M4 flat
M4 ridges
Mean speed (μm/min)
1.2
1.0
0.8
0.6
0.4
0
30
60
90
Angle relative to ridges (degrees)

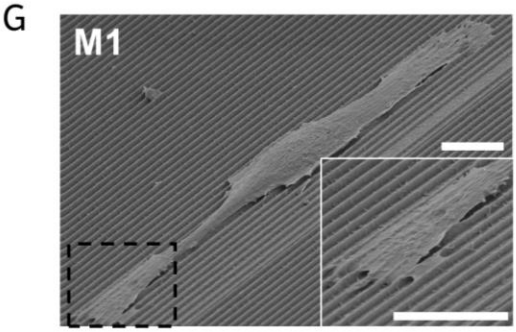
G
M1

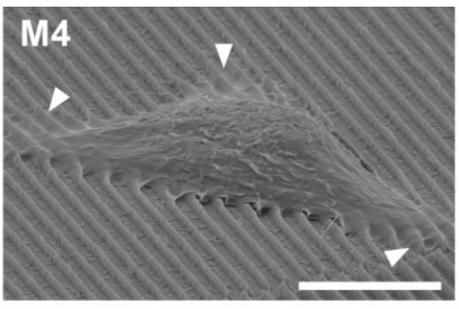
M4

Figure 2.2: Nanoridges provide bi-directional guidance for benign and metastatic breast cancer cells. (A-Di) Bright-field images of M1 or M4 cells on a flat surface (A, C) and on nanoridges (B, D). The colored outlines depict how the cell morphology changes over time, which increases from blue to red. The scale bar is 10 μm. (A-Dii) Centroid motion tracks of M1 and M4 cells, respectively, on a flat surface (A, C) and on nanoridges (B, D). n = 56 tracks (Aii); 94 tracks (Bii); 49 tracks (Cii); 68 tracks (Dii). The scale bar is 60 μm. (A-Diii) Probability distributions of cell motion directionality. The scale at the bottom corresponds to the horizontal axis in each rose plot. (E) The average cell speed of M1 and M4 cells on flat surfaces and on nanoridges. The middle solid line in each column is the mean value and the bar is standard error of the mean. ***$p<0.001$ (unpaired t test) (F) The average instantaneous speed of M1 and M4 cells relative to the orientation of ridges (0° along ridges, 90° perpendicular to ridges). Squares and triangles are experimental results, and solid lines are the fits to the experimental results. Blue solid line was fitted to a horizontal line, and the pink solid line was fitted to a one phase decay model. (G) Representative SEM images of M1 (top) and M4 (bottom) cells on nanoridges. The magnified image highlights the anchoring of M1 cell lamellipodia on top of the nanoridges. White arrows indicate sites where M4 cell lamellipodia curve over the nanoridges. The scale bar is 10 μm.

upon the spatial control of cell protrusions (Ramirez-San Juan et al., 2017), the behavior of the lamellipodia of M4 cells likely contributes to their lower contact guidance as compared to M1 cells.

2.3.2 Asymmetric sawteeth bias the movement of breast cancer cells in a cell-type dependent manner

We next consider the ability of breast cancer cells to respond to asymmetries in texture using sawtooth-shaped asymmetric nanotopographies. Each sawtooth has a maximum height of ~2 μm, a length of ~6.2 μm, and a width of ~700 nm at the head and ~500 nm in the center (Fig. 2.1B). The height of an individual sawtooth increases gradually from its tail to its head, and then drops rapidly. The pitch of the sawteeth is 8 μm along the sawtooth direction and 2 μm perpendicular to the sawtooth direction. We define a line of sawteeth along the sawtooth direction as a row. As all of the rows are in registry, we define a line of sawteeth perpendicular to the rows as a column (Fig. 2.1C). We define the direction from the tail of a sawtooth to its head (up the slope) as the positive direction along the *x* axis.

We found that M1 cells plated on the sawteeth move preferentially in the positive direction with an anterior lamellipodium (Fig. 2.3Ci & ii). A polar histogram of directionalities shows a higher percentage of orientation angles around 0° than 180° (Fig. 2.3Ciii). In contrast, M4 cells exhibit amoeboid-like migration, with ellipsoidal cell shapes and multiple pseudopods (Fig. 2.3Ei) (Friedl, 2004; Friedl and Wolf, 2010). Furthermore, the majority of the M4 cell tracks face in the negative direction (Fig. 2.3Eii), as do the cell velocities (Fig. 2.3Eiii). The preference of the M4 cells to move in the negative direction is considerably stronger than that of the M1 cells to move in the positive direction. Unlike M1 cells, M4 cells are more likely to move perpendicular to the sawteeth than to move in the positive direction.

We also measured the behavior of three other triple-negative human breast cancer cell lines, HS578T, MDA-MB-231 and BT549. HS578T and BT549 are carcinoma cell lines derived from primary tumors. MDA-MB-231 is a metastatic carcinoma cell line from pleural effusion (Kao et al., 2009). We found that MDA-MB-231 and HS578T cells exhibit a mesenchymal migration mode on the sawteeth, with multiple competing protrusions (Fig. 2.3Ai & 2.3Bi) (Bear and Haugh, 2014; Friedl and Wolf, 2010). Spider plots of cell tracks and polar histograms indicate that these cells tend to move in the positive direction (Fig. 2.3Aii, Aiii, Bii & Biii). In contrast, BT549 cells migrate in a blebby (and slightly elongated) manner on the sawteeth (Fig. 2.3Di). The BT549 cells preferentially move along the sawteeth, with a somewhat greater probability of moving in the negative direction than in the positive direction (Fig. 2.3Dii & Diii). We also found some motion of BT549 cells perpendicular to the sawteeth (Fig. 2.3Diii), as with the M4 cells. To assess the behavior of the cells on the sawteeth further, we grouped the velocity component along the sawtooth axis into motion in the positive and negative directions, + and – respectively. The velocities in each group were then averaged separately for each cell, and a paired speed difference for each cell was determined. We found that MDA-MB-231, HS578Tand M1 cells have higher mean speeds in the positive direction than in the negative direction, but the difference is smaller for M1 cells than for the other two cell lines (Fig. 2.3Aiv, Biv & Civ). For the BT549 and M4 cells, the mean speeds in the positive direction are lower than those in the negative direction (Fig. 2.3Div & Eiv). BT549 cells exhibit less paired speed difference and less unidirectional contact guidance compared with M4 cells. Together, these results show that the sawteeth provide both contact guidance and unidirectional bias in migration and speed for the breast cancer cell lines studied here. Both of these phenotypes are dependent on the cell type.

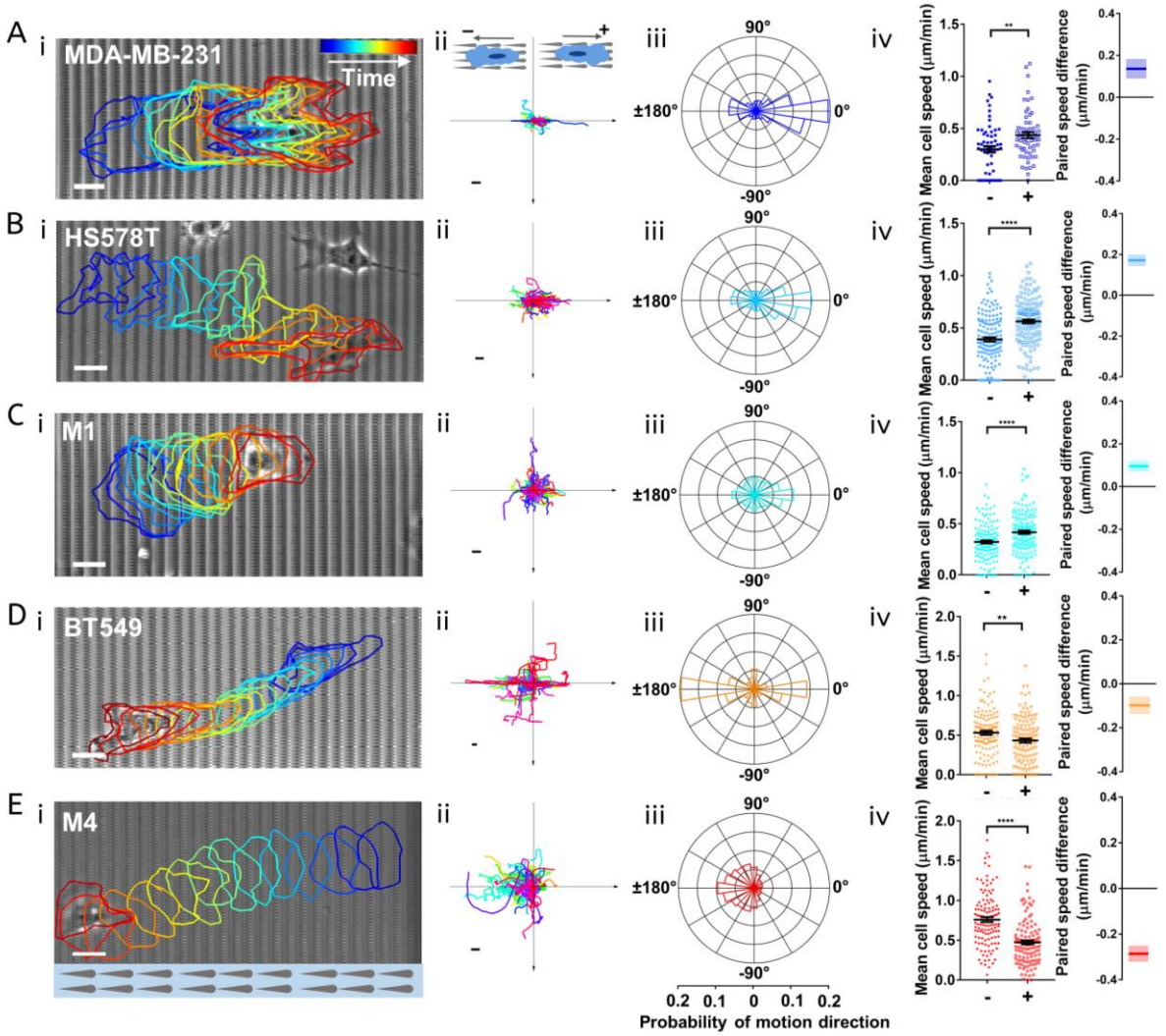

Figure 2.3: Asymmetric sawteeth bias the movement of various breast cancer cell lines. (A-Ei) Bright-field images of (A) MDA-MB-231, (B) HS578T, (C) M1, (D) BT549, and (E) M4 cells migrating on sawteeth. The colored outlines illustrate how the cell morphology changes over time, which increases from blue to red. The scale bar is 10 μm. (A-Eii) Centroid motion tracks of (A) MDA-MB-231, 62 tracks, (B) HS578T, 151 tracks, (C) M1, 143 tracks, (D) BT549, 126 tracks, and (E) M4, 122 tracks cells on sawteeth. The scale bar is 60 μm. (A-Eiii) Probability distributions of cell motion directionality. The scale at the bottom corresponds to the horizontal axis in each rose plot. (A-Eiv) Average cell velocity components of the cell lines along the positive direction (+) and the negative direction (-) and paired speed difference for each cell. The middle solid line is the mean value and the bar is standard error of the mean. The shaded areas represent standard errors in paired speed difference plots. *p<0.05, **p<0.01, ****p<0.0001.

We previously reported that *D. discoideum* cells and neutrophils exhibit biased directional migration when plated on sawtooth surfaces (Sun et al., 2015). This unidirectional topographic guidance, which is achieved by an asymmetric textures on a subcellular scale, is termed microthigmotaxis (Sun et al., 2015). Topographic gradients represent another way to guide cell migration unidirectionally - a phenomenon called topotaxis (Park et al., 2018). Kim *et al.* reported that individual fibroblasts are able to sense the anisotropic gradient of ridged patterns and modify their morphology and migration in response to the local pattern density (Kim et al., 2009b). On a 2D gradient lattice patterned substrate, the fibroblasts preferentially migrated towards the denser area and ultimately accumulated at the denser zones (Kim et al., 2009c). Anisotropic variation of the density of nanoposts along one direction has also been reported to lead to the biased migration of melanoma cells (Park et al., 2016). Recent work from Comelles *et al.* showed that large asymmetric ratchet-like structures (at the scale of single cells) biased the motion of fibroblasts towards the positive direction of the ratchet pattern, and that this ratchet-guidance was improved by superimposing a fibronectin gradient (Comelles et al., 2014). Interestingly, even without the topographic ratchet pattern, aligned ratchet-shape adhesive fibronectin patches were able to induce a biased long-term motion that was determined by asymmetric protrusion formation (Caballero et al., 2014; Caballero et al., 2015b). First introduced by the physicist Richard Feynman, this type of guidance is termed ratchetaxis (Caballero et al., 2015a). In contrast with ratchet-like topography, the asymmetry induced by the nanoscale sawteeth in our study is at sub-cellular level, suggesting that directed migration can stem from the accumulation of small biases in intracellular elements. Furthermore, we show that breast cancer cells exhibit microthigmotactic behavior that depends strongly on cell type. Although the underlying mechanism remains to be determined, it is likely that the distinct mutation patterns and intrinsic heterogeneities of the different cell lines are

reflected in the cells' contact guidance and directional bias behaviors. We speculate that such significant differences may be related to the metastatic potential of the different cancer cell lines *in vivo*.

2.3.3 The degree of bias in cell migration is related to cell speed and long-term persistence

Cell migration is a heterogeneous process, in which different cells move with distinct velocity and persistence. Indeed, the direction and speed of any given cell also vary over time. To study how cell speeds influence unidirectional guidance on sawteeth, we divided histograms of the cell speeds into four quartiles (see insets of Fig. 2.4Ai-Ei). We also plotted the normalized probabilities of the angle of cell motion relative to the sawtooth positive direction for each quartile (Fig. 2.4Ai-Ei). For HS578T and MDA-MB-231 cells, there is no observable directional preference at low speeds, but migrational bias increases with increasing cell speed (Fig. 2.4A-Bi). This trend is similarly robust for these two cell lines. In contrast, the level of directional preference of M1 cells remains low even at higher speeds, suggesting that speed and contact guidance are not strongly coupled in these cells (Fig. 2.4Ci). BT549 and M4 cells behave like HS578T and MDA-MB-231 cells: unidirectional guidance increases with increasing speed (Fig. 2.4Di-Ei). The trend is less evident for BT549 cells since the probability curves are considerable overlapping. Nevertheless, the probability of BT549 cells migrating along the sawtooth negative direction (~180°) keeps increasing with speed, while the probability for migration along intermediate angles decreases.

Using a similar segmentation approach, we investigated the effect of long-term persistence of cell motion on the unidirectional guidance of migration. We define the long-term persistence of cell motion as the ratio of the total displacement of the cell to the total length of the cell track for

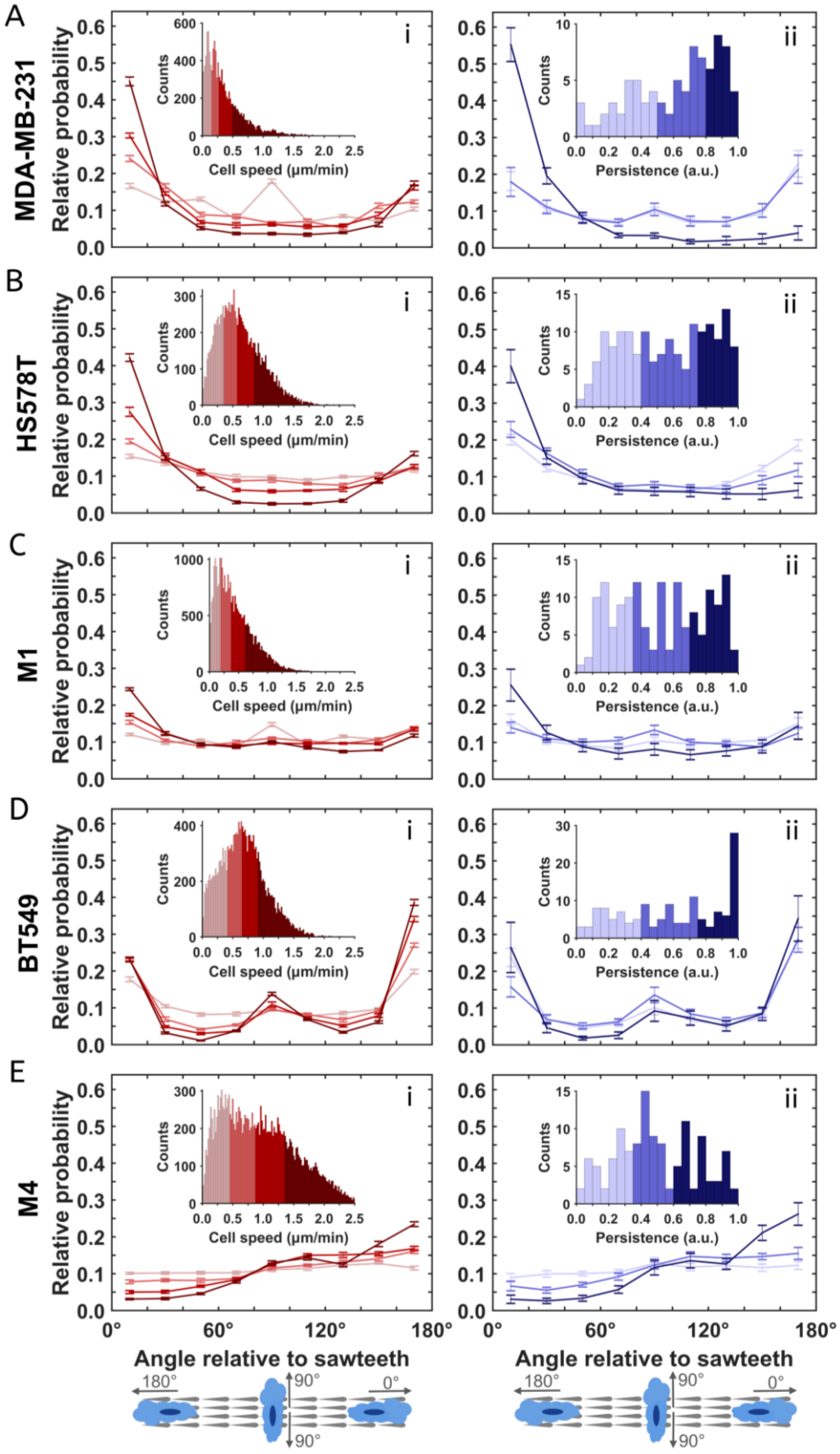
A
MDA-MB-231
B
HS578T
C
M1
D
BT549
E
M4
Relative probability
i
ii
Counts
Cell speed (μm/min)
Persistence (a.u.)
0°
60°
120°
180°
Angle relative to sawteeth
180°
90°
0°
90°

Figure 2.4: The level of biased cell motion increases with cell speed and long-term persistence. Column (i) shows the probability of the direction of motion based on speed for (A) HS578T, (B) MDA-MB-231, (C) M1, (D) BT549, and (E) M4 cells. The insets show the speed distributions of the cell lines and the ranges of four sections which were equally divided based on the total counts of cell speeds. The cell speed increases from light red to dark red in both the plots and the insets. Column (ii) shows the probability of the direction of motion based on migrational persistence for the same cells lines. The insets show the long-term persistence distributions for the cell lines and the ranges for tertiles based on the total counts of cells. The long-term persistence increases from light blue to dark blue in both the plots and the insets. All error bars represent the standard error of the mean.

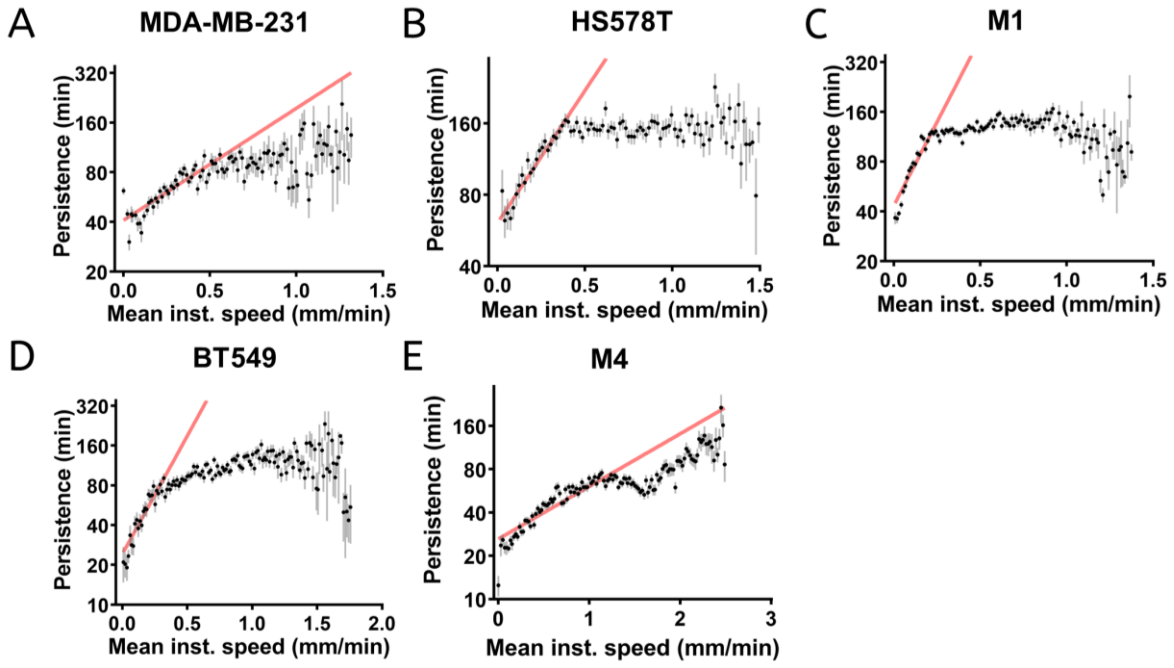

Figure 2.5: The persistence time versus mean instantaneous speed plots for breast cancer cell lines. (A-D) Persistence *vs.* mean instantaneous speed for MDA-MB-231 (A), HS578T (B), M1 (C), BT549 (D) and M4 (E) cells. The definition of persistence time in 2D geometry and the calculation method have been described previously (Maiuri et al., 2015). The black dots are the mean for the data in each bin and the shaded gray lines are standard error of the mean. The shaded red lines are fits following an exponential equation $\tau = Ae^{\lambda v}$ (Maiuri et al., 2015). The fitting parameters are listed in table 2.1 below.

Table 2.1: Fitting parameters for persistence time *vs.* instantaneous speed

	MDA-MB-231	HS578T	M1	BT549	M4
A(min)	40.91±2.11	60.75±3.37	43.25±2.78	24.16±1.89	26.94±1.03
λ (min.μm^{-1})	1.56±0.15	2.57±0.19	4.66±0.36	4.12±0.33	0.84±0.04

a chosen time interval. A cell moving in a straight line has a long-term persistence of 1, whereas random motion leads to a long-term persistence of 0. Cells were separated into three equal fractions based on their distributions of cell persistence (see insets of Fig. 2.4Aii-Eii). The normalized probabilities of the cell motion direction were then calculated by using all velocities from the cells in each of the three fractions. We found that cells with the greatest long-term persistence show the strongest contact guidance and bias towards the preferred direction of each cell line (Fig. 2.4Aii-Eii). However, the directional preference is similarly vague for cells with low and intermediate long-term persistence across all cell lines (Fig. 2.4Aii-Eii). For BT549 cells, the probability curves from all three fractions greatly overlap within the estimated uncertainty, suggesting that the correlation between contact guidance and cell persistence is weak in these cells. Together, we conclude that the propensity of cells to migrate in a biased fashion increases when the cells move with higher speeds or with higher directional persistence. Recently, a universal coupling between cell speed and cell persistence (UCSP) was discovered and proved to be valid across a variety of cells and dimensional settings (Maiuri et al., 2015). To test whether this UCSP law can be applied to our system, we plotted the persistence time *vs.* mean instantaneous speed for all cell lines by following the definition of persistence time and the quantification method in Maiuri Paolo *et al.* (Fig. 2.5) (Maiuri et al., 2015). Similar to the findings in Maiuri Paolo *et al.*, we found a correlation between the persistence time and mean instantaneous speed at low speed but a rapid saturation at larger speed range for all breast cancer cell lines (Fig. 2.5). Only M4 cells show a second rising phase at high speed range. We speculate that the rapid saturation in our results is likely due to following reasons. First, in our experimental settings, the cells are not well isolated and cell trajectories are not long enough compared with the settings in Maiuri Paolo *et al*. Second, the UCSP law assumes a linear coupling between cell speed and actin flow which may not be valid in

our settings due to the complexity induced by the sawtooth structures. Nevertheless, it will be interesting to examine further whether the UCSP law holds for the topography-guided migration.

2.3.4 Unidirectional actin polymerization drives biased cell migration

During migration and metastasis, each cancer cell dynamically reorganizes its cytoskeleton, including actin structures and microtubules, to maneuver and to adapt to complex and changing environments. Filopodia and lamellipodia are actin-rich structures that act as dynamic sensors with which cells detect their surrounding microenvironment (Bettinger et al., 2006; Ramirez-San Juan et al., 2017; Song et al., 2014). The formation of filopodia and lamellipodia requires extensive rearrangement of cytoskeletal elements. Driscoll *et al*. found that actin polymerization in *D. discoideum* migrating on nanoridges is nucleated near the nanoridges, after which actin polymerization proceeds in a wave-like manner along the ridges (a process called esotaxis) (Driscoll et al., 2014). Further, it has been established previously that the unidirectionally guided motion of *D. discoideum* cells on lines of sawteeth (microthigotaxis) arises from esotaxis, which shares the same direction as cell motion (Sun et al., 2015). We therefore explored the correlation between the directional bias in actin polymerization and cell motion for the MDA-MB-231 and M4 cell lines, as they represent two opposite extremes of contact guidance and bias. To assess actin dynamics, we used cells infected with a fluorescence-tagged protein (Lifeact-eGFP), which associates with polymerizing F-actin. Time-lapse recordings of Lifeact-eGFP/MDA-MB-231 cells reveal that these cells preferentially form distinct F-actin structures surrounding the nanosawteeth at the leading edges of cell protrusions (Movie 2.1). Actin polymerization bursts occur occasionally in the middle of migrating cells and diffuse across the nanosawteeth (Movie 2.1). We used an optical-flow algorithm to examine the local direction of the actin polymerization flux. Zooming in on one representative sawtooth (Fig. 2.6A & B), we see that actin polymerization was

initiated at the tail of the sawtooth and propagated toward the head on both sides of the sawtooth in a wave-like manner. The black arrows in Fig. 2.6B represent optical-flow vectors, which are related to the local directionality of the actin waves. The optical-flow analysis indicates that actin polymerization is nucleated at the back of the sawtooth, after which the polymerization front moves forward on both sides of the sawtooth (Movie 2.2). Finally, the waves terminate at the front of the sawtooth (Fig. 2.6B, and Movie 2.2), consistent with our previous findings in *D. discoideum* (Sun et al., 2015).

To assess the average actin flow around a sawtooth, we extracted the boundary of every sawtooth from the bright-field images, measured the average intensity at each of the 51 boundary points of each sawtooth, and generated a kymograph representing all boundary points (on the *y* axis, -25 to 25) over time (on the *x* axis). The average kymograph for all of the sawteeth shows that the average fluorescence intensity is higher at the tails of the sawteeth (position ±25) at time t_w-6, suggesting the initiation of actin polymerization. After time t_w-6, the average actin fluorescence increases near position 0 with time and gradually peaks at position 0 around time t_w. These findings support the conclusion that actin polymerization is nucleated at the tails of the sawteeth and moves towards the heads (Fig. 2.6C). A space/time plot also shows that the actin waves propagate from one sawtooth to the adjacent one in the positive direction with a speed of ~1 μm/min (Fig. 2.6D). Thus, the unidirectional guidance of actin polymerization is in the same direction as that of the cell motion.

In Lifeact-eGFP/M4 cells, actin polymerization structures form not only at the cell protrusions, but also in the middle of each cell. The actin polymerization intensity is always higher at the front of the sawteeth (Fig. 2.6E and Movie 2.3). Data from a representative sawtooth reveal

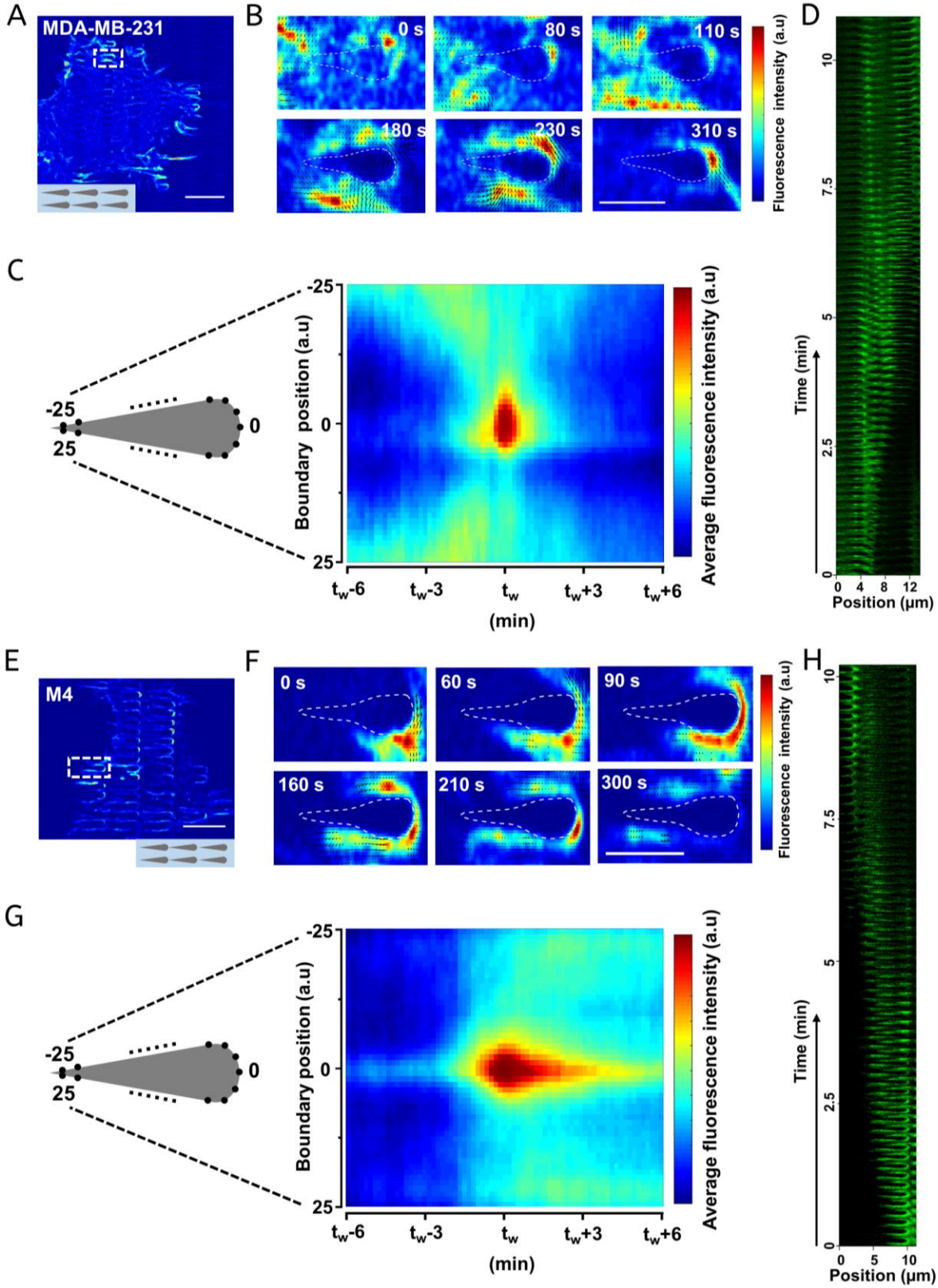
A
MDA-MB-231
B
0 s
80 s
110 s
180 s
230 s
310 s
Fluorescence intensity (a.u)
D
Time (min)
Position (μm)
C
-25
0
25
Boundary position (a.u)
Average fluorescence intensity (a.u)
t_w-6
t_w-3
t_w
t_w+3
t_w+6
(min)
E
M4
F
0 s
60 s
90 s
160 s
210 s
300 s
H
G

Figure 2.6: Sawteeth trigger unidirectional actin polymerization in the same direction as the cell motion in a cell-type dependent manner. (A & E) Fluorescence images of Lifeact-eGFP/MDA-MB-231 (A) or Lifeact-eGFP/M4 (E) cells on sawteeth. The colors indicate the intensity of fluorescence. The scale bar is 20 μm. (B & F) Actin flux at different time points around a single sawtooth highlighted by the white box in (A) and (E), respectively. The boundary of the sawtooth was generated based on the corresponding bright-field image, and due to diffractive effects does not correspond to the actual shape of the sawtooth. The different colors represent different fluorescence intensities. The black arrows illustrate the direction of actin polymerization flux. The scale bar is 5 μm. (C & G) The averaged kymograph of actin intensity along one sawtooth boundary over time for (C) Lifeact-eGFP/MDA-MB-231 and (G) Lifeact-eGFP/M4 cells. The x axis is the relative time difference from defined time point t_w, when the actin polymerization wave initiates or reaches the sawtooth position 0. The length of the x axis is 71 frames (11.83 mins). The y axis is the scaled position along one sawtooth boundary, for which 0 represents the front and ±25 represents two symmetric points near the tail. The different colors represent different fluorescence intensities. (D & H) Space/time plots of actin polymerization along two adjacent sawteeth in a sawtooth row for (D) Lifeact-eGFP/MDA-MB-231 and (H) Lifeact-eGFP/M4 cells.

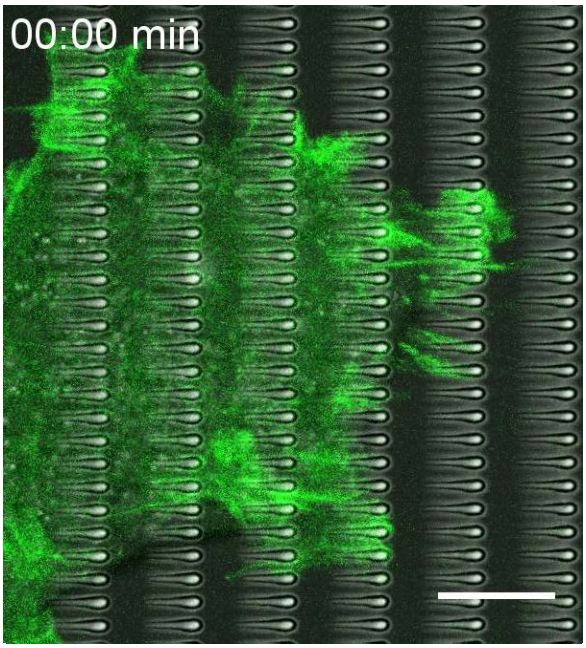

Movie 2.1: Merged fluorescence and bright-field time-lapse images of a Lifeact-eGFP/MDA-MB-231 cell migrating on sawteeth. The sawteeth are oriented horizontally with their positive direction (tail to head) facing right. The rate of the raw movie: 10 s/frame, play rate: 16 frame/s. The green is Lifeact-eGFP fluorescence. The scale bar is 10 μm.

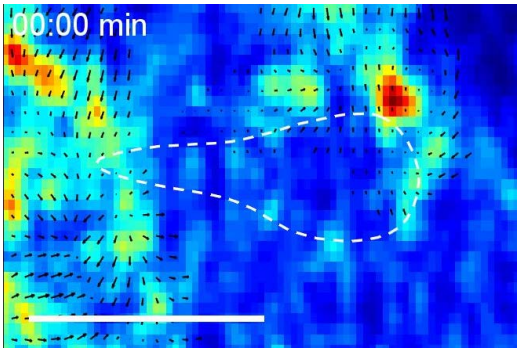

Movie 2.2: Actin waves in a Lifeact-eGFP/MDA-MB-231 cell propagating around a single sawtooth. The actin fluorescence intensity is color coded as indicated. The white dashed line marks the apparent boundary of the sawtooth and the black arrows are optical-flow vectors that show the local directionality of the flux. The rate of the movie is 10 s/frame and the play rate is 16 frame/s. The scale bar is 5 μm.

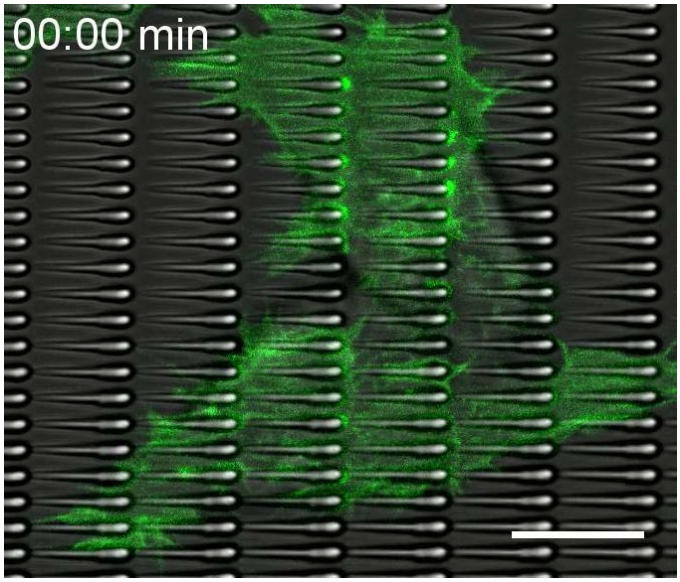

Movie 2.3: Merged fluorescence and bright-field time-lapse images of a Lifeact-eGFP/M4 cell migrating on sawteeth. The sawteeth are oriented horizontally with their positive direction (tail to head) facing right. The rate of the raw movie is 10 s/frame, and the play rate is 16 frame/s. The green is Lifeact-eGFP fluorescence. The scale bar is 10 μm.

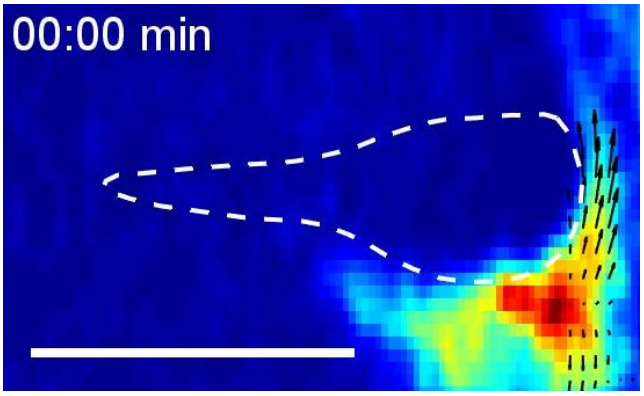

Movie 2.4: Actin waves in a Lifeact-eGFP/M4 cell propagating around a single sawtooth. The white dashed line marks the boundary of the sawtooth and the black arrows are optical-flow vectors that show the local directionality of the flux. The rate of the movie is 10 s/frame and the play rate is 16 frame/s. The scale bar is 5 μm.

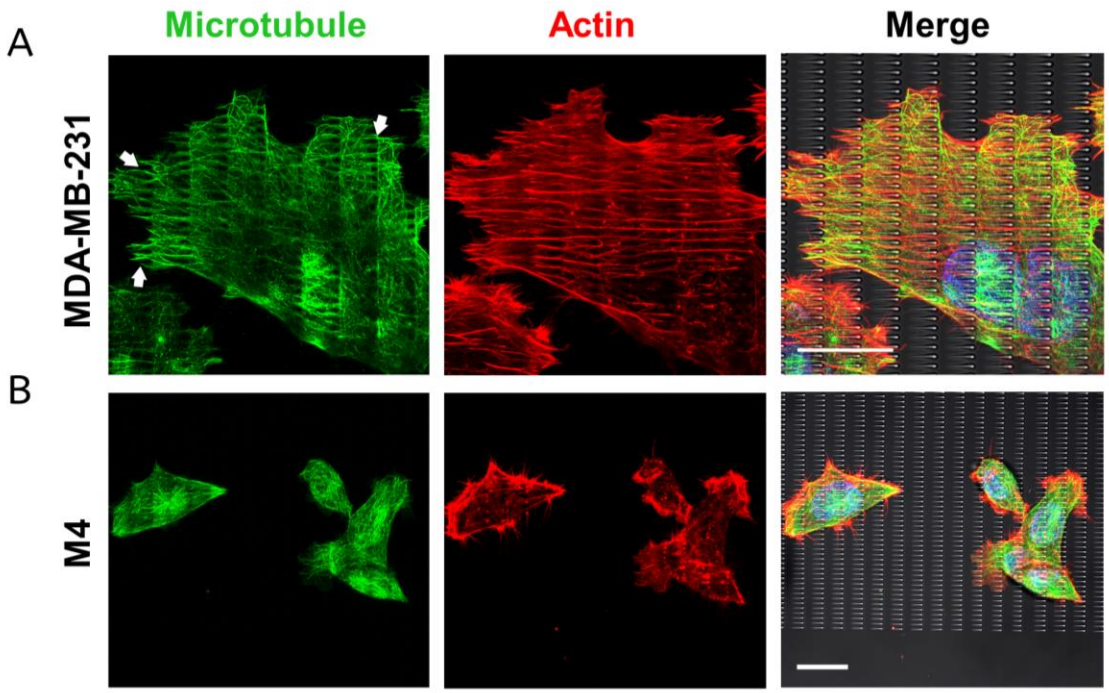

Figure 2.7: Influence of sawteeth on microtubules in MDA-MB-231 cells and M4 cells. (A, B) From left to right, fluorescence images of microtubules, actin and merge of these two with the bright-field image and DAPI labeling for (A) MDA-MB-231 cells and (B) M4 on sawteeth. The white arrows highlight two locations where microtubules coil around nanosawteeth. The scale bar is 10 μm.

that actin polymerization is nucleated at the head of the sawtooth, after which the wavefront flows towards the tail of the sawtooth (Fig. 2.6F and Movie 2.4). The average kymograph of actin polymerization activity around the sawteeth confirms that actin polymerization is nucleated at the head of sawteeth and flows towards the tail along both sides (Fig. 2.6G). The average kymograph also shows that the sawtooth head maintains a relatively higher level of actin fluorescence intensity compared to other locations on the sawtooth after time t_w, as illustrated in Movie S3. This may be because the curvature of the sawtooth heads promotes actin polymerization. The actin waves also are observed to travel from one sawtooth to the adjacent one in the negative direction (Fig. 2.6H).

Microtubules are another essential cytoskeletal component of cells. Microtubules have been shown to be the first cytoskeletal element to be aligned by micron-scale grooves during the spreading of fibroblasts (Oakley and Brunette, 1993). This process is followed by the alignment of focal contacts, actin filaments and finally cells (Oakley and Brunette, 1993). Microtubules were found to align with ridges on ridged substrates (Sun et al., 2018). Because microtubules regulate FA disassembly through integrin recycling and trafficking (Ezratty et al., 2009; Ezratty et al., 2005), it is natural to consider that microtubules play an important role in cell polarization and migration during contact guidance. To investigate this idea, we fixed MDA-MB-231 and M4 cells migrating on sawteeth and stained for microtubules using an antibody against tubulin. We found that the microtubules of MDA-MB-231 cells align with the sawtooth patterns. This alignment is particularly evident at the cell protrusions, where microtubules coil around the sawteeth (Fig. 2.7A, white arrows). This phenomenon was not observed in M4 cells (Fig. 2.7B), suggesting that the mechanisms that regulate microtubule dynamics differ in cells that respond differently to a specific nanotopographic surface.

These findings show, as previously observed in *D. discoideum* and neutrophils (Sun et al., 2015), that there is a direct connection between the migrational response to sawteeth and the underlying cytoskeletal dynamics. In other words, the esotactic guidance of the actin cytoskeleton plays an important role in microthigmotaxis. Actin waves are known to be important in cell membrane dynamics and motility. It has previously been shown that actin polymerization drives the wave-like movement of its upstream nucleator through an autoinhibitory mechanism (Weiner et al., 2007), which can further generate the directional motion of cells (Doubrovinski and Kruse, 2011; Kruse, 2016a). By using asymmetric sawtooth surfaces, we expand this concept by showing that an asymmetric topography can induce esotactic (actin) and microthigmotactic (migrational) behaviors in a cell-type dependent manner. This dependence of the direction of these phenomena on cell type suggests that multiple regulatory nodes contribute to the fine control of actin dynamics. Some of these nodes may be intrinsic, including the antagonistic interplay between GTPases signaling and the activation of different actin nucleators (Bretschneider et al., 2004; Weiner et al., 2007), whereas others may be extrinsic, such as the use of integrin-based complexes to interact with the underlying topographic guidance cues.

2.3.5 Distinct FA patterns and cortical plasticity promote biased cell migration

In addition to the actin and microtubule cytoskeletal networks, FAs are key component in contact guidance. FAs transduce extracellular forces from the ECM and induce a wide range of biochemical signals that go on to regulate cell adhesion and motility (Devreotes and Horwitz, 2015). In this context, Ohara, and Buck first proposed that the polarization and alignment of cells on ridges results from the need to maximize the area of focal contacts (Ohara and Buck, 1979). Several studies have now suggested that FA formation represents one plausible mechanism by which contact guidance is regulated (Kubow et al., 2017; Park et al., 2012; Ray et al., 2017a;

Ventre et al., 2014; Zimerman et al., 2004). We examined the distribution pattern of FAs for both MDA-MB-231 and M4 cells on sawteeth using high-resolution fluorescence imaging of actin and paxillin, the latter of which is an important scaffold protein of FAs that recruits and integrates numerous structural and signaling proteins for the transduction of ECM signals (Deakin and Turner, 2008).

To capture the paxillin fluorescent signal around each sawtooth on the *z* axis (*i.e.*, along the surface normal), we imaged cells at *z* positions ranging from below the bottom of the surface to above the top of each sawtooth, resulting in each sawtooth falling into a range of 1.2 to 3.2 μm on the *z* axis. A montage of paxillin and/or actin labeling of a MDA-MB-231 cell is presented in Figure 2.8A. The paxillin signal is first observed at a *z* of approximately 1.2 μm, which is at the bottom of the cell. The majority of the FAs are located around the cell periphery, at the tips of filopodia (Fig. 2.8A; paxillin and merge channels). FA complexes are also seen in the gaps between adjacent sawtooth columns that connect with stress fibers (Fig. 2.8A; see white arrows in merge channel). Above $z = 2.0$ μm, no obvious FAs are observed. The actin filament network starts to show up in cell lamellipodia and becomes obvious at $z = 2.8$ μm (Fig. 2.8A; see white arrow in actin channel). Surprisingly, above $z = 2.8$ μm the FA punctae are well organized, with a spacing similar to that of adjacent rows of sawteeth (Fig. 2.8A; paxillin channel). To show precisely the spatial positions of the FAs in different *z* slices, we selected FA complexes from either the bottom layer (Fig. 2.8A & B; 1-3, blue arrows) or the tips of the sawteeth (Fig. 2.8A & B; 4-6, red arrows) and generated *x*-*z* and *y*-*z* projections (Fig. 2.8B). The FAs from the bottom layer reach a peak intensity at a *z* of approximately 1.3 μm (Fig. 2.8B; blue dash lines and Fig. 2.8C; top panel). In contrast, the ordered FA complexes from the top layer are located near the tips of the sawteeth and

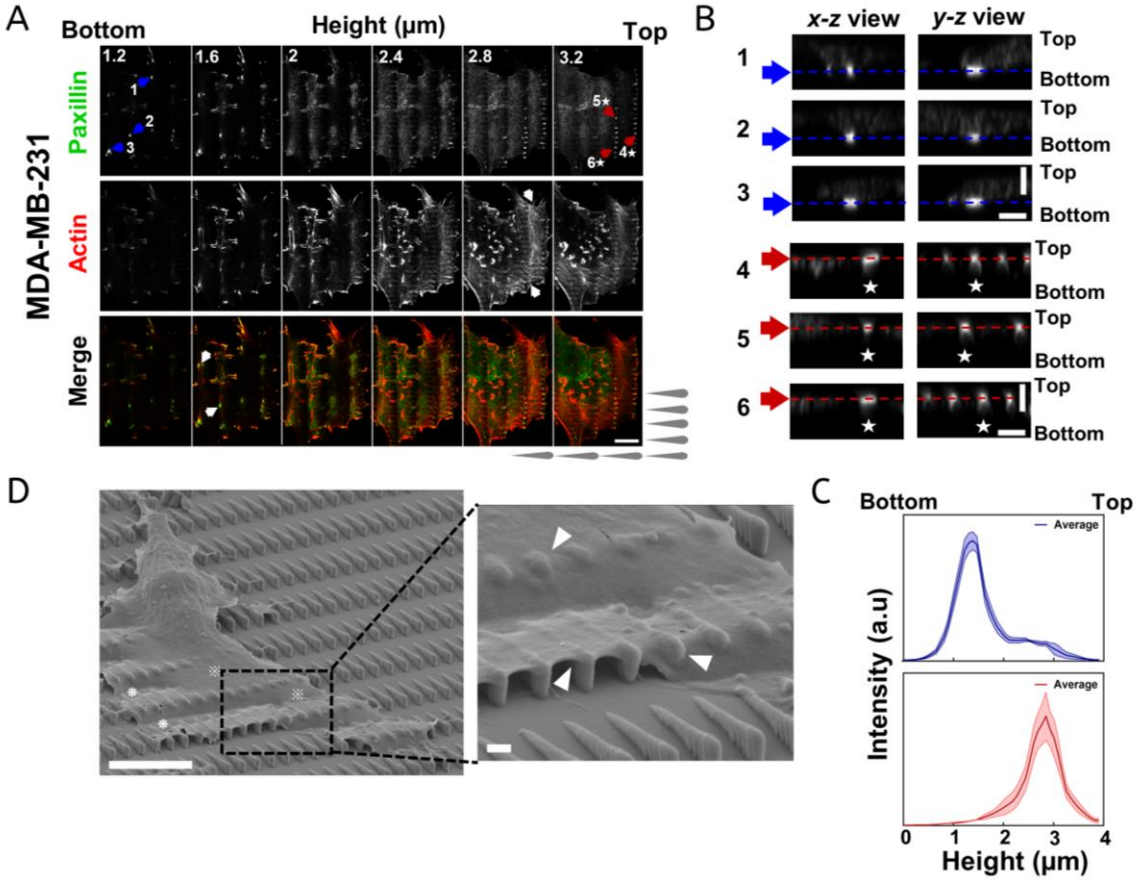

Figure 2.8: MDA-MB-231 cells form focal adhesions on top of the nanosawteeth and exhibit high cortical plasticity. (A) Fluorescence image montage of paxillin (top), actin (middle), and the merge of the two (bottom) at different *z* positions for MDA-MB-231 cells. Blue and red arrows highlight the focal adhesions chosen for further analysis in (B). The white arrows in the actin channel of (A) highlight the actin filament network. The white arrows in merge channel of (A) indicate focal adhesions located between two sawtooth columns. The scale bar is 10 μm. (B) The *x*-*z* and *y*-*z* views of representative FAs from the lowest and highest *z* positions in (A). The white stars indicate the representative FAs in the images in the *x*-*z* and *y*-*z* views. The single red and blue dashed lines in (B) mark the center *z* positions of the chosen FAs. The scale bar is 2 μm. (C) Fluorescence intensity of *x*-*z* projections of FAs in (B) for MDA-MB-231 cells. The top panel is for FAs 1-3 and bottom panel is for FAs 4-5. The solid line is the average intensity of three FAs and the shaded area represents the standard errors (D) Representative SEM images of MDA-MB-231 cells migrating on sawteeth. Magnified images of the areas are highlighted by the boxes with black dashed lines. White arrows highlight the places showing cell cortical plasticity of MDA-MB-231. The scale bars are 10 μm in the zoomed out images and 1 μm in the magnified images.

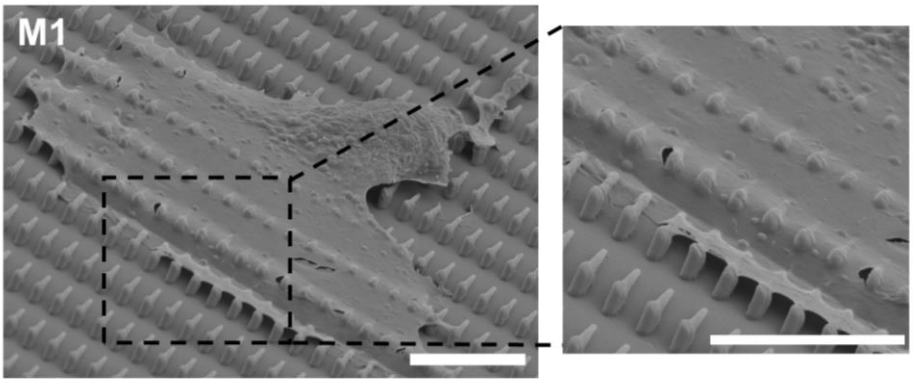

Figure 2.9: Cortical plasticity of M1 cells on sawteeth. A representative SEM image of an M1 cell on sawteeth (top) and a zoomed-in image of the area in the box (bottom). The scale bar is 10 μm.

exhibit a maximum intensity at a *z* of approximately 2.9 μm (Fig. 2.8B; red dash lines and Fig. 2.8C; bottom panel). Notably, strong fluorescence signals are not observed in the gaps between two adjacent FAs on the top of the sawteeth, suggesting that there is little membrane penetration into the grooves of the structures (Fig. 2.8B; 4-6 *y*-*z* view). Because FA complexes are indicators of the cell-ECM interfaces, we speculate that the MDA-MB-231 cells primarily interact with the tips of the nanosawteeth and that the FAs and stress fibers sustain most of the cortex above the grooves.

Indeed, SEM images of MDA-MB-231 cells on sawteeth show that the whole cell body remains on top of sawteeth like a "floating rigid blanket" (Fig. 2.8D). The leading lamellipodia spread across multiple sawteeth in the same column, whereas the membrane rests on the top of the sawteeth with no penetration into the grooves between rows of sawteeth. This behavior is further highlighted by zooming in at the front of the cell lamellipodium (Fig. 2.8D; zoom-in image). This bridging behavior is in agreement with our results on M1 cells on nanoridges (Fig. 2.8D; top panel), as well as with many previous reports (Ohara and Buck, 1979; Potthoff et al., 2014; Ventre et al., 2014; Zimerman et al., 2004). Bridging is thought to promote cellular alignment and anisotropic traction forces because of confined FA growth (Ray et al., 2017a). In fact, this bridging effect may provide an explanation for our previous observation that M1 cells preferentially form FAs on ridges (Sun et al., 2018). At the front of a sawtooth, the cell membrane curves somewhat and wraps around the head (Fig. 2.8D; white arrow heads). M1 cells, whose migration bias is in the same direction as that of MDA-MB-231 cells, exhibit a similar phenotype (Fig. 2.9). When the cell lamellipodia extend from one sawtooth column to another, the membrane can either bridge the gap (Fig. 2.8D; see ※) or droop down to the bottom surface (Fig. 2.8D; see ∗). We envision that cell

areas where the cell interacts with the bottom ECM (marked by ∗) provide support for the cell body, as observed by fluorescence imaging of actin and paxillin (Fig. 2.8A).

Profoundly different FA patterns are observed for M4 cells than for MDA-MB-231 cells. At the interface between an M4 cell and the bottom ECM, large FA complexes are formed at the front of the cell protrusions and also in the grooves between adjacent rows of sawteeth (Fig. 2.10A; paxillin channel). These FAs display a maximum intensity at a *z* of approximately 1.4 μm (Fig. 2.10B, 1-3 blue dashed lines and Fig. 2.10C; top panel). Above $z = 2.0$ μm, the M4 cells exhibit organized FA patterns surrounding each sawtooth, resulting in brighter outlines of the sawteeth (Fig. 2.10A; paxillin channel). Furthermore, thick actin structures are seen around the sawteeth through the entire *z* section (Fig. 2.10A; actin channel). This phenomenon is visible in a 3D reconstruction, which clearly shows the outlines of sawteeth. In contrast to FAs in MDA-231 cells, FAs of M4 cells interact with the ECM on the side walls of the sawteeth (Fig. 2.10B; 1-3 *y*-*z* view). Furthermore, the FA complexes are located along the slopes of the sawteeth, extend from the bottoms to the tops of the sawteeth (Fig. 2.10B; 4-6 *x*-*z* view). This finding is further substantiated by the quantification of fluorescence intensity, which shows a broad distribution over the entire *z* depth (Fig. 2.10C; bottom panel). The *y*-*z* view of FAs 4-6 further illustrates that FA complexes are assembled on the side walls of the sawteeth for a range of *z* values. SEM images provide further evidence that the cortical plasticity of M4 cells is distinct from that of MDA-MB-231 cells (Fig. 2.10D). Multiple protrusions are formed around M4 cells, compared with only one lamellipodium for MDA-MB-231 cells (Fig. 2.8D & 2.10D). The cell boundary of M4 cells is also highly dynamic, with extensive membrane ruffling and blebbing (Fig. 2.10D). Zooming in on one dominant protrusion indicates that the cell boundary, especially at the front of the protrusion, is able to wrap around individual sawteeth (Fig. 2.10D, see white arrows in the zoomed-in image). This

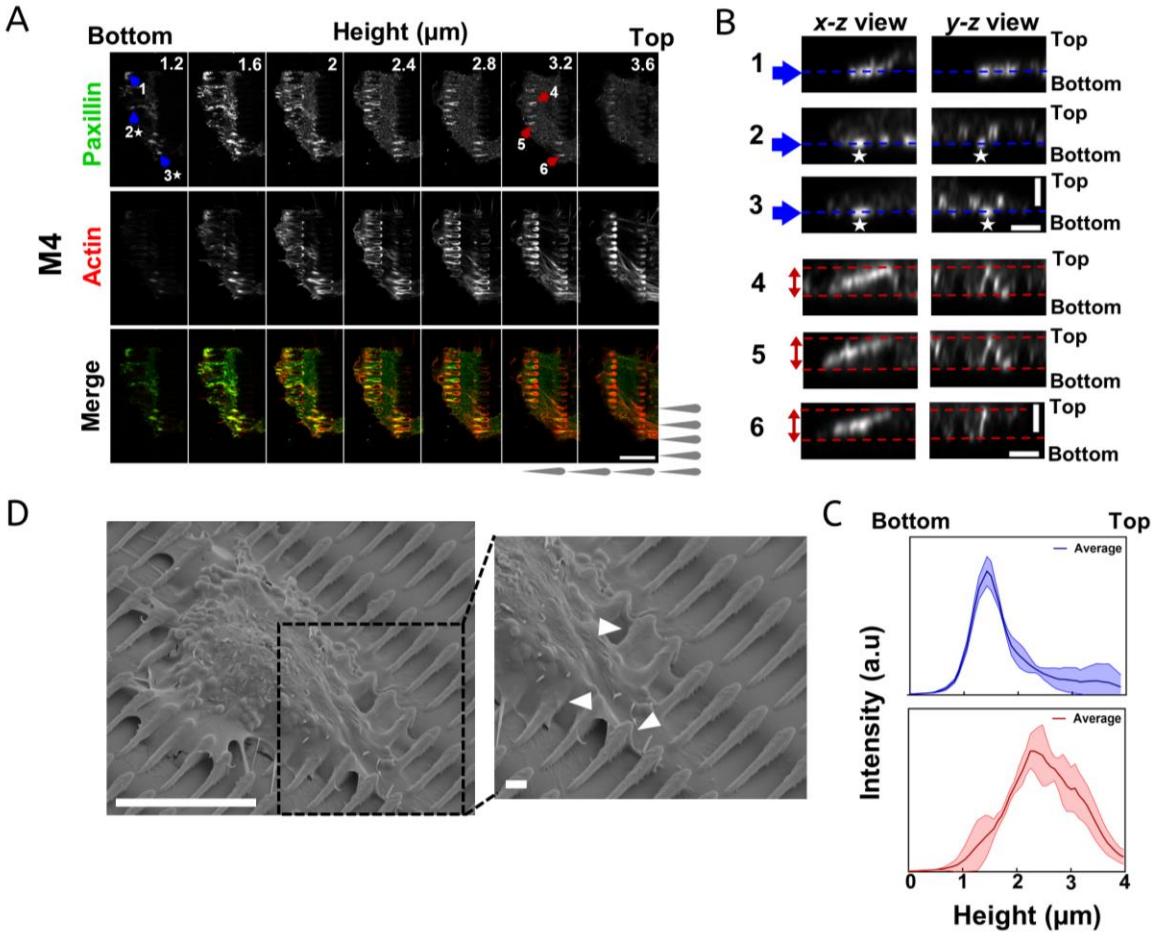

Figure 2.10: M4 cells show low cortical plasticity and assemble focal adhesion complexes sounding sawtooth structures. (A) Fluorescence image montage of paxillin (top), actin (middle), and the merge of the two (bottom) at different *z* positions for M4 cells. Blue and red arrows highlight the focal adhesions chosen for further analysis in (B). The scale bar is 10 μm. (B) The *x*-*z* and *y*-*z* views of representative FAs from the lowest and highest *z* positions in (A). The white stars indicate the representative FAs in the images in the *x*-*z* and *y*-*z* views. The single blue dashed lines in (B) mark the center *z* positions of the chosen FAs and the double red dashed lines in (B) indicate the expansion ranges of the chosen FAs. The scale bar is 2 μm. (C) Fluorescence intensity of *x*-*z* projections of FAs in (B) for M4 cells. The top panels is for FAs 1-3 and bottom panel is for FAs 4-5. The solid line is the average intensity of three FAs and the shaded area represents the standard errors. (D) Representative SEM images of M4 cells migrating on sawteeth. Magnified images of the areas are highlighted by the boxes with black dashed lines. White arrows highlight the places showing cell cortical plasticity of M4. The scale bars are 10 μm in the zoomed out images and 1 μm in the magnified images.

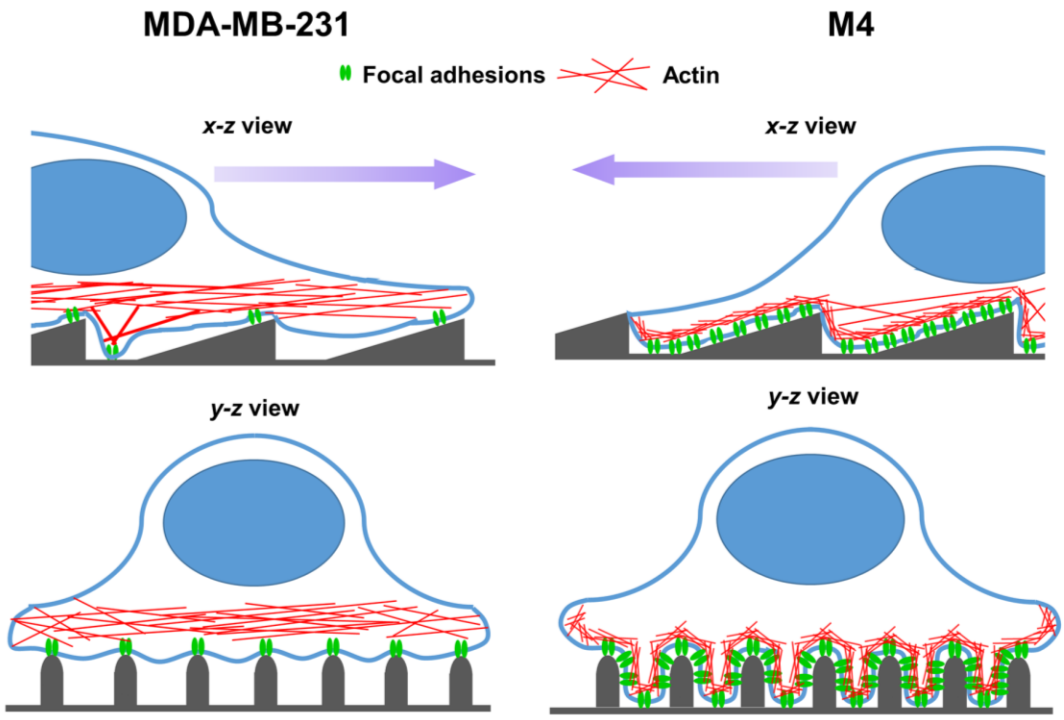

Figure 2.11: Schematic representation of the biased contact guidance for MDA-MB-231 and M4 cells on sawteeth. The red fibers represent actin cytoskeleton and green structures are focal adhesion complexes. The purple arrow represents the direction of motion.

observation is consistent with the ability of M4 cells to assemble FA complexes surrounding sawteeth. Based on these experimental results, we summarize the primary differences in actin cytoskeleton and FA patterns between MDA-MB-231 and M4 cells on sawteeth in a schematic (Fig. 2.11). For MDA-MB-231 cells, the high cortical rigidity limits the contact of membranes to the sawtooth structures. As a result, the majority of the FAs are located on the top of the sawteeth (Fig. 2.11). In contrast, the distinct cortical plasticity of M4 cells allows maximum contact with the sawteeth structures and FA formation throughout the sawteeth (Fig. 2.11).

Although it has been shown that the application of cytoskeletal force generated by cells on the ECM directly affects FA assembly (Balaban et al., 2001; Galbraith et al., 2002), the overall cell shape or distortion of the cell shape is also known to modulate the size and distribution of FAs (Chen et al., 2003). Here, we found that various cell types exhibit both distinct cell boundary deformability and FA organization. It has been suggested that FA size and distribution determine the adhesion strength (Gallant et al., 2005) and FA composition (Goffin et al., 2006), spatially control the activation of downstream messengers (Xia et al., 2008), and determine the balance among ECM-activated signaling pathways (Park et al., 2016). Thus, the distinct FA organization patterns we observed in breast cancer cells migrating on sawteeth may play an important regulatory role. Topography-induced membrane curvature could represent another critical factor. Indeed, instead of being passively determined by the actin cytoskeleton, membrane shape and deformation has been shown to actively regulate the recruitment of curvature sensitive proteins and activators of actin polymerization (Wu et al., 2018; Yang and Wu, 2018). The recruited curvature sensitive proteins can further promote membrane deformation, however the triggered actin polymerization limits this positive feedback process by stiffening the cortex (Wu et al., 2018; Yang and Wu, 2018). This antagonistic interplay generates propagating waves of both curvature-sensing proteins and

actin polymerization with changes in local membrane curvature (Gov, 2018; Wu et al., 2018; Yang and Wu, 2018). In addition, it has been determined that out-of-plane curvature provided by microscale wires or tubules also regulates the collective behavior of epithelial cell monolayer (Xi et al., 2018; Yevick et al., 2015). This raises the possibility that the different membrane deformability we observed in MDA-MB-231 and M4 cells results in the distinct recruitment of curvature-sensing proteins and actin nucleators, thereby leading to the generation of actin polymerization waves in opposite directions. We hypothesize that differences in the balance between cortex deformation and FA formation ability in MDA-MB-231 and M4 cells promote distinct cytoskeletal dynamics and migration behaviors.

2.3.6 The distinct guidance behaviors of breast cancer cells depend on their mutation profile and downstream Rho GTPase signaling

Previously, we have shown that the migration phenotype and cytoskeleton orchestration of human breast cancer cells on the same nanosawtooth surface is cell-type dependent. This finding strongly suggests a contribution of intrinsic characteristics of different cancer cells. Cancer is a genetic disease driven by an accumulation of genetic alterations in pathways that regulate cell growth, survival, and motility. Mutations in *PTEN*, *PIK3CA*, *KRAS*, *HRAS*, *NRAS*, and *BRAF* genes have been identified in a collection of human breast cancer cell lines by sequencing analysis. These mutations can activate and/or inhibit distinct downstream Rho GTPase signaling pathways that further influence cell migrational behaviors and cytoskeletal dynamics. Thus, we hypothesize that the observed differences in contact guidance responses of breast cancer cells are determined by their unique mutation profiles and downstream Rho GTPase signaling. To test the hypothesis,

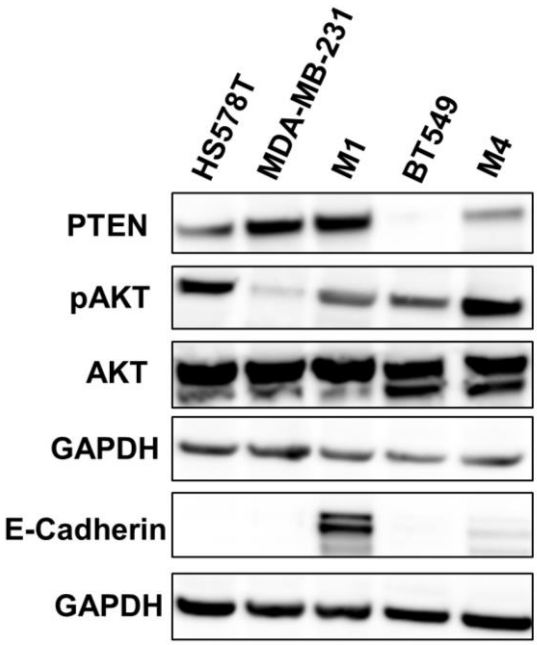

Figure 2.12: The PI3K signaling is elevated in M4 cells. Representative Western blot result (n =2) showing the expression of PTEN, AKT, and E-Cadherin proteins as well as the level of phosphorylated AKT in different breast cancer cell lines.

we treated the breast cancer cells with pharmacological inhibitors and monitored their migration phenotypes. It has been shown that dominant *BRAF* mutation in MDA-MB-231 cells activates the RhoA-ROCK pathway while the hyperactive *PIK3CA* mutation of M4 cells leads to constitutively augmented PI3K signaling. This is confirmed by the Western Blot result showing that MDA-MB-231 cells have the lowest phosphorylated AKT level while it is the highest for M4 cells (Fig. 2.12). Thus, we pre-treated MDA-MB-231 and M4 cells with PI3K inhibitor LY294002 and ROCK inhibitor Y-27632 for four hours and then imaged their migration on nanosawtooth surface in the presence of inhibitors. Compared to DMSO treated cells, ROCK-inhibited MDA-MB-231 cells exhibit multiple thin and long protrusions that can expand multiple cell lengths, probably resulting from the deficient capability in cell retraction (Fig. 2.13Ai). Moreover, ROCK-inhibition attenuates the directional migration of MDA-MB-231 cells toward the sawtooth positive direction (Fig. 2.13Aii & iii). In the contrast, cells treated with the PI3K inhibitor LY294002 polarize to a higher degree than DMSO treated cells do with extended dominant lamellipodia at the cell front (Fig. 2.13Ai). Surprisingly, the bias in migration of MDA-MB-231 cells towards the positive direction is enhanced by PI3K inhibition (Fig. 2.13Aii & iii). This finding suggests that contact guidance behaviors of MDA-MB-231 cells are related to the balance between RhoA-ROCK and PI3K pathways.

However, the results are less conclusive for M4 cells. First, the bias of M4 cell migration towards the negative direction of nanosawteeth is not evident in the preliminary experiment (Fig. 2.13Bii & iii). Similar to MDA-MB-231 cells, M4 cells treated with Y-27632 display attenuated ability to retract protrusions (Fig. 2.13Bi). The spider plot of cell tracks and polar histogram indicate that ROCK inhibited M4 cells exhibit somewhat biased migration towards the negative

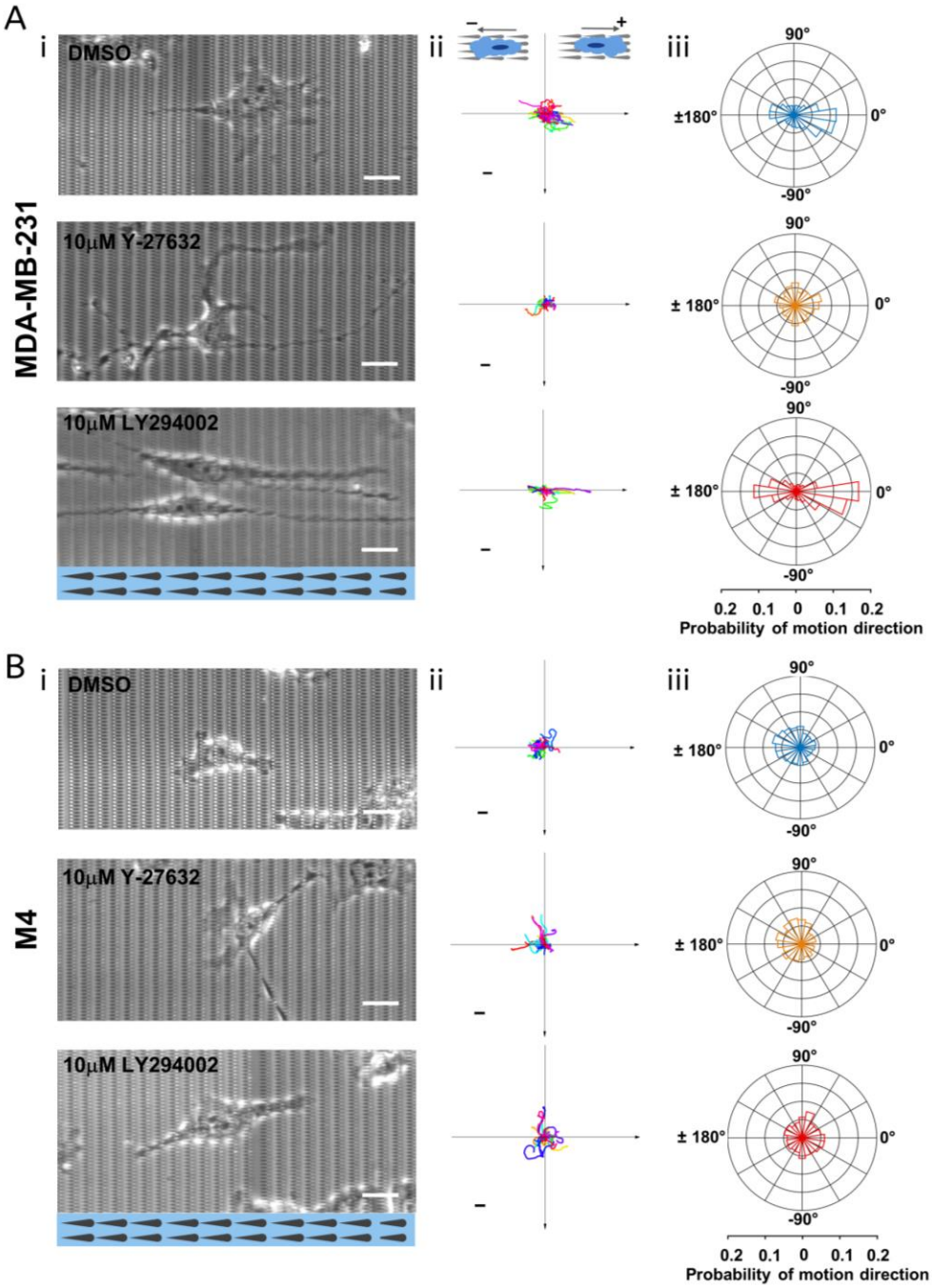

Figure 2.13: The role of Rho-ROCK and PI3K signaling pathways in the migrational phenotypes of MDA-MB-231 and M4 cells. (A & Bi) Bright-field images of MDA-MB-231 (A) and M4 (B) cells treated with DMSO or indicated inhibitors migrating on sawtooth surfaces. The scale bar is 10 μm. (A & Bii) Centroid motion tracks of MDA-MB-231 (A) and M4 (B) cells treated with DMSO or indicated inhibitors migrating on sawtooth surfaces (MDA-MB-231: DMSO 78 tracks, Y-27632 38 tracks, LY294002 63 tracks; M4: DMSO 36 tracks, Y-27632 42 tracks, LY294002 43 tracks). The scale bar is 60 μm. (A & Biii) Probability distributions of cell motion directionality. The scale at the bottom corresponds to the horizontal axis in each rose plot.

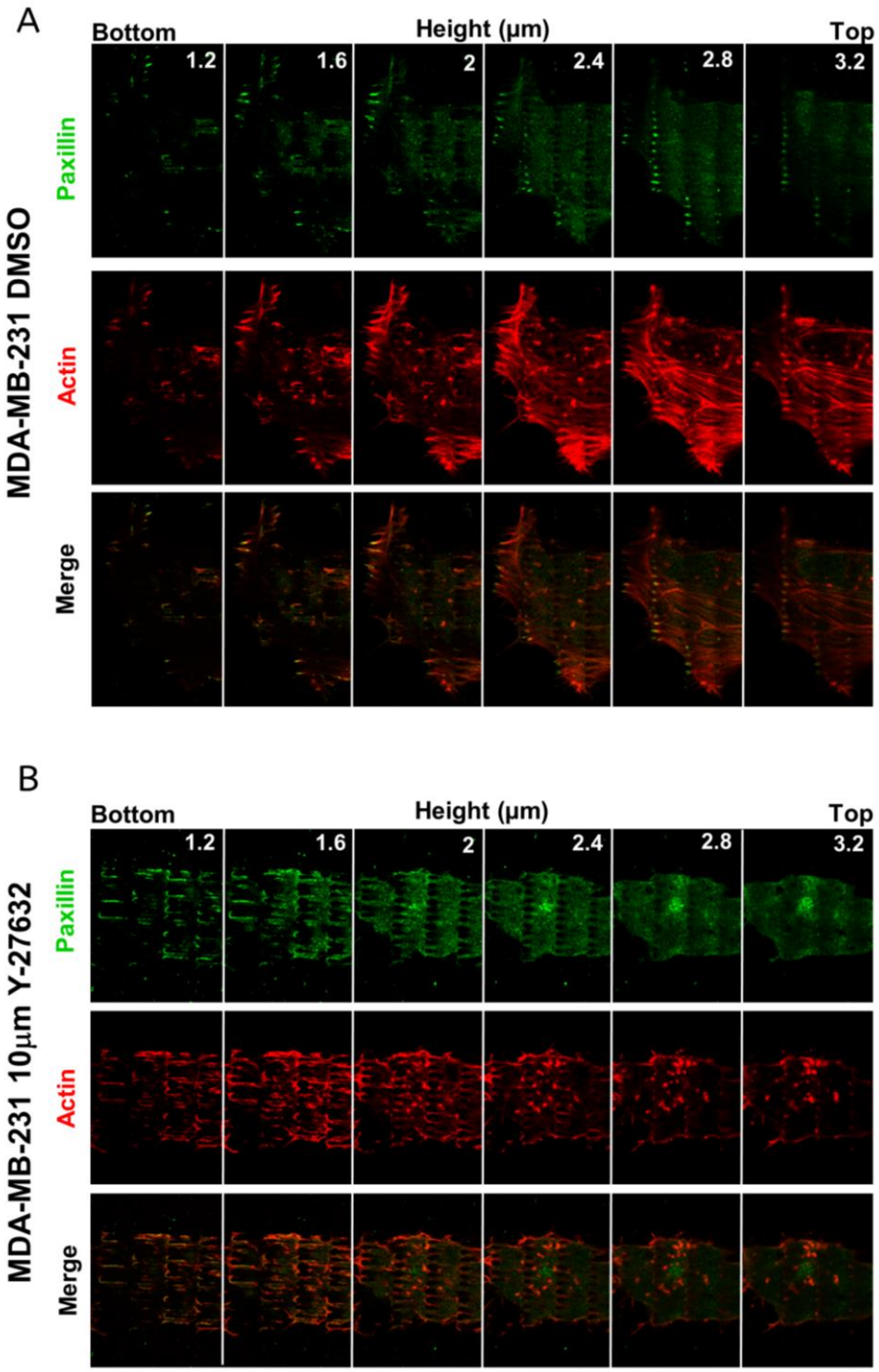

Figure 2.14: Inhibiting Rho-ROCK signaling in MDA-MB-231 cells alters cell cortical plasticity and cytoskeleton architecture. (A) Fluorescence image montage of paxillin (top), actin (middle), and the merge of the two (bottom) at different *z* positions for MDA-MB-231 cells treated with DMSO on nanosawteeth. (B) Fluorescence image montage of paxillin (top), actin (middle), and the merge of the two (bottom) at different *z* positions for MDA-MB-231 cells treated with 10μM Y-27632 on nanosawteeth.

direction as the DMSO treated cells do (Fig. 2.13Bii & iii). When PI3K signaling is inhibited, M4 cells form one or two dominant protrusions instead of several ones found in DMSO treated cells (Fig. 2.13Bi). In addition, the migrational directionality of PI3K inhibited cells is more uniform, showed by the spider plot of cell tracks and polar histogram (Fig. 2.13Bii & iii). Thus, further experiments are needed to confirm whether the biased migration of M4 cells on nanosawteeth depends on PI3K signaling.

We next sought to examine the effect of Rho-ROCK and PI3K signaling on cell cytoskeletal architecture. As previously, we performed high-resolution fluorescence imaging of actin and paxillin for actin cytoskeleton and FA pattern. We found well-organized FA punctea on top of sawtooth structures above z = 2.8 μm and that the stress fiber network becomes obvious above z = 2.8 μm, a phenomena consistent with previous results (Fig.2.14A). However, ROCK inhibition dramatically alters the cytoskeleton of MDA-MB-231 cells. The most striking difference is that ROCK inhibited cells form FA complexes around the bottom outlines of nanosawteeth at z = 1.2 μm but fail to form FA punctea on top of the nanosawteeth (Fig.2.14B). Moreover, dense actin structures can be seen around the nanosawteeth from z = 1.2 μm to z = 2.4 μm, in contrast to the stress fibers in DMSO treated cells (Fig.2.14B). This strongly suggests that inhibiting Rho-ROCK signaling by Y-27632 alters the cortical plasticity and cytoskeletal orchestration of MDA-MB-231 cells. However, no difference was observed in MDA-MB-231 cells treated with the PI3K inhibitor (data not shown). For M4 cells, we found that neither ROCK inhibition nor PI3K inhibition is sufficient to change the cell cytoskeleton. Taken together, the biased migration behaviors and cytoskeleton architectures of different breast cancer cells on nanosawtooth surface are regulated by Rho-ROCK and PI3K signaling.

2.4 Conclusions

Contact guidance plays a critical role in cancer invasion and metastatic processes. Using multiple breast cancer cell lines and symmetric and asymmetric nanotopographic designs, we examined the biophysical and molecular mechanisms behind contact guidance and directional bias. We showed that all of the breast cancer cell lines are able to sense and respond to physical guidance cues, yet they do so in distinct ways. We envision that this behavior is dependent on distinct intrinsic characteristics of the cancer cell lines. Consistent with prior findings, the bias in cell migration we measured is in the same direction as, and likely arises from, asymmetries in the direction of actin polymerization. Furthermore, we identified distinct local cell cortical plasticity and heterogeneity in FA patterns as key differences between breast cancer cell types. We hypothesize that this difference in FA patterns, and the associated difference in the deformation ability of cell boundaries into the valleys of the textures, are both driven by, and ultimately regulate, the bias in actin polymerization and cell migration. Because we can average observations over identical nanotopographic elements, our approach is well suited for in-depth investigations of intracellular signaling to identify the molecular mechanisms underlying the distinct FA patterns, actin dynamics, and cell boundary shapes.

2.5 Materials and methods

Surface fabrication and replication: The nanoridge and sawtooth topographies that were employed to study migratory and cytoskeletal responses were designed and fabricated using multiphoton absorption polymerization (MAP). More details regarding this method can be found elsewhere (Baldacchini, 2016; LaFratta et al., 2007). Briefly, the output of an ultrafast Ti:sapphire laser (Coherent Mira 900) tuned to 800 nm was passed through a high-numerical-aperture objective (Zeiss alpha-Plan Fluar 100×; numerical aperture 1.45) and focused onto a photopolymerizable resin ((1:1 w/w tris (2-hydroxy ethyl) isocyanurate triacrylate (SR368):ethoxylated (6) trimethylolpropane triacrylate (SR499) (both from Sartomer), 3 wt. % Lucirin TPO-L (BASF)) that was sandwiched between a glass coverslip and a microscope slide. Based on the experimental conditions, the photoinitiator undergoes efficient two-photon absorption only in the focal region of the objective, allowing for the fabrication of three-dimensional structures with arbitrary shape. The sample was mounted on a motorized stage that can be controlled by a computer. A LabVIEW program (National Instruments) was used to control the stage movement to fabricate the desired the patterns. The same program controlled a shutter to dictate when and where polymerization should occur. After fabrication was completed, the sample was soaked in two containers of ethanol for 3 min each to remove the unreacted monomer resin. The MAP-fabricated "master" structure was then baked/dried in oven at 110 °C for at least 1 h. To reproduce nanotopographic surfaces, we used solvent-assisted nanotransfer molding (Sun et al., 2018) to make a negative-relief mold of the "master" structure fabricated with MAP. A film of hard PDMS (Hyewon et al., 2006; Sun et al., 2018) was spin-coated onto the original pattern. This PDMS mixture included hexanes, to decrease viscosity to allow the film to conform optimally onto the structures being coated, thereby improving the resolution of the mold. After sitting at room

temperature for 2 hr, the patterned microscope slide and coated film were baked at 60 °C for 1 h. Sylgard 184 (10:1 w/w elastomer base: curing agent; Dow Corning) was poured on top of the baked sample to form a layer approximately 1 cm thick. The same was then returned to the oven for 70 min. Once baking was completed, the mold was peeled from the "master" in the direction parallel to the ridges. For sawteeths mold, peeling should occur from the tail to the head of the sawteeth to prevent damage to the pattern. Molds can be used to make replicas of the original MAP structure. A drop of the same resin used for MAP was sandwiched between a functionalized coverslip and the mold and the sandwich was exposed to UV light for 5 min. Using this process, many replicas of an original pattern can be produced in a short amount of time.

Cell culture: Benign epithelial cell line MCF10A (M1) and its metastatic mutant cell line MCF10CA1 (M4) from the MCF10A cell series were used (Barbara Ann Karmanos Cancer Institute, Detroit, MI). Cells were cultured in DMEM/F12 (Invitrogen, Carlsbad, CA) supplemented with 5% horse serum (Invitrogen) at 5% CO_2 in humidified culture incubators, as previously described. The medium for M1 cells was additionally supplemented with 10 μg/ml insulin (Invitrogen), 10 ng/ml EGF (Peprotech, Rocky Hill, NJ), 0.5 μg/ml hydrocortisone and 100 ng/ml cholera toxin (both from Sigma, St. Louis, MO). HS578T and BT549 cells, kind gifts from Dr. Stanley Lipkowitz, were cultured in RPMI supplemented with 10% fetal bovine serum (both from Invitrogen). MDA-MB-231 cells were cultured in DMEM/high glucose supplemented with 10% fetal bovine serum. The pTK92_Lifeact-GFP plasmid was a gift from Iain Cheeseman (Addgene plasmid # 46356). To generate M1 and MDA-MB-231 cells stably expressing Lifeact-eGFP, phoenix cells (human kidney epithelial) were transfected with the plasmid with Lipofectamine 2000 (Thermo Fisher Scientific) according to the manufacturer's protocol, then

then cell culture medium containing retroviral particles was collected at 48 h after transfection. After filtering the collected medium with 0.22 μm filters, viral particles were added to M1 and MDA-MB-231 cells. Stably infected cells were selected and maintained in puromycin-containing media (2.5 μg/ml).

Individual cell migration and time-lapse imaging: Prior to cell seeding, nanoridges or nanosawteeth surfaces were coated with 20 μg/ml collagen IV (BD Biosciences) at 4 ℃ for about 1 hour, then mounted back to a homemade six well plate. Cells were trypsinized and re-suspended to 1×10^4 cell/ml in each own growth medium, then 2 ml of cell suspension was added to each well. After the cells were allowed to adhere for approximately 1 h, non-adherent cells were washed off and each well was refilled with 2 ml fresh medium. The cells were then cultured overnight. Two hours before imaging, fresh growth medium was replaced for each cell line. For ROCK and PI3K inhibition experiments, 10 μM Y-27632 or LY294002 was used to treat the cells for four hours and fresh media supplemented with the specific inhibitor was replaced right before imaging. For time-lapse imaging, the plate was placed in the incubator chamber (37 ℃, 5% CO_2) of a Zeiss Observer 2.1 microscope with an automated stage. Phase-contrast images were taken every 3 min for approximate 20 h.

Live-cell actin fluorescent imaging*:* Similar to individual cell migration experiments, a nanosawtooth surface was coated with 20μg/ml collagen IV at 4 ℃ for about 1 h, then mounted in a homemade 35 mm Petri dish. Liftact-eGFP/MDA-MB-231 and Lifeact-eGFP/M4 cells were harvested following the same protocol as in the individual cell migration experiments. On the second day, cells were imaged with a Zeiss LSM 880 laser-scanning confocal microscope. Both

fluorescent and bright-field images were taken every 10 s using an oil-immersion, 63× objective and a zoom-in factor of 2.5.

Immunostaining: Cells were fixed in 4% formaldehyde without (paxillin) or with (tubulin) 2 mM EGTA (bioWORLD, Dublin, OH) and 2 mM $MgCl_2$ (Quality Biological Inc, Gaithersburg, MD) for 15 min, followed by permeabilization in 0.1% Triton X-100 for 15 min and blocking of unspecific antibody binding with 1% bovine serum albumin (BSA) for 1 h. Targets were labeled with either anti-tubulin (1:200, MAB1864, Millipore) or anti-paxillin (1:200, 612405, BD) primary antibody in 0.1% BSA at 4 ℃ overnight. On the second day, the primary antibodies were detected by secondary, fluorescently-labeled antibodies (1:200, Invitrogen). Meantime, F-actin was labeled with phalloidin-TRITC (1:200, Invitrogen), and nuclei were labeled with DAPI (Invitrogen). Superresolution images of the specimens were taken with a Zeiss LSM 880 confocal microscope in Airyscan mode, and 3D reconstruction movies were generated using ZEN software (Zeiss, Germany). Further image analysis, such as generating *x*-*z*/*y*-*z* view images, was performed in imageJ (NIH, Bethesda, MD).

Western Blot: Cells were cultured on collagen IV coated tissue dishes overnight and lysed with cold RIPA buffer (Thermal Fisher Scientific) supplemented with cOmplete Mini protease inhibitor cocktail and PhosStop phosphatase inhibitor cocktail (Roche, St. Louis, MO). The protein concentration of each sample was determined by BCA assay (Thermal Fisher Scientific). The protein samples were separated by sodium dodecyl sulfate-polyacrylamide gel electrophoresis (SDA-PAGE) and transferred to Nitrocellulose membranes. 5% dry milk in TBST buffer (50 mM Tris PH 7.2, 0.1% Tween 20) was used to block the membranes for 1 hour at room temperate or

for overnight at 4 ℃. After blocking, membranes were incubated with primary antibodies (anti-phosphoAkt (Ser 473) 1:1000 (Cell Signaling Technology), anti-AKT 1:1000 (Cell Signaling Technology), anti-PTEN 1:1500 (Cell Signaling Technology), anti-E-cadherin 1:5000 (Invitrogen) and anti-GAPHD 1:10000 (BD)) for overnight at 4 ℃ followed by incubation with a corresponding horseradish peroxidase (HRP) conjugated secondary antibody (anti-rabbit or anti-mous IgG~HRP 1:5000 (Thermal Fisher Scientific)). The membranes were visualized by enhanced chemoluminescence (Thermal Fisher Scientific).

Quantitative analysis of cell migration: After time-lapse images were post-processed, cell tracking was performed using Manual Tracking in imageJ, and cells were outlined manually in MATLAB (Mathworks). The files containing all cell tracks were imported into MATLAB for further analysis. Cell tracks were smoothed with a ten-frame (30 min) unweighted sliding window. This period is sufficient to allow cells to move about one nuclear diameter. Using the smoothed center positions, cell velocities were determined by calculating the displacement between two frames:$\overrightarrow{v_i}(t) = \overrightarrow{x_i}(t) - \overrightarrow{x_i}(t - \Delta t)$, where Δt is the interval between two frames. Assuming the uncertainty in finding cell center is 1 pixel (0.625 μm) for both the *x* and *y* directions, a velocity was only counted if the net displacement between two frames was above 1.4 pixels. The direction of the motion at each frame was determined by the angle between $\overrightarrow{v_i}(t)$ and the *x* axis, based on which histograms of direction of motion were created. All cell instantaneous velocities within a certain angle range relative to ridges were averaged to plot the velocity profile with respect to orientation. To calculate the mean velocity components relative to the nanosawtooth orientation for each cell, the velocity components along the *x* axis were separated based on their signs, with positive being the same as the nanosawtooth orientation and negative being the opposite

orientation. The velocity direction distribution was also plotted for each speed quartile and each long-term persistence tertile. The angles were determined relative to the sawtooth orientation, meaning that angles that are left-right symmetric about the sawtooth orientation are considered to be the same. This process transforms the original range of velocity direction from -180°-180°to 0°-180°. To estimate the variations in our distributions, we adapted a random resampling Bootstrap method (Efron, 1979; Efron B. and Tibshirani, 1993). First, we randomly divided all velocities into 10 groups for each speed quartile or persistence tertile. To distribute the velocities randomly, a random seed between 2^0 and 2^{32} was picked for each of the five cell lines. The seeds are 418932850, 1196140743, 2348838240, 4112460544 and 4144164703 for MDA-MB-231, HS578T, M1, BT549 and M4 cells respectively. The velocities whose speed values are zero were discarded because their directionality cannot be determined. The velocity direction distribution was then calculated for each of the 10 groups. We considered the measurement from each of the 10 groups as independent, and calculated the average velocity direction distribution and standard error of the mean from the measurements of the 10 groups.

The principle of optical flow algorithm: Optical flow algorithms of florescence images capture translational motion on a frame-by-frame basis. For each pixel in a fluorescence image, the algorithm assumes that the pixel undergoes a translation from its initial coordinate (x, y) to a new coordinate $(x + \Delta x, y + \Delta y)$ (Horn and Schunck, 1981). Therefore, each two-dimensional frame in an image series is denoted by:

$$I_t(x, y) = I_{(t+\Delta t)}(x + \Delta x, y + \Delta y)$$

In other words, the objective is to find the translations Δx and Δy that map the intensity profile in I_t to what is observed in $I_{t+\Delta t}$. Expanding the right side of this equation assuming small $\Delta x,\ \Delta y$

and Δt, and neglecting second-order and higher order terms, yields the master optical flow equation.

$$I_t(x,y) = I_t(x,y) + \frac{\partial I_t}{\partial x}\Delta x + \frac{\partial I_t}{\partial y}\Delta y + \frac{\partial I_t}{\partial t}\Delta t$$

$$0 = \frac{\partial I_t}{\partial x}\Delta x + \frac{\partial I_t}{\partial y}\Delta y + \frac{\partial I_t}{\partial t}\Delta t$$

$$-\frac{\partial I_t}{\partial t}\Delta t = \vec{\nabla} \cdot \langle \frac{\Delta x}{\Delta t}, \frac{\Delta y}{\Delta t} \rangle$$

$$-\frac{\partial I_t}{\partial t} = \vec{\nabla} \cdot \vec{v}$$

This equation is underdetermined (1 equation and 2 unknown variables) and the Lucas-Kanade technique was used to apply an additional constraint (Lucas and Kanade, 1981).

Averaged actin kymograph analysis: We measured the mean actin fluorescence and actin dynamic around one sawtooth by averaging across all sawteeth in either a single movie or multiple movies. First, the images with both bright-field and fluorescence channels were rotated in ImageJ such that all sawteeth were aligned horizontally with their positive direction (tail to head) facing right, and the image edges were discarded. The sawtooth regions and boundaries were subtracted from the bright-field channel. Because the light aberration caused by cells resulted in the inability to recognize some sawteeth, sawteeth that appeared to be connected with others or smaller than a certain threshold were excluded from the analysis. After subtraction, the sawtooth outlines were superimposed on the actin fluorescent channel, and 51 points were placed evenly about the circumference of each outline. For each sawtooth, the sawtooth centroid was used as the origin point, and the horizontal row passing the centroid was used as the x axis with its positive direction facing right (same as the sawtooth positive direction). Then, the angle of each of the 51 points was

calculated relative to the axis positive direction, and the position 0, which is the head of the sawtooth, was identified as the point with the smallest angle. The 25 points from position 0 in the clockwise direction were assigned indices 1 to 25 with position 1 near the sawtooth head and position 25 near the sawtooth tail. Similarly, the 25 points from position 0 in the counterclockwise direction were given indices -1 to -25. Since the 51 points were evenly placed, positions ±1 are nearly symmetric to the sawtooth head and positions ±25 are nearly symmetric to the sawtooth tail. The actin fluorescence intensity within a constant radius around each point was averaged. Then, we aligned the 51 points linearly so that position 0 was in the middle and positions ±25 were in the two sides. To quantify the actin dynamics for two cell lines in an unbiased way, we first calculated averaged intensity for position 0 for all frames, and then made a plot of intensity *vs.* time. The time point 0 was determined as the frame of the first peak, which has the average intensity above 90% of the maximum intensity in the plot. A kymograph showing the actin dynamic around one sawtooth was then generated by measuring the actin intensity profile as mentioned for 6 minutes before and after time point 0. The kymographs from different sawteeth were averaged by using the position 0 and time 0 as the center.

Scanning electron microscopy (SEM) imaging: For SEM imaging, cells were washed with 0.1 M Sorensen's sodium phosphate buffer for 3 times to remove any growth medium and fixed with 2.5% glutaraldehyde in same buffer at 4 ℃ for overnight. After rinsing, cells were post-fixed with 1% osmium tetroxide for 1 h. Then, cells were dehydrated through ethanol series of 35%, 50%, 85%, 95% and 100% ethanol solutions for 10 min each, followed by chemically drying with hexamethyldisilazane (HMDS, Sigma-Aldrich) for 5 min. The samples were then sputter-coated with gold and imaged using an AMRAY 1910 microscope.

Chapter 3

Membrane Curvature Induces Ligand-independent Integrin Activation in Human Primary Neutrophils

3.1 Summary

Neutrophil recruitment to inflamed or injured tissues is a key step in immune responses. During this process, nearby neutrophils migrate directionally to the inflamed or injured site and trigger dramatic swarm-like recruitment from long distances by secreting secondary chemoattractants in a process referred to as signal relay. Although it is well established that directed migration and signal replay play important roles in this response, the effects of physical changes and stimulus of the underlay ECM are poorly understood. We hypothesize that physical stimulation activates neutrophils through integrin signaling in a chemoattractant-independent manner and primes neutrophils for migration and recruitment. To test this, we use artificial nanoscale ridges to mimic collagen fibers *in vivo* and to provide physical stimulation. Calcium signaling, a well-known indicator of activation for various immune cells, is used to monitor cell activation. We found that primary human neutrophils spread extensively and exhibit rapid calcium flashes on ICAM-1-coated glass, indicating that integrin signaling can lead to neutrophil activation. Strikingly, neutrophils plated on BSA-coated nanoridges also exhibit rapid calcium flashes, while cells plated on BSA-coated flat surfaces do not. Blocking integrin activation with β_1 or β_2 inhibitory antibodies further suggests that the nanoridges mediate their effect via β_2 integrin signaling. Finally, by imaging cells with integrin conformation-specific antibodies, we found that

activated neutrophils form integrin clusters near the sidewalls of the nanoridges during migration. Together, these findings suggest that physical stimulation is involved in neutrophil activation.

3.2 Introduction

As the most abundant leukocytes in human blood, neutrophils occupy about 60% to 70% of the whole population and serve as the first line of cellular defense against various invading pathogens (Iversen et al., 2016; Taylor et al., 2014; Yipp et al., 2012). In response to infection or inflammation, floating neutrophils first become captured and undergo rolling on the vascular endothelial cell (EC) surface by interacting with the upregulated adhesion molecules on EC. The molecular guidance signals presented by EC further stimulate neutrophils, resulting in their firm attachment, polarization, and directional crawling (Ley et al., 2007). After which, fully activated neutrophils seek permissive sites on the EC for transmigration and breach through the dense venular basal membrane into the tissue (Filippi, 2019). This neutrophil recruitment process is known as neutrophil adhesion cascade. Within the tissue, neutrophils execute various defense actions against the pathogens, including phagocytosis (Autenrieth et al., 2012), release of reactive oxygen species (Autenrieth et al., 2012), and formation of extracellular traps (Yipp et al., 2012).

The neutrophil adhesion cascade is strongly mediated by integrins. Integrins are heterodimeric adhesion molecules on the cell surface that are composed of α and β subunits (Luo et al., 2007). Each subunit has an ectodomain, a single transmembrane helix, and a short cytoplasmic tail (Fig. 3.1) (Campbell and Humphries, 2011). In vertebrates, there are 18 α subunits and 8 β subunits that form 24 known heterodimeric pairs. Neutrophils majorly express $\alpha_L\beta_2$ (also known as LFA-1), $\alpha_M\beta_2$ (also known as Mac-1), and $\alpha_4\beta_1$ (also known as VLA-1) integrins that recognize distinct sets of ligands (Abram and Lowell, 2009; Humphries et al., 2006). Chemokine-

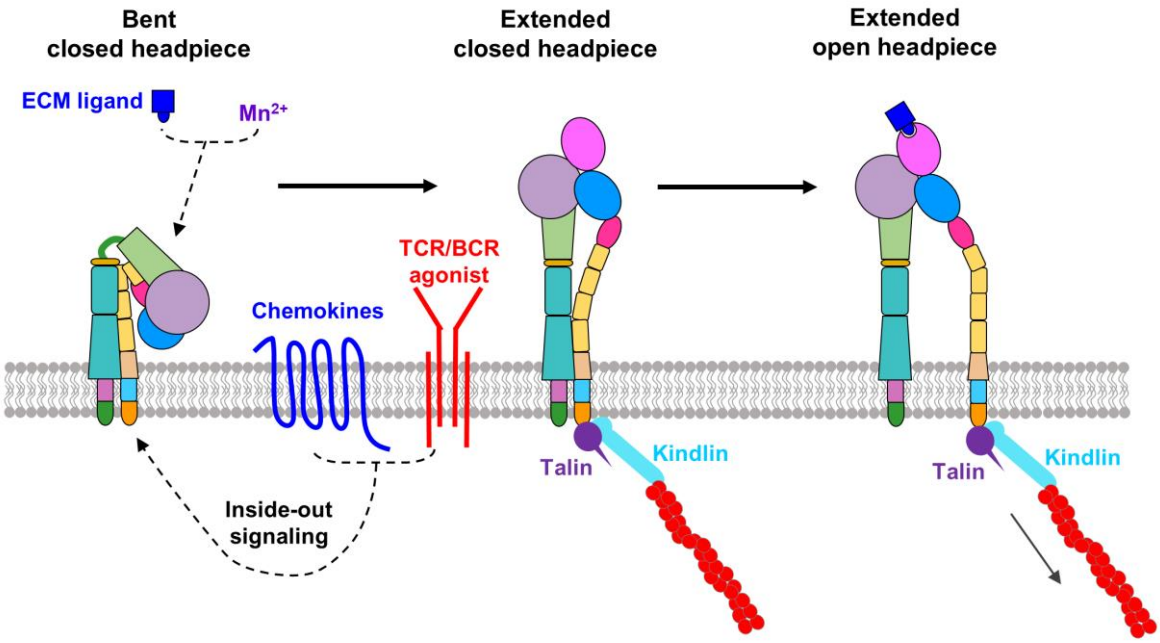

Figure 3.1: A schematic illustration of integrin activation process through inside-out signaling or outside-in signaling. An inactive integrin in a bent conformation can be shifted to an extended conformation by intracellular signaling through chemokine receptors and other receptors or by the presence of integrin ligands or Mn^{2+}. The extended integrin recruits various signaling and scaffolding proteins that can link actin cytoskeleton, such as talin and kindlin. The pulling force applied by the actin cytoskeleton drives the separation of integrin β chain from α chain, which triggers the headpiece opening for ligand binding.

or cytokine-mediated inside-out signaling, extracellular matrix (ECM) ligand binding or addition of Mn^{2+} induces dramatic conformational changes of the ectodomains from a bent conformation to an upright conformation (Fig. 3.1) (Abram and Lowell, 2009). This extension of the ectodomains increases the affinity of the integrin to its ligand, facilitates integrin clustering, as well as communicates to transmembrane domains and cytoplasmic tails that recruit adaptor proteins such as talin and kindlin to the β subunit tail (Fig. 3.1) (Cluzel et al., 2005; Kanchanawong et al., 2010). Finally, the association of actin cytoskeleton with the adaptor proteins allows the physical force applied through the β subunit tail to immobilized ECM ligands, leading to the separation of two transmembrane domains and the stabilization of extended and open integrin conformation (Abram and Lowell, 2009; Campbell and Humphries, 2011).

The role of integrin in neutrophil rolling and crawling on two-dimensional (2D) substrates has been extensively studied. In response to inflammation, the slow rolling of mouse neutrophils on muscle venules involves the engagement of LFA-1 to its ligand intercellular adhesion molecule (ICAM) -1 (Zarbock et al., 2007). Under high shear stress, neutrophils form integrin-rich processes in the front, termed"slings", to wrap around the cell bodies for efficient rolling (Sundd et al., 2012). In addition, soluble and surface-bound chemokine IL-8 stimulates the firm attachment and spreading of neutrophils on ICAM-1-coated surfaces (DiVietro et al., 2001). A recent study by Fan *et al.* shows that bent high-affinity LFA-1 and Mac-1 interact with ICAM-1 on the neutrophil surface *in cis*, which limits the arrest of rolling neutrophils (Fan et al., 2016). In contrast to 2D surfaces, it has been shown that leukocyte migration in interstitial environments is not dependent on integrin function (Lammermann et al., 2013; Lammermann et al., 2008). However, how the topographic features in the microenvironment regulate neutrophil activation and migration remains unclear, as do the mechanism by which neutrophils sense and respond to these features.

Here, we examine the activation responses of human primary neutrophils plated on glass surfaces and aligned nanoscale ridges with different coating conditions. High-speed live-cell calcium imaging enables us to monitor cell activation during the early adhering process. By using inhibitory or conformation-specific integrin antibodies, we show that neutrophil activation on nanoridges is ligand- and chemokine-independent but is mediated by membrane curvature and clustering of β_2 integrins. Our findings uncover a novel mechanism underlying neutrophil activation and migration on topographic substrates.

3.3 Results

3.3.1 Neutrophils spread and exhibit rapid calcium flashing upon ICAM-1 induced activation

Calcium signaling is conserved in various cell types throughout the phylogeny and plays a key role in many cellular processes (Berridge et al., 2000; Clapham, 2007). Calcium mobilization is one of the early signaling events in leukocyte activation, including neutrophils (Schorr et al., 1999), T cells (Tamzalit et al., 2019), and macrophages (Desai and Leitinger, 2014). To visualize the neutrophil activation events through integrin signaling, we isolate human primary neutrophils from healthy donors, plate the cells on BSA or ICAM-1-coated glass surfaces, and perform high-speed live-cell calcium imaging. BSA, which is not a ligand for any integrins, serves as a negative control (Li, 1999; Zaric and Ruegg, 2005). By analyzing the cell area and calcium fluorescence intensity over time, we found that neutrophils remain circular and floating on BSA-coated glass surfaces and the intracellular calcium fluorescence remains constant (Fig. 3.2A and B, Movie 3.1). Autocorrelation of the cell calcium fluorescence is calculated and shows no calcium signal

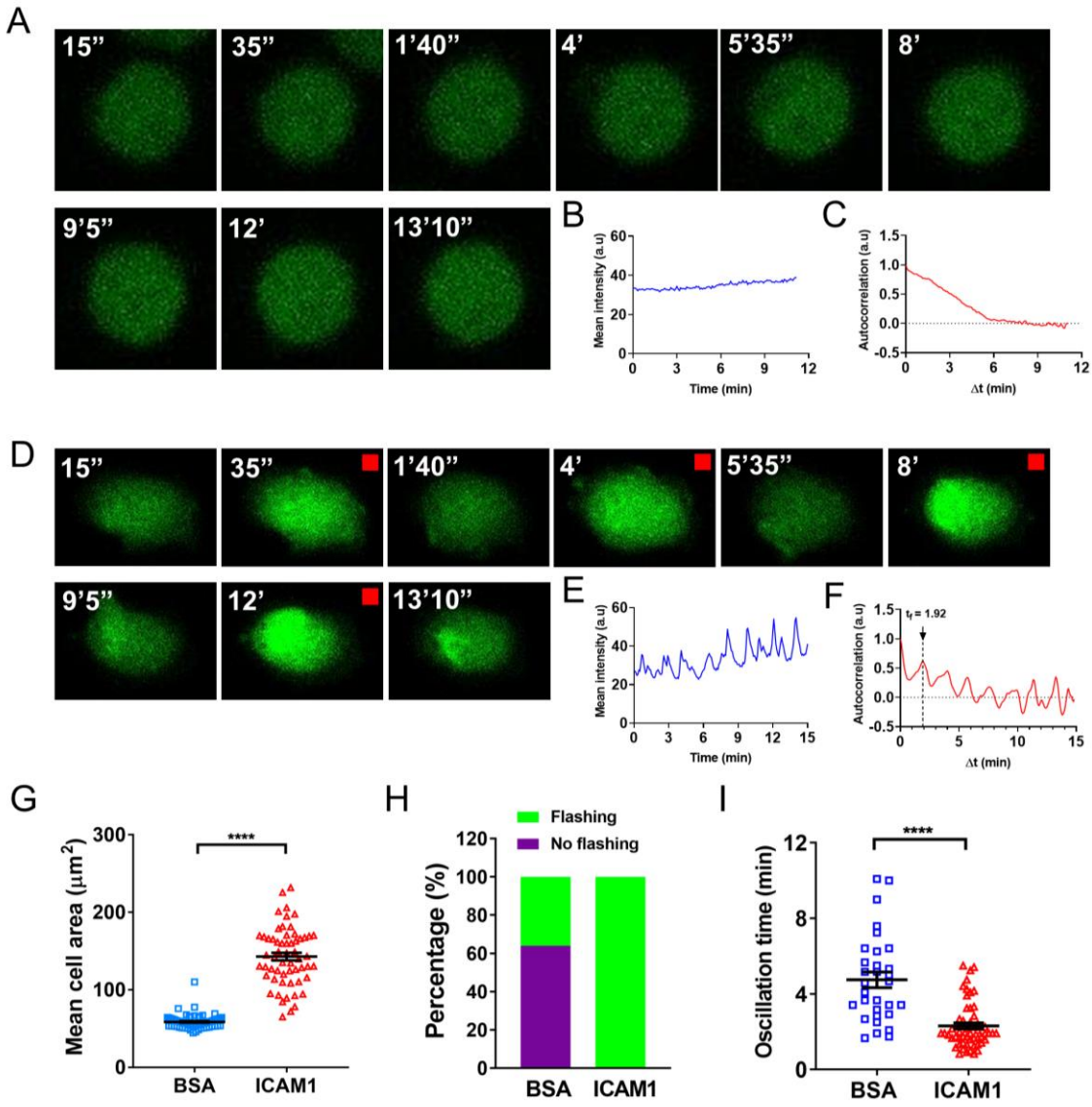

Figure 3.2: Neutrophils spread and show calcium flashes on ICAM-1 coated glass. (A & D) Montage of fluorescence images of Fluo-4 AM labeled neutrophils on BSA coated glass (A) or on ICAM-1 coated glass (D). Images are representatives of three independent experiments. Red boxes highlight the time points when cells show higher fluorescence signal. (B & E) Mean intensity plot over time for the cell on BSA coated glass (B) or on ICAM-1 coated glass (E). (C & F) Autocorrelation of the intensity plot shown in B or E, respectively. The dash line and arrow mark the oscillation time. (G) The average cell area of neutrophils on BSA or ICAM-1 coated glass. The middle solid line in each column is the mean value and the bar is standard error of the mean. ****p<0.0001 (unpaired t test). The total cell number for BSA and ICAM-1 coated glass is 81 and 58, respectively. Results are combined from three independent experiments (H) The percentage of flashing cells (green) and non-flashing cells (purple) in all neutrophils on BSA or ICAM-1 coated glass. (I) The average oscillation time of flashing neutrophils on BSA or ICAM-1 coated glass. The middle solid line in each column is the mean value and the bar is standard error of the mean. ****p<0.0001 (unpaired t test). The cell number is 27 and 58 for BSA and ICAM-1 coated glass, respectively. Results are combined from three independent experiments

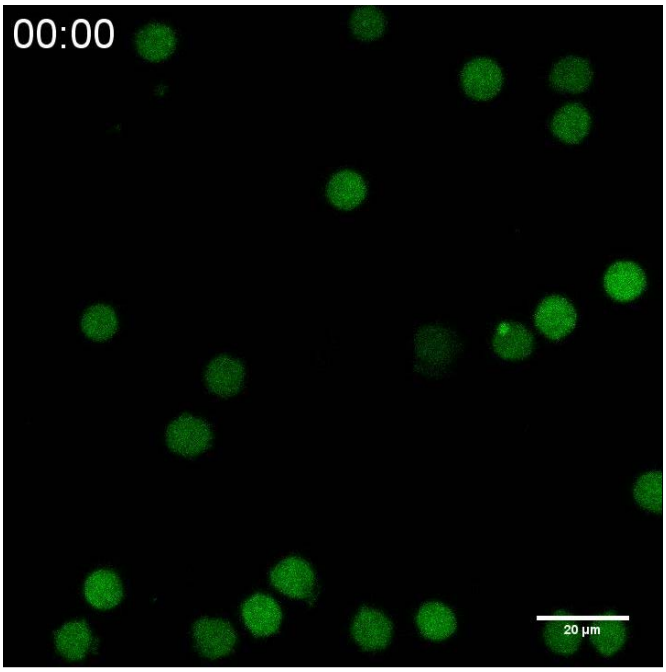

Movie 3.1: Neutrophils remain circular and floating on BSA coated glass. The green is Fluo-4 AM calcium dye fluorescence. The rate of the raw movie: 5 s/frame, play rate: 20 frame/s. The scale bar is 20 µm.

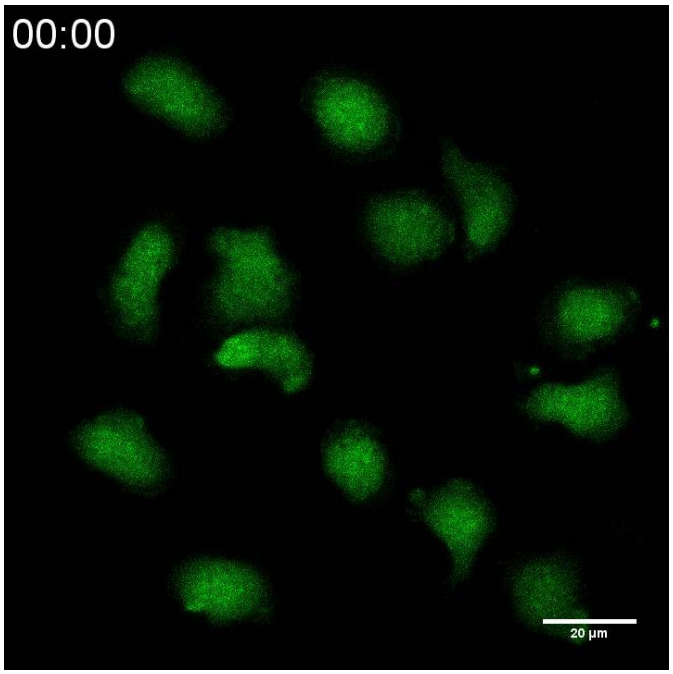

Movie 3.2: Neutrophils spread and show calcium flashes on ICAM-1 coated glass. The green is Fluo-4 AM calcium dye fluorescence. The rate of the raw movie: 5 s/frame, play rate: 20 frame/s. The scale bar is 20 µm.

fluctuation (Fig. 3.2C). However, neutrophils plated on ICAM-1-coated glass spread extensively and exhibit rapid calcium flashing for the entire imaging period (Fig. 3.2D and Movie 3.2), as is also seen in the cell fluorescence plot (Fig. 3.2E). The autocorrelation plot indicates that calcium fluorescence of the cell in figure 3.2D fluctuates with a time interval of around 1.92 minutes (Fig. 3.2F). We next quantified cells from multiple movies and confirmed that neutrophils spread on ICAM-1-coated glass but not on BSA-coated glass (Fig. 3.2G). In addition, we found that around 64% of the cell population does not show calcium flashes on BSA-coated glass (Fig. 3.2H). The percentage of neutrophils that show calcium oscillation is low and varies greatly between different experiments, suggesting that this may be due to the basal cell activation in some donors. In contrast, we found that all of the neutrophils on ICAM-1-coated glass exhibit calcium flashing, indicating a more robust activation (Fig. 3.2H). For the flashing cells on BSA-coated glass, the fluctuation interval is significantly longer than the interval of cells on ICAM-1-coated glass (Fig. 3.2I). These results suggest that integrin signaling is sufficient to activate neutrophils and calcium flashing can serve as a readout for the activation.

3.3.2 Neutrophils are activated on BSA-coated nanoridges but not on adjacent flat area

We next assess the ability of nanoscale ridges to activate neutrophils in the absence of integrin ligands. Arrays of parallel nanoscale ridges have been shown to mimic collagen fibers *in vivo* (Ray et al., 2017a), guide the migration of many different cell types (Chen et al., 2019; Driscoll et al., 2014; Kwon et al., 2012), promote the alignment and contraction of cardiomyocytes (Kim et al., 2010), and trigger preferential actin polymerization (Driscoll et al., 2014). Here the nanoridges are composed of an acrylic resin and each nanoridge has a width of ~250 nm, a height of ~1 μm, and a spacing between two adjacent nanoridges of 1.5 μm. It has been shown that this

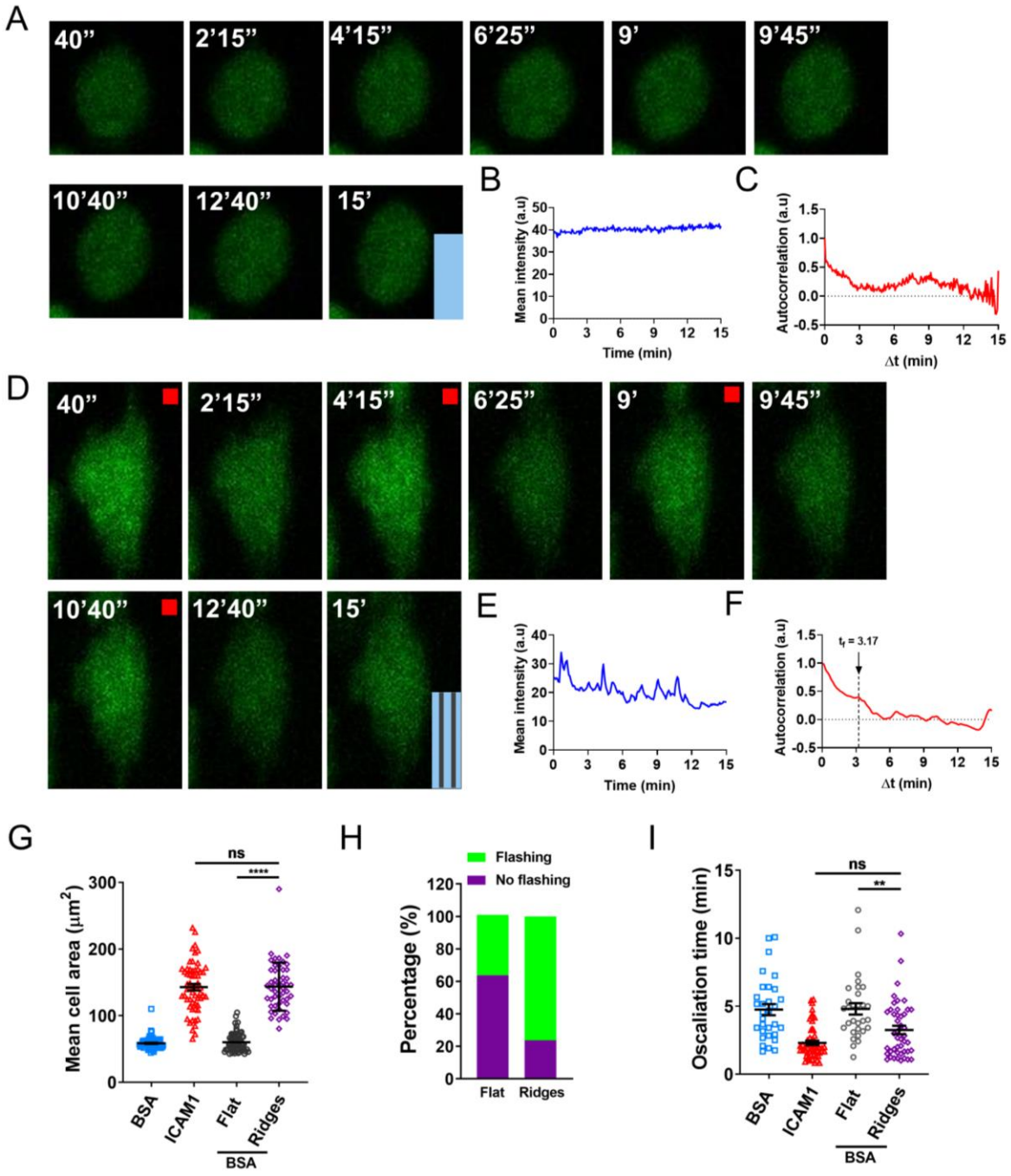
A
40”
2’15”
4’15”
6’25”
9’
9’45”
10’40”
12’40”
15’
B
Mean intensity (a.u)
Time (min)
C
Autocorrelation (a.u)
Δt (min)
D
40”
2’15”
4’15”
6’25”
9’
9’45”
10’40”
12’40”
15’
E
Mean intensity (a.u)
Time (min)
F
Autocorrelation (a.u)
t_f = 3.17
Δt (min)
G
Mean cell area (μm²)
ns
****
BSA
ICAM1
Flat
Ridges
BSA
H
Flashing
No flashing
Percentage (%)
Flat
Ridges
I
Oscaliation time (min)
ns
**
BSA
ICAM1
Flat
Ridges
BSA

Figure 3.3: Neutrophils are activated on BSA coated nanoridges but not on adjacent flat area. (A & D) Montage of fluorescence images of Fluo-4 AM labeled neutrophils on BSA coated flat surface (A) or on nanoridges (D) that is adjacent to the flat area. Images are representatives of four independent experiments. Plain blue box in A represents flat surface while the box with lines in D represents nanoridges and lines indicate the orientation of nanoridges. Red boxes highlight the time points when cells show higher fluorescence signal. (B & E) Mean intensity plot over time for the cell on BSA flat surface (B) or on nanoridges (E). (C & F) Autocorrelation of the intensity plot shown in B or E, respectively. The dash line and arrow mark the oscillation time. (G) The average cell area of neutrophils on BSA coated flat surface or nanoridges. The result showing average cell area of neutrophils on BSA or ICAM-1 coated glass in figure 3.2G is also included for comparison. The middle solid line in each column is the mean value and the bar is standard error of the mean. ****$p<0.0001$ (One-way ANOVA). The total cell number is 107 and 49 for flat surface and nanoridges respectively. Results are combined from four independent experiments. (H) The percentage of flashing cells (green) and non-flashing cells (purple) in all neutrophils on BSA coated flat surface or nanoridges. (I) The average oscillation time of flashing neutrophils on BSA coated flat surface or nanoridges. The result showing average oscillation time of neutrophils on BSA or ICAM-1 coated glass in figure 3.2I is also included for comparison. The middle solid line in each column is the mean value and the bar is standard error of the mean. ****$p<0.0001$ (One-way ANOVA). The total cell number is 39 and 45 for flat surface and nanoridges respectively. Results are combined from four independent experiments.

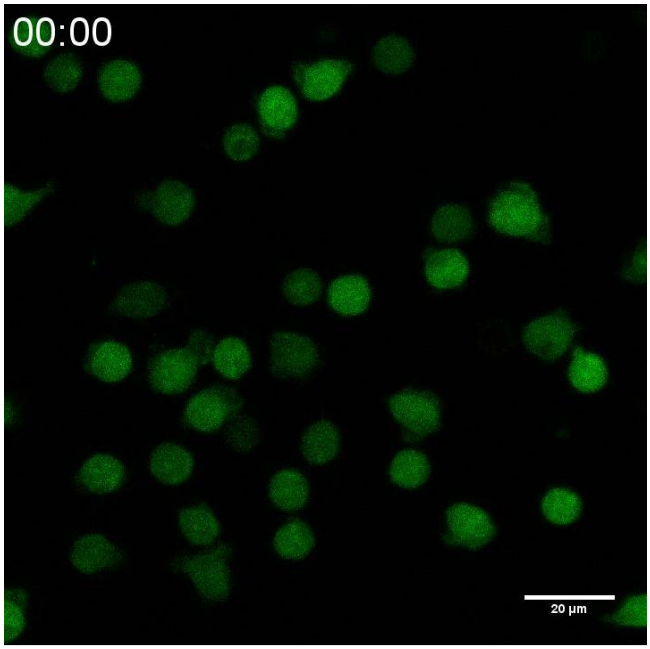

Movie 3.3: Neutrophils do not spread on acrylic flat surface with BSA coating. The green is Fluo-4 AM calcium dye fluorescence. The rate of the raw movie: 5 s/frame, play rate: 20 frame/s. The scale bar is 20 µm.

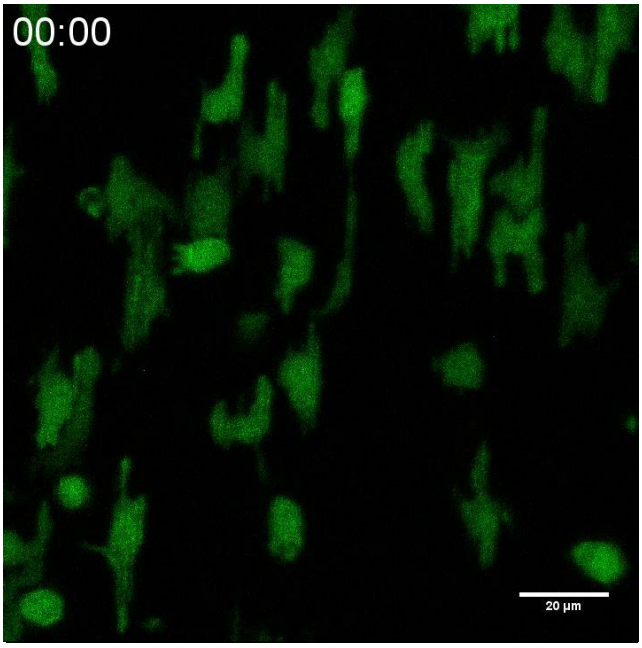

Movie 3.4: Neutrophils spread extensively and exhibit calcium flashes on BSA coated nanoridges. The green is Fluo-4 AM calcium dye fluorescence. The rate of the raw movie: 5 s/frame, play rate: 20 frame/s. The scale bar is 20 µm.

design provides optimal guidance for the migration of *Dictyostelium discoideum* (*D. discoideum*) cells (Driscoll et al., 2014).

We first image neutrophils on flat acrylic areas that are next to the arrays of nanoridges. Similar to what we observed with neutrophils plated on BSA-coated glass, we found that most of the neutrophils on the flat acrylic surface are circular, do not spread (Fig. 3.3A and Movie 3.3), and the calcium intensity remains constant (Fig. 3.3B and C, Movie 3.3). Surprisingly, we found that cells on the adjacent nanoridges instead exhibit extensive spreading and calcium fluctuation (Fig. 3.3D and E, Movie 3.4). The autocorrelation result shows that the fluctuation interval for the cell in figure D is about 3.17 minutes (Fig. 3.3F). By quantifying a number of cells from multiple experiments, we confirmed that neutrophils on BSA-coated nanoridges spread to a similar extent as they do on ICAM-1-coated glass, yet cells on BSA-coated flat acrylic areas do not spread. In addition, ~64% of neutrophils plated flat acrylic surfaces show no calcium fluctuation. However, the percentage decreases to ~24% for neutrophils plated on nanoridges (Fig. 3.3H). We also calculated the fluctuation interval for flashing neutrophils and found that the calcium flashing on ridges is significantly more rapid than it is on flat surfaces but comparable with the flashing on ICAM-1-coated glass (Fig. 3.3I). Taken together, these results suggest that nanoscale ridges are able to activate neutrophils in the absence of integrin ligands.

3.3.3 Neutrophil activation on nanoridges is not dependent on LTB_4 release and signaling

Upon primary chemoattractant activation, neutrophils release leukotriene B_4 (LTB_4) as a signal relay molecule to amplify their chemotactic migration in a paracrine fashion (Afonso et al., 2012; Lammermann et al., 2013; Majumdar et al., 2016). Released LTB_4 also potentiates the same neutrophil for primary chemotaxis signal in an autocrine fashion (Majumdar et al., 2016). It has

also been shown that LTB_4 production of neutrophils in response to IgG-containing immune complexes is dependent on integrins, even when the cells are in suspension (Graham et al., 1993). We, therefore, explore the possibility that it is the released LTB_4 that activates neutrophils and stimulates calcium oscillation in an autocrine and/or paracrine manner.

LTB_4 synthesis starts from the conversion of arachidonic acid (AA) to leukotriene A_4 (LTA_4) by 5-lipoxygenase (5-LO) and 5-lipoxygenase activating protein (FLAP) at the neutrophil nuclear envelope (Newcomer and Gilbert, 2010). LTA_4 is further hydrolyzed by LTA_4 hydrolase into LTB_4, which is released through extracellular vesicles (Majumdar et al., 2016; Newcomer and Gilbert, 2010). The FLAP inhibitor MK886 antagonizes the binding of AA to FLAP and dissociates FLAP and 5-LO at higher concentrations (Young et al., 1993). To determine whether LTB_4 plays a role in neutrophil activation on ICAM-1-coated glass and on BSA-coated nanoridges, we pretreat neutrophils with either DMSO or 100 nM MK886 and perform calcium imaging. As expected, DMSO-treated neutrophils spread and displayed rapid calcium oscillation on ICAM-1-coated glass (Fig. 3.4A-C). MK886 treatment delayed cell attachment and spreading on ICAM-1-coated glass by ~15 minutes. However, once cells attach to the surface, we observed calcium oscillations that are comparable to DMSO-treated cells (Fig. 3.4D-F, Movie 3.5). Interestingly, MK886-treated neutrophils fail to retain the calcium flashing for a long period as the DMSO-treated cells do (Fig. 3.4E & G, gray boxes), suggesting that LTB_4 may be required to maintain the activation status or that the treatment accelerates the cell apoptosis. We observed a similar response for MK886-treated neutrophils on BSA-coated nanoridges: they spread and exhibit rapid calcium oscillation for a shorter period (Fig. 3.4G-I, Movie 3.6). Based on these results, we conclude that LTB_4 release and signaling is dispensable for the initial activation of neutrophils on BSA-coated nanoridges but may be involved in maintaining the activation state.

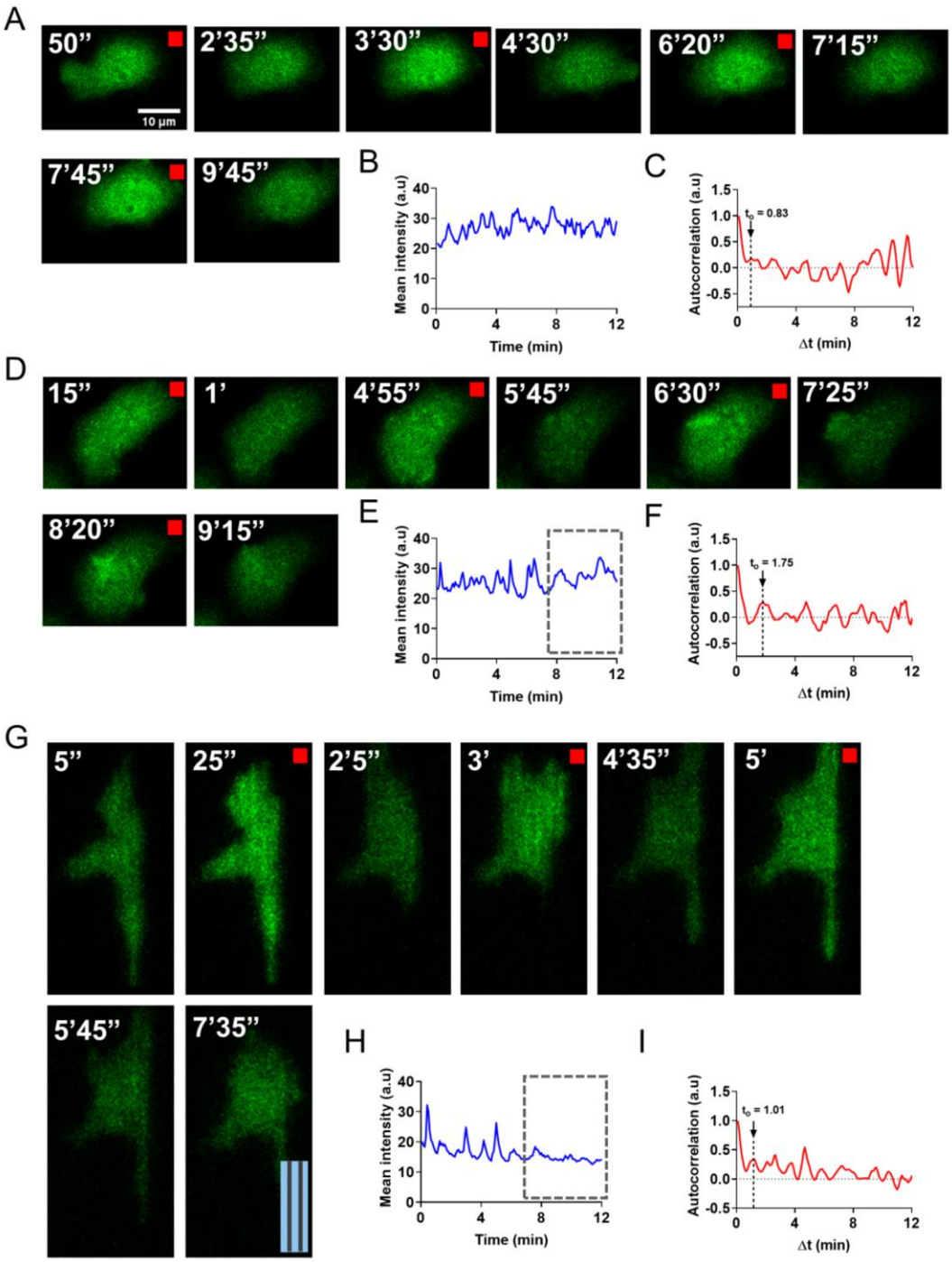

Figure 3.4: Inhibition of LTB4 synthesis does not abolish the calcium flashing in neutrophils on ICAM-1 coated glass and BSA coated nanoridges. (A, D, & G) Montage of fluorescence images of neutrophils treated with DMSO (A) or MK886 (D & G) on ICAM-1 coated glass (A & D) or on BSA coated nanoridges (G). Images are representatives of three independent experiments. Red boxes highlight the time points when cells show higher fluorescence signal. (B, E, & H) Mean intensity plot over time for the cell shown in A, D, and G, respectively. (C, F, & I) Autocorrelation of the intensity plot shown in B, E, or H, respectively. The dash line and arrow mark the oscillation time.

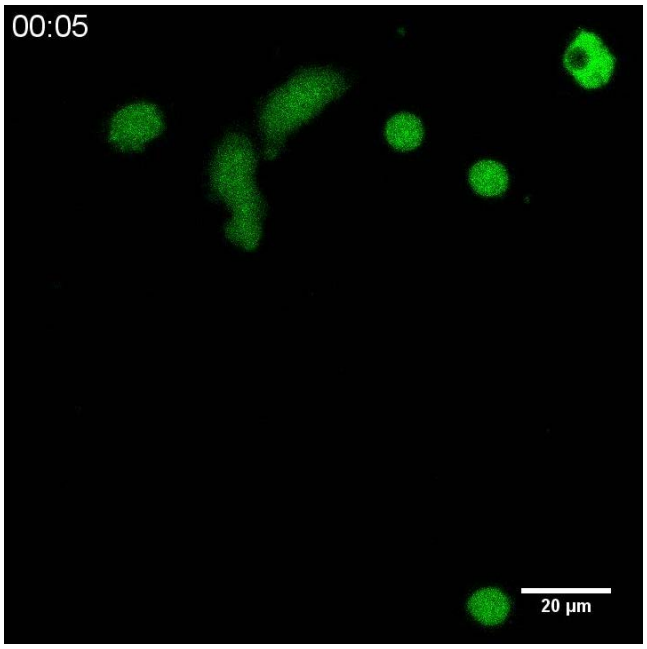

Movie 3.5: MK886 treatment does not abolish the calcium flashing in cell on ICAM-1 coated glass. Cells are incubated with 100 nM MK886 for 15 minutes at 37°C. The green is Fluo-4 AM calcium dye fluorescence. The rate of the raw movie: 5 s/frame, play rate: 20 frame/s. The scale bar is 20 µm.

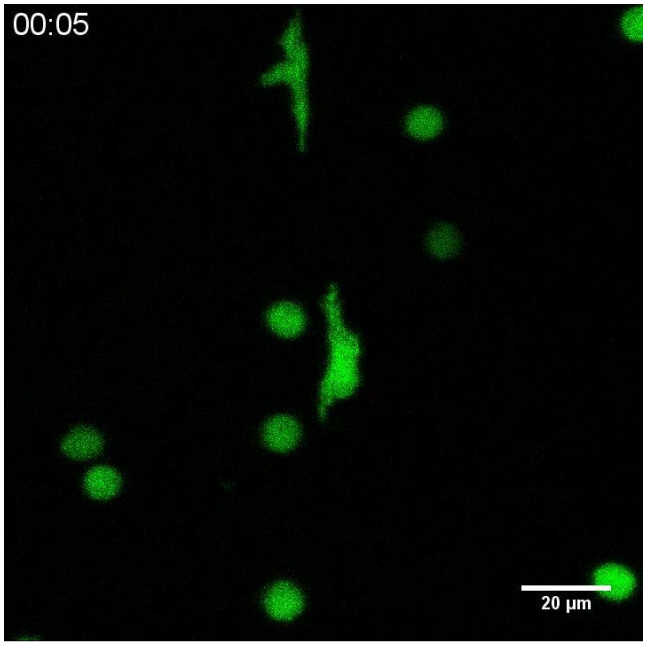

Movie 3.6: MK886 treatment does not abolish the calcium flashing in cell on BSA coated nanoridges. Cells are incubated with 100 nM MK886 for 15 minutes at 37°C. The green is Fluo-4 AM calcium dye fluorescence. The rate of the raw movie: 5 s/frame, play rate: 20 frame/s. The scale bar is 20 µm.

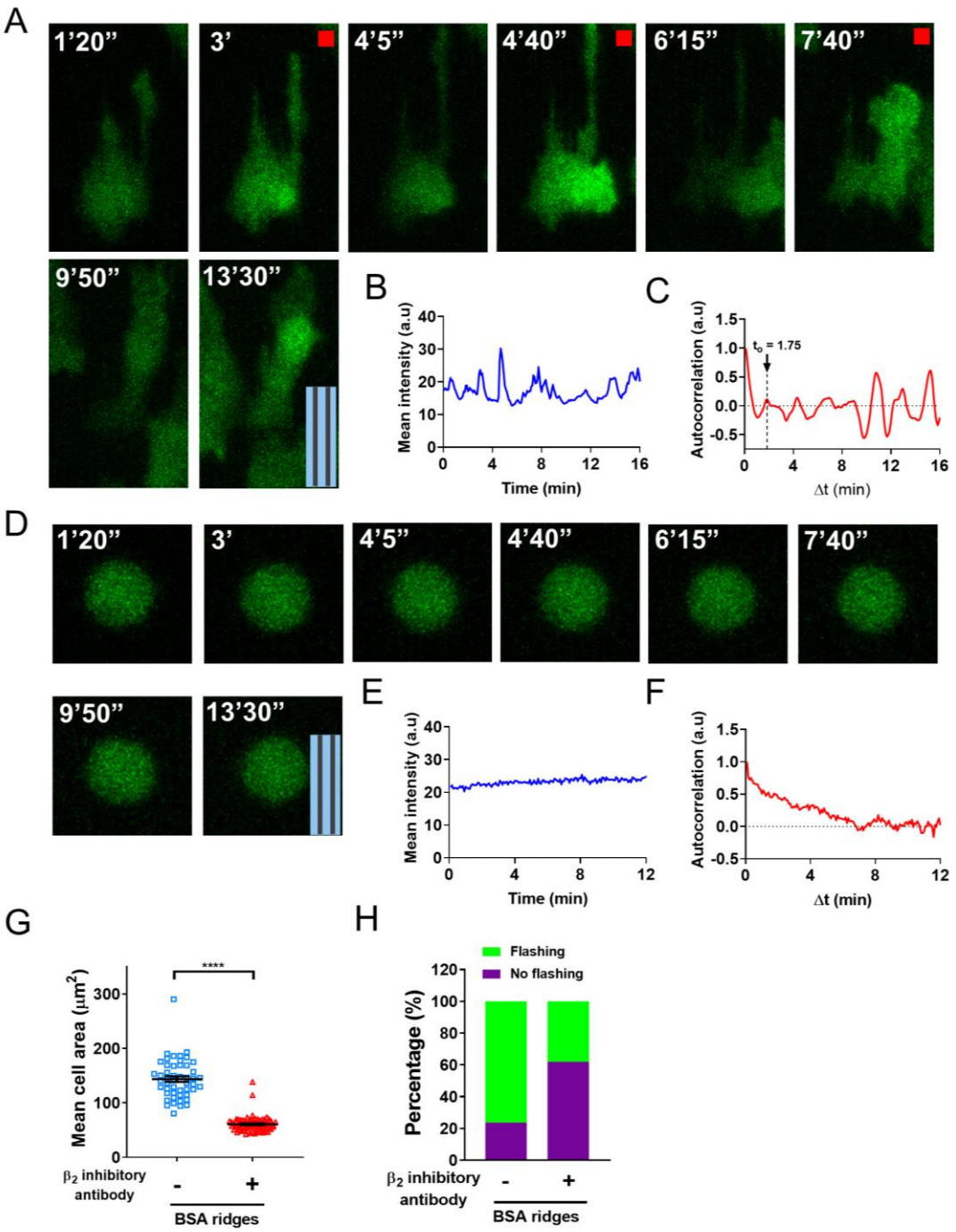

Figure 3.5: Neutrophil activation on BSA coated nanoridges is determined by β_2 integrins. (A & D) Montage of fluorescence images of Fluo-4 AM labeled neutrophils treated with β1 integrin (A) or β2 integrin (D) inhibitory antibody on BSA coated nanoridges. Images are representatives of two independent experiments. Red boxes highlight the time points when cells show higher fluorescence signal. (B & E) Mean intensity plot over time for the cell shown in A and G, respectively. (C & F) Autocorrelation of the intensity plot shown in B or E, respectively. The dash line and arrow mark the oscillation time. (G) The average cell area of neutrophils treated with DMSO or β2 integrin inhibitory antibody on BSA coated nanoridges. The middle solid line in each column is the mean value and the bar is standard error of the mean. ****p<0.0001 (unpaired t test). The total cell number is 49 and 80 for DMSO and β2 integrin inhibitory antibody treatment respectively. Results are combined from two independent experiments. (H) The percentage of flashing cells (green) and non-flashing cells (purple) in all neutrophils treated with DMSO or β2 integrin inhibitory antibody on BSA coated nanoridges.

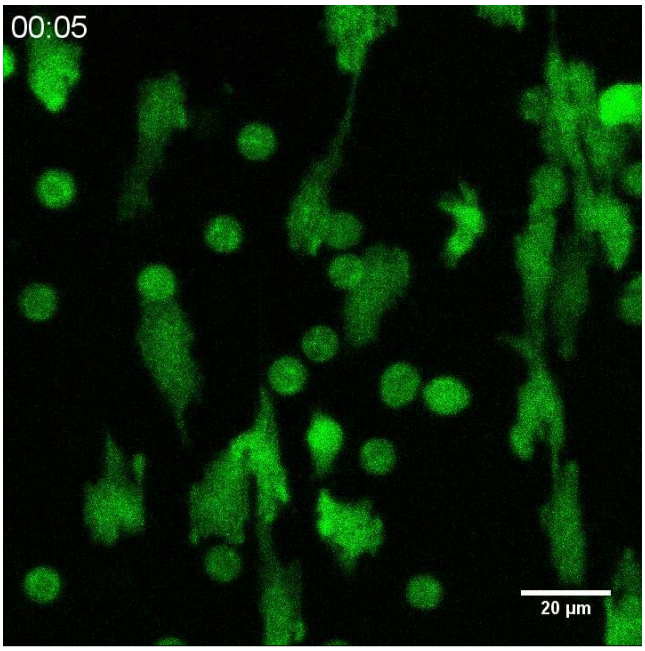

Movie 3.7: Treatment with β_1 integrin inhibitory antibody delays but does not abolish cell activation on BSA coated nanoridges. Cells are incubated with 20 µg/mL β_1 integrin inhibitory antibody for 20 minutes at 37°C. The green is Fluo-4 AM calcium dye fluorescence. The rate of the raw movie: 5 s/frame, play rate: 20 frame/s. The scale bar is 20 µm.

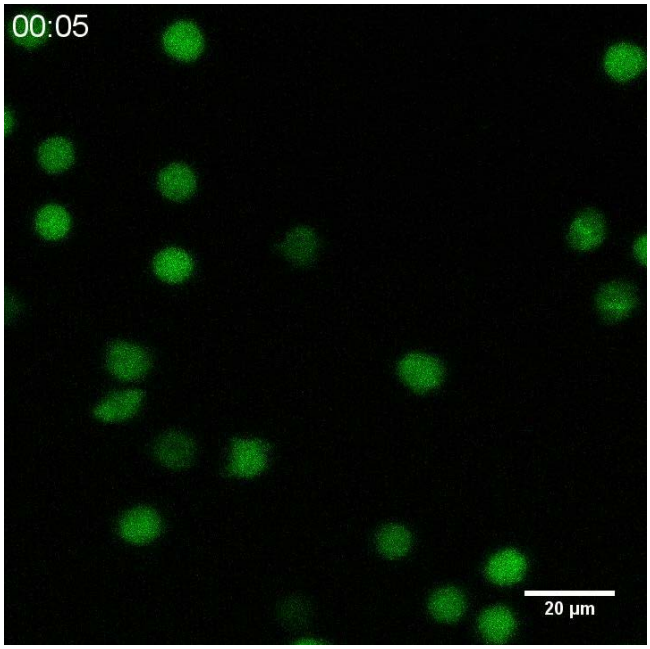

Movie 3.8: Inhibition of β_2 integrins completely abolishes cell activation on BSA coated nanoridges. Cells are incubated with 20 µg/mL β_2 integrin inhibitory antibody for 20 minutes at 37°C. The green is Fluo-4 AM calcium dye fluorescence. The rate of the raw movie: 5 s/frame, play rate: 20 frame/s. The scale bar is 20 µm.

3.3.4 Neutrophil activation on BSA-coated nanoridges is regulated by β_2 integrins

Based on previous results, we hypothesize that nanoridges activate neutrophils through integrin signaling. To directly test this hypothesis, we pre-treat neutrophils with β_1 or β_2 integrin specific inhibitory antibodies. We found that neutrophils treated with the β_1 integrin inhibitory antibody spread and show calcium oscillation on BSA-coated nanoridges but they do so in a delayed manner (Fig. 3.5A-C, Movie 3.7). The time delay is around 5 to 10 minutes, suggesting that β_1 integrins facilitate but do not dictate the activation. However, β_2 integrin inhibitory antibody treatment completely abolishes the activation. The treated neutrophils remain round, do not spread, and do not show calcium oscillations (Fig. 3.5D-F, Movie 3.8). Further quantification confirms that β_2 integrin inhibitory antibody treatment abolishes cell attachment and decreases the percentage of oscillating cells from 76% to 38% (Fig. 3.5G and H). These results indicate that β_2 integrins not β_1 integrins regulate the neutrophil activation on BSA coated-nanoridges.

3.3.5 β_2 integrin clustering induced by membrane curvature leads to ligand-independent integrin activation

We next visualize integrin activation in live neutrophils using well-categorized integrin conformational specific antibodies (Humphries et al., 2006). Monoclonal antibody (mAb) KIM127 marks the integrin extension confirmation by recognizing an epitope on the knee of β_2 integrins, which is buried in the bent conformation (Fig. 3.6A). Instead, when β_2 integrins adopt a high-affinity conformation for ligand binding, mAb24 recognizes the exposed domain on the heads (Fig. 3.6A). KIM127 and mAb24 have been shown to distinguish these two conformations during the arrest of rolling neutrophils (Fan et al., 2016). Finally, we include another non-functional antibody TS2/4, which nonspecifically binds to α_L integrins in all conformations (Fig. 3.6A).

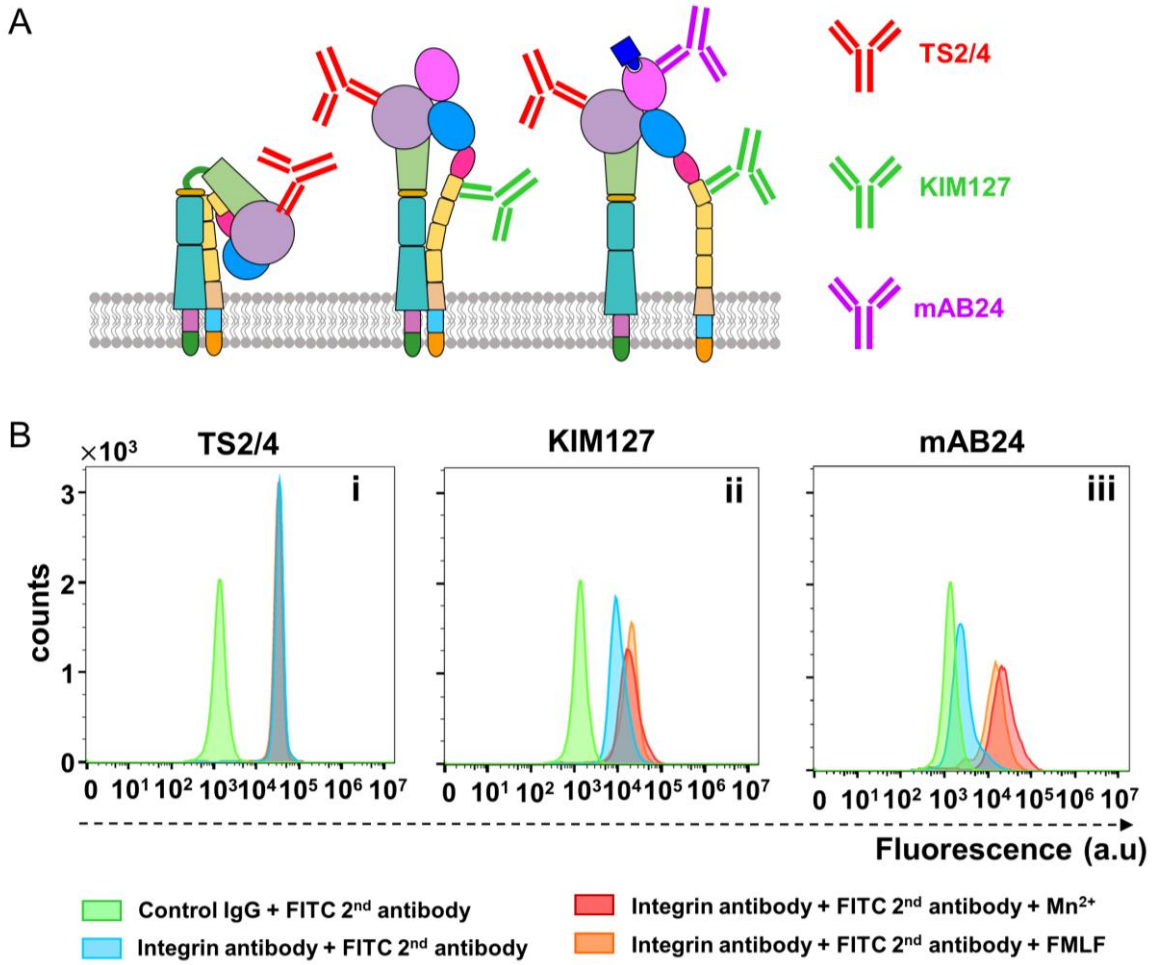

Figure 3.6: The characterization of integrin conformation specific antibodies. (A) A schematic showing the conformational binding specificity of integrin antibodies used in this study. (B) Representative flow cytometry result (n=2) of neutrophils treated with DMSO, fMLF, or Mn^{2+} for integrin antibody TS2/4 (i), KIM127 (ii), and mAB24 (iii).

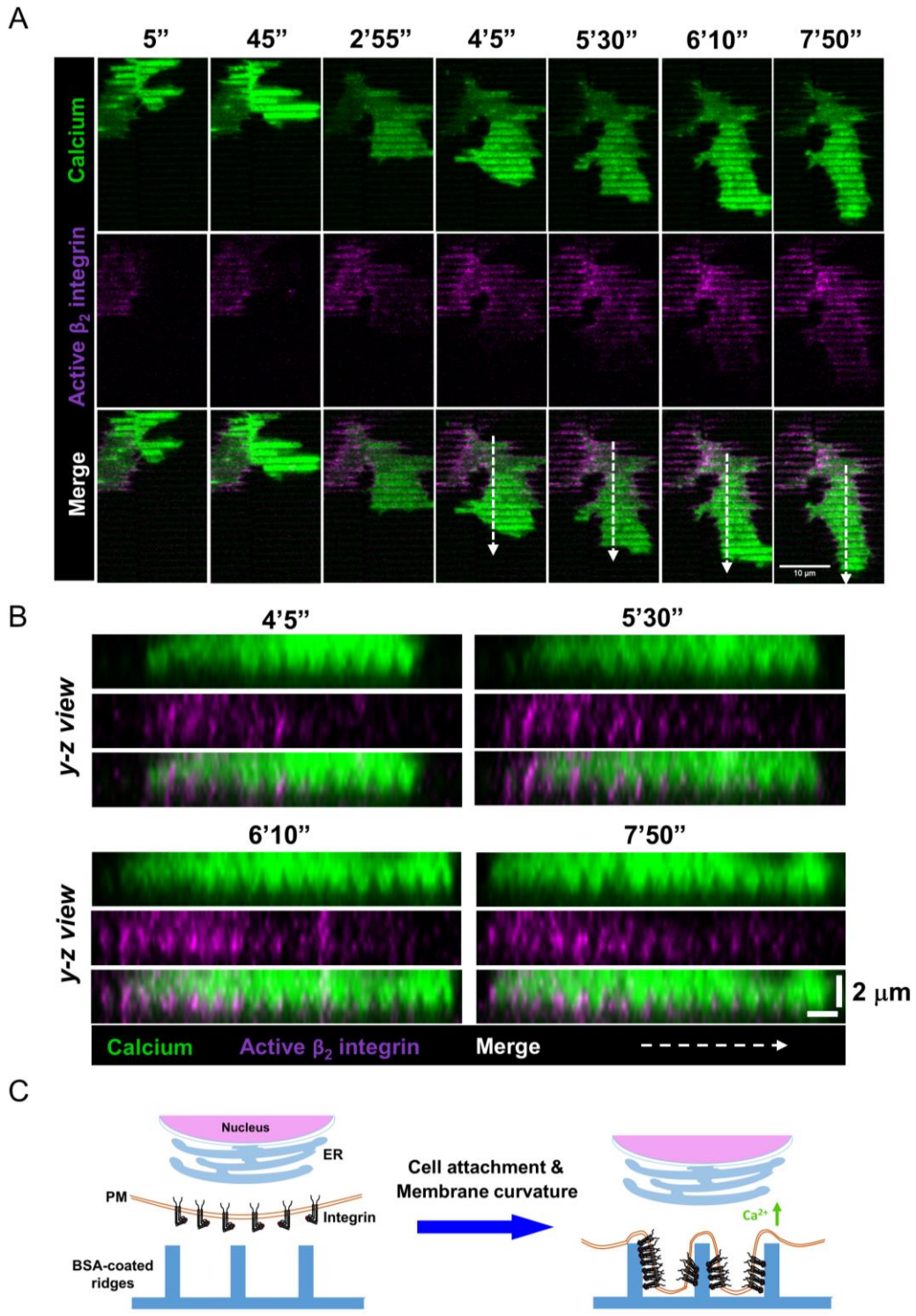

Figure 3.7: Nanoridge-induced membrane curvature triggers integrin clustering and activation. (A) Fluorescence image montage of calcium (top), active β_2 integrin labeled by mAB24 (middle), and the merge of the two (bottom) for a neutrophil migrating on BSA coated nanoridges at different time points. The dotted white lines mark the positions to generate *y-z* orthogonal views in B and arrows indicate the cell migration direction. Images are representatives of one experiment. (B) The *y-z* views of the positions marked by dotted lines in A at the representative time points. The arrow shows the cell migration direction as in A. (C) A schematic illustration of the hypothesized model that membrane curvatures induced by nanoridges cause integrin clustering and activation.

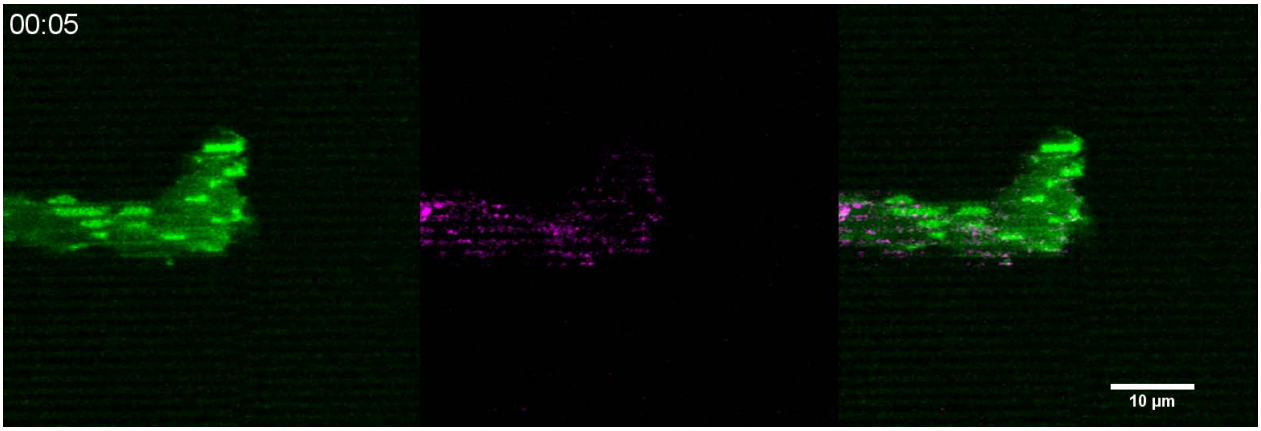

Movie 3.9: Migrating neutrophils form clusters of active β_2 integrins on the side walls of BSA coated nanoridges. The green is Fluo-4 AM calcium dye fluorescence. The magenta is Alexa-647 conjugated mAB24 antibody fluorescence. The rate of the raw movie: 5 s/frame, play rate: 20 frame/s. The scale bar is 10 µm.

To confirm the specificity of these antibodies, we perform flow cytometry with isolated human neutrophils. We activate the integrins either through inside-out signaling by treating cells with primary chemoattractant N-Formyl-met-leu-phe (fMLF) or through outside-in signaling by adding Mn^{2+}. We found that all three curves of TS2/4 stained neutrophils overlap nicely regardless of the activation status but are separated from the control IgG curve, confirming that TS2/4 indistinguishably recognizes all α_L integrins (Fig. 3.6Bi). On the other hand, the separation between the control curve and the curve of KIM127 stained naïve neutrophils suggests that the binding of KIM127 to β_2 integrins stabilizes their extended conformation (Fig. 3.6Bii) – a response that is augmented in the presence of fMLF or Mn^{2+} (Fig. 3.6Bii). For mAb24, only a small separation between the control curve and the curve of mAb24 stained naïve cells is observed (Fig. 3.6Biii). In addition, both fMLF and Mn^{2+} stimulations shift the curve dramatically towards the right (Fig. 3.6Biii). This suggests that mAb24 specifically recognizes the high-affinity conformation of β_2 integrins while has little stimulation effect by itself. Therefore, we study integrin activation dynamics using the mAb24 antibody.

By using Fluo-4 and Alexa-647 conjugated mAb24 antibody, we monitor the calcium oscillation and activation of β_2 integrins simultaneously in neutrophils on BSA-coated nanoridges. A montage of calcium and/or active β_2 integrin labeling of a neutrophil migrating on BSA-coated nanoridges is presented in Figure 3.7A. We focus on a bottom z slice of time-lapse images because the majority of the fluorescence signal of active β_2 integrins is localized on the bottom surface. Remarkably, we observed calcium oscillations from the cell bottom (e.g. time 45”, 4’5”, and 6’10” in the calcium channel of Fig. 3.7A, and Movie 3.9). The calcium channel not only shows the calcium oscillation inside neutrophils, but also marks the outline of the cell membrane: the wider, brighter streaks depict cell membranes penetrating into the grooves between ridges; the thinner,

dark lines mark the location of nanoridges (Fig. 3.7A calcium channel, Movie 3.9). Interestingly, we found puncta of active β_2 integrins formed on the nanoridges in the middle of the cell (Fig. 3.7A active β_2 integrins channel, Movie 3.9). In addition, migrating neutrophils continuously form these puncta near the protruding cell front (Fig. 3.7A merge channel, Movie 3.9). Because of the absence of active β_2 signal in the grooves, we hypothesize that β_2 integrins are clustered and activated on the sidewalls of nanoridges. To test this, we generate *y-z* projections across the white dashed arrows in the merge channel (Fig. 3.7B). The calcium channel in the *y-z* projections clearly shows that the cell membrane can penetrate into the grooves (Fig. 3.7B calcium channel). As expected, clusters of active β_2 integrins are indeed formed on the sidewalls of the nanoridges (Fig. 3.7B active β_2 integrins channel). However, a strong signal of the active β_2 integrins is not observed to co-localize with the calcium signal in the groove (Fig. 3.7B active β_2 integrins channel), suggesting that β_2 integrins are not activated on the bottom of the penetrating membrane. Furthermore, the merge channel in the *y-z* projections confirms that the puncta of β_2 integrins are formed closely following the cell front with a distance of ~ 3 μm. From these findings, we propose that membrane curvature induced by nanoridges leads to clustering and activation of β_2 integrins on the sidewalls of nanoridges (Fig. 3.7C).

3.4 Discussion

Neutrophil attachment and migration are key processes in the immune response to inflammation and infection. Although neutrophil crawling in 2D or 3D settings has been extensively studied, it is still poorly understood how the structural features in the microenvironment regulate neutrophil behaviors and through what signaling mechanism. Here, we aim to answer these questions by studying the activation and migration phenotypes of human

primary neutrophils on surfaces with arrays of nanoscale ridges. First, we found that the binding of β_2 integrins to ICAM-1 is sufficient to activate neutrophils, which is indicated by cell spreading and calcium flashing on ICAM-1-coated glass. The same activation phenomena are also observed in neutrophils plated on nanoridges in the absence of integrin ligands. Further mechanistic studies showed that the observed neutrophil activation is dictated by β_2 integrins and is not related to the release of secondary chemoattractant LTB_4. Finally, by using a conjugated mAb24 antibody that is specific to the active and high-affinity form of β_2 integrin subunit, we discovered that clusters of active β_2 integrins are formed on the sidewalls of BSA-coated nanoridges during cell spreading and migration. We therefore propose that the clustering and activation of β_2 integrins are mediated by cell membrane curvature and are responsible for the observed activation phenotype of neutrophils on nanoridges.

Calcium is a universal second messenger in the activation of a variety of cells. The increase of intracellular calcium can be due to the release from endoplasmic reticulum (ER) stores or calcium influx through channels on the plasma membrane (PM) (Clemens and Lowell, 2015). The binding of chemoattractant fMLF to its receptor induces a transient calcium spike in neutrophils, a phenomenon which is mediated by the calcium channels on both the ER stores and cell PM (Krause et al., 1990). Our preliminary experiment shows that calcium oscillations measured in the system are not affected by the depletion of extracellular calcium, suggesting that the increased calcium mainly comes from the intracellular stores. Although integrins lack intrinsic enzymatic activity, they can regulate intracellular signaling through the recruitment of other effector molecules (Abram and Lowell, 2009; Campbell and Humphries, 2011). It has been shown that integrin outside-in signaling can activate phospholipase Cγ (PLCγ), an enzyme that cleaves phosphatidylinositol 4,5-bisphosphate ($PI(4,5)P_2$) into diacylgcerol and IP_3 (Abram and Lowell,

2009). The calcium efflux from the ER stores is then triggered by the binding of IP_3 to its receptors on ER. Other studies provided evidence that tensile forces on the high-affinity form of integrin LFA-1 can initiate calcium influx, and that inhibition of PLCγ activity significantly diminishes this influx (Dixit et al., 2011; Schaff et al., 2010). One may argue that a rise in calcium can increase the affinity of integrins and lead to their activation, not the other way around. In disagreement with this hypothesis, previous studies showed that the chelation of intracellular calcium has a negligible effect on neutrophil migration (Jaconi et al., 1991; Zigmond et al., 1988). Although the integrin-induced initiation of calcium efflux from the ER is probable, the mechanisms that regulate the calcium oscillations in neutrophils remain unclear. One possibility is that the continuous activation of integrins during cell migration generates a wave-like transient IP_3 production (de Rubio et al., 2018). Further studies are needed to establish the spatial activation pattern of integrins and PLCγ.

The existence of three integrin conformational states has been observed for many integrin heterodimeric pairs by electron microscopy (Chen et al., 2010; Nishida et al., 2006; Su et al., 2016). Fan *et.al* further showed that LFA-1 and Mac-1 in their bent conformation bind to ICAM-1 *in cis* on the surface of rolling neutrophils (Fan et al., 2016), suggesting that diverse intermediate integrin conformations exist. Despite the information on the structural basis of integrin conformations using purified integrins and stabilizing antibodies, how integrin transits between conformations during activation is still under investigation. Growing evidence supports that an equilibrium between different integrin conformations exists and many factors, including chemokine stimulation, the presence of immobilized ligand, and integrin clustering, can shift this equilibrium (Lepzelter et al., 2012; Li et al., 2017; Shattil and Newman, 2004). Among different factors, integrin clustering is believed to play a key role in the initiation of outside-in signaling (Shattil and Newman, 2004). Clustering of $\alpha_{IIb}\beta_3$ integrin into oligomers from the cell interior is sufficient to

enhance integrin activation (Ye et al., 2014), and trigger the phosphorylation of Src and Syk (Arias-Salgado et al., 2003; Hato et al., 1998). The interactions between multiple integrin heterodimers are mediated by the transmembrane domains of α and β subunits (Kim et al., 2009a; Ye et al., 2014). Analysis of the energy landscape of integrins in different conformations revealed that the high-affinity, headpiece-open conformation is favored upon integrin extension (Li et al., 2017). In addition, the clustering of integrins is known to be associated with lipid rafts (Krauss and Altevogt, 1999; Solomkin et al., 2007). Thus, it is plausible that the formation of lipid raft microdomains because of membrane curvature or tension brings integrins on the cell PM into proximity and results in their clustering and activation. Supporting this, our results show that integrins in an active and high-affinity conformation are clustered near the sidewalls of nanoridges, where the membrane of a migrating neutrophil extensively penetrates into the grooves (~1.5 μm) between ridges. Further experiments are needed to examine the spatial correlation between integrin clusters and lipid raft domains.

It is well established that the distortion of cell shape modulates the size and distribution of integrin-based focal adhesions in endothelial cells (Chen et al., 2003) and breast cancer cells (Chen et al., 2019). Thus, membrane curvature may play an important regulatory role in cell behaviors. Indeed, a recent study by Ren and his colleagues demonstrated that increased membrane curvature on neutrophils recruits Slit-Robo-GTPase activating protein 2 (SRGAP2), an F-BAR-domain-containing protein, which further leads to polarization of downstream effector proteins and eventually the whole cell (Ren et al., 2019). Another study on mast cells suggested that membrane deformation actively regulates the recruitment of curvature-sensitive proteins and activators of actin polymerization (Wu et al., 2018). Interestingly, in our study, membrane curvatures generated by cell membrane penetration into grooves have a width of ~1 μm, which is on the same scale of

membrane curvatures reported in Ren *et al.* (Ren et al., 2019). Therefore, it is likely that the concave curvatures induced by nanoridges trigger the neutrophil membrane reorganization and downstream intracellular signaling. However, we cannot exclude the possibility that curvature-sensing molecules are recruited to the penetration regions and activate integrins through inside-out signaling.

In summary, we show that neutrophils plated on BSA-coated nanoridges are activated and exhibit intracellular calcium signaling in a chemoattractant- and integrin-ligand independent manner. This neutrophil activation is potentially mediated by cell membrane curvature and clustering of β_2 integrins. Our results provide preliminary evidence of a novel mechanism by which neutrophils sense, adapt, and respond to extracellular structures during their initial attachment. We envision that this mechanism may also apply to other leukocytes.

3.5 Materials and methods

Surface fabrication and replication: The nanoridge and sawtooth topographies that were employed to study migratory and cytoskeletal responses were designed and fabricated using multiphoton absorption polymerization (MAP). More details regarding this method can be found elsewhere.80-81 Briefly, the output of an ultrafast Ti:sapphire laser (Coherent Mira 900) tuned to 800 nm was passed through a high-numerical-aperture objective (Zeiss alpha-Plan Fluar 100×; numerical aperture 1.45) and focused onto a photopolymerizable resin ((1:1 w/w tris (2-hydroxy ethyl) isocyanurate triacrylate (SR368):ethoxylated (6) trimethylolpropane triacrylate (SR499) (both from Sartomer), 3 wt. % Lucirin TPO-L (BASF)) that was sandwiched between a glass coverslip and a microscope slide. Based on the experimental conditions, the photoinitiator undergoes efficient two-photon absorption only in the focal region of the objective, allowing for

the fabrication of three-dimensional structures with arbitrary shape. The sample was mounted on a motorized stage that can be controlled by a computer. A LabVIEW program (National Instruments) was used to control the stage movement to fabricate the desired the patterns. The same program controlled a shutter to dictate when and where polymerization should occur. After fabrication was completed, the sample was soaked in two containers of ethanol for 3 min each to remove the unreacted monomer resin. The MAP-fabricated "master" structure was then baked/dried in oven at 110 °C for at least 1 h. To reproduce nanotopographic surfaces, we used solvent-assisted nanotransfer molding42 to make a negative-relief mold of the "master" structure fabricated with MAP. A film of hard PDMS42, 82 was spin-coated onto the original pattern. This PDMS mixture included hexanes, to decrease viscosity to allow the film to conform optimally onto the structures being coated, thereby improving the resolution of the mold. After sitting at room temperature for 2 hr, the patterned microscope slide and coated film were baked at 60 °C for 1 h. Sylgard 184 (10:1 w/w elastomer base: curing agent; Dow Corning) was poured on top of the baked sample to form a layer approximately 1 cm thick. The same was then returned to the oven for 70 min. Once baking was completed, the mold was peeled from the "master" in the direction parallel to the ridges. For sawteeths mold, peeling should occur from the tail to the head of the sawteeth to prevent damage to the pattern. Molds can be used to make replicas of the original MAP structure. A drop of the same resin used for MAP was sandwiched between a functionalized coverslip and the mold and the sandwich was exposed to UV light for 5 min. Using this process, many replicas of an original pattern can be produced in a short amount of time.

Isolation of human primary neutrophils: The isolation of human primary neutrophils from heparinized whole blood has been previously described (Majumdar et al., 2016). Briefly,

neutrophils were isolated by using dextran (Sigma-Aldrich, St. Louis, MO) sedimentation (3% dextran, 0.9% NaCl in endotoxin-free water) and followed by differential centrifugation over Histopague 1077 (Sigma-Aldrich, St. Louis, MO). Residual red blood cells and erythrocytes were lysed with ACK lysing buffer (Lonza, Switzerland).

Antibody purification and conjugation: TS2/4 and KIM127 monoclonal antibodies were purified commercially at ProSci (ProSci, CA) by inoculating the hybridoma cells (American Type Culture Collection, Manassas, VA) into five mice for each antibody. Purified antibodies were aliquot and stored at -30℃ until use. KIM127 and TS2/4 were conjugated with Alexa-488 and Alexa-568 respectively by using an antibody labeling kit (Thermo Fisher Scientific, Waltham, MA) and following the manufacture protocol. The labeled antibodies were stored at 4℃ and validated with flow cytometry. Unlabeled (363402) and Alexa-647 conjugated mAb24 (363412) were purchased from BioLegend, San Diego, CA.

Live cell imaging: Coverslips or surfaces with nanoridges were coated with 1% BSA (Sigma-Aldrich, St. Louis, MO) or 5 μg/mL ICAM-1 (BioLegend, San Diego, CA) in DPBS (Thermo Fisher Scientific, Waltham, MA) at 37℃ for 1 hour then glued back to 8 well chamber slides (Cellvis, Mountain View, CA). Freshly isolated neutrophils were diluted to 1×10^6 in RPMI medium without phenol red (Gibco, Fisher Scientific) and stained with Fluo-4 AM calcium dye (Thermo Fisher Scientific, Waltham, MA) at 37℃ for 15 minutes. To inhibit LTB_4 synthesis, cells were pre-treated with either DMSO or 100 nM MK886 (Tocris Bioscience, UK) at 37℃ for 15 minutes during Fluo-4 AM labeling. To inhibit specific integrins, neutrophils were incubated with β_1 integrin inhibitory antibody (MAB1959, MilliporeSigmaor, MA) or β_2 integrin inhibitory

antibody (CBL158, MilliporeSigmaor, MA) at 37℃ for 20 minutes during Fluo-4 AM labeling. After which, cells were plated on indicated surfaces and immediately imaged with a Zeiss LSM 880 laser-scanning confocal microscope at 37℃. A *z* stack of fluorescent images was taken every 5 s using a water-immersion, 40× objective, and a zoom-in factor of 2.5. To visualize the integrin activation dynamic, neutrophils were stained with Fluo-4 AM, span down, and re-suspended in RPMI supplemented with conjugated integrin conformation-specific antibodies. Cells were immediately imaged using an oil-immersion, 63× objective, and a *z* stack of images were taken every 5s using a zoom-in factor of 2.5.

Quantitative analysis of cell area and calcium oscillations: For time-lapse images of neutrophils on BSA- or ICAM-1 coated glass or of β_2 inhibitory antibody pretreated cells on nanoridges, cell tracking was performed using an automated program in MATLAB (Mathworks). For the time-lapse images of neutrophils on BSA-coated nanoridges, cells were tracked manually by selecting regions of interest in imageJ. The fast floating cells or cell aggregates were excluded from the analysis. For time-lapse images of non-treated or MK886 treated or β_1 inhibitory antibody-treated cells on nanoridges, cell tracking was performed using Manual Tracking in imageJ (NIH, Bethesda, MD). The files containing cell coordinates and fluorescence intensities were imported into MATLAB for further analysis. The fluorescence intensity of each cell was calculated by normalizing the total fluorescence with the cell area. The autocorrelation of calcium fluorescence signal was then determined by the following equation:$c(l) = \frac{\sum_{i=1}^{N-l}(X_i-\bar{X})(X_{i+l}-\overline{X})}{\sum_{i=1}^{N}(X_i-\bar{X})^2}$, where l is the lag time between two signal points X_i and X_{i+l}. The calcium oscillation interval was defined as the lag time of the first positive correlation peak. To visualize the localization of active β_2 integrins,

x-z/y-z view images were generated in imageJ. All final plots were created using GraphPad Prism (GraphPad Software).

Flow cytometry: Freshly isolated neutrophils were stimulated with 10nM fMLF at 37℃ for 10 minutes or 1mM Mn^{2+} in RPMI at 4℃ for 30 minutes then incubated with either control mouse IgG or integrin conformation-specific antibody at 4℃ for 30 minutes. After washed in RPMI three times, cells were incubated with FITC conjugated anti-mouse secondary antibody on ice for 30 minutes. After washed again in RPMI three times, all samples were analyzed using a BD Accuri flow cytometer.

Chapter 4

The Membrane Organization of Reconstituted FLAP:Lipid Assemblies Visualized by Electron Microscopy

4.1 Summary

In response to tissue injury or inflammation, nearby neutrophils migrate directionally to the inflamed/injured site and trigger dramatic swarm-like recruitment of distal neutrophils by secreting the secondary chemoattractant LTB_4 - a process referred to as signal relay. Although the biosynthesis process of LTB_4 is well understood, how LTB_4 is packaged and released out of the cells to establish a gradient is not clear. Interestingly, our immunofluorescence experiments show that stimulated neutrophils generate membrane budding at their nuclei and these budding vesicles are enriched in FLAP and 5-LO. Considering the conical shape of FLAP trimers, a functional unit of FLAP, we hypothesize that the clustering of trimeric FLAP in ceramide-rich microdomains triggers membrane curvatures. To test this *in vitro*, we purify FLAP from *E.coli*, reconstitute FLAP into defined lipid environments, and visualize the membrane organization of FLAP:lipid assemblies using negative stain EM and cryo-EM. Our preliminary results demonstrate that FLAP reconstitution generates unique protein:lipid assemblies with two membrane layers and potential membrane protrusions between two layers, sometimes resembling wagon wheels. This is the first study that uncovers a structural role of FLAP, one of the LTB_4 synthesizing enzymes, in remodeling membrane architecture.

4.2 Introduction

In response to tissue infections, circulating neutrophils are recruited into the tissue following the well-established neutrophil adhesion cascade: (1) tethering and rolling on the vascular endothelial cell (EC) surface; (2) polarization and firm attachment to the ECs; (3) crawling on the vascular vessel to seek permissive sites for (4) transendothelial migration (Filippi, 2019; Ley et al., 2007; Phillipson and Kubes, 2011). The adhesion and migration cascades of neutrophils after breaching through venular basal membrane are strongly mediated by chemoattractants. When neutrophils are guided to infection sites by gradients of primary chemoattractants, they secrete secondary chemoattractants to recruit additional neutrophils that have just entered the tissue from blood vessels (McDonald and Kubes, 2010). Among the many secondary chemoattractants, leukotriene B_4 (LTB_4) has been shown to be the first and most central one that mediates proinflammatory response (Chou et al., 2010; McDonald and Kubes, 2010). Lammermann *et al.* later showed that secreted LTB_4 is required for neutrophil swarming towards the tissue damage sites (Lammermann et al., 2013), a process in which LTB_4 acts as a signal relay molecule and amplifies neutrophil chemotaxis (Afonso et al., 2012).

LTB_4 is one of the metabolites of arachidonic acid (AA) that is involved in many chronic inflammatory diseases, such as arthritis (Klickstein et al., 1980; Miyabe et al., 2017), cardiovascular disease (Qiu et al., 2006; Spanbroek et al., 2003), and cancer (Matsuyama et al., 2004; Tong et al., 2002). LTB_4 is synthesized intracellularly from AA by sequential actions of 5-lipoxygenase (5-LO), 5-lipoxygenase activating protein (FLAP), and leukotriene A_4 (LTA_4) hydrolase (LTA_4H). Among six different lipoxygenase isoforms expressed in humans, 5-LO is the only isoform that catalyzes AA in a two-step reaction, resulting in its key role in LTB_4 biosynthesis (Wan et al., 2017). Human 5-LO is a soluble enzyme that translocates to the nuclear envelope (NE)

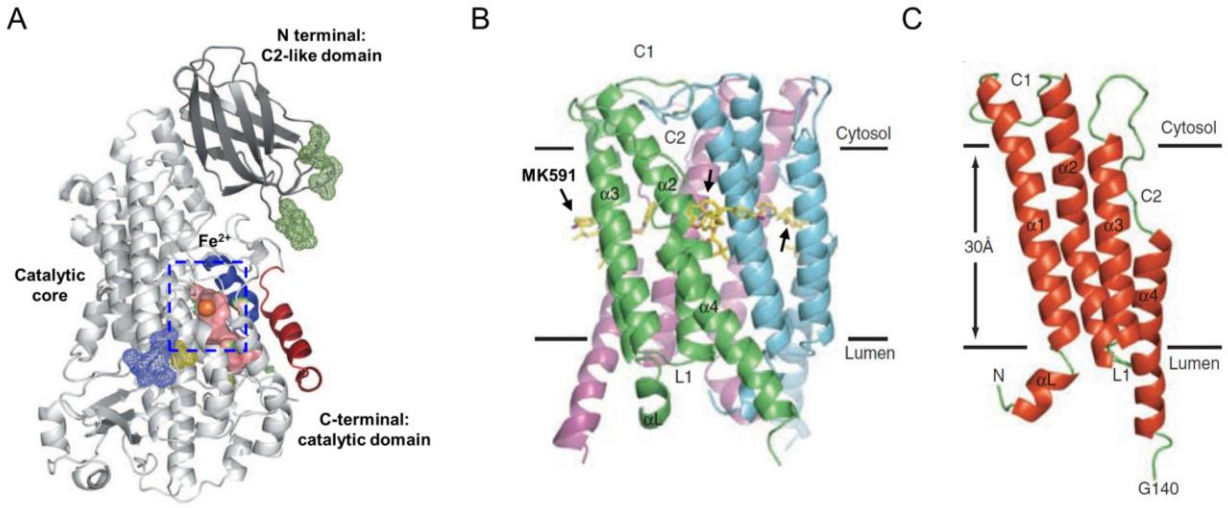

Figure 4.1: The crystal structures of a modified soluble human 5-LO, an inhibitor-bound FLAP trimer, and a FLAP monomer. (A) A cartoon illustration of 5-LO. The N- and C-terminals are labeled. The modified putative membrane insertion regions are indicated in green mesh. The catalytic core where the Fe ion is buried is highlighted by the blue box. Reproduced with permission from (Gilbert et al., 2011). (B) A cartoon illustration of a FLAP trimer with monomers colored in green, cyan, and magenta. The view is parallel to the NE membrane. The inhibitor MK591 molecules are labeled by arrows. (C) The structure of a FLAP monomer in a view parallel to the NE membrane. B and C are reproduced with permission from (Ferguson et al., 2007).

upon binding of Ca^{2+} to its N-terminal C2-like domain (Fig. 4.1A), which can be produced following chemoattractant stimulation (Gilbert et al., 2011). The C-terminal catalytic domain of 5-LO is composed of α-helices in which the nonheme iron-containing catalytic machinery is fully encapsulated (Fig. 4.1A) (Gilbert et al., 2011). Specifically, the side chains of two amino acids in the active center, phenylalanine 177 and tyrosine 181, form a cork that seals off the access channel to the catalytic iron and blocks the entry of AA (Gilbert et al., 2011). After translocation to the NE, 5-LO associates with FLAP, an integral membrane protein present at the cell nuclear membranes and endoplasmic reticulum (ER) (Haeggstrom, 2018). Although it lacks intrinsic enzymatic activity, FLAP is essential for the proper function of 5-LO. The crystal structure of homotrimeric FLAP in complex with three inhibitory molecules (Fig. 4.1B), MK591, reveals that each monomer has four transmembrane helices connected by two cytosolic loops and that both N- and C-terminals are positioned in the lumen (Fig. 4.1C) (Ferguson et al., 2007). The binding sites of MK591 molecules are located in the surface grooves between adjacent monomers within the lipid bilayer and partially overlap with the binding sites of AA (Fig. 4.1B) (Ferguson et al., 2007). Thus, it is hypothesized that laterally diffusing AA molecules can be captured by FLAP, stabilize its trimeric conformation, and then get presented to 5-LO. However, the capture dynamic of AA by FLAP, the transfer route of AA from FLAP to 5-LO, and the conformational changes of FLAP and 5-LO during their interaction have yet to be elucidated.

Although the LTB_4 biosynthesis process is well established, how neutrophils secrete LTB_4 to mediate signal relay is not fully understood. A previous study from our lab discovered that 5-LO and FLAP localize on intracellular vesicles, which are released into the extracellular environment as extracellular vesicles (EVs) that contain LTB_4 and its synthesizing enzymes (Majumdar et al., 2016). Released EVs can further activate neutrophils and induce their

chemotaxis in an LTB_4-dependent manner (Majumdar et al., 2016). Together with the fact that LTB_4 synthesizing enzymes are present at or translocate to the NE in activated neutrophils, it is natural to speculate that intracellular vesicles are formed at the NE. Indeed, using immunofluorescence, we found that membrane buds at the neutrophil NE are enriched for FLAP and 5-LO upon N-formylMethionyl-Leucyl-Phenylalanine (fMLF) stimulation (data shown in figure 1). However, how NE invaginations are initiated and whether the curvature formation is related to the clustering of FLAP and/or 5-LO has not been investigated. Mechanisms that can regulate membrane deformation have been studied, especially during endocytosis and vesicle trafficking (Farsad and De Camilli, 2003; Jarsch et al., 2016; McMahon and Gallop, 2005). One such mechanism is mediated by integral membrane proteins (Alimohamadi and Rangamani, 2018). The oligomerization, protein crowding, or simply the wedge shape of integral membrane proteins is thought to distort the lipid organization and cause membrane curvatures (Alimohamadi and Rangamani, 2018; Chou et al., 2001; Stachowiak et al., 2012). Supporting this notion, dopamine transporter, a transmembrane protein exclusively expressed in dopamine neurons, has been reported to concentrate in the axonal filopodia and maintain the high outward curvature (Caltagarone et al., 2015). In addition, the distribution of voltage-gated ion channels correlates with the local membrane curvature (Aimon et al., 2014). Interestingly, Mittendorf *et al.* demonstrated that when reconstituted into liposomes *in vitro* peripheral myelin protein 22 (PMP22), also a tetraspan helical integral membrane protein topologically like FLAP, can drive the formation of stacked and wrapped “horseshoe-like” membrane structures that share some resemblance to compact myelin membranes in Schwann cells (Mittendorf et al., 2017). Considering the homotrimerizing ability of FLAP, we hypothesize that the clustering or crowding of FLAP trimers leads to membrane curvatures at the NE upon neutrophil activation.

Here we show that upon fMLF stimulation human primary neutrophils generate FLAP-rich buds at the NE within a time frame as short as 2 minutes. To examine the ability of FLAP to induce membrane curvatures, we purified full-length FLAP from *E.coli*, reconstitute FLAP into membranes, and image the membrane organization of the protein:lipid assemblies using negative stain EM and cryo-EM. Our studies provide preliminary evidence on the role of FLAP in altering membrane architecture, which can be critical for effective LTB_4 release and signal relay.

4.3 Results and discussion

4.3.1 Activated neutrophils generate NE buds that are enriched in FLAP and 5-LO

To visualize the localization of FLAP and 5-LO in activated neutrophils, we perform immunostaining of FLAP and 5-LO on naïve or fMLF stimulated human primary neutrophils and examine their distribution using high-resolution fluorescence imaging. As shown in figure 4.2Ai, we observed FLAP distribution on the NE and ER, and 5-LO fluorescence in the cytoplasm as well as inside the cell nucleus in naïve neutrophils (Fig. 4.2Ai, 5-LO column). FLAP and 5-LO do not co-localize. After stimulating neutrophils with fMLF for 2 minutes, we found membrane budding outwards from the nucleus like an arch (Fig. 4.2Aii, FLAP column). Strikingly, the budding membrane region shows a notably higher FLAP fluorescence signal than does the rest of NE membrane (Fig. 4.2Aii, FLAP column and insert image). The magnified view of the budding region demonstrates that 5-LO fluorescence partially overlaps with the FLAP staining, which can be confirmed by the fluorescence plot along the crossing line (Fig. 4.A2ii, insert image and plot). We did not observe nuclei DNA staining in the buds, excluding the possibility that these are micro-nucleus (Fig. 4.2Aii, insert image). Interestingly, upon 5-minute stimulation, we observed dome-shape membrane structures bending away from the neutrophil nucleus (Fig. 4.2Aiii, FLAP column

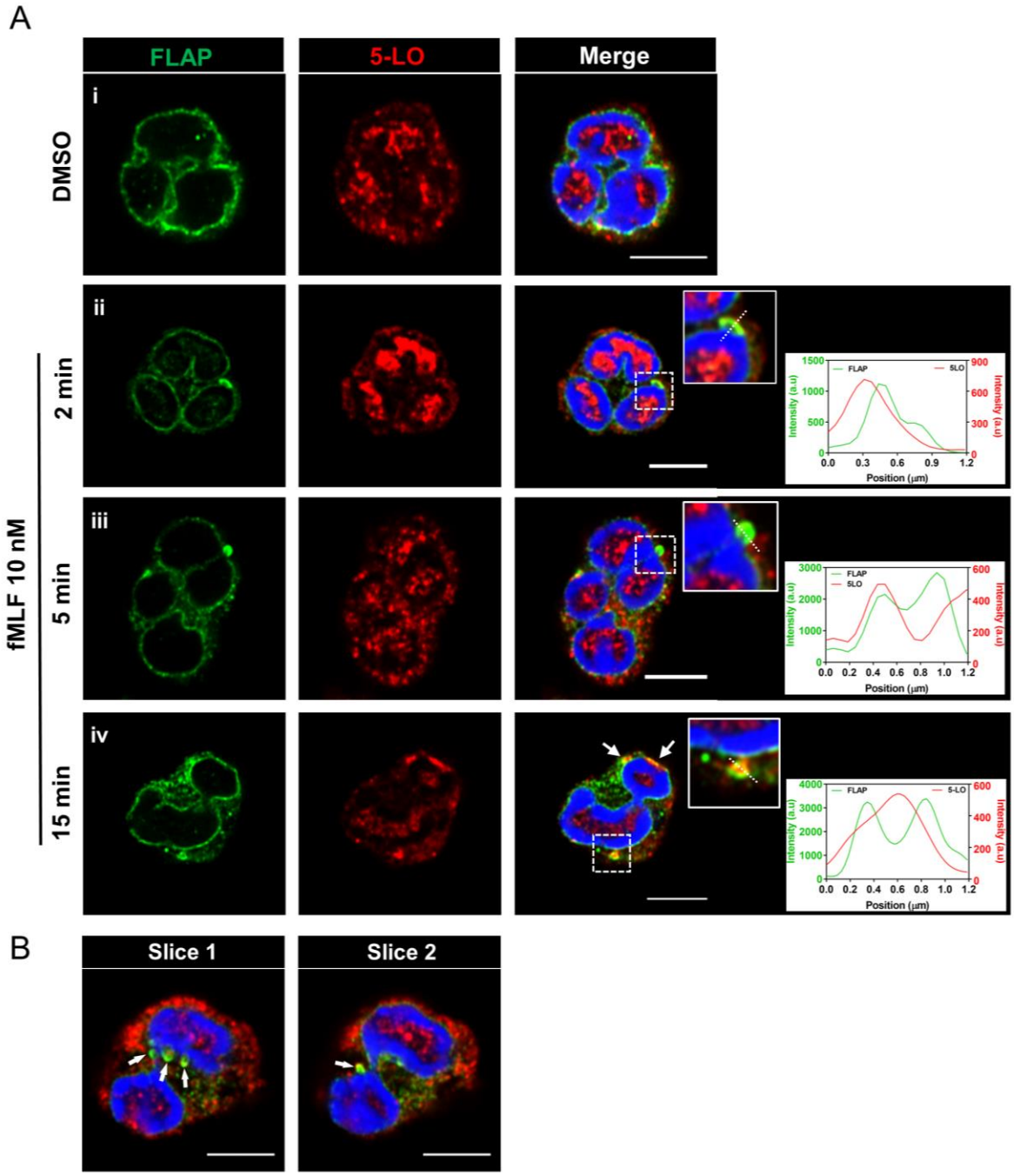

Figure 4.2: Neutrophils generate FLAP and 5-LO enriched budsat the NE upon stimulation. (Ai-iv) Fluorescence images of FLAP (left column), 5-LO (middle column), and merge of these two with DAPI (right column) for neutrophils stimulated with DMSO (i) or 10 nM fMLF for 2 (ii), 5 (iii), and 15 (iv) minutes. The magnified images highlight the budding events at cell nuclei. Images are representatives of four independent experiments. The inserted plots show the fluorescence intensity across the white dash lines in the magnified images. Green and red lines are plots for FLAP and 5-LO respectively. (B) Merge fluorescence images of FLAP, 5-LO, and DAPI for a neutrophil stimulated with 10 nM fMLF for 15 minutes and are selected from two different *z* slices. Images are representatives of four independent experiments.

and insert image). Furthermore, the fluorescence plot along the crossing line illustrates a co-localization of FLAP and 5-LO staining (Fig. 4.2iii, insert plot). After the cells are stimulated for 15 minutes, multiple membrane buds can be seen on the cell nucleus (Fig. 4.2B, white arrows). In addition, we found that some buds are connected to the NE by a narrow neck, potentially suggesting that these buds are about to be released (Fig. 4.2Aiv, FLAP column). Interestingly, these vesicles exhibit high FLAP fluorescence on the membrane but encapsulated 5-LO fluorescence inside them, as seen by the magnified image and fluorescence plot (Fig. 4.2Aiv, insert image and plot). This suggests that 5-LO may be enclosed inside the vesicles during their formation. We also noticed an increase in the co-localization of FLAP and 5-LO on the NE (Fig. 4.2Aiv, white arrows), indicating an active state of the LTB_4 synthesizing machinery. Together, these results show that stimulated neutrophils generate membrane buds at the NE that are enriched in FLAP and 5-LO, and predict that the budding can gradually evolve into a vesicle to be released into the cytoplasm.

Integral membrane proteins are known to mediate membrane organization. While the conical or wedge shape of integral membrane proteins is able to induce local membrane curvature, in some cases the oligomerization state of integral membrane proteins is thought to determine and maintain the scale of membrane bending (Voeltz and Prinz, 2007). Typical examples of this phenomenon are the reticulon (RTN) proteins and F_1F_0-ATP-synthase, important in shaping ER and mitochondrial respectively. The RTN proteins have two closely spaced hairpin transmembrane domains, resulting in a wedge-like shape (Di Sano et al., 2012; Oertle et al., 2003). It has been shown that RTN proteins are sufficient to deform the membrane for ER tubule formation and overexpression of RTN proteins increases the ratio of ER tubules to sheets (Shibata et al., 2010; Shibata et al., 2008). Similarly, the dimers of F_1F_0-ATP-synthase exhibit a conical shape, and are

key in maintaining membrane curvatures on the inner membrane of mitochondria (Dudkina et al., 2006; Everard-Gigot et al., 2005). The crystal structure of FLAP indicates that the functional unit of FLAP is a homotrimer, whose presence in cells has been reported (Ferguson et al., 2007; Mandal et al., 2008). In addition, the crystal structure highlights the cone-like shape of a FLAP homotrimer with a narrower side in the NE lumen but a wider side in cytoplasm or nucleoplasm (Ferguson et al., 2007). Thus, it is possible that upon cell activation assembled and clustered FLAP trimers can distort NE membranes. Interestingly, the oligomerization or clustering of RTN proteins has been shown to stabilize the membrane curvature at ER tubules (Hu et al., 2008; Shibata et al., 2008), also consistent with our observation of FLAP accumulation at the buds. However, it is challenging to rule out the contribution of other proteins to membrane remodeling. For example, we found that in addition to FLAP, 5-LO also co-localizes or stays adjacent to the budding over the time course of neutrophil activation and we have not specifically looked at the localization of other NE integral membrane proteins. Previous studies have demonstrated that the insertion of the hydrophobic tips of the 5-LO C2 domains can generate membrane curvature (Groffen et al., 2010; Martens et al., 2007). Thus, whether FLAP and/or 5-LO plays a role in bending membrane in our setting needs to be further explored.

4.3.2 Characterization of reconstituted protein:lipid assemblies with negative stain EM

To directly test the effect of FLAP on membrane structure, we purify full-length His-tagged FLAP from *E.coli* and reconstitute FLAP into membranes composed of defined lipids. Since FLAP is a transmembrane protein, we find FLAP to be concentrated in *E.coli* membranes, dodecyl β-D-maltopyranoside (DDM) is used for the purification. Figure 4.3A shows a representative SDS-PAGE gel of different fractions eluted from the Ni-NTA resin, stained with coomassie. A band at

~ 18 kDa size can be found in all elutions, with higher amounts in the initial three fractions (Fig. 4.3A). In contrast, we did not observe bands at ~ 18 kDa size in the eluted fractions from the mock purification (Fig. 4.3A), suggesting that the ~ 18 kDa bands are FLAP. Western Blot results with an antibody targeting FLAP or His-tag further confirm the presence of FLAP in these bands (Fig. 4.3B). We also sent the eluted fractions for Mass Spectrometry analysis, showing that FLAP is the most abundant protein in the samples, although there are also other proteins present in both the mock and FLAP purifications (Table 4.1, full list see appendix).

As there are no reports of the lipid composition of human neutrophil nuclei, we decide to reconstitute purified FLAP into a lipid mixture of 1,2-di-oleoyl-sn-glycero-3-phosphocholine (DOPC), C16-ceramide, and egg sphingomyelin (ESM) (molar ration 10:1:1). This lipid mixture is based on previous studies on the lipid composition of the human neutrophil plasma membrane (Iwabuchi et al., 2015; Nakayama et al., 2008). To reconstitute FLAP into membranes, the solubilized lipids and purified FLAP are mixed at a lipid-to-protein ration (LPR) of 1.0 (w/w) and then dialyzed to remove the detergent. This *in vitro* membrane reconstitution assays can result in the formation of lipid-protein assemblies; however, it is important to note that the orientation of FLAP in the lipid bilayer cannot be controlled. This means that the cytoplasmic side of the FLAP can face either the outside or the lumen of the membrane. After dialysis, the protein-membrane mixtures are harvested and analyzed by negative stain EM. Compared to the control reconstitutions without any protein added, *in vitro* lipid reconstitutions done in the presence of FLAP often exhibit some texture, either a stack of lines or stripes (Fig. 4.3Ci & ii). This phenomenon appears to be enhanced by adding MK591 in the dialysis solution to stabilize the FLAP trimers, although this has been difficult to carefully quantify using negative stain analysis (Fig. 4.3Ciii). We also generated a FLAP K116A mutant (the Lysine at the 116 location is mutated to an Alanine) that

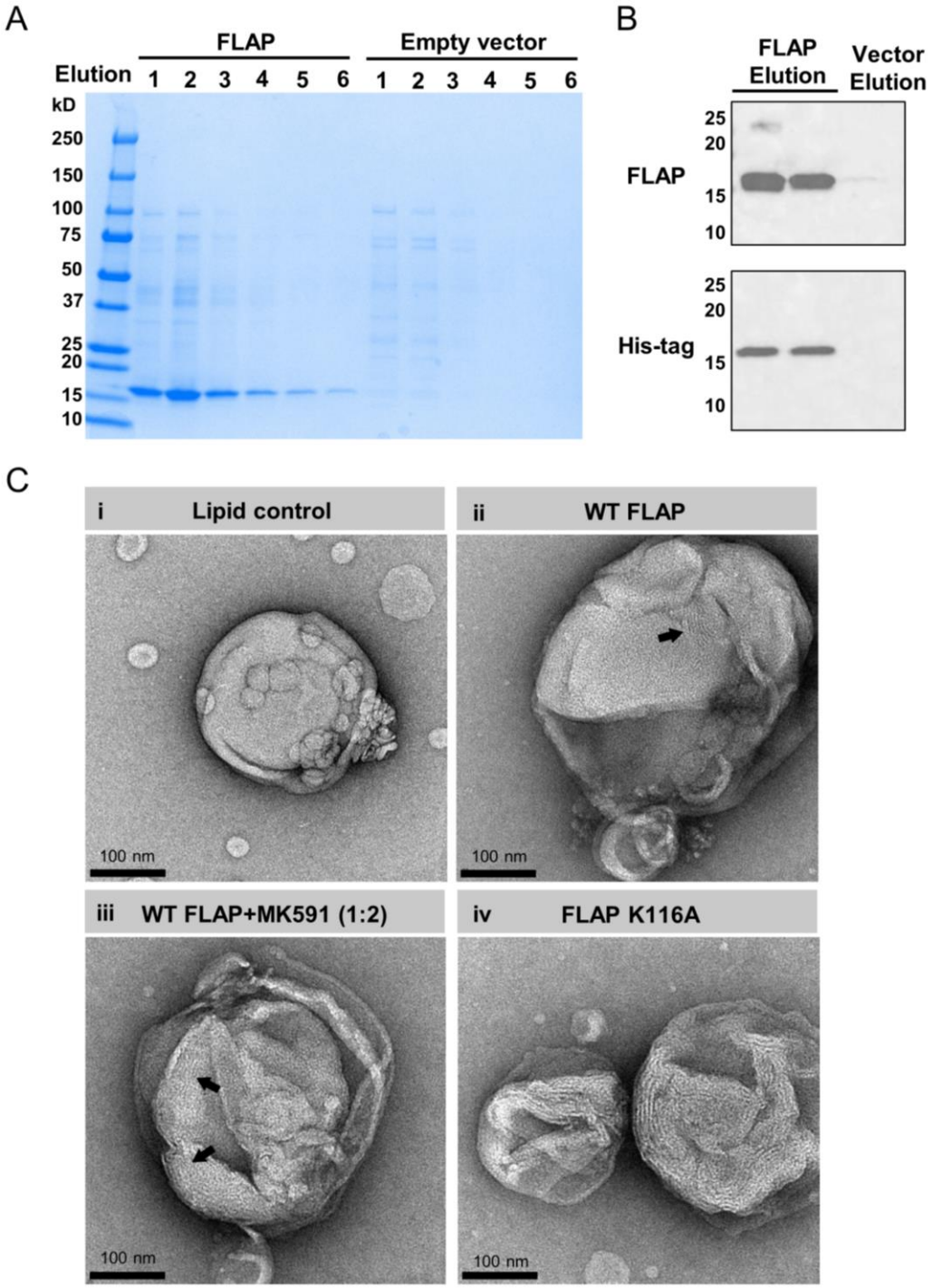

Figure 4.3: The negative stain EM visualization of reconstituted FLAP-lipid structures. (A) SDS-PAGE gel (n > 4) of elutions from Ni-NTA resin for FLAP or empty vector control purification.. (B) WB results (n > 3) of elutions from Ni-NTA resin for FLAP or empty vector control purification. The membrane is stained with either an anti-FLAP (top) or anti-His-tag (bottom) antibody. (Ci-iv) Negative stain EM images of lipid alone reconstitution (i), wide type (WT) FLAP-lipid reconstitution (ii), WT FLAP-lipid reconstitution supplemented with MK591 (iii), and K116A FLAP-lipid reconstitution (iv). The arrows point to the regions with organized lines or stripes. Scale bar: 20 nm. Images are representatives of at least three independent experiments.

Table 4.1: Top 20 proteins that are co-purified with FLAP

		Spectral Counts*	
Identified Proteins	**Gene Name**	**Sample 1**	**Sample 2**
Arachidonate 5-lipoxygenase-activating protein OS=Homo sapiens	ALOX5AP	660	801
Efflux pump membrane transporter OS=Escherichia coli	acrB	273	126
Chaperone protein DnaK OS=Escherichia coli	dnaK	271	269
Chaperone protein DnaJ OS=Escherichia coli	dnaJ	216	45
Glutamine--fructose-6-phosphate aminotransferase OS=Escherichia coli	glmS	187	294
Elongation factor Tu OS=Escherichia coli	tufB	163	138
Ubiquinol oxidase subunit 2 OS=Escherichia coli	cyoA	151	156
ATP-dependent zinc metalloprotease FtsH OS=Escherichia coli		142	85
Cell division protein FtsA OS=Escherichia coli	ftsA	124	159
Bifunctional polymyxin resistance protein ArnA OS=Escherichia coli	yfbG	117	82
L-lactate dehydrogenase OS=Escherichia coli	lldD	111	66
ATP-dependent Clp protease ATP-binding subunit ClpX OS=Escherichia coli	clpX	110	112
2-oxoglutarate dehydrogenase, E1 subunit OS=Escherichia coli	sucA	106	124
60 kDa chaperonin OS=Escherichia coli	groL	102	25
Phosphocarrier, HPr family OS=Escherichia coli	fruB	95	140
Transcriptional regulator, Crp/Fnr family OS=Escherichia coli	crp	89	18
Cytochrome o ubiquinol oxidase, subunit I OS=Escherichia coli	cyoB	88	85
PTS system, fructose subfamily, IIC subunit OS=Escherichia coli	fruA	88	56
Alanine--tRNA ligase OS=Escherichia coli	alaS	86	32
Cell division protein ZipA OS=Escherichia coli	zipA	85	89

**. Results are filtered to retain proteins with ≤ 1% False Discovery Rate (FDR) confidence then sorted based on their PSM value from sample 1, which is renamed as Spectral Counts.*

has been reported to have a ~80 fold higher affinity to AA. When the K116A FLAP is used in the *in vitro* lipid reconstitution assay, we also saw that the formation of organized lines in the protein-membrane structures is increased, even in the absence of MK591 (Fig. 4.3Civ). Although these observations appear promising, we are hesitant to draw conclusions from these results because of the pitfalls of negative stain EM: (1) the 3D architecture of the protein-membrane structures cannot be preserved due to the addition of the stain solution, and (2) the difficulty to assess the luminal organization of the structures.

4.3.3 FLAP reconstituted protein:lipid assemblies form "wagon-wheel" like structures visualized by cryo-EM

Due to the drawbacks of negative stain EM, we next vitrify the *in vitro* membrane reconstitution assays and visualize the results using cryo-EM. We found both unilamellar and multilamellar vesicles in the control reconstitutions either containing lipids alone or an empty vector purification (Fig. 4.4A & B). Interestingly, cryo-EM imaging of the vitrified FLAP-lipid reconstitutions shows some examples of assemblies with two membrane layers and what looks like multiple protrusions between two layers that resemble a wagon wheel (Fig. 4.4C). Thus, these FLAP-lipid assemblies are termed "wagon-wheel" structures. The magnified views of the "wagon-wheel" structures highlight that the protruding regions are electron-dense (Fig. 4.4C, inserts), which can suggest protein clustering. These preliminary analyses suggest that FLAP may be able to alter the membrane structure during *in vitro* membrane reconstitution. Measurements on four "wagon-wheel" structures observed so far demonstrate that they have a uniform diameter of 107.6 ± 13.2 nm and an inter-membrane distance of 30.3 ± 1.5 nm, in contrast to the variable size of the unilamellar and multilamellar vesicles. However, additional experiments are needed to carefully

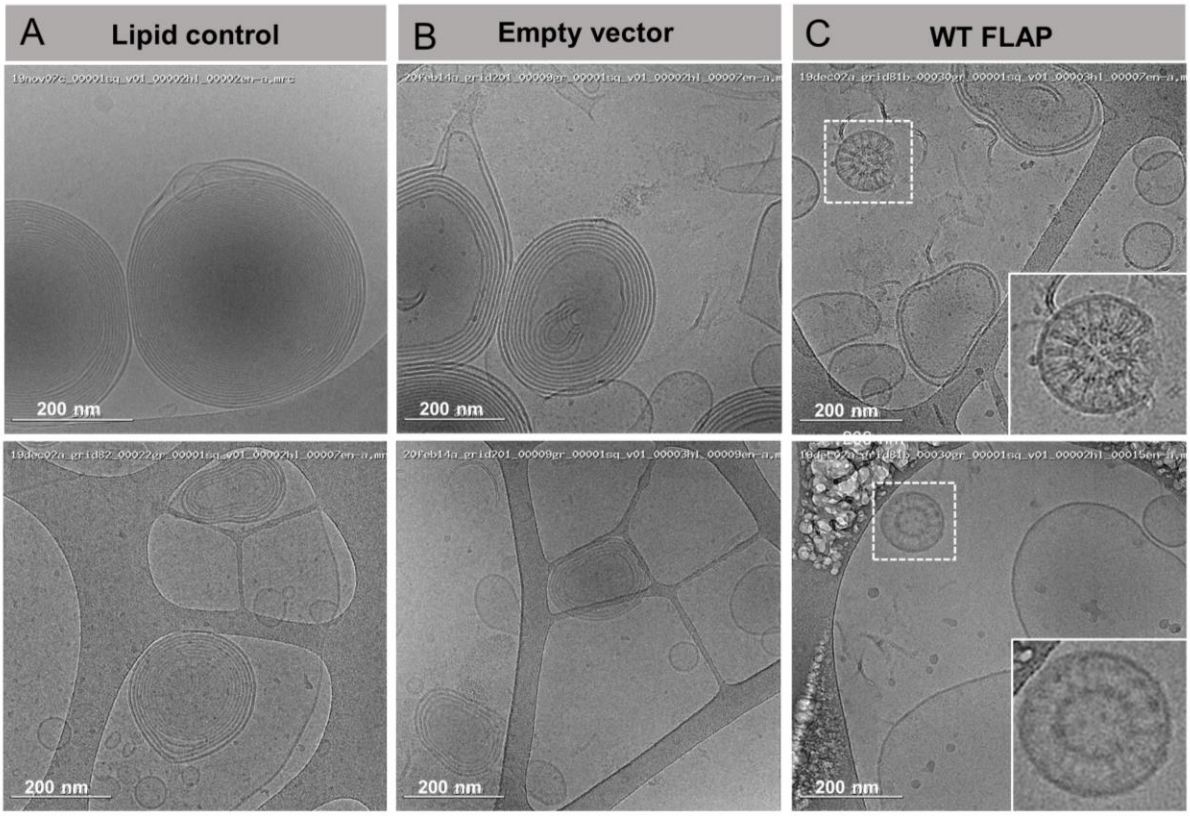

Figure 4.4: Cryo-EM reviews "wagon-wheel" structures in FLAP-lipid reconstitution. (A-C) Cryo-EM images of lipid alone reconstitution (A), bacterial protein-lipid reconstitution (B), and wide type (WT) FLAP-lipid reconstitution (C). The inserts are magnified images of the "wagon-wheel" structures. Scale bar: 200 nm. Images were obtained from one experiment.

quantify these observations. It is worthwhile to note that the percentage of the "wagon-wheel" structures in the whole lipid reconstitution assays, although reproducible, appears to be relatively low, suggesting that we do not currently understand all the requirements for this membrane remodeling. Thus, there are a number of parameters that need to be fully examined and quantification of the different structures seen in our reconstitution experiments needs to be done. For example, the lipid composition and LPR during reconstitutions need to be further optimized and it is also possible that the addition of MK591 and/or 5-LO may also be important parameters to add to our reconstitution assay.

Importantly, the neutrophil NE is much more complex than an *in vitro* lipid mixture. It is likely that in the context of a cell there are additional lipid species or proteins at the budding regions. For example, we have reported the crucial role of sphingomyelinase 2, an enzyme that converts sphingomyelin into various ceramides, in NE budding generation, which suggests the requirement of a combination of multiple ceramide species (Majumdar et al., 2016). Finally, as mentioned, because the orientation of FLAP in the lipid-protein assemblies cannot be controlled, it is possible that interactions between FLAP proteins in a direction vertical to the membranes also contribute to the high curvature that we observed in the "wagon-wheel" structures. However, our observation that FLAP alone appears to alter membrane architecture in the context of an *in vitro* lipid reconstitution assays, suggests that it plays an important role in the membrane remodeling of the NE during neutrophil chemotaxis.

4.4 Conclusions

LTB_4-mediated signal replay plays a central role in amplifying the recruitment of neutrophils in response to infections. Although the LTB_4 biosynthesis process has been well

studied, the mechanisms by which LTB_4 is released and how gradients are formed is far from clear. Our immunostaining results, in combination with previous findings, demonstrate that fMLF-stimulated neutrophils generate FLAP- and 5-LO enriched budding vesicles at the nuclei, which potentially represent the source of LTB_4-containing EVs for the generation of the secondary gradient. To directly test the hypothesis that the clustering of trimeric FLAP alters membrane organization *in vitro*, we perform lipid-FLAP reconstitutions and visualize the products using negative stain EM and cyro-EM. The initial negative stain imaging provides preliminary evidence that FLAP can alter membrane organization, and the ultrastructural analysis using cryo-EM further reveals the presence of "wagon-wheel" like lipid-protein assemblies that appear to be unique in the FLAP reconstitutions. Although more experiments are needed to validate the effects of FLAP in the *in vitro* lipid reconstitutions and ultimately determine the 3D architecture of the "wagon-wheel" structures, the present results suggest that FLAP has the ability to alter membrane organization and induce curvature *in vitro*. Our study will be the first to uncover a structural role of FLAP in membrane reorganization, a function that could have important mechanistic implications in LTB_4 release during neutrophil chemotaxis.

4.5 Materials and methods

Cloning and Protein expression in E.coli: pCDH-FLAP-GFP was used as the donor plasmid to amplify the human FLAP (NM_001639, initially purchased from Origene) full sequence. pCDH-FLAP-GFP plasmid has been previously used for functional studies in our laboratory. The FLAP gene sequence was optimized for bacterial expression and was PCR-amplified using the forward primer 5'-ATACCATGGGCATGGATCAAGAAACTGTAGGC-3' and reverse primer 5'-CGGGATCCTTAATGATGATGATGATGATGATGGGGAATGAGAAGTAGAGGG-3' to

introduce a non-cleavable C-terminal hexahistidine tag following the full-length FLAP sequence. The resulting PCR products were digested with NcoI and BamHI-HF (New England Biolabs) at 37℃ for 20 min and ligated into vector pET28a, generating a recombinant plasmid pET28a-FLAP-7xHis. Bacteria expression pET28-FLAP-7xHis plasmid was transformed into BL21 Rosetta (DE3) cells (Novagen) following the manufacture's protocol. Transformed cells were plated on LB agar plates with kanamycin. After cultured overnight, all colonies were scraped from each plate, and cells were allowed to grow in LB supplemented with kanamycin at 37°C until OD_{600} reached ~ 1. Then, FLAP expression was induced by the addition of 1.5 mM isopropyl β-d-1-thiogalactopyranoside (IPTG, GOLDBIO) at 30°C for 1.5 hours. Bacterial cells were harvested by centrifugation, flash-frozen in dry ice-cooled ethanol, and stored in -80°C until use.

Purification of FLAP from E.coli: Bacterial pellets were thawed on ice, resuspended in lysis buffer that contains 20 mM Tris–HCl pH 7.4, 50 mM NaCl, 10% (v/v) glycerol, 1 mM Tris(2-carboxyethyl)phosphine hydrochloride (TCEP) and EDTA-free protease-inhibitor tablets (Roche), and lysed using an EmulsiFlex-C5 system (Avestin). Unlysed cells were removed by centrifugation at 7000 rpm for 30 min at 4°C. The supernatant was transferred to a new conical tube, and cell membranes were pelleted by centrifugation at 35,000 g for 2.5 hr at 4°C and resuspended in lysis buffer using a dounce tissue grinder. FLAP was solubilized by adding 2% (w/v) dodecyl β-D-maltopyranoside (DDM; Anatrace) for 45 min at room temperature with gentle agitation and lipids were pelleted again by centrifugation at 40 000g for 30 min at 4°C. The supernatant contains His-tagged FLAP was mixed with 1 mL Ni-NTA agarose (Qiagen) for 1 hr at 4°C. The slurry was loaded into a gravity column to drain liquid and the resin was washed with 20 mM Tris–HCl pH 7.4, 150 mM NaCl, 20 mM imidazole, 1 mM TCEP, 10% (v/v) glycerol, and

0.1% (w/v) DDM. FLAP was eluted with 20 mM Tris-HCl pH 7.5, 50 mM NaCl, 250 mM imidazole, 1 mM TCEP, 10%(v/v) glycerol and 0.1% DDM for 4 to 6 time. The elutions containing the majority of FLAP were pooled and concentrated to 1 mg/mL using Amicon Ultra 15 10,000 NMW (Millipore). FLAP was further purified by gelfiltration chromatography using a Superdex 200 column (GE Healthcare). FLAP-containing fractions were pooled and concentrated again to 1 mg/mL.

Reconstitution of FLAP into membranes: Purified FLAP (1 mg/mL) was mixed with lipid-detergent micelles containing 5.3 mM DOPC (Avanti Polar Lipids), 0.53 mM ESM (Sigma), 0.53 mM C16-ceramide (Cayman), and 53 mM DDM in water at 1.0 LPR. The protein-lipids mixed solution was pipetted into dialysis buttons (Hampton Research), and the buttons were covered by a hydrated dialysis membrane with a molecular weight cutoff of 20 kDa (Spectra/Por Biotech RC Tubing) that had been boiled in 1mM EDTA for 5 min to remove metal ions. Buttons were dialyzed for 7 days at room temperature against the dialysis buffer containing 10mM tris (pH 8.0), 150 mM NaCl, and 0.5 mM EDTA, which was changed every 3 days. For the lipid alone control, FLAP elution buffer was used and all procedures were the same as above.

EM visualization of FLAP-lipid reconstitutions: To prepare negative stain grids, 3 μL of diluted FLAP-lipids assemblies were absorbed into a glow-discharged 200-mesh copper grid. Grids were washed in two drops of water and stained with two drops of uranyl formate (0.75%) (Electron Microscopy Sciences). After which, grids were imaged using an FEI Morgagni equipped with a 1000 × 1000 charge-coupled device (CCD) camera (Advanced Microscopy Techniques). For cryo-EM, 3 μL of diluted FLAP-lipids assemblies was pipetted on to glow-discharged Quantifoil

R2/2 Holey Carbon (200-mesh copper) grids (Electron Microscopy Sciences) and plunged into liquid ethane using a Vitrobot (2007, FEI) set to 100% humidity at room temperature. Images were collected using a Glacios Transmission Electron Microscope (Thermo Scientific).

SDS-PAGE and Western blot: The protein concentration of each sample was measured by a Nanodrop 2000 spectrophotometer (Thermo Fisher Scientific), and the required volume of each sample was calculated based on the needed protein amount. After the addition of 6x Laemmli reducing SDS sample buffer (Alfa Aesar), each sample was boiled at 95°C for 2 min and loaded to a 4-12% Bis-Tris gel (Thermo Fisher Scientific). The SDS-PAGE gel was stained by Imperial Protein Stain (Thermo Fisher Scientific) for 1.5 hours at room temperature, washed with DI water, and imaged by an Azure imaging system. For WB, the proteins were transferred to a nitrocellulose membrane (Thermo Fisher Scientific) using a mini blot module (Thermo Fisher Scientific). After blocked with 5% milk in TBST buffer for 1.5 hours at room temperature, the membrane was incubated with rabbit anti-FLAP antibody (1:1500 in 3% milk, ab85227 Abcam) overnight at 4°C. On the next day, the membrane was incubated with an HRP-conjugated anti-rabbit secondary antibody (Jackson Immuno Research) for 1 hour at room temperature, developed with SuperSignal chemiluminescent substrate (Thermo Fisher Scientific), and imaged with an Azure imaging system.

4.6 Appendix

The list of proteins that are present in FLAP purifications

		Spectral Count*	
Identified Proteins	**Gene Name**	**Sample 1**	**Sample 2**
Arachidonate 5-lipoxygenase-activating protein OS=Homo sapiens	ALOX5AP	660	801
Efflux pump membrane transporter OS=Escherichia coli	acrB	273	126
Chaperone protein DnaK OS=Escherichia coli	dnaK	271	269
Chaperone protein DnaJ OS=Escherichia coli	dnaJ	216	45
Glutamine--fructose-6-phosphate aminotransferase OS=Escherichia coli	glmS	187	294
Elongation factor Tu OS=Escherichia coli	tufB	163	138
Ubiquinol oxidase subunit 2 OS=Escherichia coli	cyoA	151	156
ATP-dependent zinc metalloprotease FtsH OS=Escherichia coli		142	85
Cell division protein FtsA OS=Escherichia coli	ftsA	124	159
Bifunctional polymyxin resistance protein ArnA OS=Escherichia coli	yfbG	117	82
L-lactate dehydrogenase OS=Escherichia coli	lldD	111	66
ATP-dependent Clp protease ATP-binding subunit ClpX OS=Escherichia coli	clpX	110	112
2-oxoglutarate dehydrogenase, E1 subunit OS=Escherichia coli	sucA	106	124
60 kDa chaperonin OS=Escherichia coli	groL	102	25
Phosphocarrier, HPr family OS=Escherichia coli	fruB	95	140
Transcriptional regulator, Crp/Fnr family OS=Escherichia coli	crp	89	18
Cytochrome o ubiquinol oxidase, subunit I OS=Escherichia coli	cyoB	88	85
PTS system, fructose subfamily, IIC subunit OS=Escherichia coli	fruA	88	56
Alanine--tRNA ligase OS=Escherichia coli	alaS	86	32
Cell division protein ZipA OS=Escherichia coli	zipA	85	89
Protein translocase subunit SecA OS=Escherichia coli	secA	84	39

Pyruvate dehydrogenase E1 component OS=Escherichia coli	aceE	83	93
NAD(P) transhydrogenase subunit alpha OS=Escherichia coli	pntA	83	47
Cell shape determining protein, MreB/Mrl family OS=Escherichia coli	mreB	80	59
ATP-dependent protease ATPase subunit HslU OS=Escherichia coli	hslU	79	77
Aldehyde-alcohol dehydrogenase OS=Escherichia coli	adhE	75	50
FAD-dependent pyridine nucleotide-disulphide oxidoreductase OS=Escherichia coli	ndh	74	53
Peptidyl-prolyl cis-trans isomerase OS=Escherichia coli	slyD	73	53
Small heat shock protein IbpA OS=Escherichia coli	ibpA	71	27
Undecaprenyl-phosphate 4-deoxy-4-formamido-L-arabinose transferase OS=Escherichia coli	yfbF	66	74
NADH-quinone oxidoreductase OS=Escherichia coli	nuoG	61	97
Methionine import ATP-binding protein MetN OS=Escherichia coli	metN	59	80
NADH-quinone oxidoreductase subunit C/D OS=Escherichia coli	nuoC	59	40
Site-specific DNA-methyltransferase (Adenine-specific) OS=Escherichia coli	hsdM	58	49
Ferric uptake regulation protein OS=Escherichia coli	fur	58	19
Alkyl hydroperoxide reductase, F subunit OS=Escherichia coli		56	79
Chaperone protein HtpG OS=Escherichia coli	htpG	55	78
Dihydrolipoyl dehydrogenase OS=Escherichia coli	lpdA	55	46
ATP-dependent Clp protease, ATP-binding subunit clpA OS=Escherichia coli	clpA	55	28
Small heat shock protein IbpB OS=Escherichia coli	ibpB	54	29
Succinate dehydrogenase flavoprotein subunit OS=Escherichia coli	sdhA	54	20
ATP synthase subunit beta OS=Escherichia coli	atpD	54	19
Ribonuclease E OS=Escherichia coli	rne	54	16
Cell division ATP-binding protein FtsE OS=Escherichia coli		53	14
Endopeptidase La OS=Escherichia coli	ycbZ	52	3
UspA domain protein OS=Escherichia coli	ybdQ	50	10
Chaperone protein ClpB OS=Escherichia coli	clpB	47	66
RNA polymerase-associated protein RapA OS=Escherichia coli	hepA	47	2
Cyclopropane-fatty-acyl-phospholipid synthase OS=Escherichia coli	cfa	46	50
Protein translocase subunit SecD OS=Escherichia coli		46	28
30S ribosomal protein S1 OS=Escherichia coli	rpsA	46	26
Co-chaperone protein DjlA OS=Escherichia coli	djlA	46	24
Sulfate/thiosulfate import ATP-binding protein CysA OS=Escherichia coli	cysA	46	14
Protein TolA OS=Escherichia coli	tolA	46	11

Aerobic respiration control sensor protein OS=Escherichia coli	arcB	45	1
Phosphoglycerol transferase I OS=Escherichia coli	mdoB	44	41
Magnesium-translocating P-type ATPase OS=Escherichia coli	mgtA	44	23
Ribosomal RNA small subunit methyltransferase I OS=Escherichia coli	yraL	43	49
Phosphoenolpyruvate synthase OS=Escherichia coli	pps	43	30
Histidine kinase OS=Escherichia coli	ygiY	43	27
30S ribosomal protein S2 OS=Escherichia coli	rpsB	43	16
Soluble pyridine nucleotide transhydrogenase OS=Escherichia coli	udhA	42	27
Histidine kinase OS=Escherichia coli	rstB	41	50
NADH-quinone oxidoreductase subunit F OS=Escherichia coli	nuoF	40	65
DNA polymerase III subunit gamma/tau OS=Escherichia coli	dnaX	40	40
Transcription termination factor Rho OS=Escherichia coli	rho	40	12
Ubiquinone biosynthesis hydroxylase, UbiH/UbiF/VisC/COQ6 family OS=Escherichia coli	ubiH	40	6
Sec translocon accessory complex subunit YajC OS=Escherichia coli	yajC	39	61
Sec-independent protein translocase protein TatA OS=Escherichia coli	tatA	39	41
Glutamate-1-semialdehyde 2,1-aminomutase OS=Escherichia coli	hemL	39	35
Efflux transporter, RND family, MFP subunit OS=Escherichia coli	acrA	39	29
NAD(P) transhydrogenase subunit beta OS=Escherichia coli	pntB	39	28
ABC transporter related OS=Escherichia coli	mglA	38	52
Copper-translocating P-type ATPase OS=Escherichia coli	copA	38	22
(P)ppGpp synthetase I, SpoT/RelA OS=Escherichia coli	relA	38	15
Diamine N-acetyltransferase OS=Escherichia coli	speG	38	5
D-amino acid dehydrogenase OS=Escherichia coli	dadA	37	48
Hydrogenase (NiFe) small subunit HydA OS=Escherichia coli	hybO	37	32
ATP synthase subunit alpha OS=Escherichia coli	atpA	37	17
Uncharacterized protein OS=Escherichia coli	yfcH	37	9
HemY protein OS=Escherichia coli	hemY	37	7
Iron-sulfur cluster binding protein OS=Escherichia coli	ykgF	36	52
Uncharacterized protein OS=Escherichia coli	ydgA	36	52
Heavy metal translocating P-type ATPase OS=Escherichia coli		36	30
Acetate kinase OS=Escherichia coli	ackA	36	24
Transcriptional regulator, PadR-like family OS=Escherichia coli	yqjI	36	20

Acetyl-coenzyme A carboxylase carboxyl transferase subunit beta OS=Escherichia coli	accD	36	19
Ferrous iron transport protein B OS=Escherichia coli		35	17
Dihydrolipoyllysine-residue succinyltransferase component of 2-oxoglutarate dehydrogenase complex OS=Escherichia coli	sucB	35	5
Acetyl-coenzyme A carboxylase carboxyl transferase subunit alpha OS=Escherichia coli	accA	34	21
Beta-lactamase OS=Escherichia coli	dacA	33	61
Keratin, type II cytoskeletal 1 OS=Homo sapiens	KRT1	33	36
Lipid-A-disaccharide synthase OS=Escherichia coli	lpxB	33	33
Sensor protein OS=Escherichia coli	narX	33	16
Pyruvate kinase OS=Escherichia coli	pykA	32	43
Sec-independent protein translocase protein TatB OS=Escherichia coli	tatB	32	32
Glycosyl transferase group 1 OS=Escherichia coli	wbbC	32	21
Biosynthetic arginine decarboxylase OS=Escherichia coli	speA	32	6
GMP synthase (glutamine-hydrolyzing) OS=Escherichia coli	guaA	31	42
Penicillin-binding protein, 1A family OS=Escherichia coli	mrcA	31	31
Cell division protein ZapE OS=Escherichia coli	yhcM	31	16
Transporter-associated region OS=Escherichia coli	ybeX	30	32
Chromosomal replication initiator protein DnaA OS=Escherichia coli	dnaA	30	17
Sulfate adenylyltransferase subunit 1 OS=Escherichia coli	cysN	30	16
UPF0227 protein YcfP OS=Escherichia coli	ycfP	30	9
Lipopolysaccharide core heptose(II)-phosphate phosphatase OS=Escherichia coli	ais	30	2
OmpA domain protein transmembrane region-containing protein OS=Escherichia coli	ompA	29	45
Sulfatase OS=Escherichia coli	eptA	29	33
Zinc metalloprotease OS=Escherichia coli	rseP	29	31
Keratin, type I cytoskeletal 10 OS=Homo sapiens	KRT10	29	29
ATP synthase subunit b OS=Escherichia coli	atpF	29	21
Ubiquinone/menaquinone biosynthesis C-methyltransferase UbiE OS=Escherichia coli	ubiE	28	33
Cysteine desulfurase IscS OS=Escherichia coli	iscS	28	24
Uncharacterized protein OS=Escherichia coli	ybeL	28	22
Cell division protein FtsQ OS=Escherichia coli	ftsQ	28	20
50S ribosomal protein L2 OS=Escherichia coli	rplB	28	7
Protein HflK OS=Escherichia coli	hflK	28	5
Triosephosphate isomerase OS=Escherichia coli	tpiA	28	
Acetylornithine deacetylase OS=Escherichia coli	argE	27	29
Keratin, type I cytoskeletal 9 OS=Homo sapiens	KRT9	27	24

Membrane protein insertase YidC OS=Escherichia coli	yidC	27	23
Cytoskeleton protein RodZ OS=Escherichia coli	rodZ	27	19
Ribonucleoside-diphosphate reductase OS=Escherichia coli	nrdA	27	16
4Fe-4S ferredoxin iron-sulfur binding domain protein OS=Escherichia coli	hybA	27	16
Uncharacterized protein OS=Escherichia coli		27	9
30S ribosomal protein S10 OS=Escherichia coli	rpsJ	27	9
Heavy metal efflux pump, CzcA family OS=Escherichia coli	cusA	27	9
Putative transferase OS=Escherichia coli	yrdA	27	1
MscS Mechanosensitive ion channel OS=Escherichia coli	yjeP	27	
Anaerobic ribonucleoside-triphosphate reductase OS=Escherichia coli	nrdD	26	25
Citrate synthase OS=Escherichia coli	gltA	26	25
Pyridoxine/pyridoxamine 5'-phosphate oxidase OS=Escherichia coli	pdxH	26	3
30S ribosomal protein S3 OS=Escherichia coli	rpsC	26	
50S ribosomal protein L13 OS=Escherichia coli	rplM	26	
UDP-glucose 6-dehydrogenase OS=Escherichia coli	ugd	25	30
NADH-quinone oxidoreductase, E subunit OS=Escherichia coli	nuoE	25	29
Uncharacterized protein OS=Escherichia coli	ygdH	25	23
NAD-dependent epimerase/dehydratase OS=Escherichia coli		25	16
Outer membrane protein assembly factor BamA OS=Escherichia coli	bamA	25	14
Bifunctional protein PutA OS=Escherichia coli	putA	25	4
Bifunctional protein Aas OS=Escherichia coli	aas	25	
1-deoxy-D-xylulose-5-phosphate synthase OS=Escherichia coli	dxs	24	34
Probable Sec-independent protein translocase protein TatE OS=Escherichia coli	tatE	24	33
ABC transporter related OS=Escherichia coli		24	13
Cardiolipin synthase A OS=Escherichia coli	cls	24	13
Bifunctional uridylyltransferase/uridylyl-removing enzyme OS=Escherichia coli	glnD	23	43
Phosphate-specific transport system accessory protein PhoU OS=Escherichia coli	phoU	23	41
Threonine--tRNA ligase OS=Escherichia coli	thrS	23	32
UPF0283 membrane protein YcjF OS=Escherichia coli	ycjF	23	28
Probable 4-deoxy-4-formamido-L-arabinose-phosphoundecaprenol deformylase ArnD OS=Escherichia coli	yfbH	23	27
Rhodanese domain protein OS=Escherichia coli	yibN	23	22
Diguanylate cyclase/phosphodiesterase with extracellular sensor OS=Escherichia coli	yhjK	23	21
Biotin carboxylase OS=Escherichia coli	accC	23	8

Histidine kinase OS=Escherichia coli	barA	23	7
30S ribosomal protein S5 OS=Escherichia coli	rpsE	23	6
Pseudouridine synthase OS=Escherichia coli	rsuA	23	5
Cytoplasmic chaperone TorD family protein OS=Escherichia coli	ycdY	22	38
L-serine dehydratase 1 OS=Escherichia coli	sdaB	22	33
Keratin, type II cytoskeletal 2 epidermal OS=Homo sapiens	KRT2	22	17
Two component transcriptional regulator, winged helix family OS=Escherichia coli		22	12
Acetyltransferase component of pyruvate dehydrogenase complex OS=Escherichia coli	aceF	22	11
Uridine kinase OS=Escherichia coli	udk	22	11
Aminotransferase class I and II OS=Escherichia coli	yfdZ	22	3
UDP-N-acetylmuramate--L-alanyl-gamma-D-glutamyl-meso-2,6-diaminoheptandioate ligase OS=Escherichia coli	mpl	21	51
DNA gyrase subunit B OS=Escherichia coli	gyrB	21	28
Peptidylprolyl isomerase OS=Escherichia coli	ppiD	21	24
Putative PTS IIA-like nitrogen-regulatory protein PtsN OS=Escherichia coli	gatA	21	23
Succinate dehydrogenase iron-sulfur subunit OS=Escherichia coli	sdhB	21	20
ABC transporter related OS=Escherichia coli	fepC	21	13
17 kDa surface antigen OS=Escherichia coli	slyB	21	10
Cell divisionFtsK/SpoIIIE OS=Escherichia coli	ftsK	21	7
50S ribosomal protein L6 OS=Escherichia coli	rplF	21	1
Guanosine-5'-triphosphate,3'-diphosphate pyrophosphatase OS=Escherichia coli	gppA	20	33
UDP-N-acetylmuramoyl-L-alanyl-D-glutamate--2,6-diaminopimelate ligase OS=Escherichia coli	murE	20	28
Phosphomethylpyrimidine kinase OS=Escherichia coli	thiD	20	27
DNA polymerase III, delta subunit OS=Escherichia coli	holA	20	24
Alpha/beta hydrolase fold protein OS=Escherichia coli	yheT	20	21
Glutathione-regulated potassium-efflux system protein KefC OS=Escherichia coli	kefC	20	18
Ribose-phosphate pyrophosphokinase OS=Escherichia coli		20	17
Fructose-1,6-bisphosphatase class 1 OS=Escherichia coli	fbp	20	8
50S ribosomal protein L5 OS=Escherichia coli	rplE	20	5
50S ribosomal protein L9 OS=Escherichia coli	rplI	20	3
Zinc import ATP-binding protein ZnuC OS=Escherichia coli	znuC	20	1
Elongation factor G OS=Escherichia coli	fusA	19	27
Histidine kinase OS=Escherichia coli		19	26
Uncharacterized protein OS=Escherichia coli	ytfL	19	25

Transcriptional regulator, LacI family OS=Escherichia coli		19	17
Protein RecA OS=Escherichia coli	recA	19	17
Probable cytosol aminopeptidase OS=Escherichia coli	pepA	19	16
Trigger factor OS=Escherichia coli	tig	19	14
DNA helicase OS=Escherichia coli	helD	19	13
NADH-quinone oxidoreductase subunit I OS=Escherichia coli	nuoI	19	12
Carbamoyl-phosphate synthase large chain OS=Escherichia coli	carB	19	9
RNA polymerase sigma factor RpoD OS=Escherichia coli	rpoD	19	8
DNA-directed RNA polymerase subunit beta' OS=Escherichia coli	rpoC	19	
Uncharacterized protein OS=Escherichia coli	ykgG	18	34
Signal transduction histidine kinase, LytS OS=Escherichia coli	ypdA	18	29
FxsA cytoplasmic membrane protein OS=Escherichia coli	fxsA	18	18
Cobalamin synthesis protein P47K OS=Escherichia coli	yeiR	18	17
Cell division protein FtsB OS=Escherichia coli	ftsB	18	14
Periplasmic serine endoprotease DegP-like OS=Escherichia coli	degP	18	14
Cell division protein FtsL OS=Escherichia coli	ftsL	18	13
TrkA-N domain protein OS=Escherichia coli	trkA	18	12
UDP-N-acetylmuramate--L-alanine ligase OS=Escherichia coli	murC	18	11
NADH-quinone oxidoreductase subunit B OS=Escherichia coli	nuoB	18	9
DNA-directed RNA polymerase subunit alpha OS=Escherichia coli	rpoA	18	7
50S ribosomal protein L1 OS=Escherichia coli	rplA	18	1
DNA-directed RNA polymerase subunit beta OS=Escherichia coli	rpoB	18	
Quinone-dependent D-lactate dehydrogenase OS=Escherichia coli	dld	17	33
Dual-specificity RNA methyltransferase RlmN OS=Escherichia coli	yfgB	17	25
Chorismate mutase OS=Escherichia coli	pheA	17	25
Ribosomal protein S12 methylthiotransferase RimO OS=Escherichia coli	rimO	17	23
Uncharacterized protein OS=Escherichia coli	dcrB	17	23
Formate acetyltransferase OS=Escherichia coli	pflB	17	22
Histidine kinase OS=Escherichia coli	cpxA	17	18
PTS system, trehalose-specific IIBC subunit OS=Escherichia coli	treB	17	17
Lipoyl synthase OS=Escherichia coli	lipA	17	11
Tyrosine recombinase XerD OS=Escherichia coli	xerD	17	10
Dihydrofolate synthase/folylpolyglutamate synthase OS=Escherichia coli	folC	17	10

Glyceraldehyde-3-phosphate dehydrogenase OS=Escherichia coli	gapA	17	9
Rod shape-determining protein MreC OS=Escherichia coli	mreC	17	8
Hpt sensor hybrid histidine kinase OS=Escherichia coli	evgS	17	5
Methionine synthase OS=Escherichia coli	metH	17	4
50S ribosomal protein L3 OS=Escherichia coli	rplC	17	1
ATP-dependent RNA helicase RhlB OS=Escherichia coli	rhlB	17	
30S ribosomal protein S7 OS=Escherichia coli	rpsG	17	
Glycerol-3-phosphate acyltransferase OS=Escherichia coli	plsB	17	
Glucans biosynthesis glucosyltransferase H OS=Escherichia coli		17	
Cell division protein FtsZ OS=Escherichia coli	ftsZ	16	26
tRNA-specific 2-thiouridylase MnmA OS=Escherichia coli	mnmA	16	22
Opacity-associated protein A OS=Escherichia coli	ytfB	16	19
High frequency lysogenization protein HflD OS=Escherichia coli	ycfC	16	17
Aminotransferase class I and II OS=Escherichia coli	avtA	16	13
Tol-Pal system protein TolQ OS=Escherichia coli	tolQ	16	12
Alcohol dehydrogenase GroES domain protein OS=Escherichia coli	gatD	16	11
Phosphate transporter OS=Escherichia coli	pitA	16	5
ADP-L-glycero-D-manno-heptose-6-epimerase OS=Escherichia coli	gumD	16	4
Transcriptional regulator, MarR family OS=Escherichia coli	emrR	16	4
Cell division protein DamX OS=Escherichia coli	damX	16	3
30S ribosomal protein S15 OS=Escherichia coli	rpsO	16	1
Sodium-dependent inorganic phosphate (Pi) transporter OS=Escherichia coli	yjbB	16	
D-tagatose-1,6-bisphosphate aldolase subunit GatY OS=Escherichia coli		15	25
Cytochrome bd ubiquinol oxidase subunit I OS=Escherichia coli	cydA	15	16
Uncharacterized protein OS=Escherichia coli	yigA	15	15
L-serine dehydratase 1 OS=Escherichia coli	sdaA	15	15
ABC transporter related OS=Escherichia coli	mdlA	15	13
PTS system, mannose/fructose/sorbose family, IIA subunit OS=Escherichia coli	manX	15	10
Bifunctional aspartokinase/homoserine dehydrogenase OS=Escherichia coli	thrA	15	10
DNA-directed RNA polymerase OS=Escherichia coli	T7-RNA-Pol	15	7
Modulator of FtsH protease HflC OS=Escherichia coli	hflC	15	7
ABC transporter related OS=Escherichia coli	yjjK	15	6
Integral membrane protein TerC OS=Escherichia coli	yoaE	15	6
Band 7 protein OS=Escherichia coli	ybbK	15	5

Translation initiation factor IF-2 OS=Escherichia coli	infB	15	5
Chromosome partition protein MukF OS=Escherichia coli	mukF	15	4
Sensor protein OS=Escherichia coli	narQ	15	3
Signal recognition particle protein OS=Escherichia coli	ffh	15	2
50S ribosomal protein L19 OS=Escherichia coli	rplS	15	1
Uncharacterized protein YhdP OS=Escherichia coli	yhdP	15	
Probable protein kinase UbiB OS=Escherichia coli	ubiB	15	
30S ribosomal protein S4 OS=Escherichia coli	rpsD	15	
Tryptophan--tRNA ligase OS=Escherichia coli	trpS	14	22
Histidine biosynthesis bifunctional protein HisB OS=Escherichia coli	hisB	14	20
Peptidase U32 OS=Escherichia coli	ydcP	14	19
Phosphoribosylformylglycinamidine cyclo-ligase OS=Escherichia coli	purM	14	18
Beta-lactamase OS=Escherichia coli	dacC	14	18
UPF0149 protein YgfB OS=Escherichia coli		14	16
Transcriptional regulator, LysR family OS=Escherichia coli	cysB	14	15
Sensor protein OS=Escherichia coli	cusS	14	11
Transcriptional repressor NrdR OS=Escherichia coli	nrdR	14	11
Aconitate hydratase B OS=Escherichia coli	acnB	14	10
Oligopeptide/dipeptide ABC transporter, ATPase subunit OS=Escherichia coli	oppF	14	7
RNA polymerase sigma-54 factor OS=Escherichia coli	rpoN	14	7
30S ribosomal protein S6 OS=Escherichia coli	rpsF	14	3
50S ribosomal protein L14 OS=Escherichia coli	rplN	14	2
Uncharacterized protein OS=Escherichia coli	yigN	14	1
rRNA (Guanine-N(1)-)-methyltransferase OS=Escherichia coli	rrmA	14	
Ppx/GppA phosphatase OS=Escherichia coli	ppx	13	19
Protein-export membrane protein SecF OS=Escherichia coli	secF	13	18
Outer membrane protein assembly factor BamB OS=Escherichia coli	yfgL	13	12
Curved DNA-binding protein OS=Escherichia coli	cbpA	13	11
NAD-dependent epimerase/dehydratase OS=Escherichia coli	ybjT	13	9
Transcriptional regulator, LysR family OS=Escherichia coli	yeiE	13	8
Glutamate--tRNA ligase OS=Escherichia coli	gltX	13	7
Histidine kinase OS=Escherichia coli	phoQ	13	7
Lipoprotein-releasing system ATP-binding protein LolD OS=Escherichia coli	lolD	13	6
Alpha-1,4 glucan phosphorylase OS=Escherichia coli		13	1
50S ribosomal protein L15 OS=Escherichia coli	rplO	13	1
50S ribosomal protein L22 OS=Escherichia coli	rplV	13	

Uroporphyrinogen-III C-methyltransferase OS=Escherichia coli	hemX	13	
PAS/PAC sensor signal transduction histidine kinase OS=Escherichia coli	phoR	13	
50S ribosomal protein L4 OS=Escherichia coli	rplD	13	
Sulfatase OS=Escherichia coli	yijP	12	28
Phosphate acetyltransferase OS=Escherichia coli	pta	12	21
Secretion protein HlyD family protein OS=Escherichia coli	ydhJ	12	16
Uncharacterized protein OS=Escherichia coli	ypfJ	12	16
DnaA regulatory inactivator Hda OS=Escherichia coli	hda	12	13
DNA mismatch repair protein MutL OS=Escherichia coli	mutL	12	12
Ribosome-binding ATPase YchF OS=Escherichia coli	ychF	12	12
ABC transporter related OS=Escherichia coli	hisP	12	8
Uncharacterized protein OS=Escherichia coli	yqjE	12	5
Protease 4 OS=Escherichia coli	sppA	12	5
Signal recognition particle receptor FtsY OS=Escherichia coli		12	4
ATP synthase gamma chain OS=Escherichia coli	atpG	12	4
DNA repair protein RadA OS=Escherichia coli	radA	12	2
1-acyl-sn-glycerol-3-phosphate acyltransferase OS=Escherichia coli	plsC	12	2
50S ribosomal protein L25 OS=Escherichia coli	rplY	12	1
Tyrosine recombinase XerC OS=Escherichia coli	xerC	12	1
Nickel-responsive regulator OS=Escherichia coli	nikR	12	
Adenylate cyclase OS=Escherichia coli	cyaA	12	
Adenosine deaminase OS=Escherichia coli	add	11	22
33 kDa chaperonin OS=Escherichia coli	hslO	11	14
Transcriptional regulator, AraC family OS=Escherichia coli	xylR	11	11
Enolase OS=Escherichia coli	eno	11	10
Arginine transporter ATP-binding subunit OS=Escherichia coli	artP	11	8
Succinate--CoA ligase subunit alpha OS=Escherichia coli	sucD	11	8
Outer membrane protein assembly factor BamC OS=Escherichia coli	nlpB	11	8
5'-deoxynucleotidase YfbR OS=Escherichia coli	yfbR	11	7
Transcriptional regulator, DeoR family OS=Escherichia coli		11	7
1,4-dihydroxy-2-naphthoate octaprenyltransferase OS=Escherichia coli	menA	11	7
Sensor protein OS=Escherichia coli		11	4
Outer membrane lipoprotein RcsF OS=Escherichia coli	rcsF	11	3
Luciferase-like monooxygenase OS=Escherichia coli	yhbW	11	3
Glycerol-3-phosphate dehydrogenase, anaerobic, C subunit OS=Escherichia coli	glpC	11	2

Adenylyl-sulfate kinase OS=Escherichia coli	cysC	11	2
30S ribosomal protein S11 OS=Escherichia coli	rpsK	11	2
DNA polymerase III subunit alpha OS=Escherichia coli	dnaE	11	
Sulfate adenylyltransferase subunit 2 OS=Escherichia coli	cysD	11	
DNA-binding transcriptional regulator NtrC OS=Escherichia coli	glnG	10	20
Phosphofructokinase OS=Escherichia coli	fruK	10	17
Glycerol-3-phosphate dehydrogenase OS=Escherichia coli	glpA	10	16
Histidine kinase OS=Escherichia coli	baeS	10	14
Transcriptional regulator, LysR family OS=Escherichia coli	oxyR	10	12
Phenylalanine--tRNA ligase alpha subunit OS=Escherichia coli	pheS	10	11
Tetraacyldisaccharide 4'-kinase OS=Escherichia coli	lpxK	10	10
PhoH family protein OS=Escherichia coli	ybeZ	10	7
ATP-dependent 6-phosphofructokinase OS=Escherichia coli	pfkA	10	6
Alpha,alpha-phosphotrehalase OS=Escherichia coli	treC	10	5
Formyltetrahydrofolate deformylase OS=Escherichia coli	purU	10	4
Gluconokinase OS=Escherichia coli		10	4
Protoporphyrinogen oxidase OS=Escherichia coli	hemG	10	4
Outer membrane protein assembly factor BamD OS=Escherichia coli	bamD	10	2
Pyruvate formate-lyase-activating enzyme OS=Escherichia coli	pflA	10	1
30S ribosomal protein S12 OS=Escherichia coli	rpsL	10	
30S ribosomal protein S19 OS=Escherichia coli	rpsS	10	
2-dehydro-3-deoxyphosphooctonate aldolase OS=Escherichia coli	kdsA	9	21
D-tagatose-1,6-bisphosphate aldolase subunit GatZ OS=Escherichia coli	gatZ	9	19
Periplasmic serine endoprotease DegP-like OS=Escherichia coli	degQ	9	18
Fatty acid metabolism regulator protein OS=Escherichia coli	fadR	9	14
DNA polymerase III, delta prime subunit OS=Escherichia coli	holB	9	12
tRNA modification GTPase MnmE OS=Escherichia coli	trmE	9	11
50S ribosomal protein L10 OS=Escherichia coli	rplJ	9	10
Lipid A 1-diphosphate synthase OS=Escherichia coli	yeiU	9	9
Histidine kinase OS=Escherichia coli	zraS	9	9
D-erythrose-4-phosphate dehydrogenase OS=Escherichia coli	epd	9	7
Histidine kinase OS=Escherichia coli	creC	9	5
Glycine betaine/L-proline ABC transporter, ATPase subunit OS=Escherichia coli	proV	9	3

Uncharacterized protein OS=Escherichia coli	yqjD	9	2
Glycogen synthase OS=Escherichia coli	glgA	9	1
MscS Mechanosensitive ion channel OS=Escherichia coli	ybdG	9	
30S ribosomal protein S13 OS=Escherichia coli	rpsM	9	
Mammalian cell entry related domain protein OS=Escherichia coli	pqiB	9	
50S ribosomal protein L11 OS=Escherichia coli	rplK	9	
UspA domain protein OS=Escherichia coli	uspF	9	
Diguanylate cyclase/phosphodiesterase OS=Escherichia coli	yfeA	9	
Peptidoglycan D,D-transpeptidase MrdA OS=Escherichia coli	mrdA	9	
Ubiquinone biosynthesis hydroxylase, UbiH/UbiF/VisC/COQ6 family OS=Escherichia coli	ubiF	9	
Peptidoglycan D,D-transpeptidase FtsI OS=Escherichia coli	ftsI	9	
3,4-dihydroxy-2-butanone 4-phosphate synthase OS=Escherichia coli	ribB	9	
Nuclease SbcCD subunit C OS=Escherichia coli	sbcC	9	
Nucleoside-specific channel-forming protein Tsx OS=Escherichia coli	tsx	8	17
Iron-sulfur cluster carrier protein OS=Escherichia coli	mrp	8	13
L-threonine 3-dehydrogenase OS=Escherichia coli	tdh	8	12
Protease HtpX OS=Escherichia coli	htpX	8	12
Carboxyl-terminal protease OS=Escherichia coli	prc	8	12
Acetylglutamate kinase OS=Escherichia coli		8	12
Threonine synthase OS=Escherichia coli	thrC	8	11
50S ribosomal protein L7/L12 OS=Escherichia coli	rplL	8	10
SdiA-regulated domain protein OS=Escherichia coli		8	9
Cyclic pyranopterin monophosphate synthase OS=Escherichia coli	moaC	8	8
Outer membrane lipoprotein, Slp family OS=Escherichia coli	slp	8	8
Site-determining protein OS=Escherichia coli	minD	8	8
Uncharacterized protein OS=Escherichia coli	wbbB	8	7
Transcriptional regulator, DeoR family OS=Escherichia coli	yihW	8	6
Lipopolysaccharide assembly protein B OS=Escherichia coli	yciM	8	5
NADH-quinone oxidoreductase subunit A OS=Escherichia coli	nuoA	8	5
Nucleoid-associated protein YbaB OS=Escherichia coli	ybaB	8	4
TrkA-N domain protein OS=Escherichia coli	kch	8	3
RNA-binding protein Hfq OS=Escherichia coli	hfq	8	3
Acyl-(acyl-carrier-protein)--UDP-N-acetylglucosamine O-acyltransferase OS=Escherichia coli	lpxA	8	3
Modulator protein MzrA OS=Escherichia coli	yqjB	8	2

Elongation factor 4 OS=Escherichia coli	lepA	8	2
Aminotransferase class I and II OS=Escherichia coli	yfbQ	8	2
30S ribosomal protein S9 OS=Escherichia coli	rpsI	8	
NADH pyrophosphatase OS=Escherichia coli	nudC	8	
Copper resistance protein CopC OS=Escherichia coli	yobA	8	
Peptidase domain protein OS=Escherichia coli	ycgK	8	
Lipopolysaccharide core heptose(I) kinase OS=Escherichia coli	rfaP	8	
30S ribosomal protein S17 OS=Escherichia coli	rpsQ	8	
GTPase Der OS=Escherichia coli	yfgK	8	
50S ribosomal protein L24 OS=Escherichia coli	rplX	8	
Magnesium transport protein CorA OS=Escherichia coli	corA	8	
Uncharacterized protein OS=Escherichia coli	yghW	8	
(P)ppGpp synthetase I, SpoT/RelA OS=Escherichia coli	spoT	8	
ABC transporter related OS=Escherichia coli	sapF	8	
Histidine kinase OS=Escherichia coli	yfhK	7	22
Signaling modulator of AmpD, AmpE OS=Escherichia coli	ampE	7	13
Uncharacterized protein OS=Escherichia coli	yiaF	7	12
Transcriptional regulator, LysR family OS=Escherichia coli	cynR	7	12
DegT/DnrJ/EryC1/StrS aminotransferase OS=Escherichia coli	ybl97	7	11
Tol-Pal system protein TolR OS=Escherichia coli	tolR	7	9
Uncharacterized protein OS=Escherichia coli	yniB	7	8
Flagellar regulator flk OS=Escherichia coli	flk	7	7
Carbonic anhydrase OS=Escherichia coli	yadF	7	7
ABC transporter related OS=Escherichia coli	yhbG	7	7
Phosphoenolpyruvate-protein phosphotransferase OS=Escherichia coli	ptsI	7	7
ATP-dependent protease subunit HslV OS=Escherichia coli	hslV	7	6
Transcription termination/antitermination protein NusA OS=Escherichia coli	nusA	7	5
Methionine--tRNA ligase OS=Escherichia coli	metG	7	5
Ubiquinone biosynthesis O-methyltransferase OS=Escherichia coli	ubiG	7	5
Endonuclease/exonuclease/phosphatase OS=Escherichia coli	ybhP	7	5
Adenylosuccinate lyase OS=Escherichia coli	purB	7	4
UPF0260 protein YcgN OS=Escherichia coli	ycgN	7	4
Ferrochelatase OS=Escherichia coli	hemH	7	3
Cell division protein DedD OS=Escherichia coli	dedD	7	3
50S ribosomal protein L17 OS=Escherichia coli	rplQ	7	3
Phosphopentomutase OS=Escherichia coli	deoB	7	2

Glucose-6-phosphate 1-dehydrogenase OS=Escherichia coli	zwf	7	2
30S ribosomal protein S16 OS=Escherichia coli	rpsP	7	
tRNA (guanine-N(7)-)-methyltransferase OS=Escherichia coli	trmI	7	
Molybdopterin-guanine dinucleotide biosynthesis protein B OS=Escherichia coli	mobB	7	
30S ribosomal protein S8 OS=Escherichia coli	rpsH	7	
Diaminopimelate decarboxylase OS=Escherichia coli	lysA	7	
tRNA (guanine-N(1)-)-methyltransferase OS=Escherichia coli	trmD	7	
Phospho-2-dehydro-3-deoxyheptonate aldolase OS=Escherichia coli	aroG	6	14
Cytochrome c-type biogenesis protein OS=Escherichia coli	ccmH	6	14
Fructose-bisphosphate aldolase OS=Escherichia coli	fbaA	6	14
EAL domain protein OS=Escherichia coli	ylaB	6	13
Sulfate ABC transporter, inner membrane subunit OS=Escherichia coli	cysW	6	11
Enoyl-(acyl-carrier-protein) reductase (NADH) OS=Escherichia coli	fabI	6	11
HAD-superfamily hydrolase, subfamily IA, variant 1 OS=Escherichia coli	yjjG	6	11
Transketolase OS=Escherichia coli	tktA	6	11
Nucleoside permease OS=Escherichia coli	nupC	6	11
Phosphatidylserine decarboxylase proenzyme OS=Escherichia coli	psd	6	11
Polyprenyl synthetase OS=Escherichia coli	ispA	6	10
Dyp-type peroxidase family OS=Escherichia coli	yfeX	6	8
Tol-Pal system protein TolB OS=Escherichia coli	tolB	6	8
LPP repeat-containing protein OS=Escherichia coli	lpp	6	7
RNA binding S1 domain protein OS=Escherichia coli		6	6
Phage shock protein B OS=Escherichia coli	pspB	6	6
DNA topoisomerase 4 subunit B OS=Escherichia coli	parE	6	6
TonB-system energizer ExbB OS=Escherichia coli	exbB	6	6
Aminoacyl-histidine dipeptidase OS=Escherichia coli	pepD	6	6
Transport permease protein OS=Escherichia coli	ybhR	6	6
Malate/L-lactate dehydrogenase OS=Escherichia coli	ybiC	6	6
UDP-N-acetylglucosamine 1-carboxyvinyltransferase OS=Escherichia coli	murA	6	6
Regulator of sigma D OS=Escherichia coli	rsd	6	6
Sodium/proline symporter OS=Escherichia coli	putP	6	5
ABC transporter, CydDC cysteine exporter (CydDC-E) family, permease/ATP-binding protein CydD OS=Escherichia coli	cydD	6	5
C4-dicarboxylate transport protein OS=Escherichia coli	dctA	6	5
Phenylalanine--tRNA ligase beta subunit OS=Escherichia coli	pheT	6	4

ABC transporter, CydDC cysteine exporter (CydDC-E) family, permease/ATP-binding protein CydC OS=Escherichia coli	cydC	6	4
UPF0441 protein YgiB OS=Escherichia coli		6	3
Uncharacterized protein OS=Escherichia coli	yjbQ	6	2
Uncharacterized protein OS=Escherichia coli	wbbA	6	2
Ribosome-binding factor A OS=Escherichia coli	rbfA	6	1
ATP synthase subunit delta OS=Escherichia coli	atpH	6	1
50S ribosomal protein L21 OS=Escherichia coli	rplU	6	1
Iron-containing alcohol dehydrogenase OS=Escherichia coli	gldA	6	1
Cytochrome-c3 hydrogenase OS=Escherichia coli	hybC	6	1
Transcriptional regulator, TetR family OS=Escherichia coli	ycfQ	6	1
Membrane-bound lytic murein transglycosylase C OS=Escherichia coli		6	1
ATP synthase epsilon chain OS=Escherichia coli	atpC	6	1
30S ribosomal protein S20 OS=Escherichia coli	rpsT	6	
Lipid A biosynthesis lauroyltransferase OS=Escherichia coli	htrB	6	
PTS system, N-acetylglucosamine-specific IIBC subunit OS=Escherichia coli	nagE	6	
Glucans biosynthesis protein G OS=Escherichia coli	mdoG	6	
Long-chain-fatty-acid--CoA ligase OS=Escherichia coli		6	
Ribosomal RNA large subunit methyltransferase J OS=Escherichia coli	yhiR	6	
50S ribosomal protein L29 OS=Escherichia coli	rpmC	6	
Negative modulator of initiation of replication OS=Escherichia coli	seqA	6	
PTS system, glucitol/sorbitol-specific, IIBC subunit OS=Escherichia coli	srlE	6	
50S ribosomal protein L16 OS=Escherichia coli	rplP	6	
L-threonine dehydratase OS=Escherichia coli		5	12
Glucosamine-6-phosphate deaminase OS=Escherichia coli	nagB	5	12
Uncharacterized protein OS=Escherichia coli	yjaG	5	11
Keratin, type I cytoskeletal 14 OS=Homo sapiens	KRT14	5	10
4-hydroxybenzoate octaprenyltransferase OS=Escherichia coli	ubiA	5	9
Binding-protein-dependent transport systems inner membrane component OS=Escherichia coli	metI	5	9
HAD-superfamily hydrolase, subfamily IA, variant 3 OS=Escherichia coli		5	8
Transport-associated OS=Escherichia coli	yraP	5	7
ABC transporter related OS=Escherichia coli	mdlB	5	7
GTP cyclohydrolase 1 OS=Escherichia coli	folE	5	7
Phosphate import ATP-binding protein PstB OS=Escherichia coli	pstB	5	7

Phospho-N-acetylmuramoyl-pentapeptide-transferase OS=Escherichia coli	mraY	5	7
Ribosomal protein S6--L-glutamate ligase OS=Escherichia coli	rimK	5	6
Endoplasmic reticulum chaperone BiP OS=Homo sapiens	HSPA5	5	6
ABC transporter related OS=Escherichia coli	ybhF	5	6
Regulator of RpoS OS=Escherichia coli	hnr	5	6
Uncharacterized protein OS=Escherichia coli	ylaC	5	6
Exoribonuclease 2 OS=Escherichia coli	rnb	5	5
Acyl carrier protein OS=Escherichia coli	acpP	5	5
GumN family protein OS=Escherichia coli	ybaP	5	4
Succinate--CoA ligase subunit beta OS=Escherichia coli	sucC	5	4
Glutamyl-tRNA reductase OS=Escherichia coli	hemA	5	4
Binding-protein-dependent transport systems inner membrane component OS=Escherichia coli	sapB	5	4
RNase adapter protein RapZ OS=Escherichia coli	yhbJ	5	4
Metabolite/H+ symporter, major facilitator superfamily (MFS) OS=Escherichia coli	proP	5	3
PTS system, mannitol-specific IIC subunit OS=Escherichia coli	mtlA	5	3
Thiol:disulfide interchange protein DsbD OS=Escherichia coli	dipZ	5	3
Permease YjgP/YjgQ family protein OS=Escherichia coli	yjgP	5	2
Alkyl hydroperoxide reductase C OS=Escherichia coli	ahpC	5	2
Sodium:dicarboxylate symporter OS=Escherichia coli	ydjN	5	2
Type 4 prepilin-like proteins leader peptide-processing enzyme OS=Escherichia coli		5	2
Inositol-1-monophosphatase OS=Escherichia coli	suhB	5	2
2,3-bisphosphoglycerate-dependent phosphoglycerate mutase OS=Escherichia coli	gpmA	5	2
S-ribosylhomocysteine lyase OS=Escherichia coli	ygaG	5	2
Uncharacterized protein OS=Escherichia coli	yejG	5	2
Lipopolysaccharide heptosyltransferase II OS=Escherichia coli	rfaF	5	1
30S ribosomal protein S18 OS=Escherichia coli	rpsR	5	1
Uncharacterized protein OS=Escherichia coli	yhcB	5	1
Chromosome partition protein MukE OS=Escherichia coli		5	
DNA polymerase III subunit epsilon OS=Escherichia coli		5	
Universal stress protein OS=Escherichia coli	uspD	5	
tRNA (cytidine/uridine-2'-O-)-methyltransferase TrmJ OS=Escherichia coli	trmJ	5	
Hornerin OS=Homo sapiens	HRNR	5	
Ribosomal-protein-alanine N-acetyltransferase OS=Escherichia coli	rimJ	5	
50S ribosomal protein L20 OS=Escherichia coli	rplT	5	

Chromosome partition protein MukB OS=Escherichia coli	mukB	5	
Glutathione-regulated potassium-efflux system ancillary protein KefF OS=Escherichia coli	yabF	5	
SH3 domain protein OS=Escherichia coli	ygiM	5	
Outer membrane chaperone Skp (OmpH) OS=Escherichia coli	hlpA	5	
GTPase HflX OS=Escherichia coli	hflX	5	
Osmosensitive K channel His kinase sensor OS=Escherichia coli	kdpD	5	
Uncharacterized protein OS=Escherichia coli		5	
D-alanyl-D-alanine carboxypeptidase/D-alanyl-D-alanine-endopeptidase OS=Escherichia coli	dacB	5	
PTSINtr with GAF domain, PtsP OS=Escherichia coli	ptsP	5	
DNA polymerase I OS=Escherichia coli	polA	5	
Two component transcriptional regulator, winged helix family OS=Escherichia coli	qseB	5	
Short-chain dehydrogenase/reductase SDR OS=Escherichia coli	ucpA	4	10
Transcriptional regulator, LysR family OS=Escherichia coli	cbl	4	9
Chaperone protein HscA OS=Escherichia coli	hscA	4	9
Sigma factor-binding protein Crl OS=Escherichia coli	crl	4	8
Uncharacterized protein OS=Escherichia coli	yicN	4	8
HAD superfamily (Subfamily IF) hydrolase, YfhB OS=Escherichia coli	yfhB	4	7
Glycosyl transferase, family 3-like protein OS=Escherichia coli	ybiB	4	7
Selenide, water dikinase OS=Escherichia coli	selD	4	7
AAA ATPase central domain protein OS=Escherichia coli	ycaJ	4	7
Efflux pump membrane protein OS=Escherichia coli	emrA	4	6
SNARE associated Golgi protein OS=Escherichia coli	dedA	4	6
Ketol-acid reductoisomerase (NADP(+)) OS=Escherichia coli	ilvC	4	6
Glycine--tRNA ligase beta subunit OS=Escherichia coli	glyS	4	6
DNA gyrase subunit A OS=Escherichia coli	gyrA	4	6
Uncharacterized protein OS=Escherichia coli	yciW	4	5
Ribose import ATP-binding protein RbsA OS=Escherichia coli	ybl121	4	5
Binding-protein-dependent transport systems inner membrane component OS=Escherichia coli	yliC	4	5
Gluconate transporter OS=Escherichia coli	gntT	4	5
Cell division inhibitor SulA OS=Escherichia coli	sulA	4	5
YecA family protein OS=Escherichia coli		4	4
Uncharacterized lipoprotein OS=Escherichia coli	yajG	4	4
Protein-export membrane protein SecG OS=Escherichia coli	secG	4	4

Hypoxanthine phosphoribosyltransferase OS=Escherichia coli		4	4
Phage shock protein C, PspC OS=Escherichia coli	pspC	4	4
Synaptotagmin-like protein 4 OS=Homo sapiens	SYTL4	4	3
NUDIX hydrolase OS=Escherichia coli	nudL	4	3
Serine hydroxymethyltransferase OS=Escherichia coli	glyA	4	3
Valine--tRNA ligase OS=Escherichia coli	valS	4	3
SmpA/OmlA domain protein OS=Escherichia coli	osmE	4	3
Protein MtfA OS=Escherichia coli	mtfA	4	3
Transcription antitermination protein NusB OS=Escherichia coli	nusB	4	3
Aspartate ammonia-lyase OS=Escherichia coli	aspA	4	3
CTP synthase OS=Escherichia coli	pyrG	4	3
Cytochrome c-type biogenesis protein CcmE OS=Escherichia coli	ccmE	4	3
Uncharacterized protein OS=Escherichia coli	ygfX	4	3
UPF0263 protein YciU OS=Escherichia coli	yciU	4	2
D-galactonate transporter OS=Escherichia coli	garP	4	2
Transcriptional regulator, LysR family OS=Escherichia coli	ybl182	4	2
DNA protection during starvation protein OS=Escherichia coli	dps	4	2
Inosine-5'-monophosphate dehydrogenase OS=Escherichia coli	guaB	4	2
Transaldolase OS=Escherichia coli	talB	4	2
ATPase RavA OS=Escherichia coli	ravA	4	2
Transcriptional regulator, RpiR family OS=Escherichia coli	yebK	4	2
Maltose/maltodextrin import ATP-binding protein MalK OS=Escherichia coli	malK	4	2
Mammalian cell entry related domain protein OS=Escherichia coli	mlaD	4	2
UPF0114 protein YqhA OS=Escherichia coli	yqhA	4	2
Keratin, type II cytoskeletal 1b OS=Homo sapiens	KRT77	4	1
50S ribosomal protein L3 glutamine methyltransferase OS=Escherichia coli	yfcB	4	1
Histone family protein DNA-binding protein OS=Escherichia coli	hupA	4	1
Polyribonucleotide nucleotidyltransferase OS=Escherichia coli	pnp	4	1
Sensor histidine kinase RcsC OS=Escherichia coli		4	1
Binding-protein-dependent transport systems inner membrane component OS=Escherichia coli	oppB	4	1
Isoleucine--tRNA ligase OS=Escherichia coli	ileS	4	1
Uncharacterized protein OS=Escherichia coli	ydcF	4	1
50S ribosomal protein L18 OS=Escherichia coli	rplR	4	1
Cell division protein ZapD OS=Escherichia coli	yacF	4	1
Uncharacterized protein OS=Escherichia coli	ycfL	4	1

OmpA/MotB domain protein OS=Escherichia coli	yiaD	4	1
50S ribosomal protein L31 OS=Escherichia coli	rpmE	4	
DNA-binding protein OS=Escherichia coli	hns	4	
Translation initiation factor IF-3 OS=Escherichia coli	infC	4	
50S ribosomal protein L28 OS=Escherichia coli	rpmB	4	
Integral membrane protein, YccS/YhfK family OS=Escherichia coli		4	
UDP-N-acetylglucosamine--N-acetylmuramyl-(pentapeptide) pyrophosphoryl-undecaprenol N-acetylglucosamine transferase OS=Escherichia coli	murG	4	
Uncharacterized protein OS=Escherichia coli	ydcY	4	
UPF0325 protein YaeH OS=Escherichia coli	yaeH	4	
Penicillin-binding protein 1B OS=Escherichia coli	mrcB	4	
Putative GAF sensor protein OS=Escherichia coli	yebR	4	
K(+)/H(+) antiporter NhaP2 OS=Escherichia coli	ycgO	4	
Formate dehydrogenase, alpha subunit OS=Escherichia coli	fdoG	4	
Histone family protein DNA-binding protein OS=Escherichia coli	hupB	4	
ABC transporter related OS=Escherichia coli	mlaF	4	
50S ribosomal protein L23 OS=Escherichia coli	rplW	4	
Cell division protein FtsN OS=Escherichia coli	ftsN	4	
Bifunctional glutamine synthetase adenylyltransferase/adenylyl-removing enzyme OS=Escherichia coli	glnE	4	
3-deoxy-D-manno-octulosonic acid transferase OS=Escherichia coli	waaA	4	
Phosphoenolpyruvate carboxylase OS=Escherichia coli	ppc	4	
GTP-binding protein TypA OS=Escherichia coli	bipA	4	
Two component transcriptional regulator, LytTR family OS=Escherichia coli	ypdB	4	
Uncharacterized protein OS=Escherichia coli	elaB	4	
Uncharacterized protein OS=Escherichia coli	ybjX	4	
ATP-dependent RNA helicase DeaD OS=Escherichia coli	deaD	4	
UPF0370 protein YpfN OS=Escherichia coli	ypfN	3	14
Transcription-repair-coupling factor OS=Escherichia coli		3	11
Penicillin-binding protein activator LpoB OS=Escherichia coli	ycfM	3	10
T-protein OS=Escherichia coli	tyrA	3	9
Branched-chain-amino-acid aminotransferase OS=Escherichia coli	ilvE	3	8
tRNA-dihydrouridine(20/20a) synthase OS=Escherichia coli	dusA	3	8
ABC transporter related OS=Escherichia coli	yehX	3	8
Lipopolysaccharide biosynthesis protein OS=Escherichia coli	cld	3	6

DnaA initiator-associating protein DiaA OS=Escherichia coli	yraO	3	6
Phosphoglucomutase, alpha-D-glucose phosphate-specific OS=Escherichia coli	pgm	3	6
Phosphoglycerate kinase OS=Escherichia coli	pgk	3	6
Thiamine-monophosphate kinase OS=Escherichia coli	thiL	3	5
PTS system, mannose/fructose/sorbose family, IID subunit OS=Escherichia coli		3	5
Aspartate--ammonia ligase OS=Escherichia coli	asnA	3	5
ATP synthase subunit c OS=Escherichia coli	atpE	3	4
Cytochrome d ubiquinol oxidase, subunit II OS=Escherichia coli	cydB	3	4
Uracil phosphoribosyltransferase OS=Escherichia coli	upp	3	4
Uncharacterized protein OS=Escherichia coli	yccF	3	4
Tyrosine--tRNA ligase OS=Escherichia coli	tyrS	3	4
Beta-phosphoglucomutase family hydrolase OS=Escherichia coli	yqaB	3	4
TonB system transport protein ExbD OS=Escherichia coli	exbD	3	4
Uncharacterized protein OS=Escherichia coli	yfhG	3	4
Ion-translocating oxidoreductase complex subunit B OS=Escherichia coli	rsxB	3	4
PTS system, glucose-specific IIBC subunit OS=Escherichia coli	ptsG	3	4
Flavohemoprotein OS=Escherichia coli	hmp	3	4
SNARE associated Golgi protein OS=Escherichia coli	yqjA	3	4
Isocitrate dehydrogenase OS=Escherichia coli	icdA	3	3
Dihydroxyacetone kinase, phosphotransfer subunit OS=Escherichia coli	dhaM	3	3
PTS system, maltose and glucose-specific IIBC subunit OS=Escherichia coli	malX	3	3
Membrane-bound PQQ-dependent dehydrogenase, glucose/quinate/shikimate family OS=Escherichia coli	gcd	3	3
UTP--glucose-1-phosphate uridylyltransferase OS=Escherichia coli	galU	3	3
Peptidoglycan glycosyltransferase MrdB OS=Escherichia coli	mrdB	3	3
Binding-protein-dependent transport systems inner membrane component OS=Escherichia coli	oppC	3	3
Holliday junction ATP-dependent DNA helicase RuvB OS=Escherichia coli	ruvB	3	3
Transcriptional regulator, TetR family OS=Escherichia coli		3	3
Thymidylate synthase OS=Escherichia coli	thyA	3	3
Glutamate racemase OS=Escherichia coli	murI	3	2
HTH-type transcriptional regulator ArgP OS=Escherichia coli	argP	3	2
Transcriptional regulator, AraC family OS=Escherichia coli	araC	3	2
AsmA family protein OS=Escherichia coli	asmA	3	2

Protein GrpE OS=Escherichia coli	grpE	3	2
Uncharacterized chaperone protein YegD OS=Escherichia coli	yegD	3	2
Beta-galactosidase OS=Escherichia coli	lacZ	3	2
Transcription termination/antitermination protein NusG OS=Escherichia coli	nusG	3	2
Alpha/beta hydrolase fold protein OS=Escherichia coli	ybfF	3	2
ABC transporter related OS=Escherichia coli	yadG	3	2
Formate/nitrite transporter OS=Escherichia coli	focA	3	2
Peptidase M48 Ste24p OS=Escherichia coli		3	2
LPS-assembly protein LptD OS=Escherichia coli	lptD	3	2
Diguanylate cyclase/phosphodiesterase OS=Escherichia coli	yhdA	3	2
Uncharacterized protein OS=Escherichia coli	yeeE	3	1
HTH-type transcriptional repressor FabR OS=Escherichia coli	fabR	3	1
Potassium efflux system protein OS=Escherichia coli	ybaL	3	1
Pantothenate kinase OS=Escherichia coli	coaA	3	1
Transcriptional regulator, IclR family OS=Escherichia coli	iclR	3	1
UDP-3-O-(3-hydroxymyristoyl)glucosamine N-acyltransferase OS=Escherichia coli	lpxD	3	1
Catalase-peroxidase OS=Escherichia coli	katG	3	1
Trypanothione synthase OS=Escherichia coli	ygiC	3	1
Uncharacterized protein OS=Escherichia coli	ycaO	3	1
Uncharacterized protein OS=Escherichia coli	yaiW	3	
ROK family protein OS=Escherichia coli	nagC	3	
Transcriptional regulator, LysR family OS=Escherichia coli	ydcI	3	
UDP-N-acetyl-D-mannosaminuronic acid transferase OS=Escherichia coli	wecG	3	
7-methyl-GTP pyrophosphatase OS=Escherichia coli		3	
Phosphoglucosamine mutase OS=Escherichia coli	glmM	3	
Lysophospholipase OS=Escherichia coli	pldB	3	
Membrane-bound lytic murein transglycosylase A OS=Escherichia coli	mltA	3	
Pyruvate ferredoxin/flavodoxin oxidoreductase OS=Escherichia coli	ydbK	3	
Endo-type membrane-bound lytic murein transglycosylase A OS=Escherichia coli	emtA	3	
3-oxoacyl-synthase 3 OS=Escherichia coli	fabH	3	
Transcriptional regulator, AraC family OS=Escherichia coli	soxS	3	
ATP-dependent RNA helicase SrmB OS=Escherichia coli	srmB	3	
tRNA (cytidine/uridine-2'-O-)-methyltransferase TrmJ OS=Escherichia coli	yjtD	3	
Arabinose 5-phosphate isomerase OS=Escherichia coli	gutQ	3	

UPF0225 protein YchJ OS=Escherichia coli	ychJ	3	
Asparagine--tRNA ligase OS=Escherichia coli	asnS	3	
Regulator of ribonuclease activity A OS=Escherichia coli	menG	3	
Phospholipid/glycerol acyltransferase OS=Escherichia coli	yihG	3	
Nucleoid occlusion factor SlmA OS=Escherichia coli	slmA	3	
Uncharacterized protein OS=Escherichia coli	yjaH	3	
Permease YjgP/YjgQ family protein OS=Escherichia coli	lptG	3	
Lipopolysaccharide kinase OS=Escherichia coli	inaA	3	
Transcriptional regulator, TyrR OS=Escherichia coli	tyrR	2	11
Adenylate cyclase OS=Escherichia coli	ygiF	2	8
Glycoside hydrolase family 4 OS=Escherichia coli	melA	2	8
Uncharacterized protein OS=Escherichia coli	yfgM	2	7
Polar amino acid ABC transporter, inner membrane subunit OS=Escherichia coli	gltJ	2	7
Glycerol kinase OS=Escherichia coli	glpK	2	6
Binding-protein-dependent transport systems inner membrane component OS=Escherichia coli	sapC	2	6
S-adenosylmethionine synthase OS=Escherichia coli	metK	2	6
4-hydroxy-tetrahydrodipicolinate reductase OS=Escherichia coli	dapB	2	6
Uncharacterized protein OS=Escherichia coli	ykgE	2	6
Uncharacterized protein OS=Escherichia coli	yggT	2	5
Serine--tRNA ligase OS=Escherichia coli	serS	2	5
Carbon starvation protein CstA OS=Escherichia coli	yjiY	2	5
Tryptophan synthase beta chain OS=Escherichia coli	trpB	2	5
Lysine--tRNA ligase OS=Escherichia coli	lysU	2	5
Fumarate hydratase class I OS=Escherichia coli	fumA	2	5
Glutamate synthase, small subunit OS=Escherichia coli	aegA	2	5
Lipoprotein releasing system, transmembrane protein, LolC/E family OS=Escherichia coli	lolC	2	5
Macrolide export ATP-binding/permease protein MacB OS=Escherichia coli	macB	2	5
Polar amino acid ABC transporter, inner membrane subunit OS=Escherichia coli	artQ	2	4
Na(+)/H(+) antiporter NhaB OS=Escherichia coli	nhaB	2	4
Chaperone modulatory protein CbpM OS=Escherichia coli	yccD	2	4
HAD-superfamily hydrolase, subfamily IIA OS=Escherichia coli	nagD	2	4
Transcriptional regulator, LysR family OS=Escherichia coli	lrhA	2	4
HTH-type transcriptional repressor NsrR OS=Escherichia coli	nsrR	2	3
Regulatory protein GalF OS=Escherichia coli	galF	2	3

2-amino-3-ketobutyrate coenzyme A ligase OS=Escherichia coli	kbl	2	3
ROK family protein OS=Escherichia coli	mlc	2	3
Protein-export protein SecB OS=Escherichia coli	secB	2	3
Phosphoadenosine phosphosulfate reductase OS=Escherichia coli	cysH	2	3
Lipoprotein OS=Escherichia coli	nlpA	2	3
Choline/carnitine/betaine transporter OS=Escherichia coli		2	3
Signal peptidase I OS=Escherichia coli	lepB	2	3
Uncharacterized protein OS=Escherichia coli	yobH	2	3
tRNA 2-selenouridine/geranyl-2-thiouridine synthase OS=Escherichia coli	ybbB	2	3
Short-chain dehydrogenase/reductase SDR OS=Escherichia coli		2	3
Serine transporter OS=Escherichia coli	sdaC	2	3
Hydroxyethylthiazole kinase OS=Escherichia coli	thiM	2	3
UPF0145 protein YbjQ OS=Escherichia coli	ybjQ	2	3
Putative trypsin-6 OS=Homo sapiens	PRSS3P2	2	3
Trp operon repressor OS=Escherichia coli	trpR	2	3
Regulator of ribonuclease activity B OS=Escherichia coli	yjgD	2	2
FTR1 family protein OS=Escherichia coli	efeU	2	2
Zinc transport protein ZntB OS=Escherichia coli	ydaN	2	2
Hydrogenase expression/formation protein HypE OS=Escherichia coli		2	2
Lipoprotein releasing system, transmembrane protein LolE OS=Escherichia coli		2	2
PTS system, galactitol-specific IIC subunit OS=Escherichia coli	gatC	2	2
Putative gluconeogenesis factor OS=Escherichia coli	ybhK	2	2
MIP family channel protein OS=Escherichia coli	glpF	2	2
Lipopolysaccharide export system protein LptC OS=Escherichia coli	yrbK	2	2
Protein translocase subunit SecY OS=Escherichia coli	secY	2	2
Acyl carrier protein phosphodiesterase OS=Escherichia coli	yajB	2	2
Ribosomal silencing factor RsfS OS=Escherichia coli	ybeB	2	2
Gluconate transporter OS=Escherichia coli		2	2
Amino-acid acetyltransferase OS=Escherichia coli	argA	2	2
Oligopeptidase A OS=Escherichia coli	prlC	2	2
ABC transporter related OS=Escherichia coli	glnQ	2	2
Integral membrane protein TerC OS=Escherichia coli	yegH	2	2
Sec-independent protein translocase protein TatC OS=Escherichia coli	tatC	2	2
Ribonucleotide reductase OS=Escherichia coli	nrdB	2	2
Uncharacterized protein OS=Escherichia coli	yfgG	2	2

Uncharacterized protein OS=Escherichia coli	ybl190	2	1
Putative lipoprotein OS=Escherichia coli	ybjP	2	1
Dihydroxyacetone kinase, L subunit OS=Escherichia coli	dhaL	2	1
CDP-alcohol phosphatidyltransferase OS=Escherichia coli	ynjF	2	1
Zona pellucida-binding protein 1 OS=Homo sapiens	ZPBP	2	1
NAD-dependent protein deacylase sirtuin-5, mitochondrial OS=Homo sapiens	SIRT5	2	1
Uncharacterized protein OS=Escherichia coli	ybl161	2	1
DNA repair protein RecN OS=Escherichia coli	recN	2	1
6-phosphogluconate dehydratase OS=Escherichia coli	edd	2	1
Glutaredoxin OS=Escherichia coli	ydhD	2	1
Sulfite reductase [NADPH] flavoprotein alpha-component OS=Escherichia coli	cysJ	2	1
Trans-hexaprenyltranstransferase OS=Escherichia coli	ispB	2	1
ATPase family AAA domain-containing protein 5 OS=Homo sapiens	ATAD5	2	1
Succinate dehydrogenase hydrophobic membrane anchor subunit OS=Escherichia coli	sdhD	2	1
Uncharacterized protein OS=Escherichia coli	yqjK	2	1
Nitroreductase OS=Escherichia coli	nfsA	2	1
Probable peptidoglycan glycosyltransferase FtsW OS=Escherichia coli	ftsW	2	1
Cupin 4 family protein OS=Escherichia coli	ycfD	2	1
Peptidyl-prolyl cis-trans isomerase OS=Escherichia coli	fklB	2	1
FAD linked oxidase domain protein OS=Escherichia coli	ydiJ	2	1
UPF0509 protein YciZ OS=Escherichia coli	yciZ	2	
Lipopolysaccharide heptosyltransferase III OS=Escherichia coli	rfaQ	2	
Transcriptional regulator, RpiR family OS=Escherichia coli	rpiR	2	
Elongation factor Ts OS=Escherichia coli	tsf	2	
Glutamine synthetase OS=Escherichia coli	glnA	2	
NAD-dependent epimerase/dehydratase OS=Escherichia coli	yraR	2	
Phage shock protein A, PspA OS=Escherichia coli	pspA	2	
Gluconate transporter OS=Escherichia coli	dsdX	2	
Regulatory protein GntR HTH OS=Escherichia coli	pdhR	2	
UPF0125 protein ECBD_1069 OS=Escherichia coli	yfjF	2	
Citrate transporter OS=Escherichia coli	ybiR	2	
Acetyltransferase OS=Escherichia coli	ybl96	2	
ECA polysaccharide chain length modulation protein OS=Escherichia coli	wzzE	2	
Biosynthetic peptidoglycan transglycosylase OS=Escherichia coli	mtgA	2	
Uncharacterized protein OS=Escherichia coli	yjeI	2	

Uncharacterized protein OS=Escherichia coli	yibQ	2	
Glycosyl transferase group 1 OS=Escherichia coli	rfaG	2	
Lipid A biosynthesis myristoyltransferase OS=Escherichia coli	lpxM	2	
Peptidyl-prolyl cis-trans isomerase OS=Escherichia coli	fkpA	2	
Transcriptional regulator, MarR family OS=Escherichia coli	marR	2	
Uncharacterized protein OS=Escherichia coli	ygjP	2	
50S ribosomal protein L30 OS=Escherichia coli	rpmD	2	
BolA family protein OS=Escherichia coli		2	
NAD kinase OS=Escherichia coli	nadK	2	
Porin Gram-negative type OS=Escherichia coli	ompF	2	
Pseudouridine synthase OS=Escherichia coli	rluD	2	
UDP-4-amino-4-deoxy-L-arabinose--oxoglutarate aminotransferase OS=Escherichia coli		2	
Spermidine/putrescine import ATP-binding protein PotA OS=Escherichia coli	potA	2	
Transcriptional regulator, LysR family OS=Escherichia coli	gcvA	2	
HTH-type transcriptional regulator HdfR OS=Escherichia coli	hdfR	2	
UPF0265 protein YeeX OS=Escherichia coli	yeeX	2	
30S ribosomal protein S14 OS=Escherichia coli	rpsN	2	
DNA-directed RNA polymerase subunit omega OS=Escherichia coli	rpoZ	2	
Carboxy-S-adenosyl-L-methionine synthase OS=Escherichia coli	yecO	2	
Peptide deformylase OS=Escherichia coli	def	2	
ATP-dependent helicase HrpA OS=Escherichia coli		2	
UPF0115 protein YfcN OS=Escherichia coli	yfcN	2	
Maltoporin OS=Escherichia coli	lamB	2	
Aspartate carbamoyltransferase regulatory chain OS=Escherichia coli	pyrI	2	
Cold-shock DNA-binding domain protein OS=Escherichia coli	cspC	2	
Putative membrane protein insertion efficiency factor OS=Escherichia coli	yidD	2	
Ribonuclease 3 OS=Escherichia coli	rnc	2	
RNA chaperone ProQ OS=Escherichia coli	proQ	2	
Na+/H+ antiporter OS=Escherichia coli	yjcE	2	
Ion-translocating oxidoreductase complex subunit C OS=Escherichia coli		2	
Peptidyl-tRNA hydrolase OS=Escherichia coli	pth	2	
Cell division topological specificity factor OS=Escherichia coli	minE	2	
Thioredoxin OS=Escherichia coli	trxA	2	
GCN5-related N-acetyltransferase OS=Escherichia coli	phnO	2	
Histidine kinase OS=Escherichia coli		2	

Succinylornithine transaminase OS=Escherichia coli	astC	1	29
Glycerol-3-phosphate dehydrogenase OS=Escherichia coli		1	10
Acetyltransferase OS=Escherichia coli	cysE	1	7
Methylenetetrahydrofolate reductase OS=Escherichia coli	metF	1	7
Mannitol dehydrogenase domain protein OS=Escherichia coli	yeiQ	1	6
Diguanylate cyclase OS=Escherichia coli	yeaJ	1	5
Ferritin OS=Escherichia coli	ftn	1	4
Peptidase M23 OS=Escherichia coli	nlpD	1	4
Efflux transporter, RND family, MFP subunit OS=Escherichia coli	cusB	1	4
Sugar transporter OS=Escherichia coli		1	4
Mannitol repressor, MtlR OS=Escherichia coli	yggD	1	4
Fumarate hydratase class II OS=Escherichia coli	fumC	1	4
UPF0597 protein YhaM OS=Escherichia coli	yhaM	1	3
Phosphotransferase system EIIC OS=Escherichia coli	murP	1	3
Homoserine/threonine efflux pump OS=Escherichia coli	rhtC	1	3
GntR domain protein OS=Escherichia coli	lldR	1	3
Bifunctional protein GlmU OS=Escherichia coli	glmU	1	3
Bifunctional aspartokinase/homoserine dehydrogenase OS=Escherichia coli	metL	1	3
Trypsin-1 OS=Homo sapiens	PRSS1	1	3
Delta-aminolevulinic acid dehydratase OS=Escherichia coli	hemB	1	2
Lysine 2,3-aminomutase YodO family protein OS=Escherichia coli	yjeK	1	2
Lipid A export ATP-binding/permease protein MsbA OS=Escherichia coli	msbA	1	2
Anti-sigma-E factor RseA OS=Escherichia coli	rseA	1	2
UPF0304 protein YfbU OS=Escherichia coli	yfbU	1	2
dTDP-4-dehydrorhamnose reductase OS=Escherichia coli	rfbD	1	2
Thioesterase domain protein OS=Escherichia coli		1	2
Polar amino acid ABC transporter, inner membrane subunit OS=Escherichia coli	hisM	1	2
Acetylornithine/succinyldiaminopimelate aminotransferase OS=Escherichia coli	argD	1	2
Cobalamin synthesis protein P47K OS=Escherichia coli	yjiA	1	2
CDP-diacylglycerol pyrophosphatase OS=Escherichia coli	cdh	1	2
Formate dehydrogenase iron-sulfur subunit OS=Escherichia coli	fdoH	1	2
Uncharacterized protein OS=Escherichia coli	hslJ	1	2
Ribonuclease T OS=Escherichia coli	rnt	1	2
Endolytic murein transglycosylase OS=Escherichia coli	yceG	1	2
Mannonate dehydratase OS=Escherichia coli	uxuA	1	2

Catalase OS=Escherichia coli	katE	1	2
3-oxoacyl-(Acyl-carrier-protein) reductase OS=Escherichia coli	fabG	1	2
3-oxoacyl-[acyl-carrier-protein] synthase 2 OS=Escherichia coli	fabF	1	2
LPS-assembly lipoprotein LptE OS=Escherichia coli	rlpB	1	2
TonB-dependent siderophore receptor OS=Escherichia coli	fepA	1	2
Uncharacterized protein OS=Escherichia coli	yccA	1	1
Bifunctional ligase/repressor BirA OS=Escherichia coli	birA	1	1
Undecaprenyl-diphosphatase OS=Escherichia coli	uppP	1	1
Immunoglobulin kappa variable 2-40 OS=Homo sapiens	IGKV2-40	1	1
Serine/threonine transporter SstT OS=Escherichia coli	ygjU	1	1
tRNA-cytidine(32) 2-sulfurtransferase OS=Escherichia coli	ttcA	1	1
Diguanylate phosphodiesterase OS=Escherichia coli	rtn	1	1
1,4-dihydroxy-2-naphthoyl-CoA synthase OS=Escherichia coli	menB	1	1
Bifunctional protein HldE OS=Escherichia coli	rfaE	1	1
TonB-dependent receptor OS=Escherichia coli	yncD	1	1
Histidine kinase OS=Escherichia coli	uhpB	1	1
Uncharacterized protein OS=Escherichia coli	yhfY	1	1
LexA repressor OS=Escherichia coli	lexA	1	1
tRNA N6-adenosine threonylcarbamoyltransferase OS=Escherichia coli	ygjD	1	1
Pyridoxine 5'-phosphate synthase OS=Escherichia coli	pdxJ	1	1
Uncharacterized protein OS=Escherichia coli	yqiC	1	1
Two component transcriptional regulator, winged helix family OS=Escherichia coli	basR	1	1
Transcriptional regulator, CdaR OS=Escherichia coli	cdaR	1	1
Protein NLRC5 OS=Homo sapiens	NLRC5	1	1
Protein-N(Pi)-phosphohistidine--sugar phosphotransferase OS=Escherichia coli	gatB	1	1
Major facilitator superfamily MFS_1 OS=Escherichia coli	yajR	1	1
Glutaminase OS=Escherichia coli	yneH	1	1
10 kDa chaperonin OS=Escherichia coli	groES	1	1
Outer membrane protein assembly factor BamE OS=Escherichia coli	smpA	1	1
Ribonuclease OS=Escherichia coli	yhjD	1	1
Fumarate reductase subunit D OS=Escherichia coli	frdD	1	1
Carbamoyl-phosphate synthase small chain OS=Escherichia coli	carA	1	1
Undecaprenyl phosphate-alpha-4-amino-4-deoxy-L-arabinose arabinosyl transferase OS=Escherichia coli	arnT	1	1
Na+/Ca+ antiporter, CaCA family OS=Escherichia coli	yrbG	1	1
SNARE associated Golgi protein OS=Escherichia coli	yghB	1	1

UvrABC system protein A OS=Escherichia coli	uvrA	1	1
Periplasmic binding protein OS=Escherichia coli	fepB	1	1
Uncharacterized protein OS=Escherichia coli	yebE	1	1
Universal stress protein OS=Escherichia coli	uspA	1	1
Putative sensory transduction regulator OS=Escherichia coli	ybjN	1	1
Endolytic peptidoglycan transglycosylase RlpA OS=Escherichia coli	rlpA	1	1
L-lactate permease OS=Escherichia coli	lldP	1	1
Carboxymuconolactone decarboxylase OS=Escherichia coli	ynjA	1	1
Uncharacterized protein OS=Escherichia coli		1	1
Probable L-ascorbate-6-phosphate lactonase UlaG OS=Escherichia coli	yjfR	1	
Peptidase S11 D-alanyl-D-alanine carboxypeptidase 1 OS=Escherichia coli		1	
ABC transporter related OS=Escherichia coli	ybbA	1	
Smr protein/MutS2 OS=Escherichia coli	ydaL	1	
PTS system fructose subfamily IIA component OS=Escherichia coli	yadI	1	
Histidine kinase OS=Escherichia coli		1	
YfaZ family protein OS=Escherichia coli	yfaZ	1	
GTPase Obg OS=Escherichia coli	obgE	1	
Phosphoglycerate mutase 1 OS=Homo sapiens	PGAM1	1	
Uncharacterized protein OS=Escherichia coli	yhbY	1	
Uncharacterized protein OS=Escherichia coli		1	
Peptide chain release factor 3 OS=Escherichia coli	prfC	1	
HNH endonuclease OS=Escherichia coli	yajD	1	
Peptidase M24 OS=Escherichia coli	pepP	1	
SseB family protein OS=Escherichia coli	sseB	1	
Conserved oligomeric Golgi complex subunit 4 OS=Homo sapiens	COG4	1	
Cyclase/dehydrase OS=Escherichia coli	yfjG	1	
DNA replication and repair protein RecF OS=Escherichia coli	recF	1	
PGC-1 and ERR-induced regulator in muscle protein 1 OS=Homo sapiens	C1orf170	1	
Transcriptional regulator, LacI family OS=Escherichia coli	galR	1	
Uncharacterized protein OS=Escherichia coli	ybgA	1	
Amino acid permease-associated region OS=Escherichia coli	proY	1	
Transcriptional regulator, MerR family OS=Escherichia coli	zntR	1	
Transcriptional regulator, LysR family OS=Escherichia coli	yhjC	1	
Uncharacterized protein OS=Escherichia coli	ytfN	1	
Aldehyde Dehydrogenase OS=Escherichia coli	aldA	1	

3-ketoacyl-CoA thiolase OS=Escherichia coli	fadA	1	
Sigma 54 modulation protein/ribosomal protein S30EA OS=Escherichia coli	yfiA	1	
PTS system, glucitol/sorbitol-specific, IIC subunit OS=Escherichia coli	srlA	1	
4-aminobutyrate aminotransferase OS=Escherichia coli	gabT	1	
Uncharacterized protein OS=Escherichia coli	yjgR	1	
Anthranilate phosphoribosyltransferase OS=Escherichia coli	trpD	1	
SsrA-binding protein OS=Escherichia coli	smpB	1	
Transcriptional regulator, CadC OS=Escherichia coli	cadC	1	
Phosphoenolpyruvate carboxykinase (ATP) OS=Escherichia coli	pck	1	
Intracellular growth attenuator IgaA OS=Escherichia coli		1	
Uncharacterized protein OS=Escherichia coli	yrbB	1	
Transcriptional antiterminator, BglG OS=Escherichia coli	csiE	1	
30S ribosomal protein S21 OS=Escherichia coli	rpsU	1	
YheO domain protein OS=Escherichia coli	yheO	1	
Uncharacterized protein OS=Escherichia coli	yifL	1	
Malate dehydrogenase OS=Escherichia coli	mdh	1	
3-ketoacyl-CoA thiolase OS=Escherichia coli	fadI	1	
Low affinity potassium transport system protein kup OS=Escherichia coli	kup	1	
Dihydroxy-acid dehydratase OS=Escherichia coli	ilvD	1	
Aminotransferase OS=Escherichia coli	aspC	1	
Oligosaccharide/H+ symporter, major facilitator superfamily (MFS) OS=Escherichia coli	lacY	1	
Uncharacterized protein OS=Escherichia coli	ybbM	1	
Single-stranded DNA-binding protein OS=Escherichia coli	ssb	1	
Thioredoxin OS=Escherichia coli	trxC	1	
Fructosamine kinase OS=Escherichia coli	yniA	1	
Ubiquinone biosynthesis hydroxylase, UbiH/UbiF/VisC/COQ6 family OS=Escherichia coli	visC	1	
2,3,4,5-tetrahydropyridine-2,6-dicarboxylate N-succinyltransferase OS=Escherichia coli	dapD	1	
Lytic murein transglycosylase B OS=Escherichia coli	mltB	1	
Molybdenum cofactor guanylyltransferase OS=Escherichia coli	mobA	1	
VacJ family lipoprotein OS=Escherichia coli	vacJ	1	
Thymidine kinase OS=Escherichia coli	tdk	1	
tRNA-2-methylthio-N(6)-dimethylallyladenosine synthase OS=Escherichia coli	yleA	1	
Corrinoid adenosyltransferase OS=Escherichia coli	btuR	1	
Transcriptional regulator, TetR family OS=Escherichia coli	acrR	1	

Chorismate pyruvate-lyase OS=Escherichia coli	ubiC	1	
UPF0250 protein YbeD OS=Escherichia coli	ybeD	1	
ATP-dependent Clp protease proteolytic subunit OS=Escherichia coli	clpP	1	
23S rRNA (guanosine-2'-O-)-methyltransferase RlmB OS=Escherichia coli	rlmB	1	
ATP-dependent Clp protease ATP-binding subunit clpX-like, mitochondrial OS=Homo sapiens	CLPX	1	
Patatin OS=Escherichia coli	rssA	1	
Superoxide dismutase OS=Escherichia coli	sodB	1	
Cell division protein FtsX OS=Escherichia coli	ftsX	1	
Glucokinase OS=Escherichia coli	glk	1	
Cold-shock DNA-binding domain protein OS=Escherichia coli	cspA	1	
Transcriptional regulator, LacI family OS=Escherichia coli	fruR	1	
Transcriptional regulator, XRE family OS=Escherichia coli	puuR	1	
Probable septum site-determining protein MinC OS=Escherichia coli	minC	1	
Fusaric acid resistance protein conserved region OS=Escherichia coli	ydhK	1	
Metabolite/H+ symporter, major facilitator superfamily (MFS) OS=Escherichia coli	shiA	1	
Xaa-Pro dipeptidase OS=Escherichia coli	pepQ	1	
Two component transcriptional regulator, winged helix family OS=Escherichia coli	arcA	1	
Leucyl/phenylalanyl-tRNA--protein transferase OS=Escherichia coli	aat	1	
Ribonuclease PH OS=Escherichia coli	rph	1	
Phosphoheptose isomerase OS=Escherichia coli	lpcA	1	
Fatty acid oxidation complex subunit alpha OS=Escherichia coli	fadJ	1	
Arachidonate 5-lipoxygenase OS=Homo sapiens	ALOX5		45
Apolipoprotein A-I OS=Homo sapiens	APOA1		12
Phosphatidylcholine-sterol acyltransferase OS=Homo sapiens	LCAT		11
Fructose-bisphosphate aldolase A OS=Homo sapiens	ALDOA		11
Glutamate 5-kinase OS=Escherichia coli	proB		8
Copper resistance lipoprotein NlpE OS=Escherichia coli	nlpE		5
L-aspartate oxidase OS=Escherichia coli	nadB		5
Maltodextrin-binding protein OS=Escherichia coli	malE		4
Two component, sigma54 specific, transcriptional regulator, Fis family OS=Escherichia coli	zraR		4
4-hydroxy-3-methylbut-2-en-1-yl diphosphate synthase (flavodoxin) OS=Escherichia coli	ispG		4
Glucose-6-phosphate isomerase OS=Escherichia coli	pgi		3
Rhomboid protease GlpG OS=Escherichia coli	glpG		3
Fructose-bisphosphate aldolase C OS=Homo sapiens	ALDOC		3

Purine nucleoside phosphorylase DeoD-type OS=Escherichia coli	deoD		3
p-hydroxybenzoic acid efflux pump subunit AaeA OS=Escherichia coli	aaeA		3
Orotidine 5'-phosphate decarboxylase OS=Escherichia coli			3
Lipopolysaccharide heptosyltransferase I OS=Escherichia coli	rfaC		3
Lysine--tRNA ligase OS=Escherichia coli	lysS		3
Transcriptional regulator, LysR family OS=Escherichia coli	yhaJ		3
Uncharacterized protein OS=Escherichia coli	yecE		3
Efflux pump membrane transporter OS=Escherichia coli	acrD		3
Lipoprotein NlpI OS=Escherichia coli	nlpI		3
Diguanylate cyclase with GAF sensor OS=Escherichia coli	yeaP		3
Sulfate transport system permease protein CysT OS=Escherichia coli	cysU		3
Probable endonuclease 4 OS=Escherichia coli	nfo		3
Pectinesterase OS=Escherichia coli	ybhC		2
CinA-like protein OS=Escherichia coli	yfaY		2
Lipopolysaccharide 3-alpha-galactosyltransferase OS=Escherichia coli	ybl158		2
UPF0231 protein YacL OS=Escherichia coli	yacL		2
Transcriptional regulator, LysR family OS=Escherichia coli	yahB		2
Type I site-specific deoxyribonuclease OS=Escherichia coli	hsdR		2
RNA polymerase sigma factor OS=Escherichia coli	rpoE		2
Phosphoribosylaminoimidazole-succinocarboxamide synthase OS=Escherichia coli	purC		2
Succinate dehydrogenase iron-sulfur subunit OS=Escherichia coli	frdB		2
Transcriptional regulator, TetR family OS=Escherichia coli	yjgJ		2
Dihydropteroate synthase OS=Escherichia coli	folP		2
Uncharacterized protein OS=Escherichia coli	yagU		2
S-adenosylmethionine decarboxylase proenzyme OS=Escherichia coli	speD		2
Endoribonuclease Dicer OS=Homo sapiens	DICER1		2
UPF0257 lipoprotein YnfC OS=Escherichia coli			2
Redoxin domain protein OS=Escherichia coli	ccmG		2
Glycine dehydrogenase (decarboxylating) OS=Escherichia coli	gcvP		2
Threonine aldolase OS=Escherichia coli	ltaE		2
Multidrug resistance protein MdtA OS=Escherichia coli	mdtA		2
Uncharacterized protein OS=Escherichia coli	yjdF		1
Signal transduction histidine kinase, LytS OS=Escherichia coli	yehU		1

Periplasmic serine protease DegS OS=Escherichia coli	degS		1
Cation/acetate symporter ActP OS=Escherichia coli	actP		1
NADH-quinone oxidoreductase subunit H OS=Escherichia coli	nuoH		1
Cellulose synthase operon protein YhjU OS=Escherichia coli	bcsG		1
Uncharacterized protein OS=Escherichia coli	ygcG		1
Cytosine deaminase OS=Escherichia coli	codA		1
Polar amino acid ABC transporter, inner membrane subunit OS=Escherichia coli	artM		1
6-phosphogluconate dehydrogenase, decarboxylating OS=Escherichia coli	gnd		1
Transcriptional regulator, LysR family OS=Escherichia coli			1
Amino acid permease-associated region OS=Escherichia coli	cycA		1
Hydrolase, TatD family OS=Escherichia coli	ycfH		1
Uncharacterized protein OS=Escherichia coli	yceP		1
Nitrate reductase molybdenum cofactor assembly chaperone OS=Escherichia coli	narJ		1
Transcriptional regulator, TetR family OS=Escherichia coli	yjdC		1
Arabinose 5-phosphate isomerase OS=Escherichia coli	yrbH		1
Binding-protein-dependent transport systems inner membrane component OS=Escherichia coli	proW		1
Polar amino acid ABC transporter, inner membrane subunit OS=Escherichia coli	gltK		1
Iron-containing alcohol dehydrogenase OS=Escherichia coli	ybdH		1
Anaerobic nitric oxide reductase transcription regulator NorR OS=Escherichia coli	ygaA		1
Uncharacterized protein OS=Escherichia coli	yjeT		1
Integration host factor subunit beta OS=Escherichia coli	himD		1
Leucine--tRNA ligase OS=Escherichia coli	leuS		1
Penicillin-binding protein activator LpoA OS=Escherichia coli	yraM		1
Phosphoglycolate phosphatase OS=Escherichia coli	gph		1
Binding-protein-dependent transport systems inner membrane component OS=Escherichia coli	gsiD		1
Membrane protein-like protein OS=Escherichia coli	yeeA		1
ErfK/YbiS/YcfS/YnhG family protein OS=Escherichia coli	ybiS		1
Oligopeptide/dipeptide ABC transporter, ATPase subunit OS=Escherichia coli	oppD		1
Beta-hexosaminidase OS=Escherichia coli	nagZ		1
Glycoprotein/polysaccharide metabolism OS=Escherichia coli	ybaY		1
Glycine--tRNA ligase alpha subunit OS=Escherichia coli	glyQ		1

Transcriptional regulator, IclR family OS=Escherichia coli	ECD_03724		1
HAD-superfamily hydrolase, subfamily IA, variant 3 OS=Escherichia coli	yieH		1
Diguanylate phosphodiesterase OS=Escherichia coli	ycgF		1
Transcriptional regulator, TetR family OS=Escherichia coli	ybiH		1
Trehalose 6-phosphate phosphatase OS=Escherichia coli	otsB		1
RNA polymerase sigma factor RpoS OS=Escherichia coli	rpoS		1
Photosystem I assembly BtpA OS=Escherichia coli	sgcQ		1
Uncharacterized protein OS=Escherichia coli	yajI		1
Cytochrome c assembly protein OS=Escherichia coli	ypjD		1
Glycerophosphoryl diester phosphodiesterase OS=Escherichia coli	glpQ		1
Flavodoxin OS=Escherichia coli	fldA		1
Serum albumin OS=Homo sapiens	ALB		1
Virulence-related outer membrane protein OS=Escherichia coli	ompX		1
Dihydroorotate dehydrogenase family protein OS=Escherichia coli	yeiA		1
Entericidin EcnAB OS=Escherichia coli	ecnB		1
Aconitate hydratase OS=Escherichia coli	acnA		1
D-alanine-- ligase OS=Escherichia coli	ddlB		1
Transcriptional regulator, DeoR family OS=Escherichia coli	sgcR		1
SNARE associated Golgi protein OS=Escherichia coli	yabI		1
Uncharacterized lipoprotein YdcL OS=Escherichia coli	ydcL		1

**. Results are filtered to retain proteins with ≤ 1% False Discovery Rate (FDR) confidence then sorted based on their PSM value from sample 1, which is renamed as Spectral Counts.*

Chapter 5

Summary and Future Directions

5.1 Summary and significance

The studies presented in this thesis investigate the role of cell membrane curvature, which can be generated passively or actively, during cell migration. Cellular membranes not only act as a physical barrier to separate the cell from the outside environment and from compartmentalize organelles but are also signaling hubs by housing numerous proteins. Membrane organization and associated signaling are key regulators of cell proliferation, differentiation, communication, as well as cell migration. Migrating cells passively bend their plasma membrane to adapt the changing topographies in the environment. Furthermore, in response to chemical or physical stimuli, cells are constantly generating intracellular membrane curvatures during migration. We are interested in understanding the mechanisms by which cells sense and respond to the topographic features in the ECM and how membrane curvatures are made at the neutrophil NE during the signal relay.

The second and third chapters of this thesis focus on solving the first question: how different cell types sense extracellular topographies and curvatures. In the second chapter, I explore the effects of surface topography on the migration phenotype of multiple breast cancer cell lines using aligned nanoscale ridges and asymmetric sawtooth structures. I found that asymmetric sawtooth structures unidirectionally bias the movement of breast cancer cells in a cell-type dependent manner. After exploring the cytoskeletal architectures of cancer cells, I have shown that

their biased migration is driven by unidirectional actin polymerization and regulated by distinct cortical plasticity and focal adhesion patterns. Preliminary results using pharmacological interventions further suggest that the differences in migration and cytoskeletal dynamics of cancer cells are determined by their unique mutation profile and unbalanced Rho GTPase signaling. In the third chapter, I examine the behaviors and responses of neutrophils to extracellular structures and curvatures by using surfaces with nanoridges, and monitoring intracellular calcium signals. I demonstrated that neutrophils plated on BSA-coated nanoridges exhibit activation responses, including cell spreading and rapid calcium flashing, in the absence of chemical stimuli and adhesion ligands. I further discovered that the neutrophil activation is dictated by β_2 integrins and that active β_2 integrins cluster on the sidewalls of BSA-coated nanoridges. Based on these findings, I hypothesize that the clustering and activation of β_2 integrins are mediated by cell membrane curvatures.

In the fourth chapter, I attempt to solve the second question: how neutrophils actively generate membrane curvature at the nuclei during their chemotaxis. I have shown that neutrophils are stimulated by a primary chemoattractant form FLAP- and 5-LO-enriched budding vesicles at the nuclei. Considering the conical shape of a functional FLAP trimer, I hypothesize that the clustering of trimeric FLAP in the ceramide microdomains promotes membrane curvature. To test this hypothesis *in vitro*, I reconstitute purified FLAP into a defined lipid environment and visualize the lipid-FLAP assemblies using negative stain EM and cryo-EM. I observed FLAP-reconstitution-specific "wagon-wheel" structures with two membrane layers and multiple protrusions between two layers.

The work described in this thesis systematically studies the role of extracellular and intracellular membrane curvatures in directed cell migration, a key process in cancer metastasis

and inflammation. The findings in the second chapter provide insights into the mechanisms by which cancer cells sense the extracellular topographies and regulate their migration during metastasis. This work may have a positive impact on understanding the invasive migration behavior of cancer cells, and developing prevention strategies for cancer metastasis. The third chapter elucidates how topography-induced membrane curvature activates neutrophils and influences their migration, which uncovers a previously undervalued role of ECM structures in neutrophil recruitment during inflammation. Finally, the fourth chapter provides preliminary evidence on the capability of FLAP, an integral membrane protein, to induce membrane curvatures at the neutrophil nuclei. This result may not only advance our understanding of the mechanisms by which pro-inflammatory leukotrienes are derived but also potentially reveal new targets to treat inflammatory diseases.

5.2 Future directions

Although this thesis has provided answers to multiple questions, it also raised further and deeper queries. In the following sections, I will discuss some of these remaining questions, and present potential approaches to address them.

Determine the role of intrinsic mutations and cell-topography contact in the migration of cancer cells on nanotopographies

In the second chapter, I showed that nanoscale sawtooth structures unidirectionally bias the movement of breast cancer cells in a cell-type dependent manner and that the overall migration response of cancer cells is directly related to the underlying cytoskeletal architectures. However, many questions remain: How do cancer cells sense and respond to topographies? Are the distinct

responses of cancer cells dependent on their genetic repertoire and altered intracellular signaling? Can the cell-ECM interaction regulate their overall migration phenotypes?

Cancer is a disease driven by the accumulation of genetic alterations (Cancer Genome Atlas, 2012). Previous sequence analyses of a collection of human breast cancer cell lines have identified mutations in *PTEN*, *PIK3CA*, *KRAS*, *HRAS*, *NRAS*, and *BRAF* genes (Hollestelle et al., 2007). These mutations can further influence distinct signaling activators and downstream effectors, which may regulate cell migration behaviors (Hollestelle et al., 2007; Makrodouli et al., 2011). Interestingly, it has been shown that *BRAF* mutations in MDA-MB-231 cells lead to elevated Rho-ROCK signaling, and activating *PIK3CA* mutation in M4 cells triggers Rac1 signaling (Hollestelle et al., 2007; Makrodouli et al., 2011; Weigelt et al., 2011). Unbalanced Rho GTPase signaling regulates cell cytoskeleton dynamics and therefore cell migration profiles (Devreotes and Horwitz, 2015). Thus, I hypothesize that the distinct guidance responses of breast cancer cells are primarily determined by their unique mutation profile and downstream Rho GTPase signals (Fig.5.1). To test this hypothesis, future studies should use pharmacological interventions, including ROCK, MLCK, Rac1, and PI3K inhibitors, to regulate the Rho-ROCK or PI3K-Rac signaling in MDA-MB-231 and M4 cells and assess the effect on their migration phenotypes. To do so, time-lapse recording should be acquired and quantified for cell speed, directionality, and persistence. Further, CRISPR/Cas9 technology should be used to knock out overactive BRAF and PI3K proteins in MDA-MB-231 and M4 cells, respectively, to confirm that the observed effects are due to upstream mutations present in breast cancer cells.

In addition, results in the second chapter showed that MDA-MB-231 and M4 cells display distinct cell-surface topography contact and FA patterns. Specifically, I found that the cortical rigidity of MDA-MB-231 cells limits the distribution of FAs on the top of the sawteeth, but the

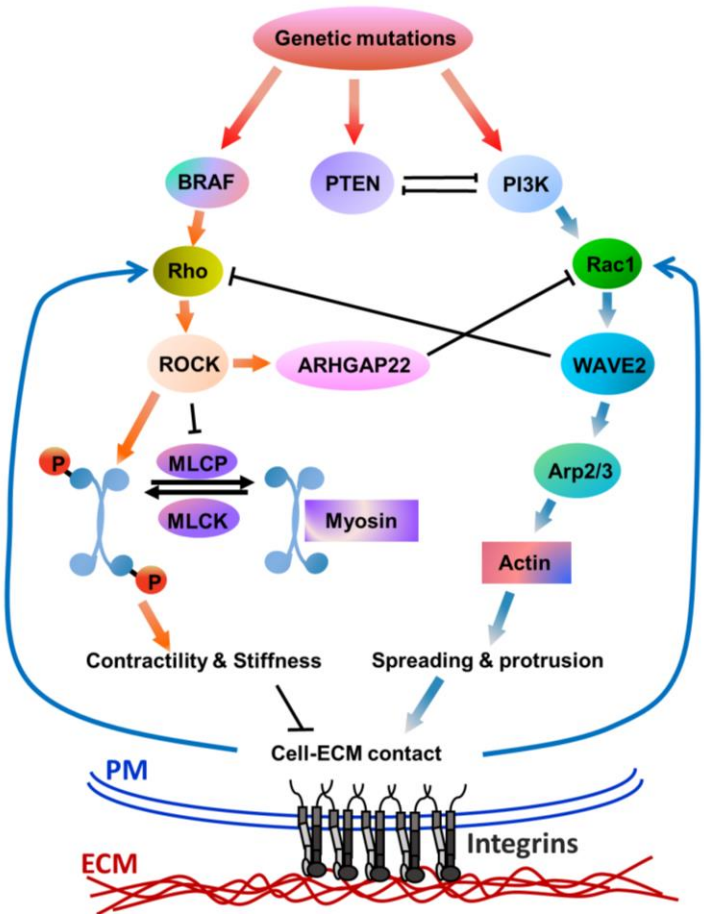

Figure 5.1: Schematic illustration of the effect of mutation profiles and cell-ECM contact on the signaling pathways controlling cytoskeletal dynamics.

distinct cortical plasticity of M4 cells allows FAs to form throughout the sawteeth. The FAs not only transduce extracellular forces but also induce multiple intracellular signaling cascades that can regulate actin polymerization and cell contractility through Rho GTPases (Mitra et al., 2005). Thus, I hypothesize that the cell-topography contact of breast cancer cells spatially controls the activation of distinct Rho GTPase signaling in a cell-type dependent manner (Fig.5.1). To address this issue, the western blot should be performed to examine the activity of Rho GTPase signaling in MDA-MB-231 and M4 cells cultured on sawteeth surfaces compared with that in cell-cultured on flat surfaces. Furthermore, the formation of FAs in live MDA-MB-231 and M4 cells on sawteeth surfaces should be examined by using a conjugated active integrin antibody or expressing paxillin-mCherry in cells. Finally, RhoA and Rac1 FRET sensors should be stably expressed in both cell types to study their spatiotemporal activity patterns during cell migration on sawteeth surfaces.

This proposed study aims to link the previously observed migration phenotypes of breast cancer cells on topographies with their unique mutation profile and intracellular signaling. By combining both upstream/downstream and intrinsic/external factors, this study will elucidate the mechanisms behind the topography-guided migration of breast cancer cell lines, and help the development of cancer prevention strategies by controlling cell migration.

Investigate the structural basis of the binding of the FLAP trimer and 5-LO

As introduced in the fourth chapter, the trimeric FLAP is required for the transfer of AA to 5-LO. However, since the proposed AA binding sites of trimeric FLAP are within the lipid bilayer and the catalytic core of 5-LO is encapsulated, how FLAP captures AA and transfers it to 5-LO, and what conformation changes occur during FLAP and 5-LO interaction are still not understood.

It has been suggested that the four cysteine residues located close to the AA entry site of 5-LO are important for its colocalization with FLAP (Hafner et al., 2015). Thus, I hypothesize that 5-LO interacts with a FLAP trimer at a specific protein-protein interface that is central for AA transfer and LTA_4 production.

To solve this problem, future studies should take advantage of the advanced nanodiscs and cryo-EM techniques. Nanodiscs are small lipid islands that are made of two membrane scaffold proteins around a lipid bilayer. The small size (~13 nm) of a nanodisc only supports the insertion of one FLAP trimer, which provides a homogeneous lipid environment for a single FLAP reconstitution. Purified 5-LO can be exogenously added to the nanodisc:FLAP assemblies. In theory, this approach will generate a single trimeric FLAP:5-LO complex in one nanodisc, whose structure can be examined using cryo-EM and single-particle reconstruction. After which, the existing crystal structures of FLAP and 5-LO can be docked into the reconstructed FLAP:5-LO complex to identify the interaction interface and conformational changes in each protein.

This study will provide valuable insights into the structural basis of membrane proteins in a native-like lipid context. In addition, the determination of the FLAP:5-LO complex will generate a molecular model for their interaction and AA transfer, which can potentially reveal novel targeting sites for inhibiting the production of pro-inflammatory LTB_4, and for the treatment of chronic inflammatory diseases.

Bibliography

Abram CL and Lowell CA (2009) The ins and outs of leukocyte integrin signaling. *Annu Rev Immunol* **27**: 339-362.

Afonso PV, Janka-Junttila M, Lee YJ, McCann CP, Oliver CM, Aamer KA, Losert W, Cicerone MT and Parent CA (2012) LTB4 is a signal-relay molecule during neutrophil chemotaxis. *Dev Cell* **22**(5): 1079-1091.

Ahn EH, Kim Y, Kshitiz, An SS, Afzal J, Lee S, Kwak M, Suh KY, Kim DH and Levchenko A (2014) Spatial control of adult stem cell fate using nanotopographic cues. *Biomaterials* **35**(8): 2401-2410.

Aimon S, Callan-Jones A, Berthaud A, Pinot M, Toombes GE and Bassereau P (2014) Membrane shape modulates transmembrane protein distribution. *Dev Cell* **28**(2): 212-218.

Alexander K. Nguyen RJN (2017) Two-photon polymerization for biological applications, *Materials Today* **20**: 9.

Alexander S, Koehl GE, Hirschberg M, Geissler EK and Friedl P (2008) Dynamic imaging of cancer growth and invasion: a modified skin-fold chamber model. *Histochem Cell Biol* **130**(6): 1147-1154.

Alford AI, Kozloff KM and Hankenson KD (2015) Extracellular matrix networks in bone remodeling. *Int J Biochem Cell Biol* **65**: 20-31.

Alimohamadi H and Rangamani P (2018) Modeling Membrane Curvature Generation due to Membrane(-)Protein Interactions. *Biomolecules* **8**(4).

Allen RD, Schroeder CC and Fok AK (1989) An investigation of mitochondrial inner membranes by rapid-freeze deep-etch techniques. *J Cell Biol* **108**(6): 2233-2240.

Amini-Nik S, Cambridge E, Yu W, Guo A, Whetstone H, Nadesan P, Poon R, Hinz B and Alman BA (2014) beta-Catenin-regulated myeloid cell adhesion and migration determine wound healing. *J Clin Invest* **124**(6): 2599-2610.

Anastasios Marmaras TL, Gianluca Civenni, Davide Franco, Dimos Poulikakos, Vartan Kurtcuoglu, Aldo Ferrari (2012) Topography-mediated apical guidance in epidermal wound healing. *Soft Matter* **8**: 10.

Antonny B (2011) Mechanisms of membrane curvature sensing. *Annu Rev Biochem* **80**: 101-123.

Antonny B, Huber I, Paris S, Chabre M and Cassel D (1997) Activation of ADP-ribosylation factor 1 GTPase-activating protein by phosphatidylcholine-derived diacylglycerols. *J Biol Chem* **272**(49): 30848-30851.

Arias-Salgado EG, Lizano S, Sarkar S, Brugge JS, Ginsberg MH and Shattil SJ (2003) Src kinase activation by direct interaction with the integrin beta cytoplasmic domain. *Proc Natl Acad Sci U S A* **100**(23): 13298-13302.

Arocena M, Rajnicek AM and Collinson JM (2017) Requirement of Pax6 for the integration of guidance cues in cell migration. *R Soc Open Sci* **4**(10): 170625.

Ashleigh Cooper CZ, Yoshito Kinoshita, Richard S. Morrison, Marco Rolandia, Miqin Zhang (2012) Self-assembled chitin nanofiber templates for artificial neural networks. *J Mater Chem* **22**: 5.

Autenrieth SE, Warnke P, Wabnitz GH, Lucero Estrada C, Pasquevich KA, Drechsler D, Gunter M, Hochweller K, Novakovic A, Beer-Hammer S, Samstag Y, Hammerling GJ, Garbi N and Autenrieth IB (2012) Depletion of dendritic cells enhances innate anti-bacterial host defense through modulation of phagocyte homeostasis. *PLoS Pathog* **8**(2): e1002552.

Badrossamay MR, McIlwee HA, Goss JA and Parker KK (2010) Nanofiber assembly by rotary jet-spinning. *Nano Lett* **10**(6): 2257-2261.

Badylak S, Obermiller J, Geddes L and Matheny R (2003) Extracellular matrix for myocardial repair. *Heart Surg Forum* **6**(2): E20-26.

Bagorda A and Parent CA (2008) Eukaryotic chemotaxis at a glance. *J Cell Sci* **121**(Pt 16): 2621-2624.

Baker BM and Mauck RL (2007) The effect of nanofiber alignment on the maturation of engineered meniscus constructs. *Biomaterials* **28**(11): 1967-1977.

Balaban NQ, Schwarz US, Riveline D, Goichberg P, Tzur G, Sabanay I, Mahalu D, Safran S, Bershadsky A, Addadi L and Geiger B (2001) Force and focal adhesion assembly: a close relationship studied using elastic micropatterned substrates. *Nat Cell Biol* **3**(5): 466-472.

Baldacchini T (ed) (2016) *Three-Dimensional Microfabrication Using Two-Photon Polymerization*. William Andrew, Oxford, UK.

Bauer M and Pelkmans L (2006) A new paradigm for membrane-organizing and -shaping scaffolds. *FEBS Lett* **580**(23): 5559-5564.

Baumann O and Walz B (2001) Endoplasmic reticulum of animal cells and its organization into structural and functional domains. *Int Rev Cytol* **205**: 149-214.

Bear JE and Haugh JM (2014) Directed migration of mesenchymal cells: where signaling and the cytoskeleton meet. *Curr Opin Cell Biol* **30**: 74-82.

Beck M, Mosalaganti S and Kosinski J (2018) From the resolution revolution to evolution: structural insights into the evolutionary relationships between vesicle coats and the nuclear pore. *Curr Opin Struct Biol* **52**: 32-40.

Beck R, Sun Z, Adolf F, Rutz C, Bassler J, Wild K, Sinning I, Hurt E, Brugger B, Bethune J and Wieland F (2008) Membrane curvature induced by Arf1-GTP is essential for vesicle formation. *Proc Natl Acad Sci U S A* **105**(33): 11731-11736.

Berk BC, Fujiwara K and Lehoux S (2007) ECM remodeling in hypertensive heart disease. *J Clin Invest* **117**(3): 568-575.

Berridge MJ, Lipp P and Bootman MD (2000) The versatility and universality of calcium signalling. *Nat Rev Mol Cell Biol* **1**(1): 11-21.

Betancourt T and Brannon-Peppas L (2006) Micro- and nanofabrication methods in nanotechnological medical and pharmaceutical devices. *Int J Nanomedicine* **1**(4): 483-495.

Bettinger CJ, Orrick B, Misra A, Langer R and Borenstein JT (2006) Microfabrication of poly (glycerol-sebacate) for contact guidance applications. *Biomaterials* **27**(12): 2558-2565.

Bigay J, Gounon P, Robineau S and Antonny B (2003) Lipid packing sensed by ArfGAP1 couples COPI coat disassembly to membrane bilayer curvature. *Nature* **426**(6966): 563-566.

Bing OH, Ngo HQ, Humphries DE, Robinson KG, Lucey EC, Carver W, Brooks WW, Conrad CH, Hayes JA and Goldstein RH (1997) Localization of alpha1(I) collagen mRNA in myocardium from the spontaneously hypertensive rat during the transition from compensated hypertrophy to failure. *J Mol Cell Cardiol* **29**(9): 2335-2344.

Blood PD, Swenson RD and Voth GA (2008) Factors influencing local membrane curvature induction by N-BAR domains as revealed by molecular dynamics simulations. *Biophys J* **95**(4): 1866-1876.

Blumenthal NR, Hermanson O, Heimrich B and Shastri VP (2014) Stochastic nanoroughness modulates neuron-astrocyte interactions and function via mechanosensing cation channels. *Proc Natl Acad Sci U S A* **111**(45): 16124-16129.

Bretschneider T, Diez S, Anderson K, Heuser J, Clarke M, Muller-Taubenberger A, Kohler J and Gerisch G (2004) Dynamic actin patterns and Arp2/3 assembly at the substrate-attached surface of motile cells. *Curr Biol* **14**(1): 1-10.

Bucaro MA, Vasquez Y, Hatton BD and Aizenberg J (2012) Fine-tuning the degree of stem cell polarization and alignment on ordered arrays of high-aspect-ratio nanopillars. *ACS Nano* **6**(7): 6222-6230.

Bursac N, Parker KK, Iravanian S and Tung L (2002) Cardiomyocyte cultures with controlled macroscopic anisotropy: a model for functional electrophysiological studies of cardiac muscle. *Circ Res* **91**(12): e45-54.

C. Vieu FC, A. Pe´pin, Y. Chen, M. Mejias, A. Lebib, L. Manin-Ferlazzo, L. Couraud, H. Launois (2000) Electron beam lithography: resolution limits and applications. *Applied Surface Science* **164**: 7.

Caballero D, Comelles J, Piel M, Voituriez R and Riveline D (2015a) Ratchetaxis: Long-Range Directed Cell Migration by Local Cues. *Trends Cell Biol* **25**(12): 815-827.

Caballero D, Voituriez R and Riveline D (2014) Protrusion fluctuations direct cell motion. *Biophys J* **107**(1): 34-42.

Caballero D, Voituriez R and Riveline D (2015b) The cell ratchet: interplay between efficient protrusions and adhesion determines cell motion. *Cell Adh Migr* **9**(5): 327-334.

Caltagarone J, Ma S and Sorkin A (2015) Dopamine transporter is enriched in filopodia and induces filopodia formation. *Mol Cell Neurosci* **68**: 120-130.

Campbell ID and Humphries MJ (2011) Integrin structure, activation, and interactions. *Cold Spring Harb Perspect Biol* **3**(3).

Campelo F, McMahon HT and Kozlov MM (2008) The hydrophobic insertion mechanism of membrane curvature generation by proteins. *Biophys J* **95**(5): 2325-2339.

Cancer Genome Atlas N (2012) Comprehensive molecular portraits of human breast tumours. *Nature* **490**(7418): 61-70.

Carson D, Hnilova M, Yang X, Nemeth CL, Tsui JH, Smith AS, Jiao A, Regnier M, Murry CE, Tamerler C and Kim DH (2016) Nanotopography-Induced Structural Anisotropy and Sarcomere Development in Human Cardiomyocytes Derived from Induced Pluripotent Stem Cells. *ACS Appl Mater Interfaces* **8**(34): 21923-21932.

Cautain B, Hill R, de Pedro N and Link W (2015) Components and regulation of nuclear transport processes. *FEBS J* **282**(3): 445-462.

Chan CK, Kumar TS, Liao S, Murugan R, Ngiam M and Ramakrishnan S (2006) Biomimetic nanocomposites for bone graft applications. *Nanomedicine (Lond)* **1**(2): 177-188.

Chen CS, Alonso JL, Ostuni E, Whitesides GM and Ingber DE (2003) Cell shape provides global control of focal adhesion assembly. *Biochem Biophys Res Commun* **307**(2): 355-361.

Chen H, Fre S, Slepnev VI, Capua MR, Takei K, Butler MH, Di Fiore PP and De Camilli P (1998) Epsin is an EH-domain-binding protein implicated in clathrin-mediated endocytosis. *Nature* **394**(6695): 793-797.

Chen S, Hourwitz MJ, Campanello L, Fourkas JT, Losert W and Parent CA (2019) Actin Cytoskeleton and Focal Adhesions Regulate the Biased Migration of Breast Cancer Cells on Nanoscale Asymmetric Sawteeth. *ACS Nano* **13**(2): 1454-1468.

Chen S, Li N, Hsu SF, Zhang J, Lai PY, Chan CK and Chen W (2014) Intrinsic fluctuations of cell migration under different cellular densities. *Soft Matter* **10**(19): 3421-3425.

Chen X, Xie C, Nishida N, Li Z, Walz T and Springer TA (2010) Requirement of open headpiece conformation for activation of leukocyte integrin alphaXbeta2. *Proc Natl Acad Sci U S A* **107**(33): 14727-14732.

Chou RC, Kim ND, Sadik CD, Seung E, Lan Y, Byrne MH, Haribabu B, Iwakura Y and Luster AD (2010) Lipid-cytokine-chemokine cascade drives neutrophil recruitment in a murine model of inflammatory arthritis. *Immunity* **33**(2): 266-278.

Chou T, Kim KS and Oster G (2001) Statistical thermodynamics of membrane bending-mediated protein-protein attractions. *Biophys J* **80**(3): 1075-1087.

Chua JS, Chng CP, Moe AA, Tann JY, Goh EL, Chiam KH and Yim EK (2014) Extending neurites sense the depth of the underlying topography during neuronal differentiation and contact guidance. *Biomaterials* **35**(27): 7750-7761.

Clapham DE (2007) Calcium signaling. *Cell* **131**(6): 1047-1058.

Clemens RA and Lowell CA (2015) Store-operated calcium signaling in neutrophils. *J Leukoc Biol* **98**(4): 497-502.

Cluzel C, Saltel F, Lussi J, Paulhe F, Imhof BA and Wehrle-Haller B (2005) The mechanisms and dynamics of (alpha)v(beta)3 integrin clustering in living cells. *J Cell Biol* **171**(2): 383-392.

Comelles J, Caballero D, Voituriez R, Hortiguela V, Wollrab V, Godeau AL, Samitier J, Martinez E and Riveline D (2014) Cells as active particles in asymmetric potentials: motility under external gradients. *Biophys J* **107**(7): 1513-1522.

Cukierman E, Huber I, Rotman M and Cassel D (1995) The ARF1 GTPase-activating protein: zinc finger motif and Golgi complex localization. *Science* **270**(5244): 1999-2002.

Cukierman E, Pankov R, Stevens DR and Yamada KM (2001) Taking cell-matrix adhesions to the third dimension. *Science* **294**(5547): 1708-1712.

da Silva Meirelles L, Chagastelles PC and Nardi NB (2006) Mesenchymal stem cells reside in virtually all post-natal organs and tissues. *J Cell Sci* **119**(Pt 11): 2204-2213.

Dalby MJ, Gadegaard N, Tare R, Andar A, Riehle MO, Herzyk P, Wilkinson CD and Oreffo RO (2007) The control of human mesenchymal cell differentiation using nanoscale symmetry and disorder. *Nat Mater* **6**(12): 997-1003.

Dang JM and Leong KW (2007) Myogenic Induction of Aligned Mesenchymal Stem Cell Sheets by Culture on Thermally Responsive Electrospun Nanofibers. *Adv Mater* **19**(19): 2775-2779.

Darland DC and D'Amore PA (2001) Cell-cell interactions in vascular development. *Curr Top Dev Biol* **52**: 107-149.

de Rubio RG, Ransom RF, Malik S, Yule DI, Anantharam A and Smrcka AV (2018) Phosphatidylinositol 4-phosphate is a major source of GPCR-stimulated phosphoinositide production. *Sci Signal* **11**(547).

Deakin NO and Turner CE (2008) Paxillin comes of age. *J Cell Sci* **121**(Pt 15): 2435-2444.

Deitzel JM KJ, Harris D, Beck Tan NC (2001) The effect of processing variables on the morphology of electrospun nanofibers and textiles. *Polymer* **42**: 12.

Delgado-Rivera R, Harris SL, Ahmed I, Babu AN, Patel RP, Ayres V, Flowers D and Meiners S (2009) Increased FGF-2 secretion and ability to support neurite outgrowth by astrocytes cultured on polyamide nanofibrillar matrices. *Matrix Biol* **28**(3): 137-147.

Demonbreun AR and McNally EM (2017) Muscle cell communication in development and repair. *Curr Opin Pharmacol* **34**: 7-14.

Desai BN and Leitinger N (2014) Purinergic and calcium signaling in macrophage function and plasticity. *Front Immunol* **5**: 580.

Deutsch J, Motlagh D, Russell B and Desai TA (2000) Fabrication of microtextured membranes for cardiac myocyte attachment and orientation. *J Biomed Mater Res* **53**(3): 267-275.

Devreotes P and Horwitz AR (2015) Signaling networks that regulate cell migration. *Cold Spring Harb Perspect Biol* **7**(8): a005959.

Di Paolo G and De Camilli P (2006) Phosphoinositides in cell regulation and membrane dynamics. *Nature* **443**(7112): 651-657.

Di Sano F, Bernardoni P and Piacentini M (2012) The reticulons: guardians of the structure and function of the endoplasmic reticulum. *Exp Cell Res* **318**(11): 1201-1207.

DiVietro JA, Smith MJ, Smith BR, Petruzzelli L, Larson RS and Lawrence MB (2001) Immobilized IL-8 triggers progressive activation of neutrophils rolling in vitro on P-selectin and intercellular adhesion molecule-1. *J Immunol* **167**(7): 4017-4025.

Dixit N, Yamayoshi I, Nazarian A and Simon SI (2011) Migrational guidance of neutrophils is mechanotransduced via high-affinity LFA-1 and calcium flux. *J Immunol* **187**(1): 472-481.

Doubrovinski K and Kruse K (2011) Cell motility resulting from spontaneous polymerization waves. *Phys Rev Lett* **107**(25): 258103.

Doucet CM and Hetzer MW (2010) Nuclear pore biogenesis into an intact nuclear envelope. *Chromosoma* **119**(5): 469-477.

Dowell-Mesfin NM, Abdul-Karim MA, Turner AM, Schanz S, Craighead HG, Roysam B, Turner JN and Shain W (2004) Topographically modified surfaces affect orientation and growth of hippocampal neurons. *J Neural Eng* **1**(2): 78-90.

Doyle AD, Carvajal N, Jin A, Matsumoto K and Yamada KM (2015) Local 3D matrix microenvironment regulates cell migration through spatiotemporal dynamics of contractility-dependent adhesions. *Nat Commun* **6**: 8720.

Driscoll MK, Sun X, Guven C, Fourkas JT and Losert W (2014) Cellular contact guidance through dynamic sensing of nanotopography. *ACS Nano* **8**(4): 3546-3555.

Dudkina NV, Sunderhaus S, Braun HP and Boekema EJ (2006) Characterization of dimeric ATP synthase and cristae membrane ultrastructure from Saccharomyces and Polytomella mitochondria. *FEBS Lett* **580**(14): 3427-3432.

Dugan JM, Gough JE and Eichhorn SJ (2010) Directing the morphology and differentiation of skeletal muscle cells using oriented cellulose nanowhiskers. *Biomacromolecules* **11**(9): 2498-2504.

Dvir T, Timko BP, Kohane DS and Langer R (2011) Nanotechnological strategies for engineering complex tissues. *Nat Nanotechnol* **6**(1): 13-22.

Efron B (1979) Bootstrap methods: another look at the Jack-knife. *Ann Stat* **7**: 1-26.

Efron B. and Tibshirani RJ (1993) *An Introduction to the Bootstrap*. New York: Chapman & Hall.

Everard-Gigot V, Dunn CD, Dolan BM, Brunner S, Jensen RE and Stuart RA (2005) Functional analysis of subunit e of the F1Fo-ATP synthase of the yeast Saccharomyces cerevisiae: importance of the N-terminal membrane anchor region. *Eukaryot Cell* **4**(2): 346-355.

Ezratty EJ, Bertaux C, Marcantonio EE and Gundersen GG (2009) Clathrin mediates integrin endocytosis for focal adhesion disassembly in migrating cells. *J Cell Biol* **187**(5): 733-747.

Ezratty EJ, Partridge MA and Gundersen GG (2005) Microtubule-induced focal adhesion disassembly is mediated by dynamin and focal adhesion kinase. *Nat Cell Biol* **7**(6): 581-590.

Fan Z, McArdle S, Marki A, Mikulski Z, Gutierrez E, Engelhardt B, Deutsch U, Ginsberg M, Groisman A and Ley K (2016) Neutrophil recruitment limited by high-affinity bent beta2 integrin binding ligand in cis. *Nat Commun* **7**: 12658.

Farsad K and De Camilli P (2003) Mechanisms of membrane deformation. *Curr Opin Cell Biol* **15**(4): 372-381.

Farsad K, Ringstad N, Takei K, Floyd SR, Rose K and De Camilli P (2001) Generation of high curvature membranes mediated by direct endophilin bilayer interactions. *J Cell Biol* **155**(2): 193-200.

Fata JE, Werb Z and Bissell MJ (2004) Regulation of mammary gland branching morphogenesis by the extracellular matrix and its remodeling enzymes. *Breast Cancer Res* **6**(1): 1-11.

Ferguson AD, McKeever BM, Xu S, Wisniewski D, Miller DK, Yamin TT, Spencer RH, Chu L, Ujjainwalla F, Cunningham BR, Evans JF and Becker JW (2007) Crystal structure of inhibitor-bound human 5-lipoxygenase-activating protein. *Science* **317**(5837): 510-512.

Filippi MD (2019) Neutrophil transendothelial migration: updates and new perspectives. *Blood* **133**(20): 2149-2158.

Ford MG, Mills IG, Peter BJ, Vallis Y, Praefcke GJ, Evans PR and McMahon HT (2002) Curvature of clathrin-coated pits driven by epsin. *Nature* **419**(6905): 361-366.

Foulkes WD, Smith IE and Reis-Filho JS (2010) Triple-negative breast cancer. *N Engl J Med* **363**(20): 1938-1948.

Frantz C, Stewart KM and Weaver VM (2010) The extracellular matrix at a glance. *J Cell Sci* **123**(Pt 24): 4195-4200.

Fraser RD, MacRae TP, Miller A and Suzuki E (1983) Molecular conformation and packing in collagen fibrils. *J Mol Biol* **167**(2): 497-521.

Friedl P (2004) Prespecification and plasticity: shifting mechanisms of cell migration. *Curr Opin Cell Biol* **16**(1): 14-23.

Friedl P and Alexander S (2011) Cancer invasion and the microenvironment: plasticity and reciprocity. *Cell* **147**(5): 992-1009.

Friedl P and Wolf K (2010) Plasticity of cell migration: a multiscale tuning model. *J Cell Biol* **188**(1): 11-19.

Fritz RD, Menshykau D, Martin K, Reimann A, Pontelli V and Pertz O (2015) SrGAP2-Dependent Integration of Membrane Geometry and Slit-Robo-Repulsive Cues Regulates Fibroblast Contact Inhibition of Locomotion. *Dev Cell* **35**(1): 78-92.

Frost A, Perera R, Roux A, Spasov K, Destaing O, Egelman EH, De Camilli P and Unger VM (2008) Structural basis of membrane invagination by F-BAR domains. *Cell* **132**(5): 807-817.

Galbraith CG, Yamada KM and Sheetz MP (2002) The relationship between force and focal complex development. *J Cell Biol* **159**(4): 695-705.

Gallant ND, Michael KE and Garcia AJ (2005) Cell adhesion strengthening: contributions of adhesive area, integrin binding, and focal adhesion assembly. *Mol Biol Cell* **16**(9): 4329-4340.

Gallop JL, Jao CC, Kent HM, Butler PJ, Evans PR, Langen R and McMahon HT (2006) Mechanism of endophilin N-BAR domain-mediated membrane curvature. *EMBO J* **25**(12): 2898-2910.

Gao H (2006) Application of fracture mechanics concepts to hierarchical biomechanics of bone and bone-like materials. *Int J Fract* **138**: 37.

Gao H, Ji B, Jager IL, Arzt E and Fratzl P (2003) Materials become insensitive to flaws at nanoscale: lessons from nature. *Proc Natl Acad Sci U S A* **100**(10): 5597-5600.

Geiger B, Spatz JP and Bershadsky AD (2009) Environmental sensing through focal adhesions. *Nat Rev Mol Cell Biol* **10**(1): 21-33.

Gentili C and Cancedda R (2009) Cartilage and bone extracellular matrix. *Curr Pharm Des* **15**(12): 1334-1348.

Ghajar CM and Bissell MJ (2008) Extracellular matrix control of mammary gland morphogenesis and tumorigenesis: insights from imaging. *Histochem Cell Biol* **130**(6): 1105-1118.

Gilbert NC, Bartlett SG, Waight MT, Neau DB, Boeglin WE, Brash AR and Newcomer ME (2011) The structure of human 5-lipoxygenase. *Science* **331**(6014): 217-219.

Goffin JM, Pittet P, Csucs G, Lussi JW, Meister JJ and Hinz B (2006) Focal adhesion size controls tension-dependent recruitment of alpha-smooth muscle actin to stress fibers. *J Cell Biol* **172**(2): 259-268.

Gov NS (2018) Guided by curvature: shaping cells by coupling curved membrane proteins and cytoskeletal forces. *Philos Trans R Soc Lond B Biol Sci* **373**(1747).

Graham IL, Lefkowith JB, Anderson DC and Brown EJ (1993) Immune complex-stimulated neutrophil LTB4 production is dependent on beta 2 integrins. *J Cell Biol* **120**(6): 1509-1517.

Grinnell F (2003) Fibroblast biology in three-dimensional collagen matrices. *Trends Cell Biol* **13**(5): 264-269.

Groffen AJ, Martens S, Diez Arazola R, Cornelisse LN, Lozovaya N, de Jong AP, Goriounova NA, Habets RL, Takai Y, Borst JG, Brose N, McMahon HT and Verhage M (2010) Doc2b is a high-affinity Ca2+ sensor for spontaneous neurotransmitter release. *Science* **327**(5973): 1614-1618.

Guilluy C, Garcia-Mata R and Burridge K (2011) Rho protein crosstalk: another social network? *Trends Cell Biol* **21**(12): 718-726.

Guo C and Kaufman LJ (2007) Flow and magnetic field induced collagen alignment. *Biomaterials* **28**(6): 1105-1114.

Haeggstrom JZ (2018) Leukotriene biosynthetic enzymes as therapeutic targets. *J Clin Invest* **128**(7): 2680-2690.

Hafner AK, Gerstmeier J, Hornig M, George S, Ball AK, Schroder M, Garscha U, Werz O and Steinhilber D (2015) Characterization of the interaction of human 5-lipoxygenase with its activating protein FLAP. *Biochim Biophys Acta* **1851**(11): 1465-1472.

Hanna MGt, Mela I, Wang L, Henderson RM, Chapman ER, Edwardson JM and Audhya A (2016) Sar1 GTPase Activity Is Regulated by Membrane Curvature. *J Biol Chem* **291**(3): 1014-1027.

Hanson PI and Cashikar A (2012) Multivesicular body morphogenesis. *Annu Rev Cell Dev Biol* **28**: 337-362.

Hato T, Pampori N and Shattil SJ (1998) Complementary roles for receptor clustering and conformational change in the adhesive and signaling functions of integrin alphaIIb beta3. *J Cell Biol* **141**(7): 1685-1695.

Haucke V and Kozlov MM (2018) Membrane remodeling in clathrin-mediated endocytosis. *J Cell Sci* **131**(17).

Henne WM, Boucrot E, Meinecke M, Evergren E, Vallis Y, Mittal R and McMahon HT (2010) FCHo proteins are nucleators of clathrin-mediated endocytosis. *Science* **328**(5983): 1281-1284.

Henne WM, Kent HM, Ford MG, Hegde BG, Daumke O, Butler PJ, Mittal R, Langen R, Evans PR and McMahon HT (2007) Structure and analysis of FCHo2 F-BAR domain: a dimerizing and membrane recruitment module that effects membrane curvature. *Structure* **15**(7): 839-852.

Hoelz A, Debler EW and Blobel G (2011) The structure of the nuclear pore complex. *Annu Rev Biochem* **80**: 613-643.

Hollestelle A, Elstrodt F, Nagel JH, Kallemeijn WW and Schutte M (2007) Phosphatidylinositol-3-OH kinase or RAS pathway mutations in human breast cancer cell lines. *Mol Cancer Res* **5**(2): 195-201.

Holmes WR, Park J, Levchenko A and Edelstein-Keshet L (2017) A mathematical model coupling polarity signaling to cell adhesion explains diverse cell migration patterns. *PLoS Comput Biol* **13**(5): e1005524.

Horn BK and Schunck BG (1981) Determining optical flow. *Artificial intelligence* **17**: 185--203.

Hu J, Shibata Y, Voss C, Shemesh T, Li Z, Coughlin M, Kozlov MM, Rapoport TA and Prinz WA (2008) Membrane proteins of the endoplasmic reticulum induce high-curvature tubules. *Science* **319**(5867): 1247-1250.

Huang NF, Patel S, Thakar RG, Wu J, Hsiao BS, Chu B, Lee RJ and Li S (2006) Myotube assembly on nanofibrous and micropatterned polymers. *Nano Lett* **6**(3): 537-542.

Humphries JD, Byron A and Humphries MJ (2006) Integrin ligands at a glance. *J Cell Sci* **119**(Pt 19): 3901-3903.

Hyewon K, Jiyeon L, Joonhyung P and Hong HL (2006) An improved method of preparing composite poly(dimethylsiloxane) moulds. *Nanotechnology* **17**(1): 197.

Iversen MB, Reinert LS, Thomsen MK, Bagdonaite I, Nandakumar R, Cheshenko N, Prabakaran T, Vakhrushev SY, Krzyzowska M, Kratholm SK, Ruiz-Perez F, Petersen SV, Goriely S, Bibby BM, Eriksson K, Ruland J, Thomsen AR, Herold BC, Wandall HH, Frische S, Holm CK and Paludan SR (2016) An innate antiviral pathway acting before interferons at epithelial surfaces. *Nat Immunol* **17**(2): 150-158.

Iwabuchi K, Masuda H, Kaga N, Nakayama H, Matsumoto R, Iwahara C, Yoshizaki F, Tamaki Y, Kobayashi T, Hayakawa T, Ishii K, Yanagida M, Ogawa H and Takamori K (2015) Properties and functions of lactosylceramide from mouse neutrophils. *Glycobiology* **25**(6): 655-668.

J. W. Lussi CT, P. A. Kuenzi , U. Staufer , G. Csucs , J. Voros , G. Danuser , J. A. Hubbell , M. Textor (2005) Selective molecular assembly patterning at the nanoscale: a novel platform for producing protein patterns by electron-beam lithography on SiO2/indium tin oxide-coated glass substrates. *Nanotechnology* **16**: 9.

Jaconi ME, Theler JM, Schlegel W, Appel RD, Wright SD and Lew PD (1991) Multiple elevations of cytosolic-free Ca2+ in human neutrophils: initiation by adherence receptors of the integrin family. *J Cell Biol* **112**(6): 1249-1257.

Jang KJ, Kim MS, Feltrin D, Jeon NL, Suh KY and Pertz O (2010) Two distinct filopodia populations at the growth cone allow to sense nanotopographical extracellular matrix cues to guide neurite outgrowth. *PLoS One* **5**(12): e15966.

Jarsch IK, Daste F and Gallop JL (2016) Membrane curvature in cell biology: An integration of molecular mechanisms. *J Cell Biol* **214**(4): 375-387.

Johansen E and Parks HF (1960) Electron microscopic observations on the three-dimensional morphology of apatite crystallites of human dentine and bone. *J Biophys Biochem Cytol* **7**: 743-746.

K. Takada H-BS, S. Kawata (2005) Improved spatial resolution and surface roughness in photopolymerization-based laser nanowriting. *Applied Physics Letter* **86**.

Kadota M, Yang HH, Gomez B, Sato M, Clifford RJ, Meerzaman D, Dunn BK, Wakefield LM and Lee MP (2010) Delineating genetic alterations for tumor progression in the MCF10A series of breast cancer cell lines. *PLoS One* **5**(2): e9201.

Kaksonen M, Toret CP and Drubin DG (2005) A modular design for the clathrin- and actin-mediated endocytosis machinery. *Cell* **123**(2): 305-320.

Kanchanawong P, Shtengel G, Pasapera AM, Ramko EB, Davidson MW, Hess HF and Waterman CM (2010) Nanoscale architecture of integrin-based cell adhesions. *Nature* **468**(7323): 580-584.

Kao J, Salari K, Bocanegra M, Choi YL, Girard L, Gandhi J, Kwei KA, Hernandez-Boussard T, Wang P, Gazdar AF, Minna JD and Pollack JR (2009) Molecular profiling of breast cancer cell lines defines relevant tumor models and provides a resource for cancer gene discovery. *PLoS One* **4**(7): e6146.

Keely PJ, Wu JE and Santoro SA (1995) The spatial and temporal expression of the alpha 2 beta 1 integrin and its ligands, collagen I, collagen IV, and laminin, suggest important roles in mouse mammary morphogenesis. *Differentiation* **59**(1): 1-13.

Kilian KA, Bugarija B, Lahn BT and Mrksich M (2010) Geometric cues for directing the differentiation of mesenchymal stem cells. *Proc Natl Acad Sci U S A* **107**(11): 4872-4877.

Kim C, Lau TL, Ulmer TS and Ginsberg MH (2009a) Interactions of platelet integrin alphaIIb and beta3 transmembrane domains in mammalian cell membranes and their role in integrin activation. *Blood* **113**(19): 4747-4753.

Kim DH, Han K, Gupta K, Kwon KW, Suh KY and Levchenko A (2009b) Mechanosensitivity of fibroblast cell shape and movement to anisotropic substratum topography gradients. *Biomaterials* **30**(29): 5433-5444.

Kim DH, Lipke EA, Kim P, Cheong R, Thompson S, Delannoy M, Suh KY, Tung L and Levchenko A (2010) Nanoscale cues regulate the structure and function of macroscopic cardiac tissue constructs. *Proc Natl Acad Sci U S A* **107**(2): 565-570.

Kim DH, Provenzano PP, Smith CL and Levchenko A (2012) Matrix nanotopography as a regulator of cell function. *J Cell Biol* **197**(3): 351-360.

Kim DH, Seo CH, Han K, Kwon KW, Levchenko A and Suh KY (2009c) Guided Cell Migration on Microtextured Substrates with Variable Local Density and Anisotropy. *Adv Funct Mater* **19**(10): 1579-1586.

Kim HN, Jang KJ, Shin JY, Kang D, Kim SM, Koh I, Hong Y, Jang S, Kim MS, Kim BS, Jeong HE, Jeon NL, Kim P and Suh KY (2017a) Artificial Slanted Nanocilia Array as a Mechanotransducer for Controlling Cell Polarity. *ACS Nano* **11**(1): 730-741.

Kim J, Bae WG, Kim YJ, Seonwoo H, Choung HW, Jang KJ, Park S, Kim BH, Kim HN, Choi KS, Kim MS, Choung PH, Choung YH and Chung JH (2017b) Directional Matrix Nanotopography with Varied Sizes for Engineering Wound Healing. *Adv Healthc Mater* **6**(19).

Kim SY, Kang JH, Seo WS, Lee SW, Oh NS, Cho HK and Lee MH (2015) Effect of topographical control by a micro-molding process on the activity of human Mesenchymal Stem Cells on alumina ceramics. *Biomater Res* **19**: 23.

Klickstein LB, Shapleigh C and Goetzl EJ (1980) Lipoxygenation of arachidonic acid as a source of polymorphonuclear leukocyte chemotactic factors in synovial fluid and tissue in rheumatoid arthritis and spondyloarthritis. *J Clin Invest* **66**(5): 1166-1170.

Klopfenstein DR, Klumperman J, Lustig A, Kammerer RA, Oorschot V and Hauri HP (2001) Subdomain-specific localization of CLIMP-63 (p63) in the endoplasmic reticulum is mediated by its luminal alpha-helical segment. *J Cell Biol* **153**(6): 1287-1300.

Klymov A, Rodrigues Neves CT, te Riet J, Agterberg MJ, Mylanus EA, Snik AF, Jansen JA and Walboomers XF (2015) Nanogrooved surface-patterns induce cellular organization and axonal outgrowth in neuron-like PC12-cells. *Hear Res* **320**: 11-17.

Ko E, Yu SJ, Pagan-Diaz GJ, Mahmassani Z, Boppart MD, Im SG, Bashir R and Kong H (2019) Matrix Topography Regulates Synaptic Transmission at the Neuromuscular Junction. *Adv Sci (Weinh)* **6**(6): 1801521.

Koo SJ, Kochlamazashvili G, Rost B, Puchkov D, Gimber N, Lehmann M, Tadeus G, Schmoranzer J, Rosenmund C, Haucke V and Maritzen T (2015) Vesicular Synaptobrevin/VAMP2 Levels Guarded by AP180 Control Efficient Neurotransmission. *Neuron* **88**(2): 330-344.

Krause KH, Campbell KP, Welsh MJ and Lew DP (1990) The calcium signal and neutrophil activation. *Clin Biochem* **23**(2): 159-166.

Krauss K and Altevogt P (1999) Integrin leukocyte function-associated antigen-1-mediated cell binding can be activated by clustering of membrane rafts. *J Biol Chem* **274**(52): 36921-36927.

Krauss M, Jia JY, Roux A, Beck R, Wieland FT, De Camilli P and Haucke V (2008) Arf1-GTP-induced tubule formation suggests a function of Arf family proteins in curvature acquisition at sites of vesicle budding. *J Biol Chem* **283**(41): 27717-27723.

Kruse K (2016a) Cell Crawling Driven by Spontaneous Actin Polymerization Waves, in *Physical Models of Cell Motility* (Aranson IS ed) pp 69-93, Springers, Cham Biological and Medical Physics, Biomedical Engineering.

Kruse K (2016b) *Cell Crawling Driven by Spontaneous Actin Polymerization Waves*. Springer.

Kubow KE, Shuklis VD, Sales DJ and Horwitz AR (2017) Contact guidance persists under myosin inhibition due to the local alignment of adhesions and individual protrusions. *Sci Rep* **7**(1): 14380.

Kwon KW, Park H and Doh J (2013) Migration of T cells on surfaces containing complex nanotopography. *PLoS One* **8**(9): e73960.

Kwon KW, Park H, Song KH, Choi JC, Ahn H, Park MJ, Suh KY and Doh J (2012) Nanotopography-guided migration of T cells. *J Immunol* **189**(5): 2266-2273.

Ladinsky MS, Mastronarde DN, McIntosh JR, Howell KE and Staehelin LA (1999) Golgi structure in three dimensions: functional insights from the normal rat kidney cell. *J Cell Biol* **144**(6): 1135-1149.

Laflamme MA and Murry CE (2011) Heart regeneration. *Nature* **473**(7347): 326-335.

LaFratta CN, Fourkas JT, Baldacchini T and Farrer RA (2007) Multiphoton fabrication. *Angew Chem Int Ed Engl* **46**(33): 6238-6258.

Lammermann T, Afonso PV, Angermann BR, Wang JM, Kastenmuller W, Parent CA and Germain RN (2013) Neutrophil swarms require LTB4 and integrins at sites of cell death in vivo. *Nature* **498**(7454): 371-375.

Lammermann T, Bader BL, Monkley SJ, Worbs T, Wedlich-Soldner R, Hirsch K, Keller M, Forster R, Critchley DR, Fassler R and Sixt M (2008) Rapid leukocyte migration by integrin-independent flowing and squeezing. *Nature* **453**(7191): 51-55.

Lanfer B, Freudenberg U, Zimmermann R, Stamov D, Korber V and Werner C (2008) Aligned fibrillar collagen matrices obtained by shear flow deposition. *Biomaterials* **29**(28): 3888-3895.

Lauria I, Kramer M, Schroder T, Kant S, Hausmann A, Boke F, Leube R, Telle R and Fischer H (2016) Inkjet printed periodical micropatterns made of inert alumina ceramics induce contact guidance and stimulate osteogenic differentiation of mesenchymal stromal cells. *Acta Biomater* **44**: 85-96.

Lee CH, Cheng YW and Huang GS (2014) Topographical control of cell-cell interaction in C6 glioma by nanodot arrays. *Nanoscale Res Lett* **9**(1): 250.

Lee I, Kim D, Park GL, Jeon TJ and Kim SM (2018) Investigation of wound healing process guided by nano-scale topographic patterns integrated within a microfluidic system. *PLoS One* **13**(7): e0201418.

Lee MC, Orci L, Hamamoto S, Futai E, Ravazzola M and Schekman R (2005) Sar1p N-terminal helix initiates membrane curvature and completes the fission of a COPII vesicle. *Cell* **122**(4): 605-617.

Lee P, Lin R, Moon J and Lee LP (2006) Microfluidic alignment of collagen fibers for in vitro cell culture. *Biomed Microdevices* **8**(1): 35-41.

Lepzelter D, Bates O and Zaman M (2012) Integrin clustering in two and three dimensions. *Langmuir* **28**(12): 5379-5386.

Ley K, Laudanna C, Cybulsky MI and Nourshargh S (2007) Getting to the site of inflammation: the leukocyte adhesion cascade updated. *Nat Rev Immunol* **7**(9): 678-689.

Li H, Wen F, Wong YS, Boey FY, Subbu VS, Leong DT, Ng KW, Ng GK and Tan LP (2012) Direct laser machining-induced topographic pattern promotes up-regulation of myogenic markers in human mesenchymal stem cells. *Acta Biomater* **8**(2): 531-539.

Li J, Su Y, Xia W, Qin Y, Humphries MJ, Vestweber D, Cabanas C, Lu C and Springer TA (2017) Conformational equilibria and intrinsic affinities define integrin activation. *EMBO J* **36**(5): 629-645.

Li X, Macewan MR, Xie JD, Siewe D, Yuan X and Xia Y (2010) Fabrication of Density Gradients of Biodegradable Polymer Microparticles and Their Use in Guiding Neurite Outgrowth. *Adv Funct Mater* **20**(10): 1632-1637.

Li Z (1999) The alphaMbeta2 integrin and its role in neutrophil function. *Cell Res* **9**(3): 171-178.

Limongi T, Cesca F, Gentile F, Marotta R, Ruffilli R, Barberis A, Dal Maschio M, Petrini EM, Santoriello S, Benfenati F and Di Fabrizio E (2013) Nanostructured superhydrophobic substrates trigger the development of 3D neuronal networks. *Small* **9**(3): 402-412.

Lockhart M, Wirrig E, Phelps A and Wessels A (2011) Extracellular matrix and heart development. *Birth Defects Res A Clin Mol Teratol* **91**(6): 535-550.

Lou HY, Zhao W, Li X, Duan L, Powers A, Akamatsu M, Santoro F, McGuire AF, Cui Y, Drubin DG and Cui B (2019) Membrane curvature underlies actin reorganization in response to nanoscale surface topography. *Proc Natl Acad Sci U S A* **116**(46): 23143-23151.

Lou HY, Zhao W, Zeng Y and Cui B (2018) The Role of Membrane Curvature in Nanoscale Topography-Induced Intracellular Signaling. *Acc Chem Res* **51**(5): 1046-1053.

Lucas BD and Kanade T (1981) An iterative image registration technique with an application to stereo vision, in *Proceedings of the 7th international joint conference on Artificial intelligence* pp 674-679.

Luna JI, Ciriza J, Garcia-Ojeda ME, Kong M, Herren A, Lieu DK, Li RA, Fowlkes CC, Khine M and McCloskey KE (2011) Multiscale biomimetic topography for the alignment of

neonatal and embryonic stem cell-derived heart cells. *Tissue Eng Part C Methods* **17**(5): 579-588.
Lundmark R and Carlsson SR (2004) Regulated membrane recruitment of dynamin-2 mediated by sorting nexin 9. *J Biol Chem* **279**(41): 42694-42702.
Lundmark R and Carlsson SR (2009) SNX9 - a prelude to vesicle release. *J Cell Sci* **122**(Pt 1): 5-11.
Luo BH, Carman CV and Springer TA (2007) Structural basis of integrin regulation and signaling. *Annu Rev Immunol* **25**: 619-647.
Maiuri P, Rupprecht JF, Wieser S, Ruprecht V, Benichou O, Carpi N, Coppey M, De Beco S, Gov N, Heisenberg CP, Lage Crespo C, Lautenschlaeger F, Le Berre M, Lennon-Dumenil AM, Raab M, Thiam HR, Piel M, Sixt M and Voituriez R (2015) Actin flows mediate a universal coupling between cell speed and cell persistence. *Cell* **161**(2): 374-386.
Majumdar R, Tavakoli Tameh A and Parent CA (2016) Exosomes Mediate LTB4 Release during Neutrophil Chemotaxis. *PLoS Biol* **14**(1): e1002336.
Makrodouli E, Oikonomou E, Koc M, Andera L, Sasazuki T, Shirasawa S and Pintzas A (2011) BRAF and RAS oncogenes regulate Rho GTPase pathways to mediate migration and invasion properties in human colon cancer cells: a comparative study. *Mol Cancer* **10**: 118.
Mandal AK, Jones PB, Bair AM, Christmas P, Miller D, Yamin TT, Wisniewski D, Menke J, Evans JF, Hyman BT, Bacskai B, Chen M, Lee DM, Nikolic B and Soberman RJ (2008) The nuclear membrane organization of leukotriene synthesis. *Proc Natl Acad Sci U S A* **105**(51): 20434-20439.
Manneville JB, Casella JF, Ambroggio E, Gounon P, Bertherat J, Bassereau P, Cartaud J, Antonny B and Goud B (2008) COPI coat assembly occurs on liquid-disordered domains and the associated membrane deformations are limited by membrane tension. *Proc Natl Acad Sci U S A* **105**(44): 16946-16951.
Marcus M, Baranes K, Park M, Choi IS, Kang K and Shefi O (2017) Interactions of Neurons with Physical Environments. *Adv Healthc Mater* **6**(15).
Marella NV, Malyavantham KS, Wang J, Matsui S, Liang P and Berezney R (2009) Cytogenetic and cDNA microarray expression analysis of MCF10 human breast cancer progression cell lines. *Cancer Res* **69**(14): 5946-5953.
Marinaro G, La Rocca R, Toma A, Barberio M, Cancedda L, Di Fabrizio E, Decuzzi P and Gentile F (2015) Networks of neuroblastoma cells on porous silicon substrates reveal a small world topology. *Integr Biol (Camb)* **7**(2): 184-197.
Martens S, Kozlov MM and McMahon HT (2007) How synaptotagmin promotes membrane fusion. *Science* **316**(5828): 1205-1208.
Matsuyama M, Yoshimura R, Mitsuhashi M, Hase T, Tsuchida K, Takemoto Y, Kawahito Y, Sano H and Nakatani T (2004) Expression of lipoxygenase in human prostate cancer and growth reduction by its inhibitors. *Int J Oncol* **24**(4): 821-827.
Mattes B and Scholpp S (2018) Emerging role of contact-mediated cell communication in tissue development and diseases. *Histochem Cell Biol* **150**(5): 431-442.
McBeath R, Pirone DM, Nelson CM, Bhadriraju K and Chen CS (2004) Cell shape, cytoskeletal tension, and RhoA regulate stem cell lineage commitment. *Dev Cell* **6**(4): 483-495.
McDonald B and Kubes P (2010) Chemokines: sirens of neutrophil recruitment-but is it just one song? *Immunity* **33**(2): 148-149.
McMahon HT and Boucrot E (2011) Molecular mechanism and physiological functions of clathrin-mediated endocytosis. *Nat Rev Mol Cell Biol* **12**(8): 517-533.

McMahon HT and Boucrot E (2015) Membrane curvature at a glance. *J Cell Sci* **128**(6): 1065-1070.
McMahon HT and Gallop JL (2005) Membrane curvature and mechanisms of dynamic cell membrane remodelling. *Nature* **438**(7068): 590-596.
Mengsteab PY, Uto K, Smith AS, Frankel S, Fisher E, Nawas Z, Macadangdang J, Ebara M and Kim DH (2016) Spatiotemporal control of cardiac anisotropy using dynamic nanotopographic cues. *Biomaterials* **86**: 1-10.
Merrifield CJ and Kaksonen M (2014) Endocytic accessory factors and regulation of clathrin-mediated endocytosis. *Cold Spring Harb Perspect Biol* **6**(11): a016733.
Mi-Hee Kim MP, Kyungtae Kanga, Insung S. Choi (2014) Neurons on nanometric topographies: insights into neuronal behaviors in vitro. *Biomater Sci* **2**: 8.
Miller SE, Mathiasen S, Bright NA, Pierre F, Kelly BT, Kladt N, Schauss A, Merrifield CJ, Stamou D, Honing S and Owen DJ (2015) CALM regulates clathrin-coated vesicle size and maturation by directly sensing and driving membrane curvature. *Dev Cell* **33**(2): 163-175.
Mitra SK, Hanson DA and Schlaepfer DD (2005) Focal adhesion kinase: in command and control of cell motility. *Nat Rev Mol Cell Biol* **6**(1): 56-68.
Mittendorf KF, Marinko JT, Hampton CM, Ke Z, Hadziselimovic A, Schlebach JP, Law CL, Li J, Wright ER, Sanders CR and Ohi MD (2017) Peripheral myelin protein 22 alters membrane architecture. *Sci Adv* **3**(7): e1700220.
Miyabe Y, Miyabe C and Luster AD (2017) LTB4 and BLT1 in inflammatory arthritis. *Semin Immunol* **33**: 52-57.
Moissoglu K and Schwartz MA (2006) Integrin signalling in directed cell migration. *Biol Cell* **98**(9): 547-555.
Moore SW and Sheetz MP (2011) Biophysics of substrate interaction: influence on neural motility, differentiation, and repair. *Dev Neurobiol* **71**(11): 1090-1101.
Motlagh D, Hartman TJ, Desai TA and Russell B (2003) Microfabricated grooves recapitulate neonatal myocyte connexin43 and N-cadherin expression and localization. *J Biomed Mater Res A* **67**(1): 148-157.
Nakayama H, Yoshizaki F, Prinetti A, Sonnino S, Mauri L, Takamori K, Ogawa H and Iwabuchi K (2008) Lyn-coupled LacCer-enriched lipid rafts are required for CD11b/CD18-mediated neutrophil phagocytosis of nonopsonized microorganisms. *J Leukoc Biol* **83**(3): 728-741.
Newcomer ME and Gilbert NC (2010) Location, location, location: compartmentalization of early events in leukotriene biosynthesis. *J Biol Chem* **285**(33): 25109-25114.
Nguyen AT, Sathe SR and Yim EK (2016) From nano to micro: topographical scale and its impact on cell adhesion, morphology and contact guidance. *J Phys Condens Matter* **28**(18): 183001.
Nie Z, Hirsch DS and Randazzo PA (2003) Arf and its many interactors. *Curr Opin Cell Biol* **15**(4): 396-404.
Nishida N, Xie C, Shimaoka M, Cheng Y, Walz T and Springer TA (2006) Activation of leukocyte beta2 integrins by conversion from bent to extended conformations. *Immunity* **25**(4): 583-594.
Oakley C and Brunette DM (1993) The sequence of alignment of microtubules, focal contacts and actin filaments in fibroblasts spreading on smooth and grooved titanium substrata. *J Cell Sci* **106 (Pt 1)**: 343-354.
Obernier K and Alvarez-Buylla A (2019) Neural stem cells: origin, heterogeneity and regulation in the adult mammalian brain. *Development* **146**(4).

Oertle T, Klinger M, Stuermer CA and Schwab ME (2003) A reticular rhapsody: phylogenic evolution and nomenclature of the RTN/Nogo gene family. *FASEB J* **17**(10): 1238-1247.

Oh S, Brammer KS, Li YS, Teng D, Engler AJ, Chien S and Jin S (2009) Stem cell fate dictated solely by altered nanotube dimension. *Proc Natl Acad Sci U S A* **106**(7): 2130-2135.

Ohara PT and Buck RC (1979) Contact guidance in vitro. A light, transmission, and scanning electron microscopic study. *Exp Cell Res* **121**(2): 235-249.

Onesto V, Cancedda L, Coluccio ML, Nanni M, Pesce M, Malara N, Cesarelli M, Di Fabrizio E, Amato F and Gentile F (2017) Nano-topography Enhances Communication in Neural Cells Networks. *Sci Rep* **7**(1): 9841.

Orlova Y, Magome N, Liu L, Chen Y and Agladze K (2011) Electrospun nanofibers as a tool for architecture control in engineered cardiac tissue. *Biomaterials* **32**(24): 5615-5624.

Ott HC, Matthiesen TS, Goh SK, Black LD, Kren SM, Netoff TI and Taylor DA (2008) Perfusion-decellularized matrix: using nature's platform to engineer a bioartificial heart. *Nat Med* **14**(2): 213-221.

Palade GE (1953) An electron microscope study of the mitochondrial structure. *J Histochem Cytochem* **1**(4): 188-211.

Parent CA (2004) Making all the right moves: chemotaxis in neutrophils and Dictyostelium. *Curr Opin Cell Biol* **16**(1): 4-13.

Park J, Holmes WR, Lee SH, Kim HN, Kim DH, Kwak MK, Wang CJ, Edelstein-Keshet L and Levchenko A (2017) Mechanochemical feedback underlies coexistence of qualitatively distinct cell polarity patterns within diverse cell populations. *Proc Natl Acad Sci U S A* **114**(28): E5750-E5759.

Park J, Kim DH, Kim HN, Wang CJ, Kwak MK, Hur E, Suh KY, An SS and Levchenko A (2016) Directed migration of cancer cells guided by the graded texture of the underlying matrix. *Nat Mater* **15**(7): 792-801.

Park J, Kim DH and Levchenko A (2018) Topotaxis: A New Mechanism of Directed Cell Migration in Topographic ECM Gradients. *Biophys J* **114**(6): 1257-1263.

Park J, Kim HN, Kim DH, Levchenko A and Suh KY (2012) Quantitative analysis of the combined effect of substrate rigidity and topographic guidance on cell morphology. *IEEE Trans Nanobioscience* **11**(1): 28-36.

Parker KK and Ingber DE (2007) Extracellular matrix, mechanotransduction and structural hierarchies in heart tissue engineering. *Philos Trans R Soc Lond B Biol Sci* **362**(1484): 1267-1279.

Pasapera AM, Schneider IC, Rericha E, Schlaepfer DD and Waterman CM (2010) Myosin II activity regulates vinculin recruitment to focal adhesions through FAK-mediated paxillin phosphorylation. *J Cell Biol* **188**(6): 877-890.

Pertz O, Hodgson L, Klemke RL and Hahn KM (2006) Spatiotemporal dynamics of RhoA activity in migrating cells. *Nature* **440**(7087): 1069-1072.

Peter BJ, Kent HM, Mills IG, Vallis Y, Butler PJ, Evans PR and McMahon HT (2004) BAR domains as sensors of membrane curvature: the amphiphysin BAR structure. *Science* **303**(5657): 495-499.

Petrie RJ, Doyle AD and Yamada KM (2009) Random versus directionally persistent cell migration. *Nat Rev Mol Cell Biol* **10**(8): 538-549.

Phillipson M and Kubes P (2011) The neutrophil in vascular inflammation. *Nat Med* **17**(11): 1381-1390.

Potthoff E, Franco D, D'Alessandro V, Starck C, Falk V, Zambelli T, Vorholt JA, Poulikakos D and Ferrari A (2014) Toward a rational design of surface textures promoting endothelialization. *Nano Lett* **14**(2): 1069-1079.

Provenzano PP, Eliceiri KW, Campbell JM, Inman DR, White JG and Keely PJ (2006) Collagen reorganization at the tumor-stromal interface facilitates local invasion. *BMC Med* **4**(1): 38.

Provenzano PP, Inman DR, Eliceiri KW, Trier SM and Keely PJ (2008) Contact guidance mediated three-dimensional cell migration is regulated by Rho/ROCK-dependent matrix reorganization. *Biophys J* **95**(11): 5374-5384.

Qiu H, Gabrielsen A, Agardh HE, Wan M, Wetterholm A, Wong CH, Hedin U, Swedenborg J, Hansson GK, Samuelsson B, Paulsson-Berne G and Haeggstrom JZ (2006) Expression of 5-lipoxygenase and leukotriene A4 hydrolase in human atherosclerotic lesions correlates with symptoms of plaque instability. *Proc Natl Acad Sci U S A* **103**(21): 8161-8166.

Ramirez-San Juan GR, Oakes PW and Gardel ML (2017) Contact guidance requires spatial control of leading-edge protrusion. *Mol Biol Cell* **28**(8): 1043-1053.

Rapier R, Huq J, Vishnubhotla R, Bulic M, Perrault CM, Metlushko V, Cho M, Tay RT and Glover SC (2010) The extracellular matrix microtopography drives critical changes in cellular motility and Rho A activity in colon cancer cells. *Cancer Cell Int* **10**: 24.

Ray A, Lee O, Win Z, Edwards RM, Alford PW, Kim DH and Provenzano PP (2017a) Anisotropic forces from spatially constrained focal adhesions mediate contact guidance directed cell migration. *Nat Commun* **8**: 14923.

Ray A, Slama ZM, Morford RK, Madden SA and Provenzano PP (2017b) Enhanced Directional Migration of Cancer Stem Cells in 3D Aligned Collagen Matrices. *Biophys J* **112**(5): 1023-1036.

Recknor JB, Sakaguchi DS and Mallapragada SK (2006) Directed growth and selective differentiation of neural progenitor cells on micropatterned polymer substrates. *Biomaterials* **27**(22): 4098-4108.

Ren C, Yuan Q, Braun M, Zhang X, Petri B, Zhang J, Kim D, Guez-Haddad J, Xue W, Pan W, Fan R, Kubes P, Sun Z, Opatowsky Y, Polleux F, Karatekin E, Tang W and Wu D (2019) Leukocyte Cytoskeleton Polarization Is Initiated by Plasma Membrane Curvature from Cell Attachment. *Dev Cell* **49**(2): 206-219 e207.

Reneker DH CI (1996) Nanometre diameter fibres of polymer, produced by electrospinning. *Nanotechnology* **7**: 8.

Riching KM, Cox BL, Salick MR, Pehlke C, Riching AS, Ponik SM, Bass BR, Crone WC, Jiang Y, Weaver AM, Eliceiri KW and Keely PJ (2014) 3D collagen alignment limits protrusions to enhance breast cancer cell persistence. *Biophys J* **107**(11): 2546-2558.

Robins SP (2007) Biochemistry and functional significance of collagen cross-linking. *Biochem Soc Trans* **35**(Pt 5): 849-852.

Robinson RA (1952) An electron-microscopic study of the crystalline inorganic component of bone and its relationship to the organic matrix. *J Bone Joint Surg Am* **34-A**(2): 389-435; passim.

Rundqvist J, Mendoza B, Werbin JL, Heinz WF, Lemmon C, Romer LH, Haviland DB and Hoh JH (2007) High fidelity functional patterns of an extracellular matrix protein by electron beam-based inactivation. *J Am Chem Soc* **129**(1): 59-67.

Rutkovskiy A, Stenslokken KO and Vaage IJ (2016) Osteoblast Differentiation at a Glance. *Med Sci Monit Basic Res* **22**: 95-106.

Sachlos E, Gotora D and Czernuszka JT (2006) Collagen scaffolds reinforced with biomimetic composite nano-sized carbonate-substituted hydroxyapatite crystals and shaped by rapid prototyping to contain internal microchannels. *Tissue Eng* **12**(9): 2479-2487.

Santner SJ, Dawson PJ, Tait L, Soule HD, Eliason J, Mohamed AN, Wolman SR, Heppner GH and Miller FR (2001) Malignant MCF10CA1 cell lines derived from premalignant human breast epithelial MCF10AT cells. *Breast Cancer Res Treat* **65**(2): 101-110.

Sarret P, Esdaile MJ, McPherson PS, Schonbrunn A, Kreienkamp HJ and Beaudet A (2004) Role of amphiphysin II in somatostatin receptor trafficking in neuroendocrine cells. *J Biol Chem* **279**(9): 8029-8037.

Scarpa E and Mayor R (2016) Collective cell migration in development. *J Cell Biol* **212**(2): 143-155.

Schaff UY, Dixit N, Procyk E, Yamayoshi I, Tse T and Simon SI (2010) Orai1 regulates intracellular calcium, arrest, and shape polarization during neutrophil recruitment in shear flow. *Blood* **115**(3): 657-666.

Schedin P and Keely PJ (2011) Mammary gland ECM remodeling, stiffness, and mechanosignaling in normal development and tumor progression. *Cold Spring Harb Perspect Biol* **3**(1): a003228.

Schmid EM and McMahon HT (2007) Integrating molecular and network biology to decode endocytosis. *Nature* **448**(7156): 883-888.

Schorr W, Swandulla D and Zeilhofer HU (1999) Mechanisms of IL-8-induced Ca2+ signaling in human neutrophil granulocytes. *Eur J Immunol* **29**(3): 897-904.

Schweizer A, Ericsson M, Bachi T, Griffiths G and Hauri HP (1993) Characterization of a novel 63 kDa membrane protein. Implications for the organization of the ER-to-Golgi pathway. *J Cell Sci* **104 (Pt 3)**: 671-683.

Schweizer A, Rohrer J, Slot JW, Geuze HJ and Kornfeld S (1995) Reassessment of the subcellular localization of p63. *J Cell Sci* **108 (Pt 6)**: 2477-2485.

Shanley LJ, Walczysko P, Bain M, MacEwan DJ and Zhao M (2006) Influx of extracellular Ca2+ is necessary for electrotaxis in Dictyostelium. *J Cell Sci* **119**(Pt 22): 4741-4748.

Shattil SJ and Newman PJ (2004) Integrins: dynamic scaffolds for adhesion and signaling in platelets. *Blood* **104**(6): 1606-1615.

Sheikh BN, Bondareva O, Guhathakurta S, Tsang TH, Sikora K, Aizarani N, Sagar, Holz H, Grun D, Hein L and Akhtar A (2019) Systematic Identification of Cell-Cell Communication Networks in the Developing Brain. *iScience* **21**: 273-287.

Shibata Y, Shemesh T, Prinz WA, Palazzo AF, Kozlov MM and Rapoport TA (2010) Mechanisms determining the morphology of the peripheral ER. *Cell* **143**(5): 774-788.

Shibata Y, Voss C, Rist JM, Hu J, Rapoport TA, Prinz WA and Voeltz GK (2008) The reticulon and DP1/Yop1p proteins form immobile oligomers in the tubular endoplasmic reticulum. *J Biol Chem* **283**(27): 18892-18904.

Shimada A, Niwa H, Tsujita K, Suetsugu S, Nitta K, Hanawa-Suetsugu K, Akasaka R, Nishino Y, Toyama M, Chen L, Liu ZJ, Wang BC, Yamamoto M, Terada T, Miyazawa A, Tanaka A, Sugano S, Shirouzu M, Nagayama K, Takenawa T and Yokoyama S (2007) Curved EFC/F-BAR-domain dimers are joined end to end into a filament for membrane invagination in endocytosis. *Cell* **129**(4): 761-772.

Silva GA, Czeisler C, Niece KL, Beniash E, Harrington DA, Kessler JA and Stupp SI (2004) Selective differentiation of neural progenitor cells by high-epitope density nanofibers. *Science* **303**(5662): 1352-1355.

Simitzi C, Ranella A and Stratakis E (2017) Controlling the morphology and outgrowth of nerve and neuroglial cells: The effect of surface topography. *Acta Biomater* **51**: 21-52.

Simunovic M, Evergren E, Callan-Jones A and Bassereau P (2019) Curving Cells Inside and Out: Roles of BAR Domain Proteins in Membrane Shaping and Its Cellular Implications. *Annu Rev Cell Dev Biol* **35**: 111-129.

Sochacki KA, Dickey AM, Strub MP and Taraska JW (2017) Endocytic proteins are partitioned at the edge of the clathrin lattice in mammalian cells. *Nat Cell Biol* **19**(4): 352-361.

Solomkin JS, Robinson CT, Cave CM, Ehmer B and Lentsch AB (2007) Alterations in membrane cholesterol cause mobilization of lipid rafts from specific granules and prime human neutrophils for enhanced adherence-dependent oxidant production. *Shock* **28**(3): 334-338.

Song KH, Kwon KW, Choi JC, Jung J, Park Y, Suh KY and Doh J (2014) T cells sense biophysical cues using lamellipodia and filopodia to optimize intraluminal path finding. *Integr Biol (Camb)* **6**(4): 450-459.

Spanbroek R, Grabner R, Lotzer K, Hildner M, Urbach A, Ruhling K, Moos MP, Kaiser B, Cohnert TU, Wahlers T, Zieske A, Plenz G, Robenek H, Salbach P, Kuhn H, Radmark O, Samuelsson B and Habenicht AJ (2003) Expanding expression of the 5-lipoxygenase pathway within the arterial wall during human atherogenesis. *Proc Natl Acad Sci U S A* **100**(3): 1238-1243.

Stachowiak JC, Schmid EM, Ryan CJ, Ann HS, Sasaki DY, Sherman MB, Geissler PL, Fletcher DA and Hayden CC (2012) Membrane bending by protein-protein crowding. *Nat Cell Biol* **14**(9): 944-949.

Staii C, Viesselmann C, Ballweg J, Williams JC, Dent EW, Coppersmith SN and Eriksson MA (2011) Distance dependence of neuronal growth on nanopatterned gold surfaces. *Langmuir* **27**(1): 233-239.

Su Y, Xia W, Li J, Walz T, Humphries MJ, Vestweber D, Cabanas C, Lu C and Springer TA (2016) Relating conformation to function in integrin alpha5beta1. *Proc Natl Acad Sci U S A* **113**(27): E3872-3881.

Sun X, Driscoll MK, Guven C, Das S, Parent CA, Fourkas JT and Losert W (2015) Asymmetric nanotopography biases cytoskeletal dynamics and promotes unidirectional cell guidance. *Proc Natl Acad Sci U S A* **112**(41): 12557-12562.

Sun X, Hourwitz MJ, Baker EM, Schmidt BUS, Losert W and Fourkas JT (2018) Replication of biocompatible, nanotopographic surfaces. *Sci Rep* **8**(1): 564.

Sundd P, Gutierrez E, Koltsova EK, Kuwano Y, Fukuda S, Pospieszalska MK, Groisman A and Ley K (2012) 'Slings' enable neutrophil rolling at high shear. *Nature* **488**(7411): 399-403.

Sunyer R, Conte V, Escribano J, Elosegui-Artola A, Labernadie A, Valon L, Navajas D, Garcia-Aznar JM, Munoz JJ, Roca-Cusachs P and Trepat X (2016) Collective cell durotaxis emerges from long-range intercellular force transmission. *Science* **353**(6304): 1157-1161.

Tamir Gabaya EJ, Eshel Ben-Jacobb, Yael Hanein (2005) Engineered self-organization of neural networks using carbon nanotube clusters. *Physica A* **350**: 11.

Tamzalit F, Wang MS, Jin W, Tello-Lafoz M, Boyko V, Heddleston JM, Black CT, Kam LC and Huse M (2019) Interfacial actin protrusions mechanically enhance killing by cytotoxic T cells. *Sci Immunol* **4**(33).

Tan J and Saltzman WM (2002) Topographical control of human neutrophil motility on micropatterned materials with various surface chemistry. *Biomaterials* **23**(15): 3215-3225.

Tang B, Vu M, Booker T, Santner SJ, Miller FR, Anver MR and Wakefield LM (2003) TGF-beta switches from tumor suppressor to prometastatic factor in a model of breast cancer progression. *J Clin Invest* **112**(7): 1116-1124.

Tang M, Song Q, Li N, Jiang Z, Huang R and Cheng G (2013) Enhancement of electrical signaling in neural networks on graphene films. *Biomaterials* **34**(27): 6402-6411.

Tang Y, Yu P and Cheng L (2017) Current progress in the derivation and therapeutic application of neural stem cells. *Cell Death Dis* **8**(10): e3108.

Taylor PR, Roy S, Leal SM, Jr., Sun Y, Howell SJ, Cobb BA, Li X and Pearlman E (2014) Activation of neutrophils by autocrine IL-17A-IL-17RC interactions during fungal infection is regulated by IL-6, IL-23, RORgammat and dectin-2. *Nat Immunol* **15**(2): 143-151.

Teixeira AI, Abrams GA, Bertics PJ, Murphy CJ and Nealey PF (2003) Epithelial contact guidance on well-defined micro- and nanostructured substrates. *J Cell Sci* **116**(Pt 10): 1881-1892.

Teo BK, Wong ST, Lim CK, Kung TY, Yap CH, Ramagopal Y, Romer LH and Yim EK (2013) Nanotopography modulates mechanotransduction of stem cells and induces differentiation through focal adhesion kinase. *ACS Nano* **7**(6): 4785-4798.

Terasaki M, Chen LB and Fujiwara K (1986) Microtubules and the endoplasmic reticulum are highly interdependent structures. *J Cell Biol* **103**(4): 1557-1568.

Terasaki M, Shemesh T, Kasthuri N, Klemm RW, Schalek R, Hayworth KJ, Hand AR, Yankova M, Huber G, Lichtman JW, Rapoport TA and Kozlov MM (2013) Stacked endoplasmic reticulum sheets are connected by helicoidal membrane motifs. *Cell* **154**(2): 285-296.

Tong WG, Ding XZ, Hennig R, Witt RC, Standop J, Pour PM and Adrian TE (2002) Leukotriene B4 receptor antagonist LY293111 inhibits proliferation and induces apoptosis in human pancreatic cancer cells. *Clin Cancer Res* **8**(10): 3232-3242.

Trajkovic K, Hsu C, Chiantia S, Rajendran L, Wenzel D, Wieland F, Schwille P, Brugger B and Simons M (2008) Ceramide triggers budding of exosome vesicles into multivesicular endosomes. *Science* **319**(5867): 1244-1247.

Tsujita K, Suetsugu S, Sasaki N, Furutani M, Oikawa T and Takenawa T (2006) Coordination between the actin cytoskeleton and membrane deformation by a novel membrane tubulation domain of PCH proteins is involved in endocytosis. *J Cell Biol* **172**(2): 269-279.

Tzvetkova-Chevolleau T, Stephanou A, Fuard D, Ohayon J, Schiavone P and Tracqui P (2008) The motility of normal and cancer cells in response to the combined influence of the substrate rigidity and anisotropic microstructure. *Biomaterials* **29**(10): 1541-1551.

Ventre M, Natale CF, Rianna C and Netti PA (2014) Topographic cell instructive patterns to control cell adhesion, polarization and migration. *J R Soc Interface* **11**(100): 20140687.

Vicente-Manzanares M, Webb DJ and Horwitz AR (2005) Cell migration at a glance. *J Cell Sci* **118**(Pt 21): 4917-4919.

Vicker MG (2002) Eukaryotic cell locomotion depends on the propagation of self-organized reaction-diffusion waves and oscillations of actin filament assembly. *Exp Cell Res* **275**(1): 54-66.

Vieira MS, Santos AK, Vasconcellos R, Goulart VAM, Parreira RC, Kihara AH, Ulrich H and Resende RR (2018) Neural stem cell differentiation into mature neurons: Mechanisms of regulation and biotechnological applications. *Biotechnol Adv* **36**(7): 1946-1970.

Voeltz GK and Prinz WA (2007) Sheets, ribbons and tubules - how organelles get their shape. *Nat Rev Mol Cell Biol* **8**(3): 258-264.

Voeltz GK, Prinz WA, Shibata Y, Rist JM and Rapoport TA (2006) A class of membrane proteins shaping the tubular endoplasmic reticulum. *Cell* **124**(3): 573-586.

Voeltz GK, Rolls MM and Rapoport TA (2002) Structural organization of the endoplasmic reticulum. *EMBO Rep* **3**(10): 944-950.

Vollmer B, Schooley A, Sachdev R, Eisenhardt N, Schneider AM, Sieverding C, Madlung J, Gerken U, Macek B and Antonin W (2012) Dimerization and direct membrane interaction of Nup53 contribute to nuclear pore complex assembly. *EMBO J* **31**(20): 4072-4084.

Wan M, Tang X, Stsiapanava A and Haeggstrom JZ (2017) Biosynthesis of leukotriene B4. *Semin Immunol* **33**: 3-15.

Wang PY, Yu HT and Tsai WB (2010) Modulation of alignment and differentiation of skeletal myoblasts by submicron ridges/grooves surface structure. *Biotechnol Bioeng* **106**(2): 285-294.

Waterman-Storer CM and Salmon ED (1998) Endoplasmic reticulum membrane tubules are distributed by microtubules in living cells using three distinct mechanisms. *Curr Biol* **8**(14): 798-806.

Weigelt B, Warne PH and Downward J (2011) PIK3CA mutation, but not PTEN loss of function, determines the sensitivity of breast cancer cells to mTOR inhibitory drugs. *Oncogene* **30**(29): 3222-3233.

Weiner OD, Marganski WA, Wu LF, Altschuler SJ and Kirschner MW (2007) An actin-based wave generator organizes cell motility. *PLoS Biol* **5**(9): e221.

Weiner S and Traub W (1986) Organization of hydroxyapatite crystals within collagen fibrils. *FEBS Lett* **206**(2): 262-266.

Westrate LM, Lee JE, Prinz WA and Voeltz GK (2015) Form follows function: the importance of endoplasmic reticulum shape. *Annu Rev Biochem* **84**: 791-811.

Wicha MS, Liotta LA, Vonderhaar BK and Kidwell WR (1980) Effects of inhibition of basement membrane collagen deposition on rat mammary gland development. *Dev Biol* **80**(2): 253-256.

Wojciak-Stothard B, Curtis AS, Monaghan W, McGrath M, Sommer I and Wilkinson CD (1995) Role of the cytoskeleton in the reaction of fibroblasts to multiple grooved substrata. *Cell Motil Cytoskeleton* **31**(2): 147-158.

Wolf K, Te Lindert M, Krause M, Alexander S, Te Riet J, Willis AL, Hoffman RM, Figdor CG, Weiss SJ and Friedl P (2013) Physical limits of cell migration: control by ECM space and nuclear deformation and tuning by proteolysis and traction force. *J Cell Biol* **201**(7): 1069-1084.

Wu M, Wu X and De Camilli P (2013) Calcium oscillations-coupled conversion of actin travelling waves to standing oscillations. *Proc Natl Acad Sci U S A* **110**(4): 1339-1344.

Wu Z, Su M, Tong C, Wu M and Liu J (2018) Membrane shape-mediated wave propagation of cortical protein dynamics. *Nat Commun* **9**(1): 136.

Xi W, Sonam S, Lim CT and Ladoux B (2018) Tubular microscaffolds for studying collective cell migration. *Methods Cell Biol* **146**: 3-21.

Xia N, Thodeti CK, Hunt TP, Xu Q, Ho M, Whitesides GM, Westervelt R and Ingber DE (2008) Directional control of cell motility through focal adhesion positioning and spatial control of Rac activation. *FASEB J* **22**(6): 1649-1659.

Xu XY, Li XT, Peng SW, Xiao JF, Liu C, Fang G, Chen KC and Chen GQ (2010) The behaviour of neural stem cells on polyhydroxyalkanoate nanofiber scaffolds. *Biomaterials* **31**(14): 3967-3975.

Xue J, Wu T, Dai Y and Xia Y (2019) Electrospinning and Electrospun Nanofibers: Methods, Materials, and Applications. *Chem Rev* **119**(8): 5298-5415.

Yang K, Yu SJ, Lee JS, Lee HR, Chang GE, Seo J, Lee T, Cheong E, Im SG and Cho SW (2017) Electroconductive nanoscale topography for enhanced neuronal differentiation and electrophysiological maturation of human neural stem cells. *Nanoscale* **9**(47): 18737-18752.

Yang Y and Wu M (2018) Rhythmicity and waves in the cortex of single cells. *Philos Trans R Soc Lond B Biol Sci* **373**(1747).

Ye F, Kim SJ and Kim C (2014) Intermolecular transmembrane domain interactions activate integrin alphaIIbbeta3. *J Biol Chem* **289**(26): 18507-18513.

Yevick HG, Duclos G, Bonnet I and Silberzan P (2015) Architecture and migration of an epithelium on a cylindrical wire. *Proc Natl Acad Sci U S A* **112**(19): 5944-5949.

Yim EK, Pang SW and Leong KW (2007) Synthetic nanostructures inducing differentiation of human mesenchymal stem cells into neuronal lineage. *Exp Cell Res* **313**(9): 1820-1829.

Yipp BG, Petri B, Salina D, Jenne CN, Scott BN, Zbytnuik LD, Pittman K, Asaduzzaman M, Wu K, Meijndert HC, Malawista SE, de Boisfleury Chevance A, Zhang K, Conly J and Kubes P (2012) Infection-induced NETosis is a dynamic process involving neutrophil multitasking in vivo. *Nat Med* **18**(9): 1386-1393.

You MH, Kwak MK, Kim DH, Kim K, Levchenko A, Kim DY and Suh KY (2010) Synergistically enhanced osteogenic differentiation of human mesenchymal stem cells by culture on nanostructured surfaces with induction media. *Biomacromolecules* **11**(7): 1856-1862.

Young RN, Gillard JW, Hutchinson JH, Leger S and Prasit P (1993) Discovery of inhibitors of the 5-lipoxygenase activating protein (flap). *J Lipid Mediat* **6**(1-3): 233-238.

Yu H, Lui YS, Xiong S, Leong WS, Wen F, Nurkahfianto H, Rana S, Leong DT, Ng KW and Tan LP (2013) Insights into the role of focal adhesion modulation in myogenic differentiation of human mesenchymal stem cells. *Stem Cells Dev* **22**(1): 136-147.

Zarbock A, Lowell CA and Ley K (2007) Spleen tyrosine kinase Syk is necessary for E-selectin-induced alpha(L)beta(2) integrin-mediated rolling on intercellular adhesion molecule-1. *Immunity* **26**(6): 773-783.

Zaric J and Ruegg C (2005) Integrin-mediated adhesion and soluble ligand binding stabilize COX-2 protein levels in endothelial cells by inducing expression and preventing degradation. *J Biol Chem* **280**(2): 1077-1085.

Zhang B, Koh YH, Beckstead RB, Budnik V, Ganetzky B and Bellen HJ (1998) Synaptic vesicle size and number are regulated by a clathrin adaptor protein required for endocytosis. *Neuron* **21**(6): 1465-1475.

Zhao W, Hanson L, Lou HY, Akamatsu M, Chowdary PD, Santoro F, Marks JR, Grassart A, Drubin DG, Cui Y and Cui B (2017) Nanoscale manipulation of membrane curvature for probing endocytosis in live cells. *Nat Nanotechnol* **12**(8): 750-756.

Zigmond SH, Slonczewski JL, Wilde MW and Carson M (1988) Polymorphonuclear leukocyte locomotion is insensitive to lowered cytoplasmic calcium levels. *Cell Motil Cytoskeleton* **9**(2): 184-189.

Zimerman B, Arnold M, Ulmer J, Blummel J, Besser A, Spatz JP and Geiger B (2004) Formation of focal adhesion-stress fibre complexes coordinated by adhesive and non-adhesive surface domains. *IEE Proc Nanobiotechnol* **151**(2): 62-66.

Zong X, Bien H, Chung CY, Yin L, Fang D, Hsiao BS, Chu B and Entcheva E (2005) Electrospun fine-textured scaffolds for heart tissue constructs. *Biomaterials* **26**(26): 5330-5338.